

UNIVERSITÉ PARIS DIDEROT - SORBONNE PARIS CITÉ

ÉCOLE DOCTORALE 518
CONDENSED MATTER
AND INTERFACES

T H È S E

pour obtenir le grade de

Docteur en Sciences

de l'Université PARIS DIDEROT (Paris 7)

Présentée et soutenue par

Matthias BUSSONNIER

Actin Gel mechanics

Thèse dirigée par Timo BETZ et Cécile SYKES

préparée à l'Institut Curie

Soutenance le 16 Septembre 2014, devant le jury composé de :

<i>Président :</i>	Atef ASNACIOS	- Université Paris Diderot
<i>Rapporteurs :</i>	Karsten KRUSE	- Universität des Saarlandes
	Guillaume ROMET-LEMONNE	- LEBS
<i>Examinateurs :</i>	Laurent BLANCHOIN	- CEA Grenoble
<i>Directeurs :</i>	Timo BETZ	- Institut Curie
	Cécile SYKES	- Institut Curie

REMERCIEMENTS

Depuis pratiquement aussi loin que je me rappelle, j'ai été guidé dans la direction de la recherche et de la science. Le nombre de personnes qui ont participé à ma réussite de ce jour sont nombreux, et vu mon parcours relativement chaotique quant à ma discipline de prédilection ces dernières années, j'aurais pu me retrouver à faire une discipline bien différente de ce que je fais maintenant.

En bonne et due forme je me dois donc de remercier les différentes parties responsables de mon titre de Docteur.

Je fais partie des rares élus qui eurent durant leur trois (ou plus) années de thèse un financement au dessus de la médiane des doctorants. Bien que ce financement ne permette pas de s'acheter un 120 mètres carrés dans les quartiers chics de Paris, le surplus m'a permis de vivre un petit peu plus confortablement et avec un peu plus de liberté d'esprit pour travailler sur mon sujet de recherche. Je dois donc ceci en grande partie au Fond Pour la Recherche AXA qui sélectionne des candidats chaque année et promeut la recherche aussi bien en France qu'à l'international. Au-delà du geste financier, je remercie les employés d'AXA pour les événements organisés et les complexités administratives que je leur ai apportées.

Obtenir un financement dépend non seulement du candidat, mais aussi de son environnement scientifique. L'Institut Curie a bien sûr été un élément crucial non seulement dans la sélection de mon projet de thèse, mais aussi dans l'encadrement au cours de ces un peu plus de trois années passées à l'UMR 168. Mes Directeurs et Directrice de thèse font évidemment partie de la majorité de l'encadrement que j'ai reçu.

Je tiens donc à remercier Cécile premièrement pour m'avoir accepté dans son équipe, mais aussi pour avoir réussi à supporter mon caractère relativement opposé au sien durant tout ce temps. Bien que je pense que tu n'en sois pas certaine, je pense avoir appris beaucoup de choses et je ne serais pas là où je suis sans toi. Je te remercie aussi d'avoir été ma directrice de thèse et d'avoir progressivement laissé Timo prendre ton relais au fur et à mesure de mes progressions. Je sais que notre manière de fonctionner n'était pas toujours adaptée à la tienne.

Mon second directeur de thèse, Timo, a eu son habilitation à diriger les recherches juste en temps et en heure pour ma thèse. Je suis donc ton premier doctorant, et je pense que non seulement tu m'as beaucoup appris pendant ces quelques années, mais tu as aussi beaucoup évolué. J'ai beaucoup apprécié les défis intellectuels que l'on avait régulièrement afin de comprendre mon sujet de thèse, et je suis toujours persuadé que tu surestimes mes compétences dans certains domaines. J'apprécie toujours beaucoup les tournures de phrase sournoises que tu mets dans les lettres de recommandation, et j'ai remarqué que "les meilleurs 20% des 5 étudiants" que tu as eu dans ta carrière ça fait bien 1. Je pense que j'ai été très chanceux d'avoir un directeur de thèse comme toi, qui a passé du temps à faire des manips, monter de l'optique, faire de la théorie et écrire des articles. J'ai aussi beaucoup apprécié que tu essayes de comprendre les "nouvelles

Actin Gels dynamics,

technologies” que j’utilisais, et de te voir autant intéressé pour apprendre que pour enseigner. Tes futurs étudiants sont particulièrement chanceux. Merci pour ces 3 années et demi.

Lors de mon travail de thèse, j’ai aussi été encadré par Laurent Blanchoin qui s’est avéré être un très bon tuteur de thèse et d’excellent conseil, apportant toujours un regard neuf sur mes travaux. Laurent m’a aussi fourni la Protéine de coiffe sans laquelle je n’aurais pu avoir effectué mes expériences. Je te remercie pour tout cela, ainsi que pour avoir fait partie de mon jury de thèse.

J’ai eu l’occasion pendant ma thèse de rencontrer Guillaume Rommet-Lemone, qui est venu présenter ses travaux, en particulier sur la mécanique de filament unique d’actine. Merci d’avoir accepté de faire partie de mes rapporteurs, et d’avoir attentivement lu mon manuscrit. J’ai beaucoup apprécié tes remarques et questions.

Je tiens aussi à remercier Karsten Kruse pour avoir aussi accepté d’être rapporteur. Je pense que les gallicismes de mon manuscrit ont rendu sa lecture plus difficile que pour un francophone natif. Merci aussi pour la lecture attentive et les améliorations recommandées pour mon manuscrit.

Enfin je remercie Atef Asnacios pour avoir accepté d’être le président de mon jury de thèse. J’ai apprécié en particulier la petite interview surprise où j’ai dû présenter mon travail de thèse en 3 minutes.

Enfin globalement à tous les membres du jury : je redoutais les questions qui ont suivi mon exposé de thèse, mais j’ai finalement beaucoup apprécié l’exercice, que j’ai ressenti plus comme une véritable discussion scientifique que comme un examen. Merci donc pour vos encouragements, questions et sympathie, qui me semble-t-il n’est pas coutume dans toutes les thèses.

Au-delà de mes directeurs de thèse et de mon jury, l’ensemble de l’équipe et de l’UMR 168 m’a encadré, bien sûr les gens vont et viennent au gré des contrats et le temps passé avec chacun varie. Il y a bien sûr les gens avec qui j’ai travaillé, mais aussi ceux avec qui j’ai partagé un bureau pendant plus ou moins longtemps. Je ne vais pas citer chacun explicitement, mais ceux qui m’ont supporté se reconnaîtront bien, qu’il soit Grec, Indien, Australien, Américain, Français, ou plus généralement scientifique !

Quelques personnes se détachent en particulier, je pense à Julie qui avait toujours les réponses en biochimie et avait la main pour choisir les longs articles lors des “Journal Club”, Fabrice qui malgré nous avoir supporté pendant de longs mois et vu notre état déplorable a décidé de rester faire un thèse et garde sa joie de vivre, John pour sa touche d’exotisme et sa bonne humeur, Kasia pour avoir toujours eu plus de motivation que je n’en n’aurai jamais et qui n’a passé qu’un trop court moment en post-doc à l’Institut Curie, et enfin Wylie pour son dynamisme inépuisable !

J’ai aussi bien sûr tissé des liens avec des personnes avec qui je n’avais pas forcément de raison particulière pour collaborer mais avec qui j’ai eu de très bon contacts et dont je garderai de bons souvenirs : Benjamin, Jonathan, Mathilde, Coline, Mathieu, Sylvain et Simon restez comme vous êtes.

Un des derniers groupes de personnes que je souhaiterai remercier, sans qui j’aurais eu bien du mal à faire ma thèse bien que n’ayant pas particulièrement eu d’impact directement sur le contenu scientifique est le personnel d’entretien et les secrétariats. Je tiens donc à remercier Brigitte pour avoir toujours été présente à l’accueil. Un grand merci aussi à Karen, Laurence et Agnès pour avoir géré les complexités administratives ainsi que gérer les crises entre personnes durant ces trois années. Vous avez été d’un grand secours.

Au sein de mon équipe je tiens en particulier à remercier deux personnes, qui après 3 années passées ensemble sont aussi devenues des amis. Je parle bien sûr de Joël et Kevin. Joël a eu le bon goût de faire pratiquement le même parcours que moi mais un an à l’avance et donc d’essuyer tous les plâtres. Que ce soit des 6 mois de retard de salaire, à l’Université Paris VI qui égarait les convocations du ministère de l’enseignement afin de valider l’agrégation. J’avais donc un expert presque pré-cognitif à portée de main

pour toutes les problématiques qui allaient m'attendre. On remarquera aussi que la majorité des problèmes étant souvent rattachée à la même source au voisinage de la Bibliothèque François Mitterrand. Cela étant dit, Joël était aussi présent quand il s'agissait de Science avec un grand S aussi. L'humeur et la motivation de l'individu semblait être relativement bien corrélée à l'activité des protéines du Labo, il était relativement simple de connaître la fructuosité de la semaine : tel le météorologue qui observe les grenouilles, il suffisait d'observer le niveau de déprime de Joël dès le Lundi matin.

Le troisième larron de notre groupe qui probablement d'après les sources extérieures était en permanence fourré à la cafétéria était Kévin. Physiquement on pourrait comparer Joël et Kévin à Laurel et Hardy, cependant, contrairement à Kévin, Hardy faisait plus de 1m50 les bras levés. Portugais de base, le Kévin compense son manque de verticalité par sa capacité à débiter des bêtises de manière continue, et si rapidement qu'il lui arrive de se faire rire lui-même. Kévin, tu as donc apporté la bonne humeur et la joie de vivre pendant une grande partie de ma thèse, ta capacité à engranger toute cette bibliographie m'étonne toujours, et tes compétences expérimentales restent inégalées. Je pense que tu aurais été un très bon atout pour la Recherche, cependant le système semble ne pas t'apprécier. Étant donné que tu as décidé de postuler à Pôle Emploie le dernier de mes jours en thèse, je continuerai à m'imaginer que c'est me perdre qui t'a fait t'arrêter !

Au-delà de tous mes collègues et amis qui m'ont soutenu pendant ces trois années, je voudrais remercier tous ceux que je connais depuis plus longtemps. En particulier il existe un petit groupe de huit personnes avec qui j'ai vécu pendant les années précédent ma thèse. Il faut croire que malgré notre QI combiné on a presque tous fait le choix de partir en thèse, comme quoi il ne faut pas toujours faire confiance à un groupe de scientifiques livrés à eux-mêmes. Je pense donc bien sûr aux gens de la LMDB (et associés) qui m'ont donné toutes ces compétence multi-disciplinaires que je n'aurais pas eu à l'ENS, et pour tous ces instants de vie passés, avant pendant et après avoir vécu sous le même toit. Merci donc à Félix, Émilien, Pierre, Pierre, Cécile, Jben, Elsa et Olivier pour, parmi tant d'autres choses: les sites de propagande soviétique, les oeufs en chocolat sur les oreillers, les vaches, les tomates, la conduite sur la neige à 3h du mat' pour aller aux urgences, les pagnes, les "vous êtes tous moches", les chaussettes trouées, Le jeu (The Game), les communications laser avec la tour Montparnasse, le gruyère aux pâtes, les enregistrements et montages audio subtils, les pots de yaourt pleins d'eau, le mouflon, les lapins à l'arbalète, le cheval, le poulet élevé en plein air et autre procédure en justice.

Je remercie aussi tous ceux qui faisaient partie intégrante de notre délire, et qui ont, ou pas, fait partie intégrante d'une fiction poste apocalyptique écrite par une des personnes sus-citées. Toute ressemblance de personnage de cette fiction avec d'autre(s) doctorant(s) de l'UMR 168 serait purement non fortuite.

Et je garde un remerciement spécial pour Jean Boucasier, et les TGV du jeudi matin pour Bordeaux.

Une pensée pour les acteurs, réalisateurs et équipe technique du "Sociologue et du Physicien" (que je vous invite à regarder sur DailyMotion). Ce fut un grand moment de n'importe quoi que de condenser 3 ans de thèse en 5 minutes de film. Merci donc à Smaïl, Émilien, Simon, Fabrice, Jben, Kéevin et Camille pour ces moments qui resteront dans les archives de l'Internet.

Un grand merci aussi à ces quelques personnes à l'autre bout du monde que j'ai rencontrées par le biais d'Internet, et grâce à qui maintenant je suis en post-doc. Merci donc à la communauté de SciPy et d'IPython au sens large.

Je dois admettre que pendant ses trois années de thèse, je n'ai pas été particulièrement communicatif, et que je dois un grand merci à toute ma famille qui a supporté ma mauvaise humeur ainsi que mon silence pendant de longues périodes.

Si vous lisez ce manuscrit dans sa version finale, je dois la bien plus faible teneur en erreurs d'anglais à ma tante qui a tenté de comprendre ce que je voulais dire et a dû bien souffrir pour corriger toutes ces pages.

Je tiens à remercier mes grand-parents paternels, que j'ai relativement peu vu durant mon doctorat, bien qu'ils étaient eux aussi dans la région parisienne. Merci d'organiser tous les ans les réunions où toute la famille se retrouve.

Merci à tous mes frères, soeurs, et cousins qui ont pu venir me voir soutenir, ou pas, ainsi que pour leur soutien.

Et bien sûr remercier mes grands-parents maternels, qui depuis que je suis tout petit m'ont aussi soutenu dans mon envie de devenir chercheur, et continuent à me soutenir aujourd'hui. Il est vrai cependant que ma notion de chercheur a bien évolué en une vingtaine d'années. Ma première définition de chercheur lorsque j'étais encore bien plus jeune était plus proche de l'image caricaturale du scientifique fou dans son garage que de ce que je suis actuellement. Le fait est que j'ai en grande partie réussi grâce à vous. Merci de m'avoir soutenu pendant toutes ces années, et d'avoir tenté de comprendre ce que je faisais, bien que ce soit en anglais. Merci aussi d'avoir appris à utiliser Internet, rien que pour me laisser des messages pour me rappeler que j'étais trop absent, et de ne pas me l'avoir reproché.

Un grand merci et de grandes excuses à ma mère. Je pense que le côté scientifique de la famille a sauté une génération, mais j'envie beaucoup ton caractère artistique, et j'ai beaucoup aimé voir les progressives déformations des métaphores que j'utilisais pour t'expliquer mon travail. Je sais que l'on était pas très doués en communication et que si que pendant que tu attendais de mes nouvelles, j'attendais que tu m'en demandes. J'espère que maintenant que la thèse est terminée je vais être un peu plus communicatif, et que si je ne le suis pas tu n'hésiteras pas à me le dire ! Merci aussi à toi Paul, je sais que gagner un fils qui est déjà adolescent n'a pas dû être une chose facile, et merci de m'avoir accepté tel que je suis. J'espère que vous viendrez me voir continuer mes recherches à l'autre bout de la planète, et que vous passerez des heures à vous extasier devant la végétation et les différentes formes d'art qui diffèrent de ce que l'on croise ici.

Finalement je voudrais te remercier toi, ma Camille. On a emménagé ensemble le jour où j'ai reçu mon acceptation pour ma bourse de thèse, et tu as supporté plus que tout le monde mon caractère pendant mes périodes de baisse de morale, ainsi que les autres jours aussi. C'est toi qui m'a donné le courage au jour le jour, et la motivation pour avoir un peu plus d'énergie chaque jour. Tu as toi aussi décidé de faire une thèse, et contrairement à toi, je serai loin lors de ta troisième année. Malgré la distance je vais faire tout ce que je peux pour te rendre tout ce que tu m'as donné pendant ces années. Je dois admettre que le langage que tu utilises dans ta thèse de mathématiques appliquées est loin de ce que moi j'utilise et fut souvent source de discorde et dispute, reste néanmoins que tu es quelqu'un de bien plus doué que tu ne veux le croire. En plus d'être une mathématicienne, tu es aussi une dessinatrice, et je resterai toujours émerveillé de la façon dont tu capturais ces instants si particuliers avec ton crayon, ou reproduisait si bien les anecdotes que je te racontais. Dessiner fait partie de toi, continue quoi qu'il arrive ! Enfin tu as ce talent unique, parmi tous ceux qui font ton charme, tu sais me comprendre.

Merci pour tous ces instants passés, et futurs que nous passons ensemble.

Une petite pensée pour toi qui est parti pendant ces trois années. Tu me manqueras.

CONTENTS

1	Background	3
1.1	Introduction	3
1.2	Living Cells	4
1.3	Oocyte	4
1.3.1	Cell Organelles	5
1.3.2	The Cytoskeleton	7
1.4	The Role And Composition Of The Cytoskeleton	7
1.4.1	Composition of the cell cytoskeleton	8
1.4.2	The actin cortex	17
1.4.3	Cell Motility	17
1.4.4	Organelle Positioning	20
1.5	In vitro reconstituted actin networks	21
1.5.1	Bead motility assay	22
1.5.2	Liposomes	23
1.6	Membrane Physics	24
1.7	Actin networks as viscoelastic material	26
1.7.1	Elastic Modulus	27
1.7.2	Poisson's Ratio	29
1.7.3	Viscosity	29
1.7.4	Viscoelasticity	29
1.8	Optical tweezer	31
1.8.1	Determination of trapping forces and bead displacement	32
2	Materials and Methods	35
2.1	Buffers	35
2.1.1	G-Buffer	35
2.1.2	Polymerisation Buffer	35
2.1.3	X-Buffer with BSA	36
2.1.4	ATP-Mix Buffer	36
2.2	Protein preparation	36
2.2.1	pWA (also called pVCA)	36
2.2.2	Actin	36
2.2.3	Profilin	36
2.2.4	Arp2/3	37
2.2.5	Capping protein	37

2.2.6	Myosin II	37
2.3	Lipids, reagent and proteins	37
2.4	Doublet preparation	37
2.5	Bead Preparation	38
2.5.1	Actin-Bead Preparation	38
2.5.2	Probe Bead Preparation	39
2.6	Force indentation experiments	39
2.6.1	Preparation of sample	39
2.6.2	QPD positioning and calibration of microscope	39
2.6.3	Initial bead trapping	40
2.6.4	Indentations	41
2.7	Time Shared Optical Traps	41
2.8	Oocyte	43
2.8.1	Oocyte obtention	43
3	Mechanical properties of a far reaching actin cloud	45
3.1	Introduction	45
3.2	Actin-Bead System	46
3.3	Probe Bead System	48
3.4	Experimental description	48
3.4.1	Approach Phase	48
3.4.2	Relaxation Phase	49
3.4.3	Retraction part	49
3.4.4	Reconstitution of Force-distance-curve	49
3.4.5	Repetitive indent	50
3.4.6	Effect of approach speed	50
3.5	Experimental observations	52
3.5.1	Approach phase modeling	52
3.5.2	Variation of parameters with Capping Protein	56
3.5.3	Determination of Young's Modulus	56
3.5.4	Mechanical properties	61
3.5.5	Interpretation	65
3.6	Relaxation phase	67
3.6.1	Retraction Phase	69
3.7	Discussion	71
4	Cortical tension measured on liposome doublets	73
4.1	Introduction	73
4.2	Experimental description	74
4.2.1	Formation of liposomes doublets	74
4.2.2	Formation of actin cortex on doublets	74
4.2.3	Visualisation of the interface	74
4.2.4	Geometrical parameters	76
4.3	Experimental Observations	77
4.3.1	Effect of myosin-II injection	77
4.3.2	Relation between the angles and tension	77
4.3.3	Contact angle dispersion	79
4.3.4	Tension of actin-shell	80

4.4	3D observation	80
4.5	Discussion	81
4.5.1	Cortical tension is homogeneous for single doublet	81
4.5.2	Relative increase in cortical tension	85
4.5.3	Cortical tension increase in doublets and in cells	85
4.5.4	Different contributions for cortical tension	85
4.5.5	Conclusion	86
4.6	3D fitting	86
4.6.1	First step: Fitting a single liposome	86
4.6.2	Fitting a doublet	88
4.6.3	Discussion	95
4.6.4	Conclusion	95
5	Active cytoplasm movement in mouse oocytes	99
5.1	Introduction	99
5.2	Oocytes	99
5.3	Measure of activity	99
5.4	Conclusion	103
6	Conclusion	105
7	Appendix	107
7.1	Mechanical detection of a long range actin network emanating from a biomimetic cortex Preprint	107
7.2	Cell-sized liposome doublets reveal active cortical tension build up Draft	127
Bibliography		149

PREAMBLE

During my PhD, I decided to investigate the effect of the actin network on the mechanical properties of cells. Indeed, cell mechanics are a key parameter that has crucial impact on cellular and organisms functions. Being able to detect changes in the mechanical properties and to understand the mechanism that governs these changes is an important step in the study of cellular behavior as well as in the differentiation of healthy from cancerous cells and tissue. Understanding the mechanisms that are at the origin of cell motion and shape changes, is also a decisive step in controlling cell behavior, with the ultimate goal to prevent cancer cell invasion and division without impairing healthy cells.

During the last three years, I decided to focus on biomimetic systems and to determine the characteristics of actin networks. Actin is a highly conserved component across the living domain, and it plays a major role in cell mechanics. By interacting with a number of other components of the cell, actin is able to form various different types of networks. I decided to focus my research on such networks that were created under controlled conditions.

Along this dissertation, we will mainly focus on three systems.

First, we reconstituted an already observed actin network — the actin cortex — on a biomimetic system, then showed that a second sparse actin network, which was previously unseen, emanates from it, and finally characterized its mechanical properties. We developed the idea that the effect of this second network cannot be neglected in cells and investigated a few of the phenomena it may be involved in.

As the effect of such a sparse actin has not been demonstrated in living cells, we decided to investigate the effect of another sparse actin network found in a living cells. In collaboration with the group of Marie Hélène Verlhac at the College de France, we studied the mechanical properties in the cytosol of mouse oocytes. We saw in this system that actin-related proteins had hi-impact on the structure and the mechanics of both the cell and the actin network.

Characterizing the dynamics of a network in a living cell by controlling the conditions remains complex. In a third research stream, we characterized the dynamical changes of tension created by reconstituted actin cortices, that are linked to a lipid membrane. By studying liposome “doublets”, we could measure the variation of tension generated by the acto-myosin cortex over time. This system is composed by a liposome doublet covered with an actin network. By imaging with Spinning disk microscopy, we could reconstruct the changes in the acto-myosin network and deduce them in its properties, from the geometrical variation during the network contraction.

CHAPTER

ONE

BACKGROUND

1.1 Introduction

Cells are the basic components of living organisms. Understanding their individual behavior and the way they function is a key step to understand how they interact with their environment. One of the key components within most cells is the actin cytoskeleton, which is made up of actin monomers, a highly conserved protein across species, which plays an important role for cell mechanics, ranging from cell migration to cell differentiation and division. Hence the crucial role it plays for the mechanical properties of the cell and its mechanical interaction with the environment. Under the cell membrane lies a thin actin network which controls the mechanical properties of the cell: the actin cortex. The mechanical behavior of this actin cortex is itself driven by the dynamics and interactions within the actin network it is made of. So, understanding this actin network is a key to learn how the actin cortex behaves, leading to a better understanding of cells and tissue.

The properties of an actin network highly depend on its structure. The structure itself depends on many parameters that influence how the network is formed. The network structure and formation, influenced both by the physical and chemical conditions and the spatial and temporal variation of these parameters, such as mechanical stress or ion-concentration, can determine the fate of the network. It is therefore important to study these networks and their dynamic behavior in order to grasp the changing structure of the cell.

Cells are complex systems that adapt their shape, mechanical properties and biochemical conditions permanently. The spatial repartition of these properties is also variable as the cell regulates the concentration of proteins all across its cytoplasm. In order to achieve a thorough study of the effect of each component independently, it is crucial to study actin networks in a controlled environment.

Biomimetic systems allow to respond to most of these concerns. First they provide a controlled environment that mimics *in-vivo* phenomena. Second, biochemical conditions can be well controlled, both in space and time, hence allowing to precisely fine tune experimental conditions. Biomimetic systems are also particularly adapted to be combined with optical traps, which allow us to study local mechanical properties of actin networks with high temporal resolution. The combination of both allows us to get insight into the variation of these mechanical properties as a function of time and space, with high precision.

During my PhD, I have focused on the mechanical properties of branched actin networks polymerizing on optically trapped polystyrene beads. Such networks have already been studied before [Kawska et al. 2012] but have been suspected to be highly inhomogeneous. Optical traps allow to probe the mechanics of yet inaccessible parts of the network. I further studied actin networks on other biomimetic systems constituted of liposomes, in order to better understand the effect of actin cortex polymerisation on membrane tension and

to characterize network dynamics over time. Finally, I participated in a collaboration in order to understand the implication of such actin networks in living mouse oocytes.

1.2 Living Cells

Cells are the basic building blocks of life, and all living beings are composed of cells, from unicellular up to multicellular organisms like us. Unicellular organisms must accomplish all their functions within a single cell. At the other end, in multicellular organisms cells differentiate in order to accomplish specialised tasks often by regrouping into organs. Despite sharing the same genetic material, for each cell to accomplish a different task often requires different mechanical properties. The variation of elasticity and other mechanical properties of cells derive from the structure they are composed of.

Cells are hence able to adapt to their environment and develop functions and behavior that may change over time. A small change of timing and/or biochemical conditions can highly injure the development of an organism: for example modification of the actin network at a given time during the cell cycle prevents symmetric division [Lenart et al. 2005], [Vasilev et al. 2012]. Furthermore, the mechanical properties of the substrate can govern the differentiation of cells: Soft substrate will favor brain-tissue cell, where stiff substrates increase the appearance of muscle cells [Engler et al. 2006].

Nonetheless, even with all these different behavior and phenotypes, cells have a common structure. The exterior of the cell is separated from the inside by a plasma membrane. The interior of the cell is filled with the cytoplasm which contains diverse structures such as organelles, genetic material, and a large number of proteins that the cell uses to accomplish its functions. To communicate with the outside, cells have a series of mechanisms that allow signals and cargo to pass the membrane. This communication can be chemical, but mechanics is also known to participate in the process. To sense their mechanical environment, cells often use adhesion complexes to attach to the substrate, and integrins as trans-membrane protein to transfer the force to the cell cytoskeleton situated inside the cell. Chemical signals can either cross the membrane through trans-membrane proteins, while endocytosis and exocytosis are ways for the cell to import and export proteins and chemicals through its membrane.

1.3 Oocyte

A particular cell type I was interested in during my PhD are mouse oocytes. Oocytes are female germinal cells in the process of gametogenesis. Unlike somatic cells that undergoes symmetric division via mitosis which leads to two identical cells sharing the same genetic material, oocytes undergo a different process called meiosis. Meiosis in oocytes is a highly asymmetric process necessary for the specificity of being large haploid cells, containing at the end of meiosis only one chromosome of each pair that constitutes the genetic material of a mouse. The second chromosome of each pair will be provided during fertilisation of the oocyte by the male sperm.

The exact process of oocyte formation can vary among species, and in the following we will describe the main mechanisms.

The complete process of egg maturation starts with primordial germ cells that undergo mitosis to replicate until they enter the first meiosis (Meiosis I) at which state they are called primary oocytes and are still diploid, that is to say still contains two chromosomes of each pair.

The primary oocyte will start maturation and growth and then undergo a first asymmetric division just after prophase I. This first division is asymmetric both in the genetic material separation and in the unequal size of the formed daughter cell. Indeed, the primary oocyte will divide into a secondary oocyte and a polar body. Both, the secondary oocyte and the polar body are haploid and contain only half of the genetic material of the primary oocyte. The secondary oocyte can go through Meiosis II in which it undergoes a second asymmetric division and expulsion of a second polar body. These polar bodies will eventually degenerate ([Fig 1.1](#)).

During meiosis, the process of cell division also differ from mitosis. Instead of separating into two identically sized cells through the formation of a cytokinetic ring, the primary oocyte will become the secondary oocyte by expulsion a polar body. The formation expulsion of the polar body require precise positioning of the cell organelles. During prophase I the nucleus of the oocyte is carefully centered, undergoes a nuclear breakdown and spindle formation. The first meiotic spindle will migrate toward the oocyte cortex along its major axis. Once at the cortex, half of the genetic material of the spindle will be expelled through the membrane forming the first polar body of much smaller size than second oocyte.

Mouse oocyte are good model systems to study the mechanical properties inside cells. They form big spherical cells with a diameter of around 80 μm which allow to study the mechanical properties at different locations in the cytoplasm.

In the third part of my PhD I participated in a collaboration with Marie-Hélène Verlhac and Maria Almonacid at Collège de France who are interested in the effect of actin dynamics in oocyte cytoplasm during the different parts of oocyte gametogenesis.

1.3.1 Cell Organelles

Inside the cytoplasm, cells have a number of structures with different and specialised functions which are called organelles. The position and state of organelles is of great importance for the cell to achieve its functions. Probably the most known organelle is the cell nucleus of eukaryotic cells that contains the genetic material. Attached to the nucleus is the endoplasmic reticulum which is the organelle responsible for translating RNA coming from the nucleus to functional proteins that will be delivered across the cell after maturation in vesicles. These vesicles are transported across the cell both by dyneins and kinesins — molecular motors — that walk along microtubules originating from the centriole part of the centrosome but also by myosins walking along actin filaments. All of those processes consume energy in the form of ATP, generated within the mitochondria spread across the cytoplasm. A schematic of the cell with some organelles can be seen on [figure 1.2](#).

The positioning of organelles is crucial for the life of the cell. During meiotic division of cells, for example, it has been seen that the positioning of the nucleus at the center of mouse oocytes happens before its migration closer to the cortex to expel the first polar body. Failure to do so results in an incorrect amount of DNA in germinal cell that can lead to infertility.

It is already known that microtubules play a key role in organelle positioning. Microtubules emanating from centrosome position at the two ends of the cell during its division are used to fetch the correct chromosomes. Each chromosome is pulled towards the centrosome which leads to each daughter cell having the same amount of DNA.

Actin plays also an determinant role in organelle positioning process, like in drosophila oocyte maturation where it positions the nurses cell away from the dumping canal [[Huelsmann et al. 2013](#)]. In a later

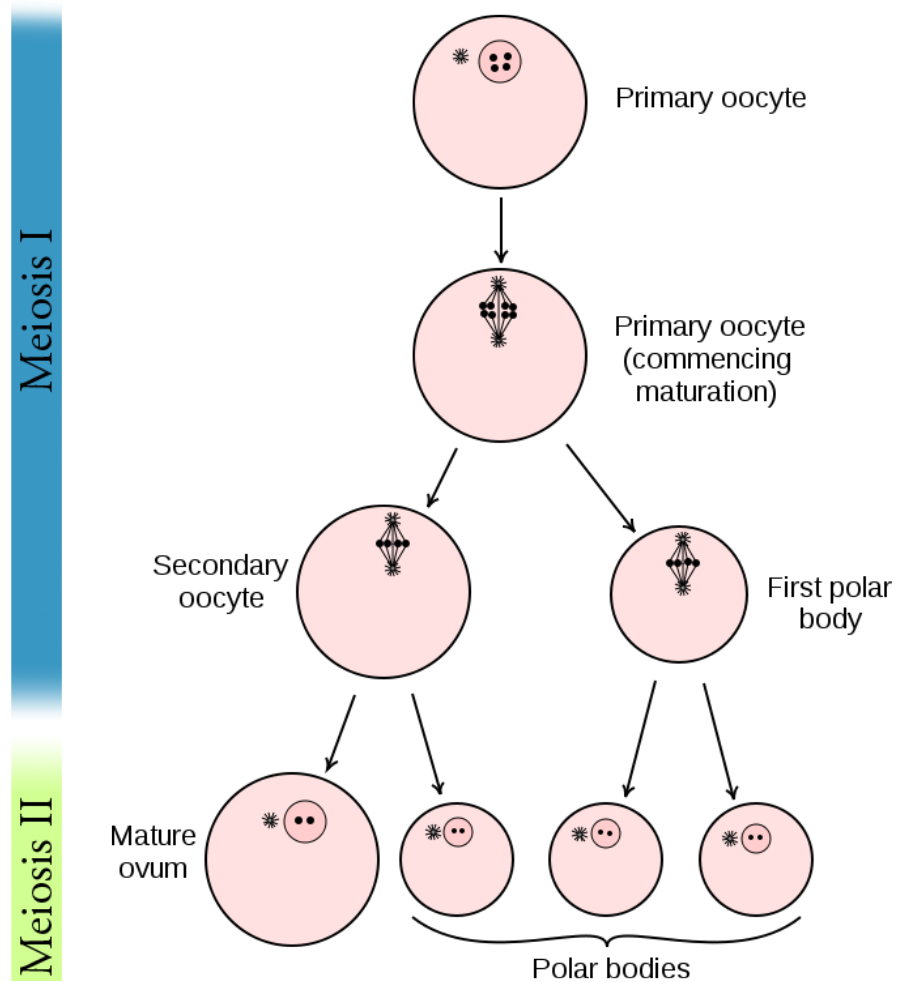


Figure 1.1: Asymmetric division of oocytes into polar bodies. The primary oocyte asymmetrically divides into a secondary oocyte and a smaller polar body each containing half the DNA of the mother cell. The secondary oocyte will divide asymmetrically a second time to become the mature ovum while expelling a polar body. This asymmetric division process allows the formation of a large haploid cell. Adapted from Wikipedia – Gray's Anatomy – and [Alberts et al. 2008].

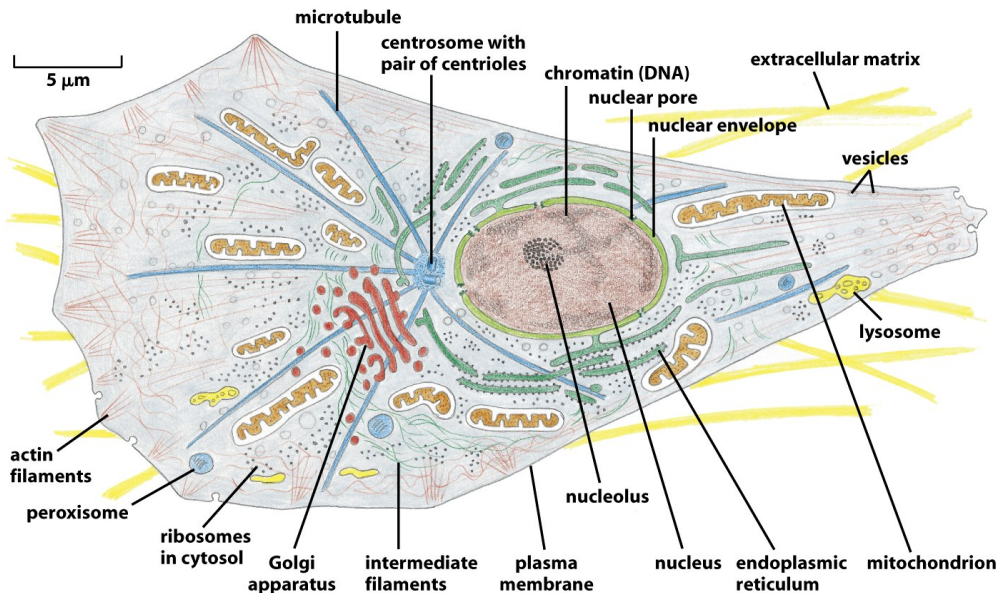


Figure 1-30 Molecular Biology of the Cell 5/e (© Garland Science 2008)

Figure 1.2: Schematic of an eukaryotic cell, adapted from [Alberts et al. 2008]. Visualized are the many components that constitute the majority of cells. Cell shape and size can highly vary, from quasi spherical with a typical size of ten micrometers to elongated neurones that can be tens of centimeters long.

chapter (*Organelle Positioning*) we will develop a few keys points where actin is indispensable in organelle positioning and how this relate to the biomimetic actin networks we reconstitute.

1.3.2 The Cytoskeleton

The cytoskeleton, literally skeleton of the cell, is the structure which gives the shape to a cell. As for other multicellular animals that posses skeleton, its shape is often a hint on how an organism moves. As feet, fins and wings are characteristics that will tell you whether a animal prefer land, sea or air, the cytoskeleton will tell you many things about a cell.

Unlike the (exo)-skeleton of animals which is rigid and static, the cytoskeleton of cell is a highly dynamic structure that keeps remodeling itself on a short time scale compared to the speed at which a cells move. Thanks to these dynamics, the cytoskeleton can achieve its functions. As vertebrates skeletons are necessary to transmit force from one part of the body to another, the cytoskeleton is responsible not only to transmit the forces the cell is exerting, but also to generate these forces. The cytoskeleton connect a cell to its environment, both mechanically and biochemically.

We will consecrate a longer part of this work to describe the cytoskeleton.

1.4 The Role And Composition Of The Cytoskeleton

We have already introduced the cell cytoskeleton in the previous part, and we will now describe its components and functionality more in detail here. The cytoskeleton has three main functions, it connects the cell both physically and biochemically to the external environment, generate and coordinate the forces that

give the cell its shape and allows it to move. It is also responsible for organising spatially the cell content [Fletcher et al. 2010]. The cytoskeleton is also in particular sensitive to spatial and temporal information that can affect cell fate and the assembly of the cytoskeletal structure. This can be seen for example with the bud scar of budding yeast that persists after division.

1.4.1 Composition of the cell cytoskeleton

The cytoskeleton is mainly composed of three types of filaments. Microtubules, intermediate filament and actin filament, also known as microfilaments.

Microtubules are the widest structure with a diameter of 20nm (Fig 1.3) and the stiffest of the three kinds of filaments with a *persistence length* in the order of millimeters, much longer than the size of the usual cell. Microtubules are extensively studied [Valiron et al. 2001]. Microtubules are formed by the polymerisation of a heterodimer of tubulin that leads to the formation of polar (oriented) filaments that can be walked on by molecular motors. These molecular motors can be decomposed in two families – kinesins and dyneins – depending on the end towards which the motor preferably walk. Microtubules are mostly known for their action during mitosis where they will form the majority of the mitotic spindle that drive the segregation of the chromosomes in two groups, each group ending in one of the daughter cells.

Microtubules have the characteristic of being highly dynamic by alternating between two states of rapid growth and a rapid shrinkage. The transition from microtubule growth to shrinkage is called a *catastrophe*, the transition from shrinkage to growth is called a *rescue*.

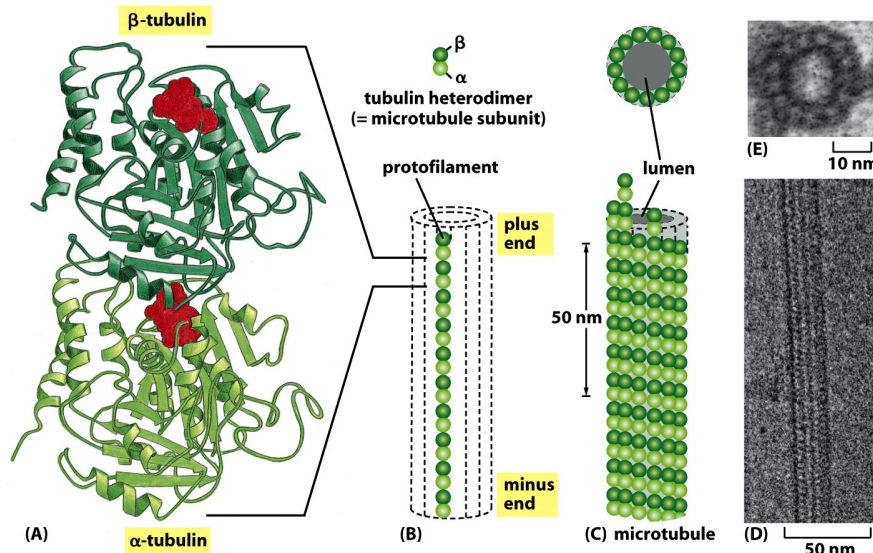


Figure 16-11 Molecular Biology of the Cell 5/e (© Garland Science 2008)

Figure 1.3: Structure of an heterodimer of tubulin and assembly into a microtubule. Electron microscopy of a single microtubule filament. From [Alberts et al. 2008]. A) Structure of heterodimer of tubulin B) Heterodimers can assemble forming polar filaments. C) Filaments can assemble into microtubules. D,E) Electron microscopy image of microtubules.

Intermediate filaments are of medium diameter in the order of around 10nm, in between actin and microtubules filaments, hence their name. Unlike microtubules and actin filaments, intermediate filaments are composed by several sub-families of proteins and are non-polar.

Intermediate filament have an important role in the mechanical properties of cells due to the fact that they are particularly resistant to stretching.

Unlike actin and microtubules, they are thought to be passive, with mechanical properties mainly deriving from how multiple filaments are linked together laterally.

Actin, is the third component of the cytoskeleton, the one on which we will focus on most of our efforts. Actin monomers, also called *G-Actin* for globular actin can polymerise. By polymerizing actin monomers (*G-actin*) into actin filaments (*F-actin*), the thinnest of the three cytoskeletal components forms. Actin is produced in the cell as a globular protein of ~40 kDa (Fig 1.4) that once associated with ATP or ADP polymerises into helicoidal filament with a diameter between 7 and 9nm. The formed actin filaments are polar, where both extremities are respectively called the plus (+) or barbed end, and the minus (-) or pointed end. The polarity of the actin filament is of importance as this gives rise to a preferred direction for most processes that can happen on the filaments.

The actin protein is highly conserved across species, and is known to directly interact with hundreds of proteins [DosRemedios et al. 2003].

Single undecorated filaments will behave as semi-flexible polymers at the scale of the cell with a persistence length in the order of 10 μm [Isambert et al. 1995]. When they assemble into different structures and networks, or associate with other proteins and molecules the resulting mechanical and dynamic properties can be highly variable.

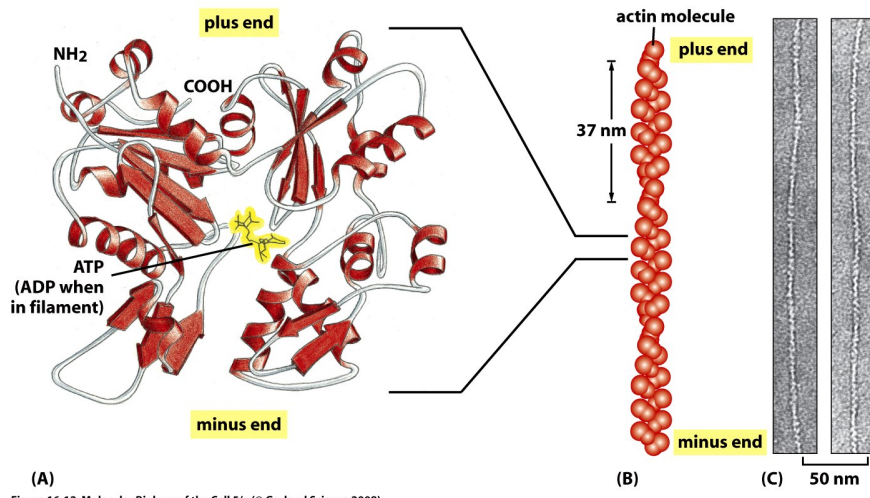


Figure 1.4: A) Structure of a single monomer of actin, and electron microscopy snapshot. — from [Alberts et al. 2008].

Dynamics of actin polymerisation

The assembly mechanisms that allow to go from single monomers of actin (also refer to as *G-actin* for globular actin) to actin filament (also refer as *F-actin*) need to be well understood to explain the different network structures created by actin filaments in the presence of other proteins.

The polymerisation of ATP/ADP actin monomers to form an actin filament need to go through the step of forming an actin proto-filament which is constituted of at least 3 actin monomers. This will most of the

Actin Gels dynamics,

time be the kinetically limiting step. Once proto-filaments are present in solution, single monomers can be freely added or removed on both ends of the filament. The process of forming these proto-filaments is called nucleation and it is the rate limiting factor to form actin filaments. To circumvent this limitation experimentally one can use preformed actin filament seeds, or actin nucleators to direct the polymerisation on the cell.

We need to distinguish between the dynamics of polymerisation and depolymerisation on both ends of the filament. Indeed, it has been show that the association and dissociation rates are differ between the pointed (-) and barbed (+) end. The barbed end has higher dynamics than its pointed counterpart which is the reason for its (+) name. The dynamics of polymerisation is higher both in the case of ATP and ADP, though the rate constant of association and dissociation differ for both kind of filaments ([Figure 1.5](#))

Elongation rate constants



Figure 1.5: Association and dissociation rate of both ATP and ADP actin on pointed and barbed end as measured in [\[Pollard 1986\]](#) (scheme from [\[Pollard et al. 2003\]](#)). The difference of equilibrium constant between the barbed end (bottom) and pointed end (top) in the presence of ATP allow filament treadmilling.

The equations that drive the polymerisation can be written as follow

:label : roa1

$$\frac{dn}{dt} \Big|_{\text{barbed}} = k_{+, \text{barbed}} \cdot nGActin - k_{-, \text{barbed}}$$

$$\frac{dn}{dt} \Big|_{\text{pointed}} = k_{+, \text{pointed}} \cdot nGActin - k_{-, \text{pointed}}$$

Where *barbed* and *pointed* designate respectively the barbed and pointed end, $\frac{dn}{dt}$ represent the variation of the number of actin monomers in the actin filament which is due to addition or removal at the barbed (respectively the pointed) end. The association rate

constant k_+ and dissociation rate constant k_- are the polymerisation and de-polymerisation rate. The concentration in barbed and pointed-end denoted by $C_{barbed/pointed}$. By assuming that the number of pointed ends is equal to the number of barbed ends, one can derive the steady state which give rise to the critical monomer concentration below which an actin filament cannot grow: $[GActin]_c$.

The rate constants of elongation of actin have been determined and depend on whether the monomer is bound to ADP or ATP [Pollard 1986]. We should consider the fact that the ATP bound to actin will hydrolyse to ADP-Pi before releasing the inorganic phosphate. The hydrolysis and phosphate release rates also depend on whether the monomer is part of a filament or in solution. The hydrolysis of ATP-bound actin into ADP bound actin in the filament leads to an imbalance of actin (de)-polymerisation on both ends. The actin filaments preferably grow from the barbed end and shrink preferably from the pointed end.

This will lead to a phenomenon known as treadmilling where a single actin monomer bound to an ATP molecule, will be incorporated at the + end of the filament and progressively migrate toward the - end, eventually hydrolysing its ATP into ADP before detaching from the filament on the pointed end. During this process the filament will grow / shrink until it reaches the stationary state where its length would stay constant but the treadmilling continues.

Treadmilling requires an imbalance in the global rate constant on the barbed and pointed end and an energy source, in the case of actin this is provided by the hydrolysis of ATP into ADP+Pi before releasing the inorganic phosphate, without which treadmilling would not occur.

Practically, this can be approximated by having only ATP monomers at the barbed end of actin filaments while the pointed end is typically constituted only of ADP monomers, thus the critical concentration is lower at the pointed end compared to the barbed end. The growth speed of the filament on both ends depends on the monomer concentration in solution. In between the critical concentration of both ends, there exists a concentration at which the polymerisation on (+) exactly compensates the depolymerisation on (-).

Actin network can be controlled by a host of actin binding proteins

Despite the already complex process of actin polymerisation and the number of parameters that we have already introduced, the formation of an actin network is an even more complex process that involves many other components. Especially, actin monomers and filaments can interact with a high number of proteins that will affect the previously introduced dynamics. We will present some categories of such proteins in the following.

Formins

Formins are polymerase proteins that will increase the polymerisation rate of actin filaments by dimerizing and binding to the barbed end. It has the particularity of being processive, meaning that it will stay bound to the barbed end while catalysing the addition of new monomers. The processivity of formins also permits the control of the localization of actin polymerisation where formin proteins are present, like the tip of filopodia [Faix et al. 2006] [Bornschlogl 2013]. *Formins* posses domains rich in proline, capable of binding to profilin (*FH1*) which allows formin to elongate F-Actin using actin monomers bounds to profilin [Pruyne et al. 2002] [Pring et al. 2003].

Capping Protein

To regulate polymerisation, cells also have the possibility to reduce or stop the polymerisation. To achieve this, some proteins will bind to the growing end of actin filaments and prevent the addition of new monomers. *Capping Protein* (CP) being one particular example that will specifically bind to the barbed end of a growing filament and prevent it from growing. Capping proteins are necessary to prevent polymerisation of actin in undesired area and are essential for the structure and mechanical properties of actin gel [Kawska et al. 2012]. *Gelsoline* is another example of Capping Protein, that unlike CP can only attached to the barbed end of an actin filament after severing it. Gelsoline is hence both a severing and a Capping Protein.

Cross-linkers

We have seen that some proteins were able to attach to actin filaments. When such a protein is able to attach to many filament at once, it can act as an attachment point between the two filament, preventing them to move with respect one to each other. Such proteins, are referred to as cross-linkers.

The amount of freedom in movement between the two filaments depends on the cross-linker used. For example , α -actinin will allow rotation of the two filament at their anchoring point whereas cross-linkers like fascine will prefer a parallel conformation of the filament and favor the formation of actin bundles.

Cross-linkers are essential for the formation of elastic network as they allow forces to be carried from one actin filament to the other. The quantity of cross link of a network will often be a key parameter for the elastic properties. The distance between the link points in the network (both cross links and entanglement points) will give the typical network mesh-size which is used to calculate the viscoelastic response of networks : [Morse 1998a].

Stabilizing actin filaments

As actin networks are dynamic constructs that are changing shape and properties over time, it is convenient to be able to stabilize those networks. Tropomyosins are proteins capable to bind on the side of actin filament to stabilize them.

The use of phalloidin, a toxin extracted from fungus (*Amanita phalloides*), binds between F-actin subunits on the filament, and hence prevents it from de-polymerising. Though, it is known that stabilizing actin filaments with phalloidin will increase their stiffness as measure by the persistence length which can change the mechanical properties of the formed actin network.

Profilin

Profilin is a protein that will bind to the barbed end of single monomers of actin in solution. By doing so it will first prevent the association of monomers into dimers and trimmers, thus preventing the nucleation of actin filament. It thus allows a better control of localisation of actin filament both in vivo and in vitro in the presence of actin seeds of actin nucleator.

Profilin was for a long time believed to be only a sequestering protein that inhibit polymerisation [Yarmola et al. 2009], though it has a more complex behavior, and if it prevent polymerisation of actin filaments by

the pointed end, it can facilitate polymerisation. One of the cause of increase in polymerisation speed by profilin is the fact it binds preferably to ADP-Actin and increase the exchange rate of ADP into ATP.

Branching Agent

A type of network found of the leading edge of cells lamellipodia is dendritic network. It is characterised by tree-like structure of actin filaments in which thanks to the Arp2/3 complex branching agent a mother actin filament will form a daughter filament on its side.

We have seen previously that crosslinkers are proteins capable of linking two or more actin filaments together by binding on their side. Another mechanism involving binding on the side on actin filament is responsible for a closely related network, the branching mechanism.

The Arp2/3 complex is composed of seven subunits, two of which are highly similar to actin, forming the Arp2 and Arp3 family for Actin Related Proteins, giving the complex its name. Typically Arp2/3 will bind on the side of a pre-existing actin filament, hence initiating the growth of a daughter filament with an angle of 70° to the mother filament. The newly created daughter filament pointed end is terminated by the Arp2/3 complex that will stay attached to the mother filament, thus increasing the number of available barbed end, without changing the number of available pointed end. See Nature Review by Erin D. Goley and Matthew D. Welch [[Goley et al. 2006](#)] for a longer review about the Arp2/3 complex.

In cells, the Arp2/3 complex needs to be activated by a Nucleation Promoting Factor (NPF). Among them is the WASp protein (Wiskott-Aldrich Syndrome protein) and its neural homologue N-WASP which are from the same family as SCAR/WAVE [[Machesky et al. 1999](#)]. All these activators of Arp2/3 have in common a WCA motif. The wild type protein need to be activated in order to activate Arp2/3. The activation is done by a change in conformation that exposes the active region and provides the first actin monomer necessary for nucleation of the daughter filament ([Figure 1.6](#)). To circumvent the activation process of these proteins, we use a reconstructed version of the protein that cut all region before the poly-proline. This confer to pVCA the ability to be permanently active. This region can also be replaced by streptavidin in order to selectively bind pVCA to selected regions. Characterisation and more detailed description of pVCA can be found in [[Noguera 2012](#)].

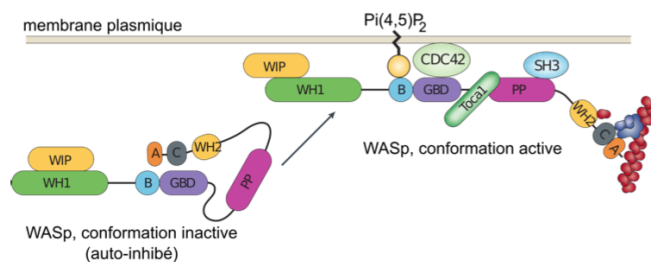


Figure 1.6: Organisation of Wasp domains. A change in conformation make the protein active, which allow the activation of the Arp2/3 complex and the nucleation of a daughter filament. Adapted from [[Goley et al. 2006](#)]

Unlike Cells that are able to control the localisation of actin nucleation processes thanks to activation of WASp and its homologue, the ‘*in vitro*’ control of localisation of actin polymerisation is directly done by the localisation of pVCA.

Actin Gels dynamics,

The network formed by Arp2/3 is called a dendritic network, and is in particular found at the leading edge of the cell in the lamellipodia. It is such a network that is present in the bead system we will study hereafter.

As for crosslinkers, dendritic networks are able to carry forces across single actin filaments by the intermediary of Arp2/3. Two dendritic network of Arp2/3 can also entangle and allow forces to be carried across them [Kawska et al. 2012].

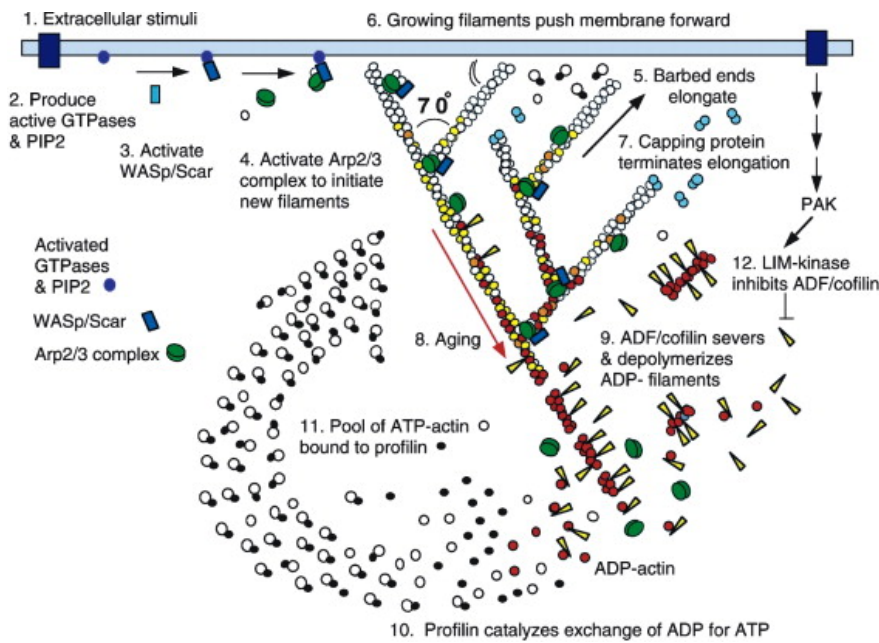


Figure 1.7: Schematic recapitulating the formation of a dendritic network at the leading edge of a cell were several of the function of protein can be seen. An actin nucleation promoting factor (Active WASp, blue rectangle at the membrane) will activate Arp2/3 (green blob) which will act both as nucleation factor and a branching agent. From an activated Arp2/3 will grow an actin filament pointing towards the membrane. Newly growing barbed ends, rich in ATP-actin (white circle) can eventually be capped by Capping Protein (light-blue pairs of circle) which will terminate their growth. Aging monomers in actin filament will slowly hydrolyse their ATP (yellow and red circle), eventually releasing the inorganic phosphate before detaching from the pointed end. Depolymerisation is helped by severing protein (sharp triangle) and Actin Depolymerisation Factor (ADF). ADP-actin monomer will bind to profilin (Black dots) increasing the turn over rate to ATP-actin which will be reused by the leading edge of the cell. Adapted from [Pollard et al. 2000].

A schematic that recapitulate the interaction of actin with other protein and the formation of a dendritic network at the leading edge of the cell is presented on figure 1.7.

Molecular Motor

A particular kind of protein that can bind to the cytoskeletal filaments are molecular motors. Molecular motors are proteins that will consume energy in the form of ATP, hydrolyse it to change conformation and produce forces.

The motors that move along actin filaments are part of the myosin superfamily, they are both responsible for the transport of cargo along filaments, cell motility, division, and muscle contraction. They acquire their

name from their discovery in 1864 by Willy Kühne who extracted the first myosin II extract from muscle cell [Hartman et al. 2012].

The myosin super family is divided into subfamilies numbered with roman literals. As of today we count more than 30 families of myosin [Berridge 2012]. Muscle myosin is part of the myosin II family and is often referred to as conventional myosin for historical reason as being the first discovered. Non-muscle myosin are also referred to as unconventional myosin.

Myosin motors seem to be shared among the living domain, hinting for an early emerging of myosin in the evolution. All the myosin motors move on actin filaments toward the barbed end, with the exception of myosin VI which moves towards the pointed end [Buss et al. 2008].

Different subfamily of myosin are used for different function in cells. Even in subfamilies each type of myosin can have specific functions. For example, conventional myosin found in muscle cells are use for large scale cell contraction. In contrast, myosin V is known to transport cargo and is found to be responsible for actin network dynamics and vesicle positioning [Holubcova et al. 2013].

Myosin II As stated before, the myosin II family both encompass conventional myosin as well as Non-muscle myosin II (NMII). Both have a similar structure (Fig 1.8).

All myosin IIs are dimers constituted of two heavy chains and light chains. The heavy chains are held together by a coil-coiled alpha helix referred to as the tail. On the other side of the protein sequence is a globular head, which is responsible for ATP hydrolysis and is able to convert the energy from the hydrolysis into mechanical force. It is also the part that will bind to the actin filaments. In between the tail and head is the neck domain that acts as a lever to transmit the force generated by the head to the tail. The length of the neck influences the length of the movement done by the cargo at each step of the myosin as well as the size of the step the myosin can effect. The two light chains are situated in the neck region and are responsible for the myosin activity regulation.

Myosin II dimers can align and assemble by the tail region, forming myosin minifilaments. These minifilaments are bipolar, having numbers of myosin head with the same orientation at each extremity.

In the myosin II family, conventional myosin and NMII differentiate by the size of the minifilaments they form. Muscle myosin will form minifilaments aggregating around 200 dimers, where NMII minifilaments will be composed only of 10 to 20 minifilaments. The other characteristic of unconventional myosin with muscle myosin is the mode of activation. Conventional myosin activity is regulated by the amount of Ca^{2+} available, which frees the actin filaments to let the myosin motor bind. However, its counterparts are typically activated by the phosphorylation of the Myosin Light Chain (MLC).

Another parameter that discriminates muscle from non-cell myosin is their duty ratio. The duty ratio is define as the ratio of the time the myosin stays attached to an actin filament over the typical time of a contraction cycle. By noting τ_{on} and τ_{off} the time the myosin head spent attached/detached from the filament, the duty-ratio or duty-cycle can be noted :

$$r = \frac{\tau_{on}}{\tau_{on} + \tau_{off}} \quad (1.1)$$

We will see in the following that the duty-ratio might have an important effect on the processivity of the myosin.

It should be noted that as minifilaments can attach to actin filaments on both ends, they can also act as a bridge that holds two points close to each other, though having the properties of crosslinkers.

Myosin V Myosin V is an unconventional myosin. Unlike myosin II it does not aggregate into minifilaments. Though, myosin V has a similar structure to myosin II but with a longer neck, this confers to myosin V the ability to realize longer steps on actin filaments. Indeed, the myosin V step size is of 36nm, which is close to the twisting length of actin filaments. This allows myosin V motors to walk along actin filament without having to rotate around it with the helix they form. At the end the tail domain myosin V posses another globular domain capable of binding to its cargo, and the variability of this region is what mostly define the difference between the different type of myosin V.

Myosin V also has a high duty-ratio, this leads to dimers having almost always one of the two head of the myosin to be bound to actin. It grants to the myosin V the ability to walk in a processive manner toward the barbed end of the actin filaments, both head successively binding 36 nm in front of the other head.

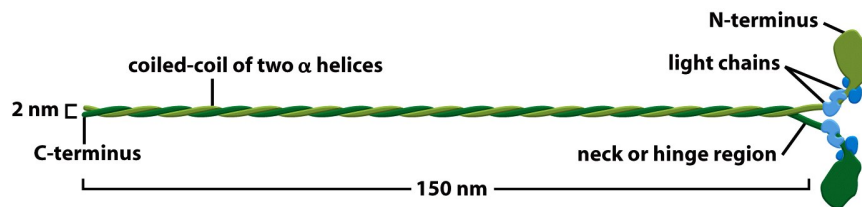


Figure 16-54a Molecular Biology of the Cell 5/e (© Garland Science 2008)

Figure 1.8: Schematic of a dimer of myosin motors with the example of Myosin II. Each of the myosin monomer is colored in a different shade of green. From Right to Left, the myosin head, with the N terminal, is the part of the myosin that binds to the actin filaments. The neck region with the light chain act as a lever arm. Finally the tail, constituted with coiled-coil alpha-helix that aggregate to form minifilaments. Adapted from [Alberts et al. 2008].

Myosin cycle We saw earlier that the duty ratio of myosin was the ratio of time the head of the myosin spent attached to the actin filament. Indeed, myosin can generate displacement through a cycle of ATP hydrolysis and attachment/detachment described below for a Myosin II motor:

The cycle can be decomposed in 5 steps, last of which will be responsible for the forced exerted on the myosin cargo.

- The myosin start in the ‘rigor’ conformation where it is lightly bound to the actin filament.
- An ATP molecule binds to the myosin head inducing the detachment of the myosin from the actin filament.
- ATP molecule is hydrolysed into ADP+Pi, providing energy which is stored into a conformational change of the myosin which effects a recovery stroke.
- Inorganic phosphate is released as the myosin head attaches to the actin filament.
- The actin-bound myosin change conformation, applying forces on it’s cargo. This step is known as the power-stroke and is responsible for most of the applied forces or displacements of the myosin. During the power-stroke the ADP bound to the myosin head is released, leading back to first step of the cycle.

This principle is the same for all kinds of myosins. In the case of Myosin II the duty-ratio is only of about 5%, which leave Myosin II detached from the actin filament most of the time. A single dimer cannot achieve processivity. The tail of myosin II can bundle itself with the tail of other myosin II motors. They from large

bipolar thick filaments of hundreds of dimers. As each myosin dimer attaches and detaches independently from the actin network the effective attachment of the filament increases with the number of motors in the minifilaments. Indeed the probability of having at least one motor attached increases with the number of motors. The constant attachment of at least one myosin II head in minifilaments insure that the filament does not displace with respect to the actin network when others myosin heads recover from their power stroke and reattach, thus conferring processivity to myosin II minifilaments.

The bipolar nature of myosin II minifilaments also allow them to act as force dipoles, each of the extremity pulling the surrounding actin network or filament towards the center of the minifilaments. This is the mechanism at the origin of muscle contraction and can allow to build-up tension in actin network.

1.4.2 The actin cortex

The actin cortex is a thin layer of between 200 to 500 nm that can be found just underneath the plasma membrane of a cell (Fig 1.9). The properties of the actin cortex makes it a key component to diverse processes. Its capacity to resist to, and transmit forces is indispensable for locomotion of many cells by allowing the retraction of the rear of the migrating cell and will be described in more detail in the next section. Its structure is also essential for the cellular division as contractility is necessary to generate cortical tension and achieve the separation of the two daughter cells.

The actin cortex is constituted of actin filaments that can be parallel or orthogonal to the membrane as one can see using electron microscopy on cells [Morone et al. 2006].

We saw through the bud scar of budding yeast that the full cytoskeleton could retain memory of past events. It is also the case for simple actin networks as shown in [Parekh et al. 2005] who describe how actin-network growth can be determined by network history, showing actin cortex could also act as a memory for cell.

1.4.3 Cell Motility

The way cells move highly depends on their environment and the cell type. We can distinguish several strategies of movement, mainly categorised into amoeboid and mesenchymal movement. The type of motility for certain cells can be characteristic for malignant tissue, and plays a significant role in the ability of the cells to invade nearby tissues.

Lamellipodium based Motility

We can have a first look into the mesenchymal mode of locomotion of cells, which is also often referred to as crawling. To understand how a cell is able to crawl, to move itself, we will in particular take the example of the lamellipodium. The lamellipodium is a characteristic structure found in cells moving on a 2D substrate. By its nature, motion using lamellipodia is one of the easiest to study using microscopy which might explain why it is one of the best known process of cell displacement. None the less, it does not diminish its importance in tissues behavior as all epithelial cell can be considered as moving on a 2D substrate. Beyond lamellipodia, further structures that are responsible for cell motion are filopodia and pseudopodia. They mainly differ from lamellipodia by their shape and the organisation of the actin structure inside (Fig 1.10). Lamellipodia-based motion can move a cell up to a few micrometers per minute.

The action necessary to move in an mesenchymal way can be decomposed into three steps. First the cell needs to grow a protrusion. Growing this protrusion is typically governed by actin polymerisation just

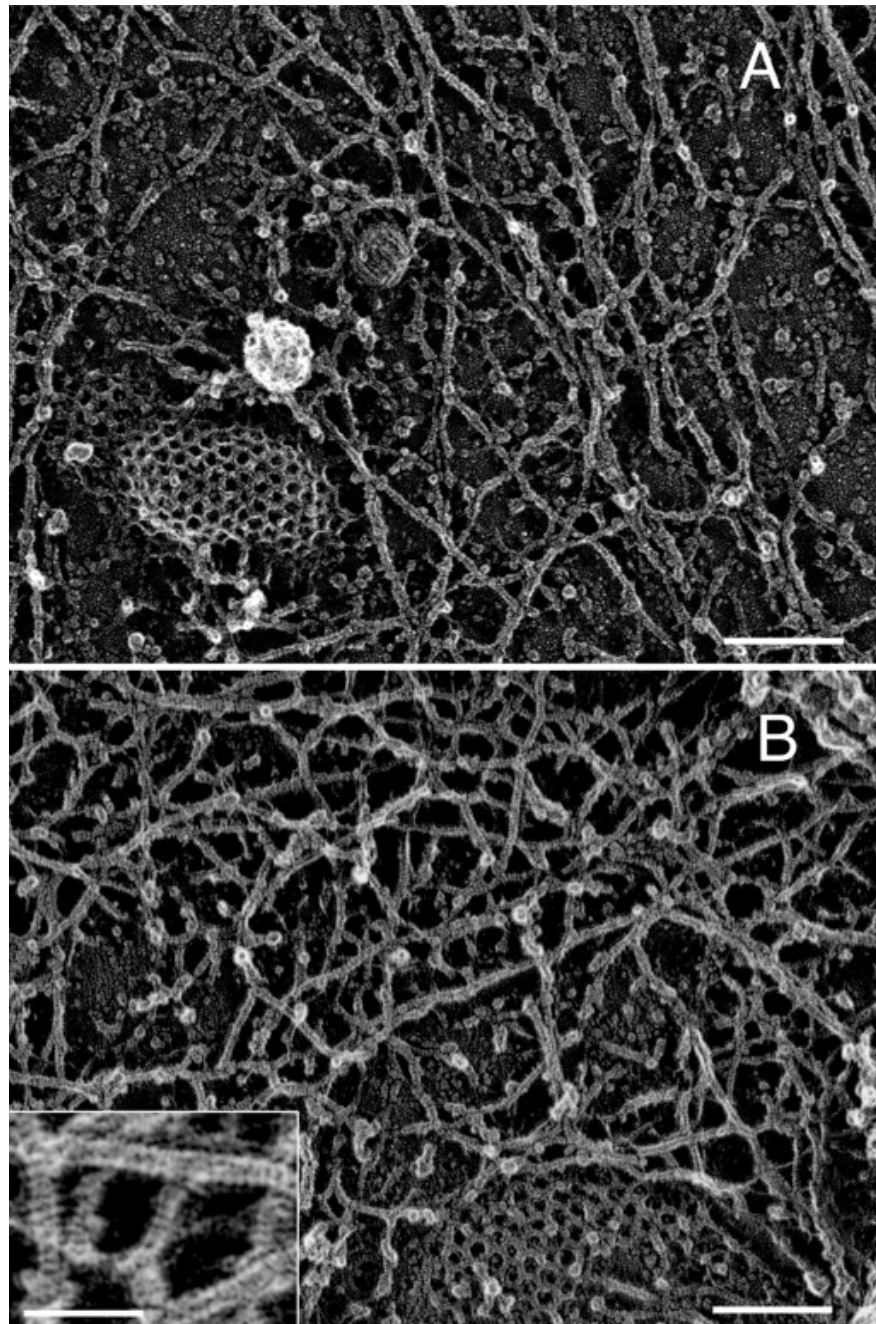


Figure 1.9: Electron microscope view of the actin cortex in rat cell. The inset show a periodicity of ~5nm in filaments characteristic for actin. Scale bars are 100nm, inset 50 nm. Extracted from [Morone et al. 2006].

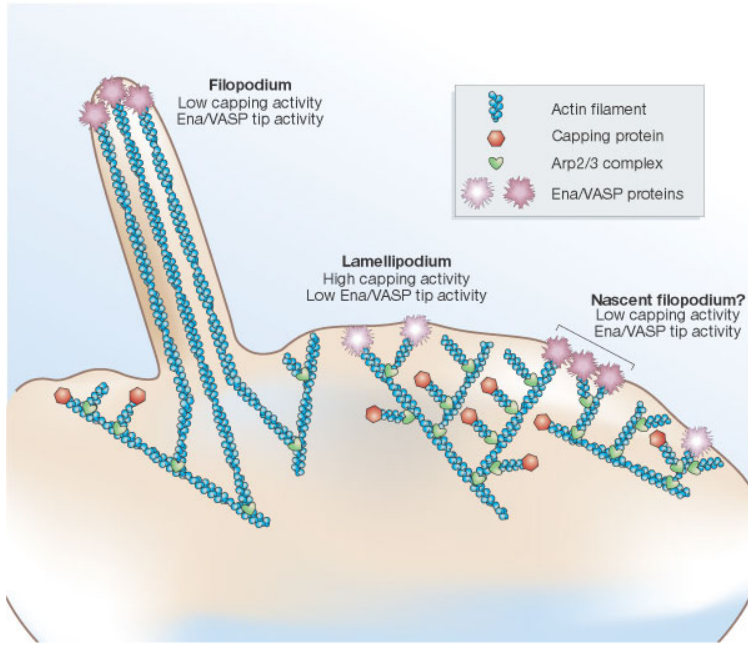


Figure 1.10: Polymerisation at the leading edge of the cell. NPF situated on the membrane of the cell localize the polymerisation. The lamellipodium will be characterized by a dendritic network formed by Arp2/3. Parallel actin structures can form a growing protrusion called filopodium. Adapted from [Schafer 2004]

underneath the plasma membrane. The lamellipodium is such a protrusion which is constituted by a 2D dendritic actin network that polymerize at the leading edge. Second the cell's protrusion need to attach to the surface. This is done through trans membrane proteins that are bound to the actin cortex on the inside of the cell. The actin cortex will act as a scaffold to transmit the force across the cellular to these anchor points. The last part is the generation of traction in which the rest of the cell is pulled toward the attached protrusion. The traction force is mediated through the cytoskeleton and actin cortex while the contraction force themselves can origin from actin network contraction and reorganisation due to myosin motors (Fig 1.11).

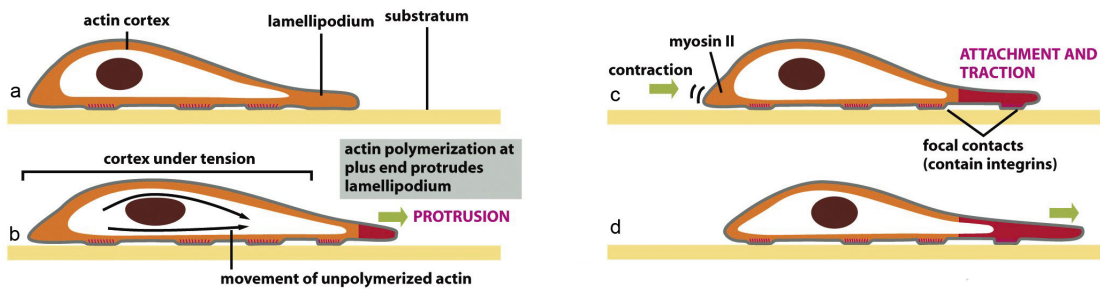


Figure 1.11: Schematic of Lamellipodium base motility. The lamellipodium grows at the leading edge of the cell and attach to a focal point. The actin cortex under tension contract and is capable to pull the rear of the cell. Adapted from [Alberts et al. 2008].

Blebbing based Motility

The second mode of motility which is known as amoeboid is more characteristic of 3D displacement of cells. In this mode, the cell will also form protrusions but will not rely on adhesion to move its body. This motility rely on blebs, that are blister-like protrusion that appear on the cell surface. A bleb forms on the surface of cell when the membrane detach from the actin cytoskeleton underneath it, or when the cortex ruptures (Fig 1.12). The small protrusions are formed, quickly grow as they lack the force supporting layer that the actin cortex provides. While growing, the bleb fills with cytosol. The actin cortex can rapidly reform on the bleb slowing down its growth. In some cases, the reformation of the actin cortex in the bleb and the rebuilding of the tension inside the bleb by myosins mediated contraction is enough to reverse the bleb. Though, the content of the cell can also drain itself into the bleb as it grows and while the main body of the cell contract and empties, thus moving the cell from its old position to a new one in the direction of the initial growth of the bleb.

At their initial state, blebs are simple membrane protrusions filled with cytosol and empty of organelles. The stop of their growth is due to the spontaneous formation of an actin cortex on the inner side of the bare membrane.

By their relative simplicity to the rest of the cells, blebs are the perfect system to be reconstituted *in vitro* in liposomes.

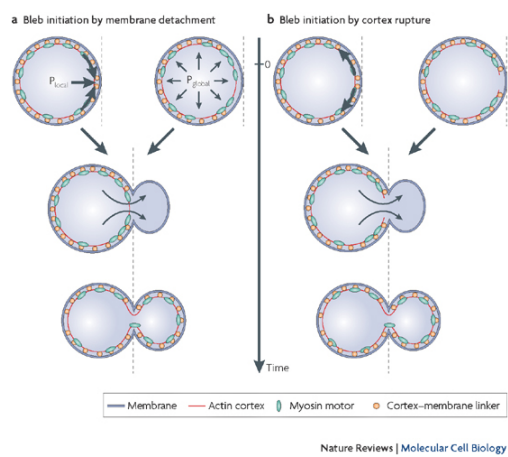


Figure 1.12: Formation of bleb can be done either by a) detachment of the membrane from the cytoskeleton, or b) by a rupture of the cytoskeleton. In both cases the inner pressure of the cell leads to the inflation of the membrane at the point of rupture/detachment. The acto-myosin cortex will rapidly re-polymerize on the inside of the bleb slowing down its growth until the expansion stops. Extracted from [Charras et al. 2008]

1.4.4 Organelle Positioning

We have seen previously that organelle positioning plays an important role in cell function. Several mechanisms involving actin are at the origin of structure positioning in cells. The positioning of organelles by actin can have a wide impact from being necessary for the correct cell division, to allowing locust eyes to adapt in the dark by repositioning mitocondrion [Sturmer et al. 1995].

We already know that the actin cortex is a necessary element in cell motility. It also plays a determinant role in organelle positioning. It has been shown [Chaigne et al. 2013] that the correct range of elasticity of the

actin cortex during oocyte division is needed for proper spindle positioning. The correct spatial position of this spindle is necessary to perform a viable division of the cell.

The actin cortex is not the only actin structure in the cell, beyond the thin and dense layer just below the membrane lies a softer and sparser actin structure that has a crucial role in organelle positioning.

During cell division, there are several stages that require actin structures. As shown previously [Azoury et al. 2011] the expulsion of polar body during oocyte asymmetric division is strongly dependent on the time evolution of a sparse actin network that can be found in the cell. Actin structures are also required at a later stage to permit the correct capture of chromosomes by microtubules and achieve correct haploid division. [Schuh et al. 2008] also shows that a similar sparse actin network contracted by myosins is necessary for spindle migration.

Especially in oocyte that are typically large, the effect of gravity is not negligible. The presence of a sparse “actin scaffold” is discussed in [Feric et al. 2013], where it is found that an actin network is present to balance the gravitational force.

In drosophila, nurses cell need to expel their content into oocytes. It has been observed [Huelsmann et al. 2013] that during this phase, the nurse cells’ nucleus is pushed away from the dumping canal by single actin filaments polymerising from the membrane and forming a soft and sparse actin network.

1.5 In vitro reconstituted actin networks

Living cells are complex organisms, for which each function requires a number of interacting proteins and components. To understand the action of each individual component, it is necessary to isolate or modify their actions independently.

In order to achieve the precise tuning of each component independently, two approaches are possible. First, an approach referred to as “Top-Down”, where starting from the full system — in our case the cell — we will modify or remove single or multiple components and study the global change of behavior. This is a complex process that might be difficult to interpret, as biological systems often have multiple pathways and feedback loops to regulate each of their processes. Taking into account the large number of components that constitute a living cell, it is also difficult to come up with the minimal system required to replicate certain behaviors.

The other approach, also referred to as the bottom-up approach, requires the reconstitution of the system part by part until it replicates the expected behavior. This is also a complex process, as there is a large number of potential components likely to be added to the reconstituted system. This vast complexity often leads to a wide range of testable parameters. These controlled systems allow in principle for a deeper understanding of the governing working mechanisms, and often permit access to a wider range of accessible conditions and individual tweaking of components.

In our lab, we are mainly interested in the bottom-up approach and the use of biomimetic systems. We try to reconstitute biologically relevant behavior within minimal systems, constituted from pure protein components.

In this manuscript in particular, we focus on mimicking the motility process by which the *listeria* pathogen is able to hijack cellular mechanisms, by recruiting proteins responsible for actin polymerisation at the leading edge of the cell, and use them to polymerize actin on the pathogen surface. This is what allows

'listeria' to propel itself fast enough (1.5 to $2 \mu\text{m}/\text{min}$) [Dabiri et al. 1990] to be able to penetrate the cell membrane to move from one cell to the other.

The bead motility system is a minimal *in-vitro* system capable of replicating the listeria motility.

1.5.1 Bead motility assay

The *Listeria* pathogen is a 1.5 to 5 micrometer cylindrical bacteria that enters cells, hijacks its actin polymerisation machinery to propel itself and infect neighbour cells. It does so by the recruitment of a single protein on its surface : ActA, that activates the Arp2/3 complex. By the recruitment of Arp2/3, a dense branched and entangled actin network grows that will eventually form a comet behind the bacteria propelling it at the speed of actin comet polymerisation. Listeria comets are composed of a wide range of proteins. It has been shown [Loisel et al. 1999] that the number of required components can be highly reduced, still maintaining the motility features.

A simpler system replicating the listeria motility is the bead motility assay. Consisting of a micrometer-sized bead covered with a nucleation promoting factor (NPF), it will activate the Arp2/3, present in the solution.

In the case of listeria, this NPF can be ActA, but such other NPF such as N-WASp or pVCA can also be used. We chose pVCA in the experiments presented in this work. The NPF covered bead is mixed with a G-Actin solution. Capping Protein is added to prevent polymerisation from happening away from the bead surface as well as the components required for actin polymerisation (ATP, Salt..., see *Material and methods*)

Due to the presence of Capping Protein in the solution and NPF on the surface of the bead, the polymerisation of actin will only happen on the bead surface, forming a thin and dense actin gel capable of sustaining stress, depending on the different protein concentrations. Unlike listeria, which seems to control on which of its sides the nucleation process happens, this is not controlled in bead motility assays. In the right condition, though, [Kawska et al. 2012] the dense actin gel formed on the bead surface can accumulate the stress induced by the inner layer polymerisation, until symmetry breaking occurs. The gel ruptures on one side of the bead, leading to the formation of a comet on the opposite side (Fig 1.13).

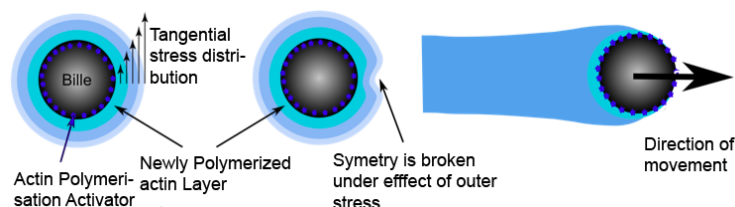


Figure 1.13: Scheme of bead motility assay. The NPF (yellow stars) will localize the actin polymerisation on the surface of the bead, thus increasing the stress on the outer actin layer. At a sufficient level of stress, the outer layer ruptures, leading to symmetry breaking, formation of a comet, and propulsion of the bead. Adapted from [Plastino et al. 2005]

Due to the further polymerisation of the actin network on the surface of the bead, the comet will grow, propelling the bead forward. This is the reason why the bead system is a biomimetic system replicating the listeria motion.

It should be noted that during the movement of this system, two phases can be distinguished. In the first phase, the system presents a spherical symmetry with an homogeneous actin network around the bead. The

gel is growing from the surface and is accumulating stress, due to the polymerisation of inner layers.

If the gel has accumulated sufficient stress by polymerisation, the symmetry breaking event happens, and the system enters into a second phase with the formation of a comet.

The conditions that lead to symmetry breaking have been investigated in detail [Kawska et al. 2012]. In the absence of Capping Protein, the actin polymerisation does not seem to be restricted enough near the surface of the bead, and thus the formed network is not able to generate or sustain enough stress to achieve symmetry breaking. At high Capping Protein concentration, the growth of the gel is heavily impaired, thus preventing symmetry breaking. The concentration of Arp2/3 is also critical, as Arp2/3 forms branched networks, and these branched networks are primordial essential for the ability to sustain stress.

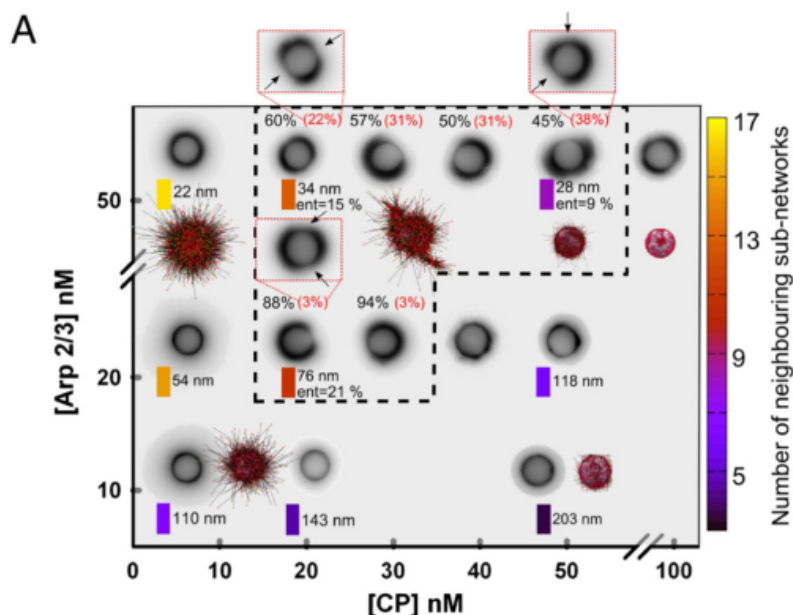


Figure 1.14: Phase diagram showing symmetry breaking in bead motility assay as a function of concentration of Arp2/3 and Capping Protein. Symmetry breaking only occurs inside the area delimited by the dashed line on 4.5 μm beads, both *in vitro* and *in silico*. Experiments are displayed as inverted fluorescence image. Adapted from [Kawska et al. 2012]

In the rest of this chapter, we use the bead motility system, but only consider it during the first phase, where the symmetry breaking has not yet occurred, or in condition where it should not occur. In particular, we will investigate a condition at 25 nM Arp2/3 with a concentration of Capping Protein varying from 0 to 50 nM. As shown in fig 1.14 this range corresponds to conditions where no symmetry breaking occurs, but also to conditions in which symmetry breaking is expected. It should be noted that unlike other studies that also characterize actin network growing on beads [Pujol et al. 2012], our system is still dynamically polymerising and thus changing with time.

1.5.2 Liposomes

Beads are used as a model biomimetic system that replicates the polymerisation mechanism happening on the leading edge of cells. Because of their composition and rigidity, the phenomenon observed on beads

cannot necessarily reproduce all the interactions and processes that take place on the cell membrane. Cells are finite compartments with a limited amount of actin that acts on the dynamics of polymerisation. The fact that cell size is in the order of the persistence length of actin filaments also plays a role on the structure of actin networks. Indeed, at these scales, a single filament can never reach the length at which it can be considered fully flexible.

Liposomes are one of the biomimetic systems able to capture some interactions between cell membranes. Liposomes are lipid bilayers that imprison an aqueous compartment and exhibit many characteristics similar to cells. The inside of liposomes can act as a biochemical reactor of limited size, with the lipid bilayer acting as a separation from the outside, like the cell membrane. The composition of the lipid layer can be varied in order to reflect the composition of a cell membrane. In particular, it is possible to attach proteins to the liposome membrane. Finally, the size of the liposomes can be varied, leading to actin networks, the size and shape of which are similar to those found in cells.

It is possible to mimic the cellular actin cortex using liposomes, and especially its contractility. A crosslinked actin network can be formed and attached to the outer leaflet of liposomes, and contractility can be triggered by injecting molecular motors. The behavior of the system will depend on the attachment between the reconstituted actin cortex and the liposome membrane. A weak attachment leads to a favorable rupture of the actin cortex during the increase of tension, implying a symmetry breaking, as in the bead motility system. In the case of strong attachment, the liposome actin-cortex will accumulate tension until it has enough force to crush the supporting lipid layer, thus collapsing the liposome [Carvalho et al. 2013b],(Fig 1.15). This system also allows the observation over time, giving extra insight into the dynamics of the actin network (Fig 1.16).

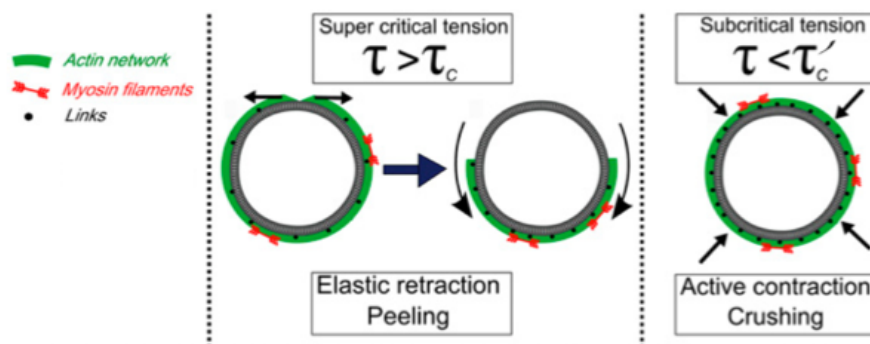


Figure 1.15: Effect of reconstituted rigid actin cortex attachment to a liposome membrane under constraints generated by myosin filaments. Under weak attachment, the actin network ruptures thus leading to a “peeling” of the actin cortex. With stronger attachment, the actin cortex can sustain higher stresses, until the underlying liposome ruptures (“Crushing”). Adapted from [Carvalho et al. 2013b]

1.6 Membrane Physics

The cell’s plasma membrane is a biological membrane that separates the cell from its outside environment. It consists of a lipid bilayer containing a high number of proteins. A lipid bilayer is formed by two layers of lipids and has a thickness of a few nm. The classical theoretical description of these bilayers has been done

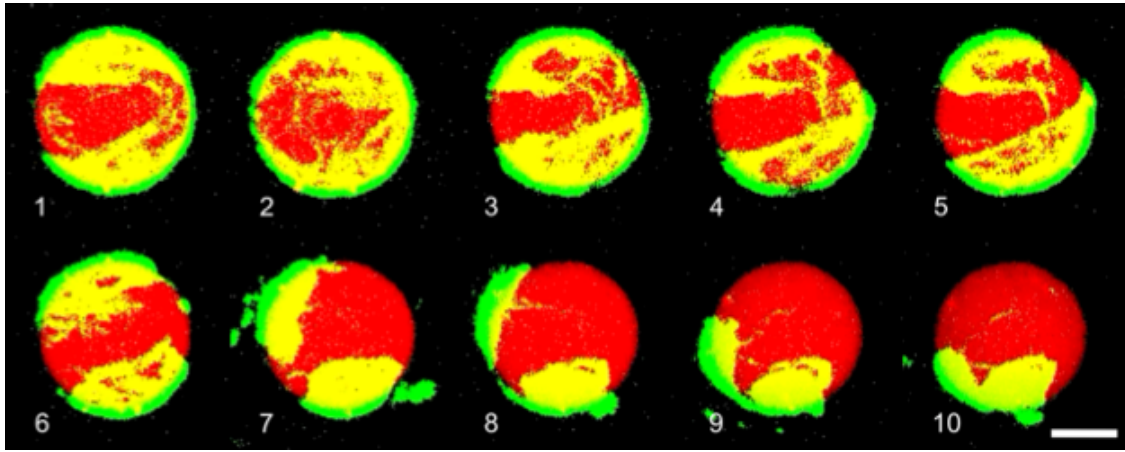


Figure 1.16: 3D reconstruction of an acto-myosin cortex (green actin) peeling off a liposome (red) over time (1.4 second between frames). The actin cortex contraction happened after the injection of Myosin II. Scale bar is 5 μm . Experiments and reconstruction done by Joël Lemière.

by W. Helfrich [Helfrich 1973] in 1973 in a model based on the elasticity and fluidity of lipid bilayers as well as the self assembly properties of lipids.

In the case of a close lipid bilayer, the potential energy stored by the deformation of a lipid bilayer by unit area can be written as

$$H = H_{ext} + H_{curv} \quad (1.2)$$

In which H_{ext} is due to the extension/compression of the membrane, and H_{curv} is due to the local curvature of the membrane.

The density of energy cost to extend the membrane H_{ext} can be written as a function of the elastic area compressibility modulus K_a and the relative variation surface of the membrane A :

$$H_{ext} = \frac{1}{2} K_a \left(\frac{\Delta A}{A} \right)^2 \quad (1.3)$$

K_a expresses how much energy is required to expand the surface of the lipid bilayer and is due to the exposition of more hydrophobic surface to water when expanding it. K_a is expressed in J.m^{-2} , or N/m and is close to twice the surface tension between the lipids and water.

For closed lipid bilayers, the total curvature energy can be expressed as the sum of the curvature energy H_{curv} :

$$H_{curv} = \frac{1}{2} \kappa (c_1 + c_2 - c_0)^2 \quad (1.4)$$

In which κ is the bending modulus of the membrane and c_1, c_2 are the principal curvatures of the membrane. c_0 is the spontaneous curvature of the membrane, which is defined as the curvature the membrane would adopt, when free of external constraints.

An important parameter introduced in membrane mechanics is the membrane tension, σ which is the stress associated with an increase in the membrane surface. The tension σ is linked to the energy required to

expand the membrane H_{ext} by :

$$\sigma = \frac{\partial H}{\partial \left(\frac{\Delta A}{A} \right)} \quad (1.5)$$

i.e.

$$H_{ext} = \sigma \left(\frac{\Delta A}{A} \right) \quad (1.6)$$

In which

$$\sigma = K_a \left(\frac{\Delta A}{A} \right) \quad (1.7)$$

Membrane tension is a key parameter as it can be measured in cells. It is one of the parameters responsible for cell sorting [Maitre et al. 2012]. In particular between cells, the tension of the couple (membrane+actin cortex) can be determined by using the contact angle between cells which is the angle between interfaces, as defined in figure 1.17.

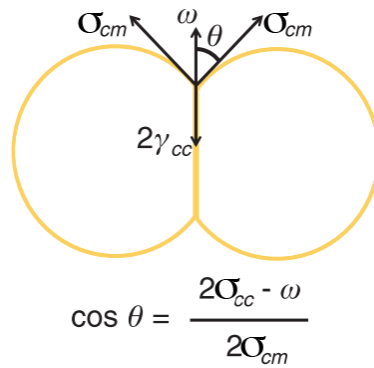


Figure 1.17: Surface tension governs doublet shape, adapted from [Maitre et al. 2012]. The equilibrium of forces on the contact line governs the angle of contact 2θ . ω corresponds to the adhesion tension between the two cells, σ_{cm} corresponds to the tension between the cell and the medium, σ_{cc} corresponds to the cortex tension between the two cells.

In a later part, we use a reconstituted biomimetic system made of liposomes. The injection of myosin motors changes the tension of the acto-myosin cortex attached to a membrane. By determining the geometrical parameters of this system, and in particular the evolution of the contact angle with time, we are able to measure the variation of tension of the acto-myosin cortex due to the contraction by molecular motors.

1.7 Actin networks as viscoelastic material

We have previously seen that while polymerising, G-actin assembles into F-actin filaments. The stiffness of filaments can be measured by a characteristic number called the persistence length (l_p). More precisely, the persistence length characterizes the average loss of correlation between the tangents along the considered

polymer. With s the curvilinear abscissae along the polymer, and $\Theta_{(x,y)}$ the angle between the two tangents at two different abscissae (Fig 1.18):

$$\langle \Theta_{(s,s+l)} \rangle = \exp\left(\frac{-l}{l_p}\right) \quad (1.8)$$

For actin filaments, the persistence length is in the order of $10 \mu\text{m}$ [Isambert et al. 1995]. This means that for much smaller scales, the actin filament can be considered as rigid. This is the case in the cell cortex where the meshwork has a typical size, smaller than 250 nm . In the other extreme, at length scale much bigger than l_p , filaments can be considered as flexible. While in typical cells, the filament length is rarely much bigger than the persistence length of actin, *Xenopus* eggs can reach 1 mm , so hundreds fold the actin persistence length. Still, for the majority of cells, the typical size we are interested in is about the persistence length of an actin filament, thus at this scale, the filament can neither be considered purely rigid nor completely flexible.

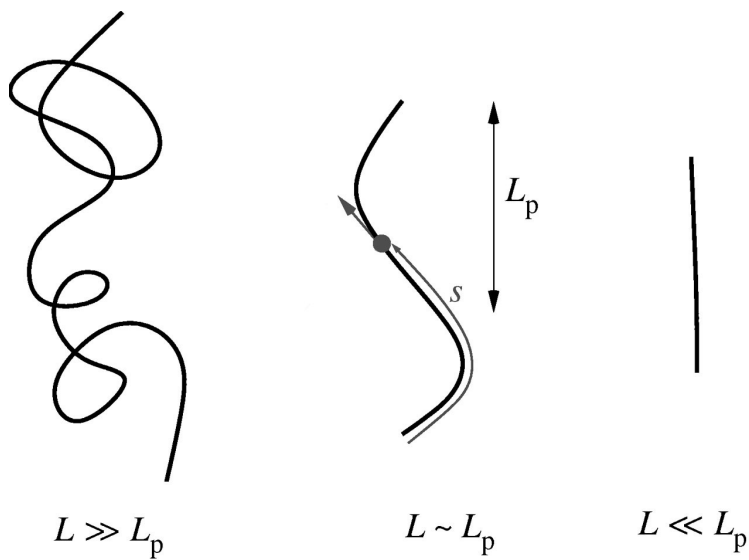


Figure 1.18: Schematic of polymers with respectively big length compared to the persistence length (A), in the order of the persistence length (B) and small compared to persistence length (C), s as defined on (B) is the *curvilinear abscissae*, that is to say the distance between two points of the polymer, measured by “following” the polymer. Adapted from [Liverpool 2006]

For the above reasons, actin solutions are often compared to semi-flexible polymers, and models that predict the behavior of actin networks often take foundation on polymers physics [Morse 1998b] [Morse 1998a]. Still, if these models rely on local microscopic parameters, experimental methods only have access to bulk properties of the studied material, and it is from these properties, and through the models, that we can deduce possible values for the microscopic models [MacKintosh et al. 1995].

1.7.1 Elastic Modulus

The elastic moduli are probably the easiest to understand. They are characteristic of how a material will deform non-permanently under an applied

force. The stiffer something is, the higher its elastic moduli will be. There are two specific elastic moduli of interest in this manuscript, *Young's Modulus* and *shear modulus*. The first one describes how a material will

react to compression or extension, while the second describes how a material resists shearing. For isotropic and homogeneous materials, the Young's modulus (E) and the shear models (G) are related by the Poisson's ratio (ν):

$$G = \frac{E}{2(1 + \nu)} \quad (1.9)$$

Both G and E units are homogeneous to N/m^2 or Pa . It is instructive to have an idea of the order of magnitude of a few usual materials. Aluminium will have an elastic modulus $G_{Al} \simeq 70 \text{ GPa}$ while rubber will be more in the order of $G_{rubber} \simeq 0.1 \text{ GPa}$. The elastic modulus of muscle cell is in the order of $G_{muscle} \sim 10 \text{ kPa}$ and brain tissues around $G_{brain} \sim 0.1 \text{ to } 1 \text{ kPa}$ [Engler et al. 2006].

A more formal definition of the Young's modulus is the ratio between the stress σ along the direction of the deformation and the relative deformation ϵ .

$$\begin{aligned} E &= \frac{\sigma}{\epsilon} \\ &= \frac{F/S}{\Delta L/L_0} \end{aligned} \quad (1.10)$$

In which F is the applied force, S is the cross section of the material, ΔL is the elongation and L_0 is the initial length of the considered material. (Figure 1.19 A):

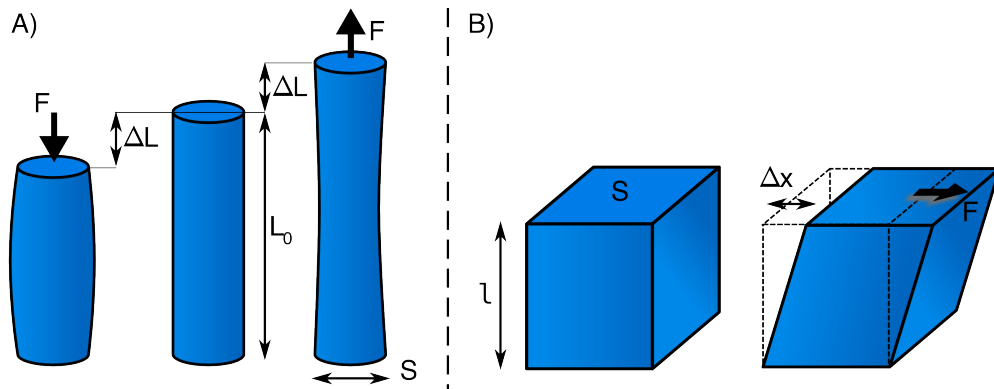


Figure 1.19: Schematic of the Young Modulus definition. F , force applied to a sample, S surface of cross section when uncompressed, L_0 , length when no load is applied. For both compression and extension, in the regime of small deformation, the relative change of length is proportional to the applied force. Here, the material can be seen to expand/contract in the orthogonal direction to the direction of the, applied force. In the case of an incompressible material ($\nu = 0.5$) this can be seen as the conservation of the material volume.

The shear modulus is defined for a deformation, parallel to the surface on which it is applied :

$$\begin{aligned} G &= \frac{\tau_{xy}}{\gamma_{xy}} \\ &= \frac{F/S}{\Delta x/l} \end{aligned} \quad (1.11)$$

In which τ_{xy} is the shear stress, γ_{xy} is the shear strain, F is the applied force on the cross section of the material S . l is the thickness of the material and Δx is the transverse displacement (Fig 1.19 B).

Other characteristic numbers can also be defined, such as the bulk modulus. In the case of isotropic elastic materials, only two of those parameters are required to completely define the properties of the material.

1.7.2 Poisson's Ratio

We have seen that the shear modulus is linked to the Young modulus using the Poisson's ratio. It is another characteristic of a material that defines how much a material will compress/expand in the orthogonal directions to its elongation. The Poisson's ratio is the negative ratio of transverse to axial strain :

$$\nu = -\frac{d\epsilon_{trans}}{d\epsilon_{axial}} \quad (1.12)$$

In which ϵ_{axial} is the relative deformation along one of the axis of compression/elongation and ϵ_{trans} corresponds to the relative deformation along an axis, orthogonal to the axis of deformation.

Volume conservation during compression or elongation requires a Poisson's ratio of 0.5. Such values have been found in bulk measurements of actin networks at actin concentrations of 21.5 μM in G-actin [Gardel et al. 2003]. Materials with a Poisson's ratio of 0.5 are said to be incompressible. A Poisson's ratio lower than 0.5 corresponds to materials expanding less than incompressible materials, and some cells and tissues are known to have a Poisson's ratio lower than 0.5 [Mahaffy et al. 2004]. Another critical value is 0, where the materials only expand or contract in the direction of the main stress.

Materials with a Poisson's ratio superior to 0.5 would show a bigger deformation in the orthogonal direction than incompressible materials, leading to a global volume increase, if compressed.

1.7.3 Viscosity

Like elasticity, viscosity is something tangible we are used to work with in everyday life. The more viscous a material is, the more difficult it is to move something in it, at high speed. And indeed, viscosity is the pendant of the elastic modulus, but considering forces induced by the deformation rate instead of displacement

$$\begin{aligned} \frac{F}{S} &= \tau_{xy} \\ &= \eta \frac{\partial v}{\partial z} \end{aligned} \quad (1.13)$$

In which τ_{xy} is the shear stress, F is the force exerted on the surface S . η is the viscosity, and is expressed in Pa.s , v is the deformation rate along the direction z .

At room temperature, water has a viscosity of around 1 mPa.s, and honey of 10 Pa.s. The consideration of viscosity in problems will often depend on the timescale and deformation rate. At a short timescale, tissue often behaves elastic, whereas at a long timescale, the effect of viscosity will be seen [Thoumine et al. 1997]. In actin networks, the effect of viscosity at short time scale can be similar to elasticity [Gardel et al. 2003].

1.7.4 Viscoelasticity

Typically, no material is purely elastic or purely viscous. While glaciers seem purely solid at the time scale of a few days, observation on a longer time scale, ranging from months to years, show that ice is not only a solid, but can also flow. Of course, ice in its solid form is not the only material which is both solid and viscous. In order to describe such behaviour, one can use the theory of viscoelastic materials. A number of models have been and are still developed to describe viscoelastic behavior. The Kelvin-Voigt and Maxwell models are two of the simpler ones (Fig 1.20). A thought experiment, conducted to understand each of

these models, consists of putting a spring and a dash pot in parallel or series. Such model systems exhibit viscoelastic behavior.

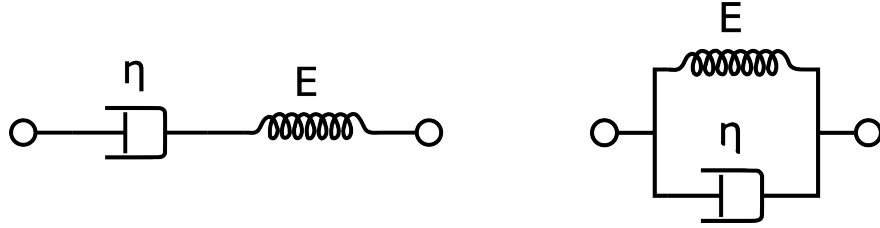


Figure 1.20: Maxwell model schematic on the left and Kelvin-Voigt model on the right. Both are simple approaches to express the properties of a viscoelastic solid. The response to a creep compliance will differ in both cases. The Maxwell model will mostly behave like a fluid with viscosity η after a long time, whereas the Kelvin-Voigt model will mostly reflect the elastic components at constant exerted stress. (Schematic in Public Domain, adapted from Wikimedia).

The idea for more complex models is similar: any material can be considered as an (infinite) combination of springs (for elasticity), and dash-pots, (for viscosity).

The theory of viscoelastic materials explains the mechanical properties of a system by using a single parameter: the viscoelasticity of a material. This can be done by describing E as a relaxation modulus depending on time. In the case of a linear system, we can express the strain on the material at a given time, as a function of its history :

$$\sigma(t) = \int_{-\infty}^t E(t - \tau) \frac{du}{d\tau} d\tau \quad (1.14)$$

In which $\sigma(t)$ is the time dependent stress, and $u(t)$ is the known strain.

Through the use of rheology, it is common to measure the properties of a material using a sinusoidal strain of known amplitude u_0 and frequency $f = \omega/2\pi$: $u(t) = u_0 \cos(\omega t)$, which also implies a sinusoidal strain rate. Using the complex notation $\dot{u} = u_0 i \omega e^{i\omega t}$ in equation (1.14), and operating the change of variable $t - \tau \rightarrow t'$ leads to :

$$\sigma(t) = u_0 \int_0^\infty E(t') i \omega e^{i\omega(t-t')} dt' \quad (1.15)$$

By factoring out the time dependent part, the rest can be rewritten as two integrals with respectively a real and an imaginary prefactor:

$$\sigma(t) = u_0 e^{i\omega t} \times \left(\omega \int_0^\infty E(t') \sin(\omega t) dt' + i\omega \int_0^\infty E(t') \cos(\omega t) dt' \right) \quad (1.16)$$

The two integrals in brackets only depend on the pulsation ω and the properties of the considered material. They are both in factors of the complex strain $u(t) = u_0 e^{i\omega t}$. We thus define the storage modulus of the material as the real part of ((1.16) in bracket) E' :

$$E'(\omega) = \omega \int_0^\infty E(t') \sin(\omega t) dt' \quad (1.17)$$

And the loss modulus as the imaginary part of ((1.16) in bracket)

$$E''(\omega) = \omega \int_0^\infty E(t') \cos(\omega t) dt' \quad (1.18)$$

And define the complex frequency dependent Young's modulus as :

$$E^*(\omega) = E'(\omega) + i.E''(\omega) \quad (1.19)$$

Thus we can write (1.16) as :

$$\sigma(\omega) = E^*(\omega).u(\omega) \quad (1.20)$$

In this representation of $E^*(\omega)$, the real part will correspond to the elastic response of the material (in-phase response under oscillatory strain) and the imaginary part corresponds to the viscous response of the system (out of phase under sinusoidal strain). The complete knowledge of $E^*(\omega)$ at all frequencies completely characterizes the material.

Models for actin networks have been extensively studied as viscoelastic material both theoretically [Morse 1998a], [Kruse et al. 2005] , and experimentally [Mizuno et al. 2007]. Actin networks have also been shown to exhibit linear characteristic behavior, but at certain concentration ranges, a non-linear behavior has also been observed [Yao et al. 2011], [Gardel et al. 2003].

The actin networks we will study hereafter, being in the condition where a linear behavior is expected, we will thus use the viscoelastic theory to interpret the observed relation stress/strain, in order to determine the mechanical properties of the formed actin gels.

1.8 Optical tweezer

Optical tweezers, or optical traps, are a technique that allows to trap objects near the focal plane of a microscope, at the focal point of a high-power laser. It is a versatile technique that allows to trap both fabricated objects and parts of living cells. Optical traps typically allow to apply forces up to a few tenth of pico Newton.

In order to understand that light can trap an object, it is instructive to keep in mind that, despite having no mass, photons carry momentum and that, as for any massive object, changing the trajectory requires a force. According to Newton's third law, when applying a force via a photon on an object, the object will in turn exert the opposite force on the photon, thus changing its trajectory. If a photon changes its trajectory in a material, the material has to apply a force on it([Fig 1.21](#)), meaning that the photon also applies a force on the material. In particular, the higher the refractive index of a material, the more light beams are deviated, and hence the more photons apply forces on material.

More specifically, it can be shown that objects with a higher refractive index than the surrounding medium, are attracted towards higher light intensities ([Fig 1.21](#)). In particular, laser beams with a Gaussian intensity profile, will lead to the object being attracted towards their center.

In addition to the lateral trapping, the laser focus leads to another intensity gradient along the direction of beam propagation, the intensity being at its maximum at the laser waist.

So, a laser coupled into a microscope objective acts as a three dimensional potential that traps particles, similar to a tweezer. Usually the trapping in a parallel to the laser direction, is only about half as strong if compared to the trapping in the lateral direction.

Among the qualities of optical traps, one is that in principle, multiple traps can be obtained. A simple method to generate two traps is to split the incoming light into two orthogonally polarized independent

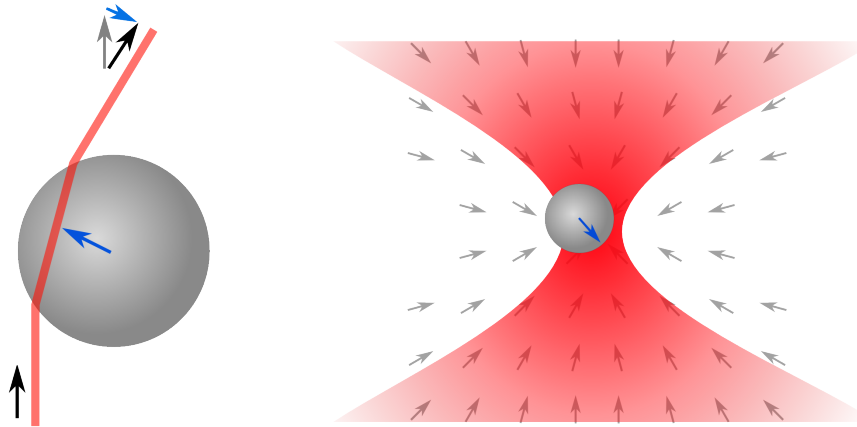


Figure 1.21: Light deflected by a transparent bead changes the light momentum, so the light is exerting a force on the bead, which will be attracted towards the highest intensity. For a focused laser beam, the bead will be attracted near the laser focus.

beams. Instead of sharing the laser power between the different traps by using polarisation, one can use what is known as multiplexing by time sharing. This is achieved by rapidly switching the laser between different positions at a much faster speed than the diffusion of the particles. By using this method, it is possible to virtually achieve multiple traps on the same sample.

In this work, we use a multiplexed system, where the rapid switching is achieved, by means of Accousto Optic Deflectors (aka AODs). An AOD consists of a crystal in which a high frequency sound-wave propagates perpendicular to the incoming laser beam. This sound-wave generates local changes in the refractive index of the material, which acts as a diffraction grating. In the right conditions, a laser passing through the crystal will be deflected by this grating under the Bragg angle.

In practice, rapidly controlling the frequency and amplitude of the sound-wave in the crystal, allow direct adjustment of laser deflection and hence the trap position. Not only does the use of AODs offer the advantage of controlling the number and position of multiple traps, but also the individual power allocated to each trap, hence their stiffness. ... _ots:

A schematic of the optical setup used to trap beads in the focal plane on the microscope, can be found in figure ???. The scheme also contains the detection part of the setup used to measure the force exerted on each bead, technique which is explained in the following part.

1.8.1 Determination of trapping forces and bead displacement

In addition to allowing the objects to be held in place, the use of a QDP (Quadrant Photo Diode, a precise position detector) with optical traps, has the advantage to acquire the high frequency quantitative measurements of the displacement and force exerted on an object. Indeed, when the trapped particle is not in the trap center, the laser applies a force on the object. Reciprocally, the object applies the opposite force on the light beam, thus deflecting it. With a proper use of optics and lenses correctly placed on the Fourier plane of the sample, it is hence possible to translate this orientation change of the light beam into a displacement of a light spot, onto a photo detector with high sensitivity to applied forces.

Through a careful calibration of the trap, which gives the force/displacement relationship, [Jahnel et al. 2011], [Vermeulen et al. 2006], one can then also recover the sample displacement inside the optical trap.

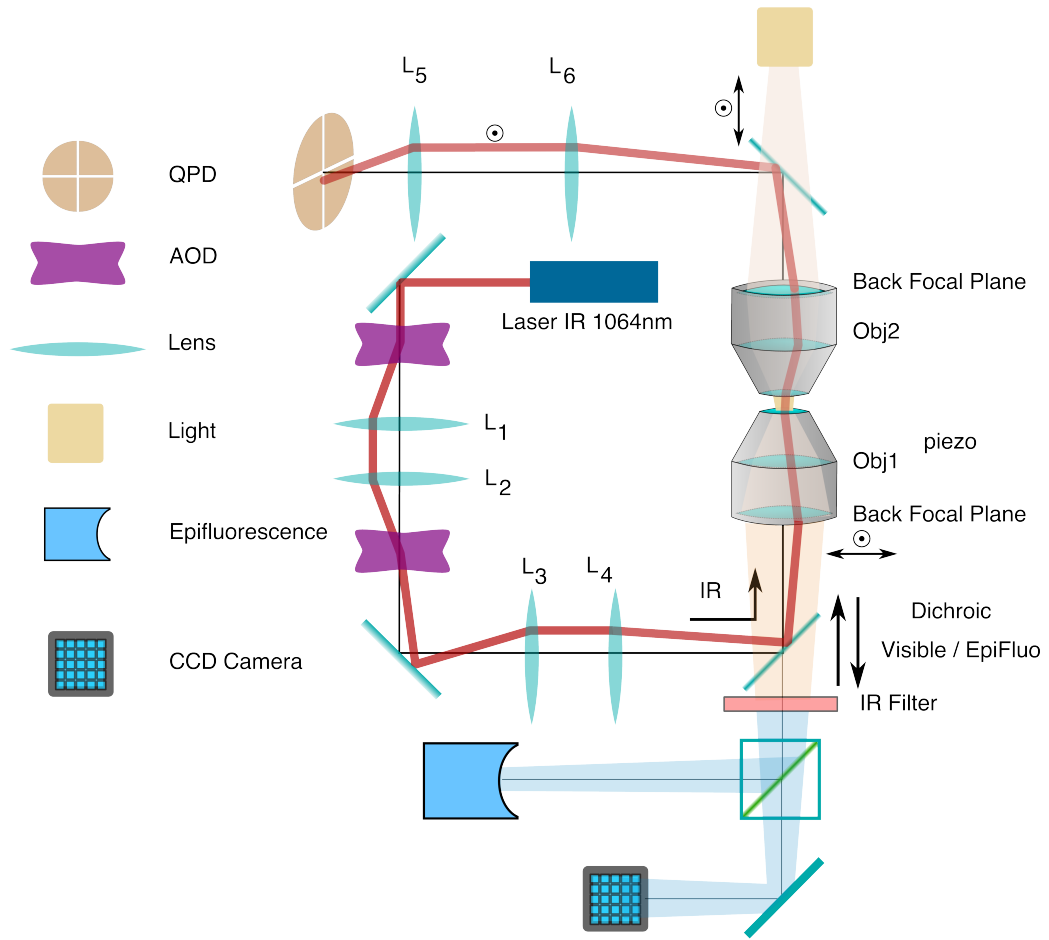


Figure 1.22: A schematic of setup used. The following elements can be distinguished. An 1064nm laser is used for trapping. It first passes through two AODs that move the position of the trap in the X and Y direction. The first couple of lenses (L_1, L_2) between AODs assures that AODs are in conjugated planes. The second pair of lenses (L_3, L_4) image the AODs plane in the back-focal plane of the first objective. Thus, a change of angle of the light beam induced by the AOD, results in a change of the trap position. The trapping light is collected by a second objective, and illuminates a quadrant photodiode (QPD) conjugated to the back focal plane of the collecting objective. By construction, QPD and AODs should be conjugated, so the deviation of the light beam induced by one of the AODs is not supposed to induce any change of the laser spot position on the QPD. Additional dichroic mirrors allow to use bright field and epifluorescence simultaneously with the optical tweezer.

Actin Gels dynamics,

Using an optical tweezer, not only aiming at holding a particle in position, but also at getting a quantitative measurement of its displacement and the exerted force, requires to calibrate each probe particle. Polystyrene beads are common artificial probes, used to achieve such a goal.

The use of polystyrene beads has multiple advantages. First, one can obtain mono-dispersed beads, leading to reproducible and predictable trap stiffness. Secondly, theory can predict the shape of the potential felt by such a bead in a Gaussian beam [Nieminens et al. 2007].

The third advantage is that beads can be fictionalized, allowing specific interaction to be controlled, both *in vitro* and *in vivo*. Of course, the calibration is essential for the correct measurement of the different systems mechanical property , and the choice of the bead diameter has an impact both on the biological side and in the measurement physics.

CHAPTER
TWO

MATERIALS AND METHODS

2.1 Buffers

2.1.1 G-Buffer

G-Buffer is used to conserve actin in the monomeric form. Actin is diluted in G-Buffer and kept on ice for at least 12 hours before further use. G-buffer is aliquoted and stored at -20°C. For weekly use it is thawed and conserved on ice for up to a week. G-buffer is never refrozen. pH is adjusted to 7.4.

Composition of G-Buffer:

- 0.2 mM $CaCl_2$
- 0.5 mM DTT (Dithiothreitol, or (2S,3S)-1,4-bis(sulfanyl)butane-2,3-diol)
- 2.0 mM Tris (tris(hydroxymethyl)aminomethane or 2-Amino-2-hydroxymethyl-propan)
- 0.2 µM ATP (Adenosine triphosphate)

2.1.2 Polymerisation Buffer

Polymerisation buffer or X-Buffer is used for the polymerisation of actin gels on beads as well as bead dilution and buffer cleaning. It is aliquoted and conserved at -20°C. During experiments, it is stored on ice for up to a week. X-Buffer is never refrozen.

Composition of X-Buffer :

- 10 mM Hepes (2-[4-(2-hydroxyethyl)piperazin-1-yl]ethanesulfonic acid)
- 0.1 M KCl
- 1 mM $MgCl_2$
- 1 mM ATP (Adenosine triphosphate)
- 0.1 mM $CaCl_2$

2.1.3 X-Buffer with BSA

Same as X-Buffer, with the addition of 1% BSA (10 mg/ml). BSA is used to prevent non specific adsorption. X-BSA buffer is used in place of X-Buffer for probe-beads conservation.

2.1.4 ATP-Mix Buffer

ATP-Mix buffer or simply *Mix* contains the required ATP for actin polymerisation. It is aliquoted and stored at -20°C. Kept on ice for weekly use. pH is adjusted to 7.4.

- 12.0 mM ATP,
- 20,0 mM DDT
- 0.88 mM Dabco
- 24.0 mM $MgCl_2$

2.2 Protein preparation

2.2.1 pWA (also called pVCA)

pWA is used as a nucleation promoting factor. It is expressed from Human pVCA (verprolin homology central and acidic domain) into Rosetta 2(DE3) pLysS (Novagen) Cell. Purified pWA is aliquoted and conserved at -80°C, never refrozen, and conserved on ice for daily use.

2.2.2 Actin

Actin and biotinylated actin are purchased from Cytoskeleton (Denver, CO, USA), and stored at -80°C. Fluorescent Alexa-488 actin is obtained from Molecular Probes, stored at -80°C, and prepared according to manufacturer recommendation.

Actin is stored in 5 μ L aliquots at a concentration of ~238 μ M, and fluorescent actin in 3 μ L aliquots at a concentration of ~106 μ M.

G-actin with 20% fluorescently labeled actin monomers is prepared the day before the experiment, by mixing 1 aliquot of actin with 1 aliquot of fluorescently labeled actin, and by diluting the mix with G-Buffer until the desired concentration is reached.

2.2.3 Profilin

Human profilin is expressed by competent cells and purified in our laboratory as described in [Carvalho et al. 2013a]. Profilin is conserved at 4°C for a few months and kept on ice for daily use.

2.2.4 Arp2/3

Bovine Arp2/3, complex, is purchased from Cytoskeleton, prepared as recommended by the manufacturer, aliquoted at 1 μ M and conserved at -80°C. Aliquots are never refrozen and stored on ice for weekly use.

2.2.5 Capping protein

Mouse capping protein (CP; a1/b2) is purified as previously described in [Soeno et al. 1998]. CP was a gift from Laurent Blanchoin.

2.2.6 Myosin II

Myosin II is purified from rabbit skeletal muscle and fluorescent myosin II is prepared as previously described in [SoareseSilva et al. 2011]. The Myosin II functionality is confirmed by motility assays. Gliding speed shows an average of 4.5 + 1.5 μ m/s (N = 27).

The working buffer for Myosin contains

- 25 mM imidazole
- 50 mM KCl
- 70 mM sucrose
- 1mM Tris
- 2 mM MgCl₂
- 1 mM ATP
- 0.1 mM DTT
- 0.02 mg/ml β -casein,

Then, pH is adjusted to 7.4. In the working buffer, myosin II forms monofilaments about 0.7 μ m long, which roughly correspond to about 100 motors.

2.3 Lipids, reagent and proteins

Chemicals are purchased from Sigma Aldrich (St-Louis, Mo, USA, unless stated otherwise. EPC (1- α -phosphatidylcholine) and *1,2-distearoyl-sn-glycero-3-phosphoethanolamine-N-[biotinyl polyethylene glycol 2000]* (biotinylated lipids), *1,2-dioleoyl-sn-glycero-3-phosphocholine* are purchased from Avanti Polar Lipids (Alabaster, USA). Monomeric actin containing 10% or 20% of labeled Alexa-488 actin and 0.25 % of biotinylated actin is diluted in G-Buffer

2.4 Doublet preparation

Cell-sized liposomes are formed by electro formation [Angelova et al. 1986]. A 20 μ L mix of EPC lipids and PEG-biotin lipids (present at 0.1 %, mol), at a 2.5 mg/ml in chloroform/methanol 5:3 concentration, is

deposited on glass plates coated with ITO. Glass is then dried with nitrogen and placed under vacuum for 2 hours.

A chamber is formed, using the ITO plates with their conductive sides facing inside, then filled with sucrose buffer (200mM sucrose, 2mM Tris adjusted to a pH of 7.4). The Chamber is finally sealed with hematocrit paste (Vitrex Medical, Denmark).

An alternate current voltage of 1V at 10 Hz is applied between the ITO-coated surfaces for 75 minutes, to form liposomes.

The same preparation is done a second time and, by adding 0.9 μ m sulphorhodamin to the sucrose buffer, the liposomes inside buffer are marked fluorescently.

The two solutions are mixed in order to have the inside buffer of half the liposomes marked in red, and being to be able to distinguish the interface in some of the formed doublets.

The formed liposomes are incubated 15 minutes with 160 nM streptavidin in order to get them coated with it. Streptavidin-coated liposomes tend to aggregate. The solution containing doublets is then diluted 30 times. Waiting 15 minutes increases the ratio doublets/single liposomes, by still avoiding the aggregates of more liposomes.

A bulk solution of 40 μ M actin monomers — 10% fluorescent and 0.25% biotinylated — is diluted 40 times in a working buffer (25 mM imidazole, 50 mM KCl, 70 mM sucrose, 1mM Tris, 2 mM $MgCl_2$, 1 mM ATP, 0.1 mM DTT, 0.02 mg/ml β -casein, adjusted at to a pH of 7.4) and polymerized for one hour. The adjunction of 1 μ m of phalloidin after 1 hour prevents further depolymerisation.

Actin filaments are diluted to 0.1 μ M (10x), mixed with streptavidin-coated doublets of liposomes, and incubated for 15 min. The mix is diluted 5 times to reduce the fluorescent background due to actin monomers in solution.

2.5 Bead Preparation

Carboxylated polystyrene beads (Polysciences, Philadelphia, PA) of $4.34 \pm 0.239 \mu$ m (Standard deviation) diameter were used as actin-beads and probe-beads.

Beads are stored at 4°C.

Before being coated by BSA (probe-bead) or pWA (actin-bead), the bead solution is cleaned by centrifugation at 5000 rpm, 2min. After removing the supernatant, the pellet is resuspended in X-Buffer. This procedure is repeated twice.

2.5.1 Actin-Bead Preparation

Cleaned polystyrene beads are incubated for 20 min at 20°C under agitation with 2 μ M pVCA. Centrifuged at 5000rpm 2min, the supernatant is removed and the pellet diluted 4 times in X-buffer. The beads are stored on ice for one day.

2.5.2 Probe Bead Preparation

Cleaned polystyrene beads are incubated under agitation with 10 mg/ml BSA at room temperature for 30 minutes. Passivated beads are then centrifuged, separated from supernatant, the pellet is resuspended in X-BSA buffer and stored at 4°C for weekly use.

2.6 Force indentation experiments

2.6.1 Preparation of sample

An equal amount of both actin and probe beads are placed in the polymerization mix consisting of :

- 2 μ L BSA at 10%
- 3 μ L of ATP-Mix Buffer
- 1.5 μ L Profilin (114 μ M)
- 1 μ L beads (50% actin-bead 50% probe bead)
- 0.5 μ L Arp2/3 (22,3 μ M)
- between 0 and 2 μ L CP (0.5 μ M)
- Completed to 15 μ L using X-Buffer.

5 μ L of G-Actin (20% fluorescent) is then added to the previous mix. This moment marks the time $t=0$ for the experiment and recording. The experimental chamber is made of 2 coverslips, separated by VaLaP, which is a mix of vaseline (33%) Lanoline (33%) and Parafine(33%) in equal mass proportion. The chamber is prepared by gently depositing 20 μ L of the final beads mix at the lower coverslip center and 4 drops of VaLaP where the corner of the upper (18x18mm) coverslip will rest. The VaLaP, acting as a spacer, prevents the sample from being squashed. The upper coverslip is then placed on top of the sample and the chamber is sealed with VaLaP.

2.6.2 QPD positioning and calibration of microscope

The prepared sample is placed on the microscope and a drop of water is deposited on top of the upper coverslip to assure the immersion of the light collecting objective. The collecting objective and the quadrant photodiode are placed on top of the sample (*Optical tweezer*).

The trapping laser is then aligned with the photodiode, checking in the meantime that no object is trapped during the process. The conjugation of the objective back focal plane with the AODs and the QPD, is optimized by adjusting the distance of both objectives with respect to the sample.

A trapping laser is positioned near the center of the microscope field of view, using the custom written LabView program (Fig 2.1). The QPD is adjusted in X and Y direction to $\Delta X = \Delta Y = 0V$. This has to be done while no object is trapped in the laser focus.

2.6.3 Initial bead trapping

Two maximum strength traps (~50mW/trap) are created near the center of the microscope field of view, separated by 15 to 20 μm . The sample plane is then moved in the Z-direction, by displacing the 3D piezo controlled sample stage, to position the traps near the chamber middle plane. A temporary removal of the infrared filter from the microscope allows to see the trapping lasers reflection on both the upper and lower coverslips and to determine the localisation of the observation chamber middle plane .

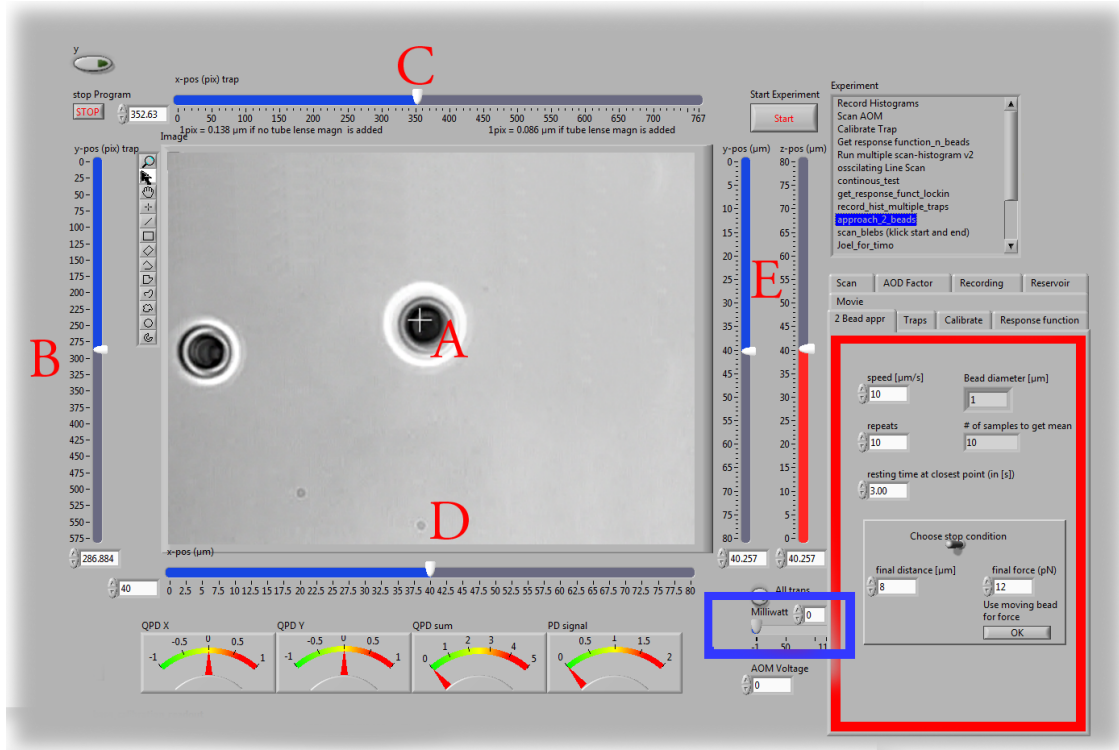


Figure 2.1: Software interface responsible for controlling the optical tweezer. Sample image showing 2 polystyrene beads and a single trap (A, white cross) holding one bead. Cursors (B,C) are available to displace the optical trap(s). Cursors can control the position of the stage: X (D), Y (E, blue) and Z (E,red). The blue rectangle highlights the slider that allows the control of the traps power. The red rectangle highlights the area where the different parameters of the experiment can be set (approach speed and resting time at closest point). 3 indicators at the bottom of the screen indicate the voltage on the QPD.

The operator then captures one probe-bead and one actin-bead in each trap. Both types of beads can be recognized using fluorescent microscopy, as actin-beads, promptly covered with a fluorescent actin, can clearly be distinguished from the probe-beads, which remain dark. If two identical beads are trapped, one of the two traps can selectively be disabled or decreased in stiffness, letting the bead escape from it , and the procedure can be repeated.

The operator will then roughly move the two traps one micrometer in each direction, to check that the two beads are effectively trapped in the tweezer and that no external forces act on the beads.

For practical reasons, the traps are aligned along one of the principal axis of the AOD, before starting the indentation experiments.

2.6.4 Indentations

The operator sets the experiment parameters in the software:

- Average bead radius,
- Approach/Retraction Speed.
- Resting Time
- Laser Power

For each pair of actin/probe beads, the initial minimum approach distance of the traps is set to 5 to 8 μm , before doing a single indentation cycle. If the maximum measured force between the two beads is not higher than 8 to 10 pN, the minimum approach distance is reduced by 0.25 to 1 μm and the procedure repeated. Once the maximum force measured is in the 10-15pN range, the right distance is found and up to 10 automatic force-indentation experiments are performed (Fig 2.2) . Before each indentation, the software automatically does a “scan” of each bead, to ensure correct calibration. An indentation cycle has the following steps :

- Probe trap is approaching the actin-bead at constant speed until the minimal approach distance has been reached.
- At the minimal distance, the traps remain stationary for the predefined (typically 3 seconds) resting time.
- Probe trap returns to its initial position at constant speed.
- Cycle is repeated as many times as set.

During this cycle, the deflection of the laser induced by both probe-bead and actin-bead are recorded by the QPD.

After an indentation cycle is finished, the experimenter can try to perform the indentation on the actin-bead from another direction, or release the actin-bead, proceeding to a new one.

In case the indented actin network shows signs of inhomogeneity or symmetry breaking, the experiments are stopped and not taken into account for further analysis.

The date and time of each indentation cycle is recorded, to extract the time of polymerisation for each sample.

2.7 Time Shared Optical Traps

The optical trap is built on an inverted microscope (Olympus, IX71) equipped with a fluorescence (200W mercury lamp, Osram, Munich, Germany). The sample is observed through an Olympus 60X water immersion objective (Olympus) with numerical aperture NA=1.2, that also serves as the entry point of the optical tweezer laser. The light source is an infrared fiber laser ($\lambda = 1064\text{nm}$, YLP-1-1064, IPG, Germany). The X, Y positionings and the trapping force stiffness are controlled by 2 Acousto Optic Deflectors (AODs, AA-Optoelectronics, France) that are placed in the conjugated plane of the objective back focal plane . Multiple traps can be achieved by switching the laser between multiple positions within a switching time, in the order of 5 μs , and resting on each position 20 μs or more.

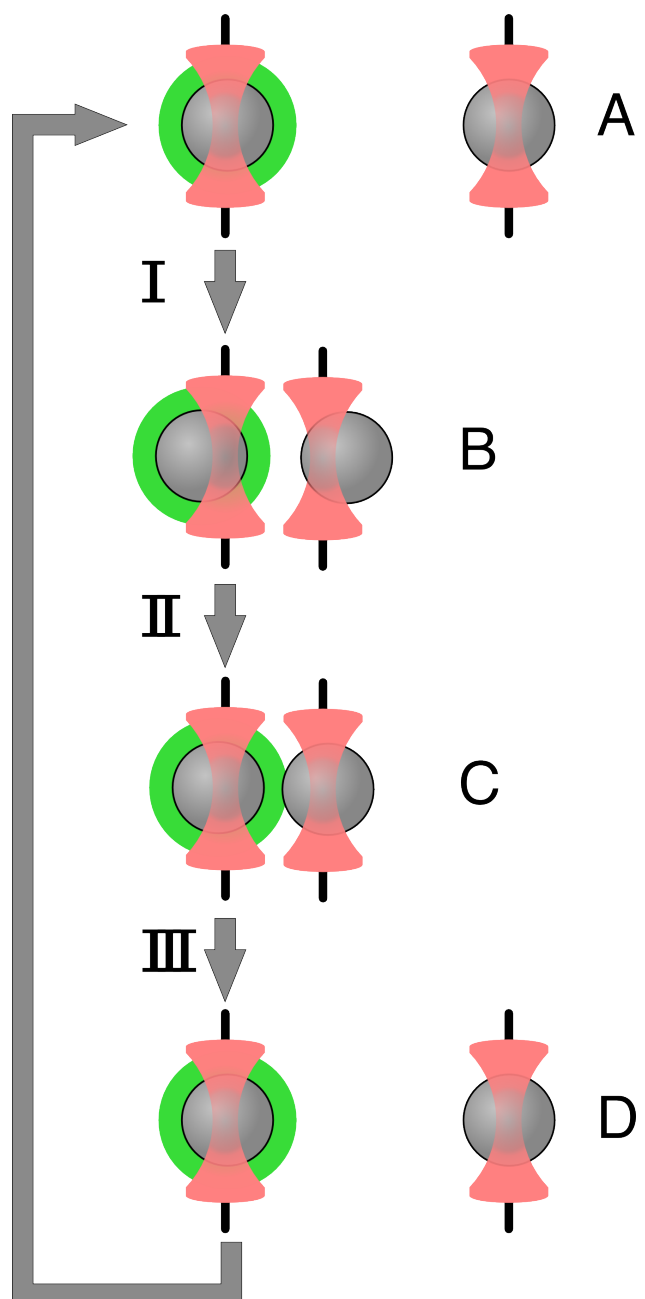


Figure 2.2: Schematic of indentation experiment. On the left is the actin-bead, covered with actin, in the static trap, on the right the probe-bead in the mobile trap. At the beginning of the experiment (A) the probe-bead is situated far from the actin-bead. During the approach phase (I) the moving trap approaches the static trap at $10\mu\text{m/sec}$ until it reaches the minimal approach distance (B). The moving trap stays at the minimal approach distance for 3sec (II), which constitutes the relaxation phase.C) The actin gels are relaxed, the distance between bead is smaller than on B. III), the moving trap retracts at $10\mu\text{m/sec}$ back to its initial position.

Light refracted by the trapped sample is collected by a 40X (N.A:0.9, Olympus) water immersion objective, and imaged on a quadrant photodiode (QPD) conjugated with the back focal plane of the light collection objective. Signals from the QPD (ΔX , ΔY and Σ) are sampled at 500kHz, by a Digital To Analogic Aquisition card (NI PCIe-6363, National Instruments, Austin, Texas) and controlled by a custom written Labview software (National Instruments) coupled with Matlab (Mathworks, Natick, MA). Raw signals are preprocessed by binning all voltages measured during the laser resting time (typically 20 μ s, at one position). Finally, the mean and standard deviation for each trap visit is stored for further processing.

The trap stiffness is inferred from bead radius, laser power, number of present traps and controlled experiment data. In controlled experiments, the trap stiffness was calibrated using the power spectral density method, and was determined to be as high as 80 pN/ μ m at full laser power (119mW) for a single trap. In the case of multiplexing, both traps as used in this work, were calibrated before the experiment. The sample coarse positioning was achieved through a pair of micrometer precision screws, capable of translating the microscope stage in X and Y, and finer positionings in X,Y and Z directions with the help of a 3D piezo stage, with an accessible range of 80 μ m in each direction and a sub-micrometer accuracy.

2.8 Oocyte

2.8.1 Oocyte obtention

Oocyte culture, collection, and micro injection?, were done at the College de France by Maria Almonacid.

Oocytes were collected from 11 to 15 week old mice (WT), fmn2-/- as previously described in [Holubcova et al. 2013] and maintained in Prophase I in M2+BSA supplemented with 1 μ M Milrinone. Oocyte were then injected with cRNA, using a micro-injector Eppendorf FemtoJet. Imaging was carried out at 37°C.

MECHANICAL PROPERTIES OF A FAR REACHING ACTIN CLOUD

3.1 Introduction

We have seen that the actin cytoskeleton plays a major role in cellular mechanics. Essential for force generation, it is a key component for cell motility. It has also been extensively studied both in cells and biomimetic systems.

Actin can form a variety of cells networks, ranging from dense branched networks at the lamellipodia leading edge to bundled parallel structures forming the filopodia. The actin network reconstruction has been achieved in biomimetic systems using purified components [Plastino et al. 2005], [Loisel et al. 1999], [BernheimGroszasser et al. 2002], [Pontani et al. 2009], and many properties of these networks have been measured.

It has been determined that the actin cortex provides mechanical support for the plasma membrane and that it extends over a few hundreds of nanometers. Many cellular processes hint that actin structures connected to this cortex, are key elements in organelle and chromosome positioning.

In this part of the manuscript, we will investigate how a sparse actin structure can emanate from the actin cortex, and explore its properties. Through the use of the *bead-motility* biomimetic system aiming at reconstituting the actin cortex and its dendritic structure, we will show that a sparse actin filaments network emanating from the cortex has a mechanical effect, sufficient to displace objects of cells organelles size at distances up to tens of micrometers away from the actin cortex.

The actin cortex branched structure underneath the plasma membrane of cells implies a structure governed by Arp2/3. To what extend can Arp2/3 and CP be used to form a biomimetic actin cortex has already been widely studied. In [Kawska et al. 2012], both *in vitro* measurements on reconstituted actin cortices on beads and simulations investigate the effect of cross-linking and Capping Protein on the formed actin gel. It can be observed both experimentally and in simulation that a filaments network escapes from what is defined as the actin cortex (Fig 3.1). The effect of these long filaments is not taken into account in the *in-silico* system, where the analysis is restricted to filaments shorter than 10 μm . The effect of dense entangled actin networks generated from randomly placed primers on the bead surface only participates in the tension increase and contributes to symmetry breaking.

The limit of the dense network, visible in epifluorescence, is defined in [Kawska et al. 2012] by the position of the half-maximum fluorescent intensity (Fig 3.2). The networks properties are measured by [Pujol et al. 2012] using magnetic beads and phalloidin-stabilized actin. Though, they do not investigate the sparse and softer actin networks that originate from the visible part.

Using *time-shared optical tweezer* we are able to probe the mechanics of this soft actin structure at a

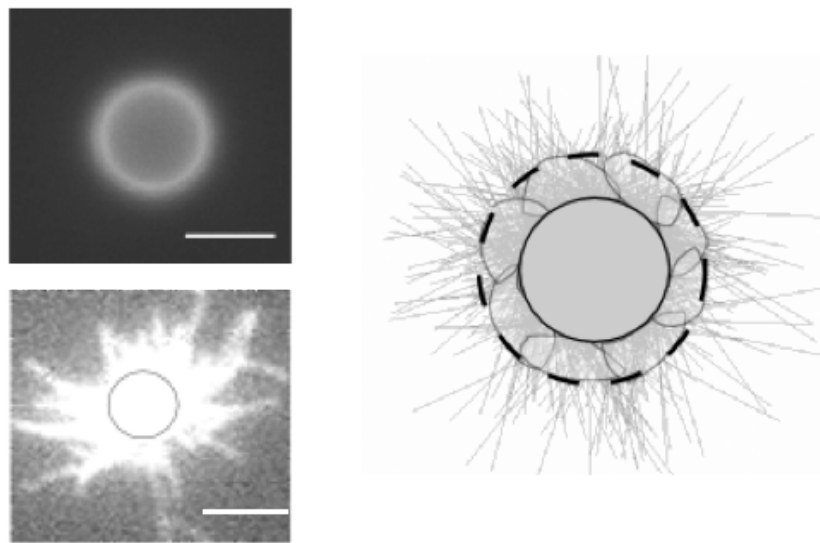


Figure 3.1: Upper Left : Fluorescence image of an actin bead with a growing actin cortex. Escaping filaments form the actin cloud that can hardly be seen in fluorescence. Scale bar is $2 \mu\text{m}$. Lower Left: Total Internal Reflexion (TIRF) image of actin polymerising on an actin bead. Escaping filaments can directly be observed. The gray circle represents the bead size. Right : Representation of the actin growth simulation with delimitation between the entangled branched actin network and escaping filaments. Adapted from [Kawska et al. 2012].

timescale shorter than the characteristic time of actin polymerisation and forces in the pN range. We will show that beyond the dense dendritic network mimicking the actin cortex, which has been measured to have an *elastic modulus* in the order of kPa [Pujol et al. 2012], the soft actin cloud is much softer with a stiffness in the Pa regime. This might explain why such a structure has not previously been observed with less sensitive techniques than optical tweezers. The size of this actin cloud and its ability to sustain forces suggest that in cells, the actin cortex is not sharply delimited and that structures escaping from it may play a role in organelle positioning.

Hereunder are the questions we address in this part of the manuscript : How far does the soft part of the gel extend ? What are its precise mechanical properties? How does it change over time? Is the actin cloud elastic or viscous?

3.2 Actin-Bead System

Reproducing the actin cortex and studying the mechanics of actin structures emanating from it *required 4.3 μm diameter polystyrene beads* coated with a nucleation promoting factor. These beads were placed in the *ATP mix buffer* in presence of 25nm of Arp2/3 complex, 4 μm of monomeric actin (20% fluorescently labeled), 12 μM profilin and a variable amount of Capping Protein. *see Material and Methods*. These beads are referred to as actin-beads.

These conditions were chosen in order to grow a dense network on the actin-bead surface as in [Kawska et al. 2012]. We determined at an amount of 25nM ATP and a varying amount of Capping Protein concentration in order to cover conditions where the dense gel formed on the actin-bead was able to accumulate sufficient

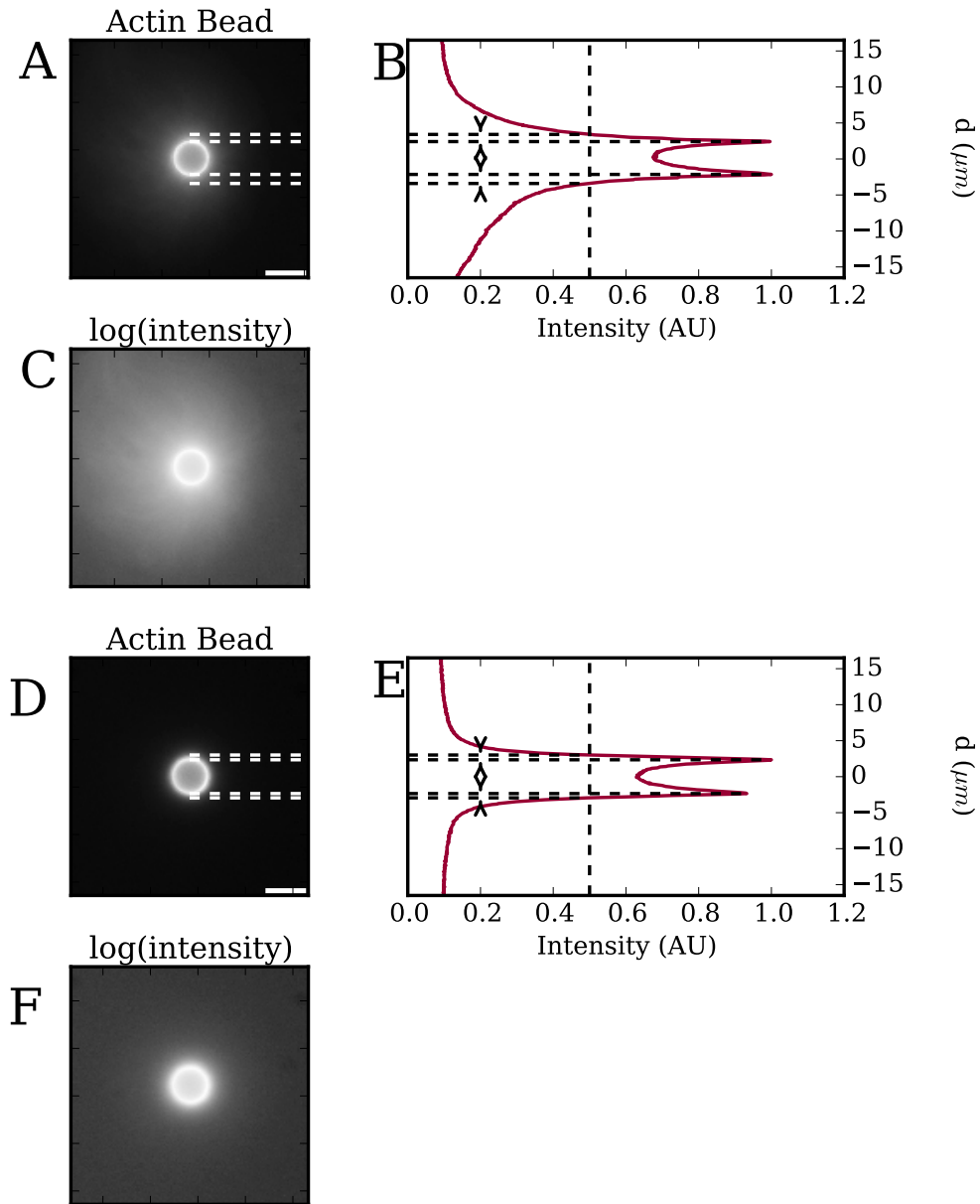


Figure 3.2: A) Epifluorescence image of polystyrene bead with a growing actin gel in presence of 25 nM of Arp2/3 and 25 nM of Capping Protein. Scale bar is 5 μm . B) Normalized intensity profile of fluorescence image with gel thickness shown with dashed line as defined in [Kawska et al. 2012] : Distance between maximum intensity and half-maximum intensity. C) Epifluorescence image of log(intensity). D,E,F) Same as A,B,C, in absence of Capping Protein

stress to lead to symmetry breaking (CP between 15 and 35 nM, see part *Bead Motility Assay*). We also investigated conditions where the amount of Capping Protein was too low (< 15nM) or too high (>35 nM) to permit symmetry breaking.

We selected a 4.3 μm bead diameter in order to get a characteristic symmetry breaking time of 20 to 40 minutes. A smaller bead radius implies a faster increase of stress and a shorter symmetry breaking time. Chosing 4.3 μm provides sufficient time to proceed with the experiments before symmetry breaking occurs.

All measurements were made on an actively growing actin network which was not stabilized before symmetry breaking occurred for Capping Protein concentration in the range 15 to 35 nM [Kawska et al. 2012].

3.3 Probe Bead System

Beside actin-bead, the experiment required a polystyrene bead passivated with BSA. These beads are referred to as probe-beads. The probe-bead size, similar to the actin-bead's, ensured the optical trapping of both beads in the same observation plane. In the case of different beads diameters, the axial forces on the beads were different. This axial displacement of the two beads during the indentation process led to a component along the z-axis which eventually pushed one bead out of the trap.

3.4 Experimental description

In order to probe the actin network, we trapped an actin-bead with a growing actin-network and a probe-bead using time-shared *optical trap*, and measured the forces on the actin-bead, using a QPD placed in the back focal plane of the condenser (*material and methods*).

Moreover, all force recordings used for analysis were made on the static bead, in our case the actin bead, to avoid systematic errors of force measurements on the moving trap.

The indentation is a three step process (Fig 3.3):

- An approach phase at constant velocity 10 $\mu\text{m/sec}$ unless specified otherwise
- A 3 second relaxation phase during which both traps remain static
- A retraction phase during which the probe trap returns to its initial position at 10 $\mu\text{m/sec}$.

3.4.1 Approach Phase

During the approach phase, the probe-trap will approach the actin-trap at constant speed (10 $\mu\text{m/s}$), as shown in figure 3.3 for times $t < t_1$, and the actin-bead will repel the probe-bead, due to the actin network growing on it. The force undergone by the actin-bead will progressively increase during the probe-bead approach, eventually reaching the maximum as the probe-trap reaches its nearest position to the actin-trap. It should be noted that during this process, the force between the beads pushes them out of their respective trap centers. The beads displacement in the trap remains negligible compared to the distance between the two beads. Hence, in the following we will consider that the probe-bead speed is equivalent to the trap approach speed of 10 $\mu\text{m/sec}$.

3.4.2 Relaxation Phase

After the approach, the trap remains static for a 3 seconds relaxation phase . The relaxation phase starts at t_1 and finishes at t_3 as shown on figure 3.3. The duration of the relaxation phase is sufficient to allow the actin cloud partial relaxation but remains sufficiently short compared to the actin polymerisation speed. Hence, the polymerisation is not expected to change the network properties during indentation cycle and repetitive indentation (Figure 3.6)

While the actin network relaxes, the forces between the two beads will slowly decrease, thus leading to the beads getting closer to their trap center and to each other. There is a slight decrease in distance during the relaxation phase, compared to the distance between beads. The force decrease as well as the minimal change in distance between the two beads can be seen observed? on Fig 3.3 in the middle part.

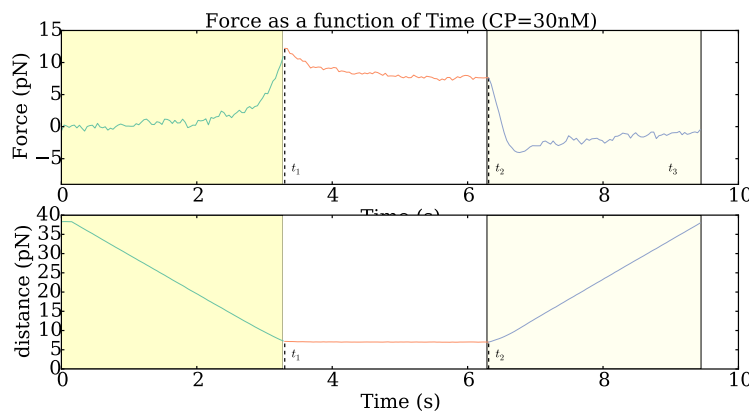


Figure 3.3: Upper graph : Force as a function of time on the actin-beads. Lower graph : distance between beads (distance between traps + beads displacement from the trap center) as a function of time. The first part of each graph (green curve, yellow back) represents the approach phase. The middle part (orange on white) corresponds to the relaxation phase, and the right part (blue on pale yellow) is the retraction. The observed data is a subsample of around 1 out of every 1000 acquired points. We can see on the second graph that the beads displacement on their respective traps is negligible compared to the trap displacement and justifies the approximation of a probe-bead speed equivalent to the probe-trap speed.

3.4.3 Retraction part

After the three seconds of the retraction phase, the probe-trap returns to its initial position at $10 \mu\text{m/s}$ ($t > t_2$). During this phase, the force exerted between the two beads decreases, becomes negative, reaches a minimum, and eventually returns to zero as the probe-bead recovers its initial position (shown on Figure 3.3 right part). Negative forces represent the forces that tend attract the two beads towards each other.

3.4.4 Reconstitution of Force-distance-curve

The beads position in the trap as well as the force exerted on each bead can be calculated from the position of the trap over time (and the signal measured by the QPD. We can then recover the distance between bead centers as a function of time. The force-distance curve representing the force exerted by the probe-bead on

the actin-bead as a function of the distance can be computed and is shown in [figure 3.4](#) where we can still distinguish the three phases of the indentation cycle, also marked by the color used for the data.

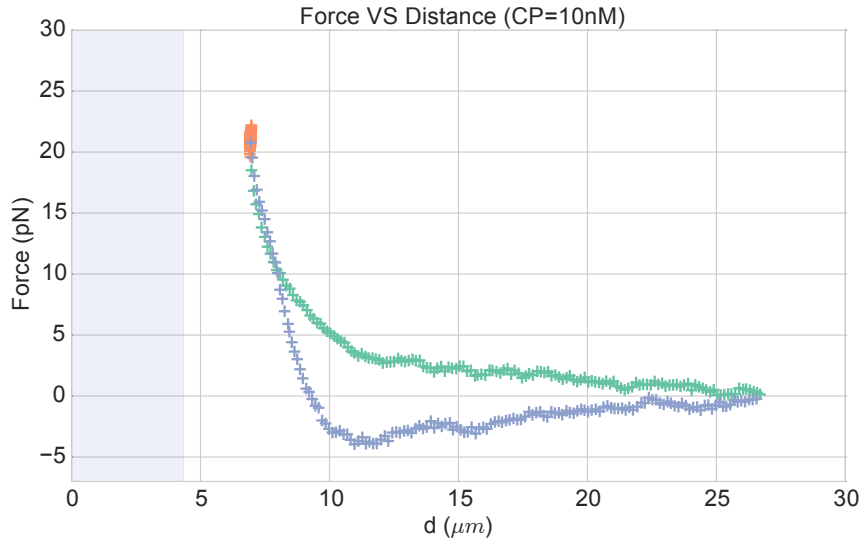


[Figure 3.4](#): Force exerted on the actin-bead as a function of the distance between the two bead centers. Colors and data are the same as in [Fig 3.3](#). The probe-bead starts from the far right, and gets closer while the force increases (green upper part of the curve), reaches a maximum, and enters the relaxation phase (orange part), where the force between both probe-beads and actin-bead decreases, while the distance also slightly decreases. During the retraction part (blue), the force rapidly decreases and reaches negative values as the bead returns to its initial position. The observed data is a subsample of 1 in? every 1000 points of acquired data. Shaded regions represent areas where the two polystyrene beads should interpenetrate.

3.4.5 Repetitive indent

The indentation cycle can be repeated several times every few seconds, to check for reproducibility and non-plastic deformation of the network after indentation. As the network is constantly growing during the measurement, this repeat also allows to check for possible changes of the network properties, due to actin polymerisation. The force-distance plot is shown in [Figure 3.6 , 3.5](#).

3.4.6 Effect of approach speed

[Gardel et al. 2003] suggests that, for frequencies higher than 0.1 Hz, the force due to the actin network viscous behavior can be in the same order as the one due to the elastic component . In order to test whether such a relaxation effect is important, we measured the effect of the approach speed on the force measurements. [Fig 3.7](#) presents the indentation speed affecting the measurement by varying the approach speed from 10 to 30 $\mu\text{m/s}$ on the same actin-bead.

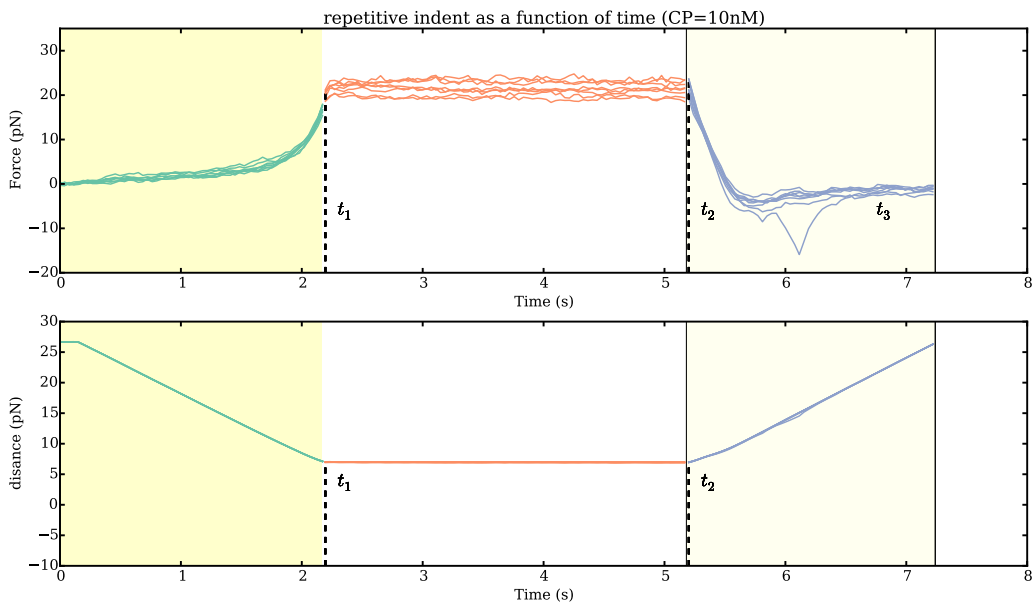


Figure 3.5: Upper graph : Force exerted on actin-bead as a function of time for ten repetitive indents. In one of the cycles, a sticking event can be identified in the retraction phase, 6 seconds after the beginning of the cycle. Lower graph: Distance as a function of time for ten repetitive indents. The ten curves can hardly be distinguished from one another, which shows the reproducibility of indentation curves.

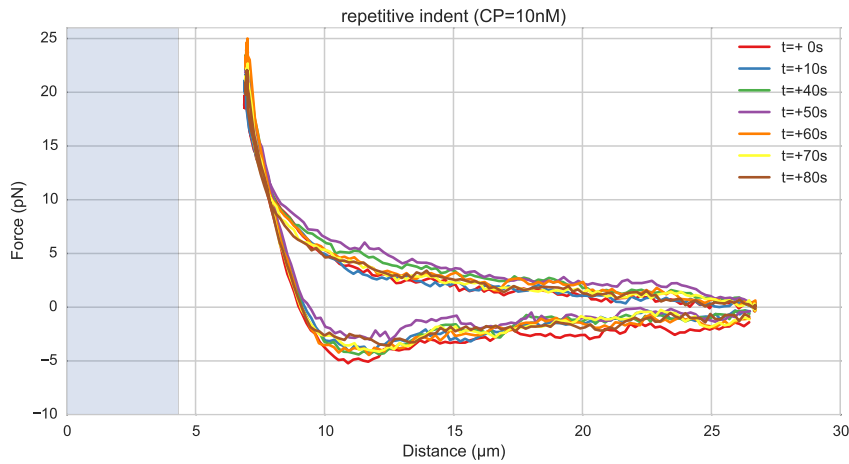


Figure 3.6: Figure showing the indentation process reproducibility on a bead with 25nM Arp2/3 and 10nM CP Subset of data from Fig 3.5 highlighted with different colors to represent the evolution of the indentation curve over time. Time is relative to the first indentation. Shaded areas represent zones where the two beads should interpenetrate.

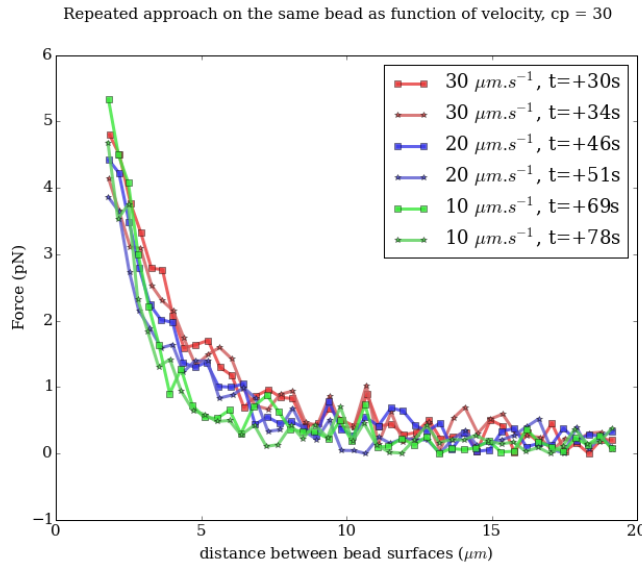


Figure 3.7: Approach phase of repetitive indents at multiple speeds on the same actin-bead. The approach phase in the different conditions is similar, hinting at a negligible effect of the viscosity in the actin cloud at the considered speed.

3.5 Experimental observations

Through the use of the bead system, we are able to reconstruct actin cortices *in vitro* and to investigate the mechanical properties inaccessible to other microscopy techniques like TIRF. Beyond the visible actin cortex, we can detect the presence of an actin structure with mechanical effects starting at distances of $> 10\mu m$, hence far beyond the thickness of the actin cortex ($\sim 1\mu m$). Figure 3.8 presents a video qualitatively showing that the actin cloud growing on actin-beads is able to repel free floating probe-beads, before they reach the visible reconstituted cortex.

In order to quantify the distance at which the probe-beads start to be affected by the actin-cloud, we measured the experimental noise by studying the fluctuations of the trapped probe-bead.

During the indentation, we defined d_0 as the distance at which the average force received by the probe-bead is higher than the experimental noise. Typically the standard deviation is 2pN.

The repartition of d_0 with the concentration of Capping Protein is plotted in figure 3.9.

3.5.1 Approach phase modeling

We decided to model each part (approach, relaxation and retraction) independently, to extract their mechanical properties, by using the three phases of the experiment. In particular, we fitted the force-distance curve of the approach phase using a power law with 3 fit parameters α, β, δ :

$$F(d) = \beta \times (d - \delta)^\alpha \quad (3.1)$$

in which F represents the force exerted on the probe-bead, and d is the distance between bead centers. The power law exponent α is expected to be negative as the force decreases with the distance d , and to charac-

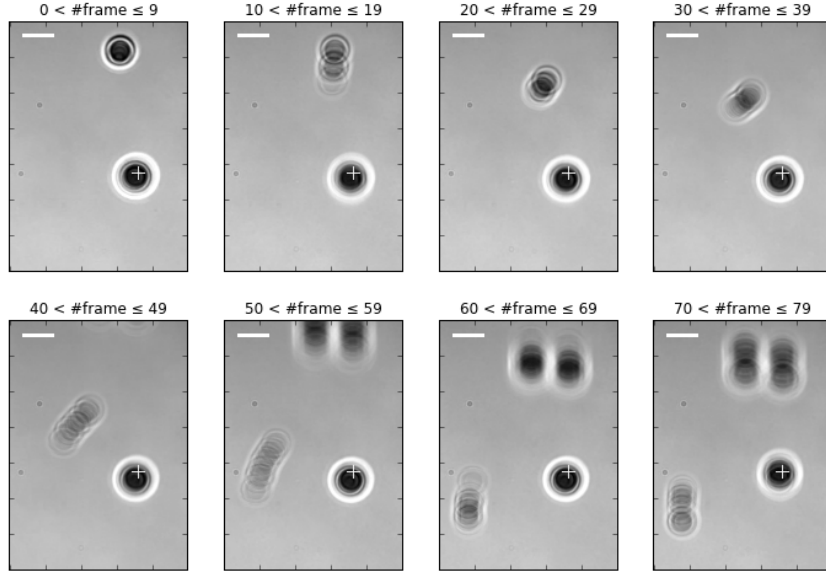


Figure 3.8: Chronophotography representing the displacement of a trapped actin bead in a solution including probe-beads. During this experiment, the actin bead is kept static in the optical trap (marked by the cross) while the stage is moved. Scale bar is 5 micrometers. The total movie duration is 21 seconds.

terize how fast the force increases as the two beads approach each other. The prefactor β acts as a scaling factor of the force. The offset parameter δ shifts the curve on the distance axis. This phenomenological model presents the particularity that the force on the probe bead tends to $+\infty$ when the distance d gets to δ . The force is undefined for values of $d < \delta$. Hence, the offset distance δ practically describes the distance at which the optical trap is no longer able to indent the network.

In the case of a hard sphere, the value of α would tend towards $-\infty$ leading to a infinite force increase at the contact between the two hard-spheres of same diameter, and a value of δ equal to the diameter of the hard sphere. In this case $F(d > \delta) = 0$ and $F(d < \delta) = \infty$

The used optical tweezer being able to apply forces up to 20pN, and the beads having a diameter of $4.34\mu\text{m}$, we hence determined a cross-sectional surface of roughly $14.7\mu\text{m}^2$. Before escaping the trap, the probe-bead did move up to $1\mu\text{m}$ from its trap center. To estimate the maximal stiffness achievable, we considered that we could provide a clear measure of deformation in the order of $1/10$ of μm , this leading to a maximum detectable Young's modulus of :

$$\begin{aligned} E_{max} &\sim \frac{F_{max}L_{0,max}}{A_0.\Delta L} \\ &\sim \frac{50.10^{-12} \times 1.10^{-5}}{(\pi \times 2.17 \times 10^{-6})^2 \times 1.10^{-7}} \\ &\sim 300\text{Pa} \end{aligned} \tag{3.2}$$

Any material with a stiffness much higher than 300 Pa can be considered as infinitely rigid.

The elasticity of dense actin gels around polystyrene beads has been measured in [Pujol et al. 2012] and

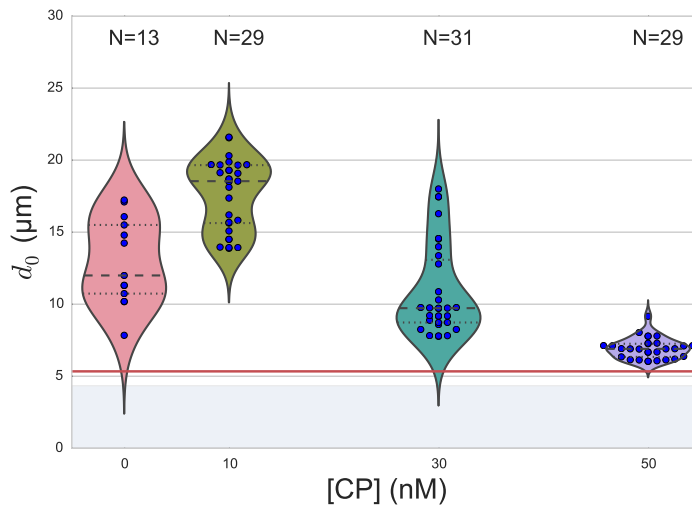


Figure 3.9: Repartition of the bead-center distance at which the actin cloud exerts a force higher than the noise (d_0) on the probe-bead, as a function of Capping Protein. The shaded region represents the bead surface position ($4.34 \mu\text{m}$) and the red line represents the bead surface+ $1\mu\text{m}$ (upper bound for the in vitro Capping Protein concentration). The shaded region represents the bead surface position($4.34 \mu\text{m}$) and the red line represents the bead surface+ $1\mu\text{m}$ (upper bound for the in vitro reformed actin cortex measured in [Kawska et al. 2012]). We can see in this graph that for symmetry breaking conditions (CP 10 nM and 30 nM, the distance at which the actin cloud starts to apply forces on the probe-bead is larger than the thickness of the actin cortex. The distance at which the probe-bead is able to detect the presence of the actin cloud decreases when increasing the concentration of the Capping Protein that restricts the actin filament growth. The condition in the absence of Capping Protein is a particular case, as no dense actin network forms on the surface of the actin bead.

found to be in the order of kPa. Therefore, the optical tweezers are not able to probe the mechanics of the dense gel on the bead surface. The value of δ is expected to be $> 4.34\mu m$ as it partially includes the dense actin gel.

The model can be fitted independently on each experimental approach phase. An example of such a fit is shown in [figure 3.10](#) and the fit quality can be measured by the coefficient R^2 which has a media value of 0.97 across all fits.

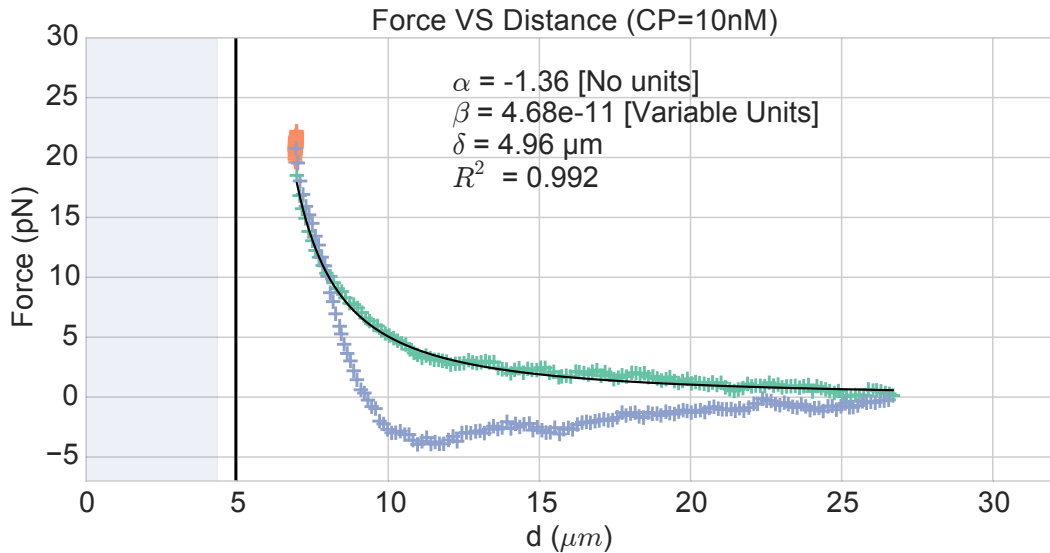


Figure 3.10: Power law model fitted on the approach phase data for one experiment in the presence of $[CP]=10\text{nM}$, with the particular values found for the fit parameters. The vertical line represents the point where the model diverges and the force goes to infinity, that is to say δ . The shaded region corresponds to the distance at which the two beads should interpenetrate. Relaxation (orange) and retraction (blue) data are not fitted.

The approach phase data can be corrected for the distance offset δ and plot in a log-log scale allowing for a better appreciation of the fit result ([Fig 3.11](#)). The corrected distance is noted with c indices $d_c = d - \delta$. In the model the force tends to infinity at $d_c = 0$.

In our experiments, the polystyrene beads have an average diameter of $4.34\mu m$, thus we expect δ to be higher than the bead diameter, since the beads cannot interpenetrate. Data with δ values lower than $4.34\mu m$ (21 out of 127) are considered as unphysical and removed from further analysis.

As expected, we found negative values for α . Surprisingly, the value of alpha does not vary significantly when comparing experiments with different amounts of Capping Protein and remains close to -1, with a mean value of -1.10, and a standard deviation of 0.38. The distribution of the power law exponent can be seen on [figure 3.12](#)

Due to the scale invariance of the inverse power law found above, all the approach phases data can be rescaled into a single master-curve ([Fig 3.13](#)). This is achieved by dividing the force by the maximum force F_{max} reached during the approach, and rescaling the distance by the minimum approach distance from which δ is subtracted.

The rescaled data confirm an average power law exponent of ~ -1 , the breakdown of the average exponent

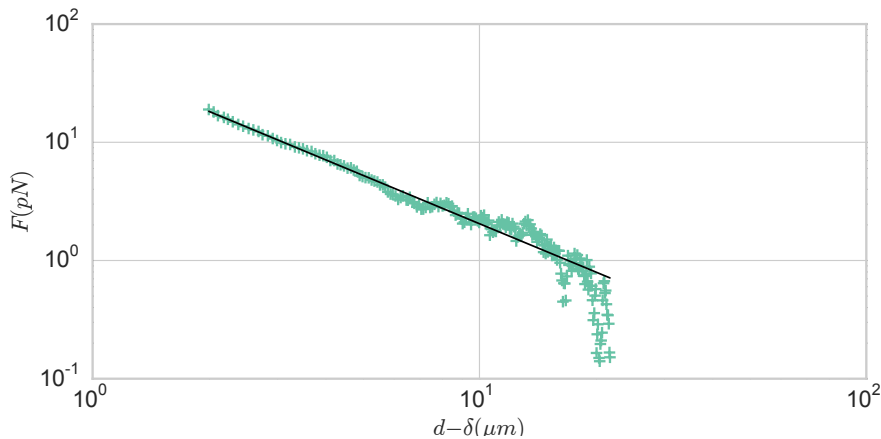


Figure 3.11: Force on the actin bead during the approach phase as a function of bead distance minus distance offset δ plotted on a log-log scale. Black line represents the power law model with the offset distance correction. Same data as Fig 3.4 but showing only the approach phase.

beyond $d_c/d_{c,min} = 10$ can be explained by the statistical effect due to a lack of data for long distance.

3.5.2 Variation of parameters with Capping Protein

At the chosen concentration of Arp2/3, the bead system can show symmetry breaking in the correct range of a Capping Protein concentration of 10 to 30 μM . In absence of Capping Protein, the dense dendritic network does not form on the surface [Kawska et al. 2012]. At low Capping Protein concentrations ($< 10\mu\text{M}$) it seems not able to generate enough stress to rupture, and at too high concentrations ($> 35\text{nM}$, the visible gel is thin and does not break symmetry either. We then investigated the variation of each fit parameters for Capping Protein concentrating ranging from 0 to 50 nM.

We have already seen that the power law exponent factor α didn't vary with the amount of Capping Protein in solution (Fig 3.12). The two other investigated parameters are the prefactor β and distance offset δ . For the same value of α and δ , the higher β is, the stronger the interaction between the two beads for the same distance d_c . We can see on figure 3.14 that the average value for the prefactor decreases in accordance with the increasing of Capping Protein concentration.

The last parameter of our model is δ , the distance at which the force diverges. It can be seen in Figure 3.15 that with the exception of zero Capping Protein, the distance at which the model diverges gets closer to the polystyrene bead diameter, as the concentration of Capping Proteins in the medium increases. It is interesting to note that the distance offset δ is very close from the bead diameter in the absence of Capping Protein, when no biomimetic actin cortices forms.

3.5.3 Determination of Young's Modulus

In order to determine the gel mechanical properties between the actin and the probe bead, we modelled it as a purely elastic material. The viscous effects are neglected in the approach part, as the approach at different speeds shows no clear effect on the approach curves (Figure 3.7). We considered the compression of the material between the two beads. The surface of the compressed material is approximated by the bead

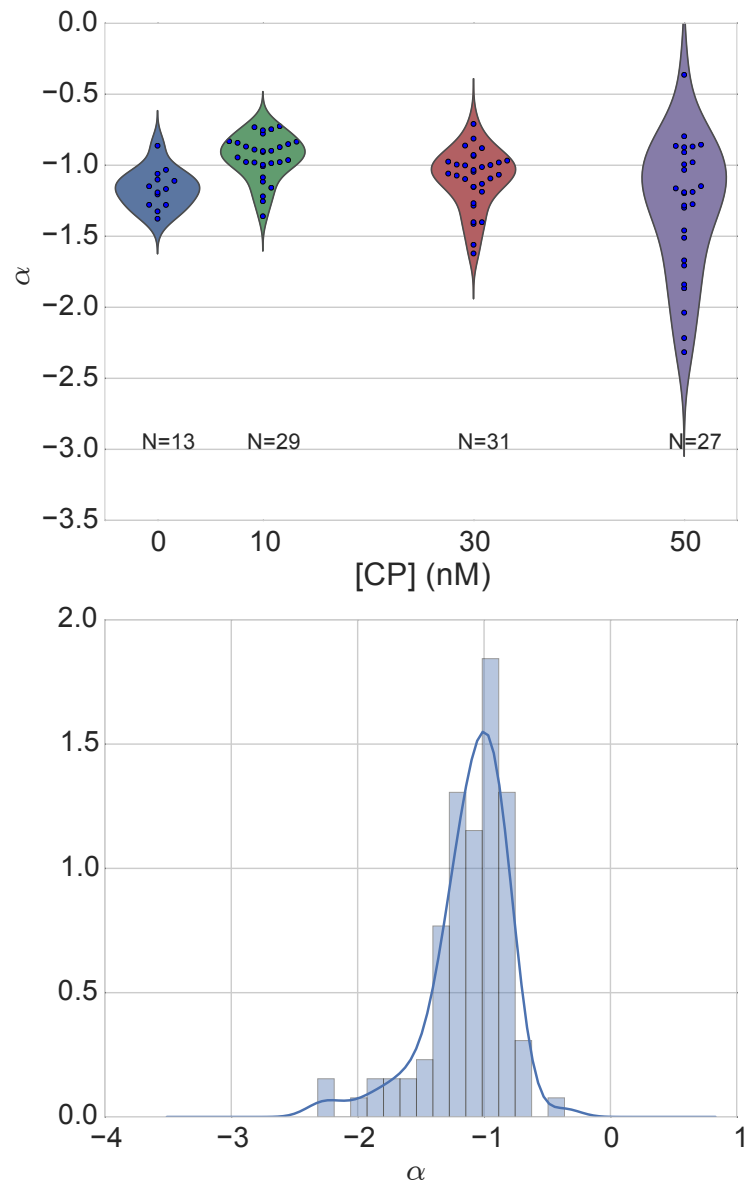


Figure 3.12: Right : Violin plot showing the repartition of power law exponents as a function of concentration in Capping Protein. Left: distribution of power law exponent α regardless of the concentration in Capping Protein. Value of exponent lies close to -1 .

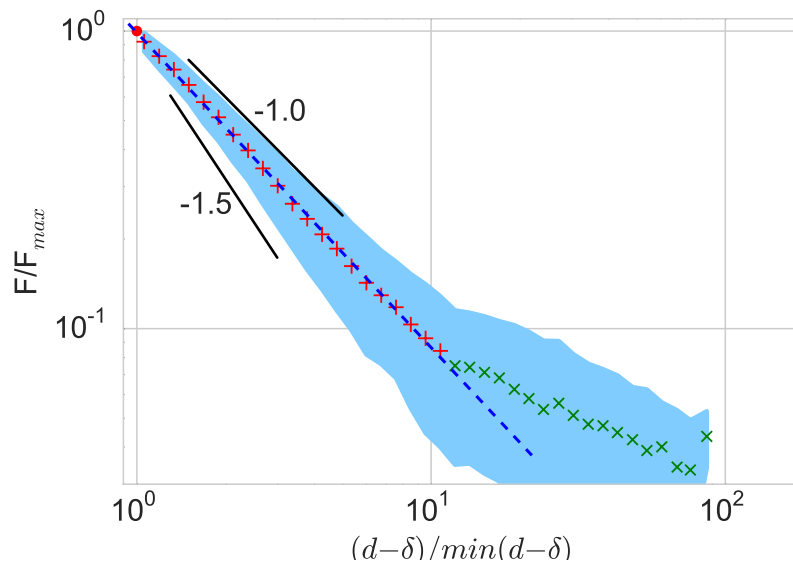


Figure 3.13: Representation of rescale approach data on a log-log scale. Red and green crosses correspond to average values. Blue area corresponds to average \pm standard deviation for each average bin. Red dot in the upper right corner corresponds to the point $(1,1)$ with respect to which all data have been rescaled.

Blue dashed line shows a power law fit of the average data for $d_c/d_{c,min} < 10$ (red cross), fitted slope is -1.06 . As an eye guide, the slopes of -1 and -1.5 have been represented.

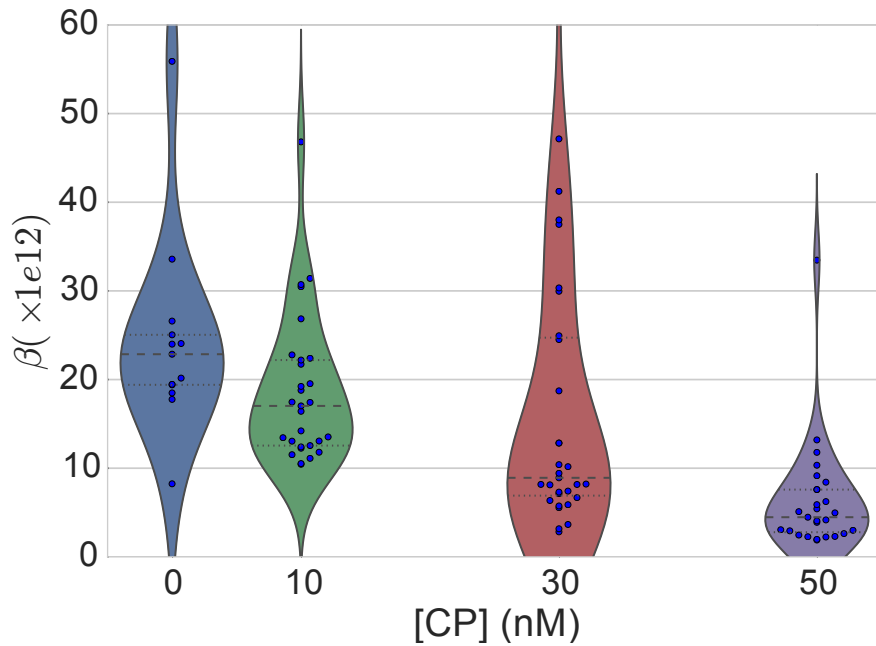


Figure 3.14: Violin plot showing the repartition of the prefactor with the quantity of Capping Protein. The decrease of prefactor with an increasing amount of Capping Protein indicates a lower force between the probe-bead and the actin bead, for the same corrected distance between bead centers.

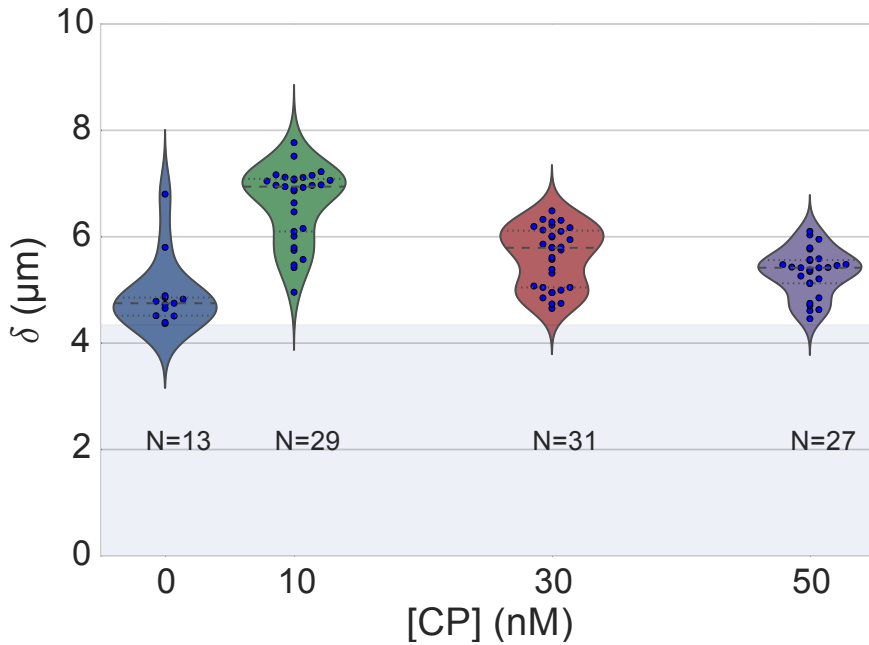


Figure 3.15: Violin plot showing the variation of the offset distance δ with the Capping Protein concentration. The shaded area represents the non-physical region which would correspond to a diverging force beyond the contact of the two polystyrene beads. Experimental data with δ value in this region have been excluded from further analysis.

projected surfaces of the bead along the direction of compression (πR^2). The thickness of the compressed material is regarded as the distance between bead centers corrected by the distance offset δ , as any material below delta can be considered as infinitively rigid for the optical tweezer.

The stress exerted onto the material projected onto the bead surface or radius R can be written :

$$\sigma = \frac{F}{\pi R^2} \quad (3.3)$$

For a minor deformation, the local strain of the material u can be written as a function of the corrected bead position d_c and the considered location along the axis between the two bead center as x :

$$u(x) = \frac{d_c - x}{d_c} \quad (3.4)$$

We can express the local differential strain around the bead position d_c : $\partial u = -\partial x / \partial d_c$ in which the minus sign reflects the choice of the coordinate system: a decrease in x with a positive Young's modulus E should lead to an increase of the exerted force. The locally felt Young's modulus at the distance d_c is then

$$E(d_c) = \left. \frac{\partial \sigma}{\partial u} \right|_{d_c} \quad (3.5)$$

By injecting the expression of u and σ this lead to :

$$\begin{aligned} E(d_c) &= -\frac{d_c}{\pi R^2} \times \left(\frac{dF}{dx} \right) \Big|_{x=d_c} \\ &= E_0 d_c^\alpha \end{aligned} \quad (3.6)$$

in which the value of E_0 can be expressed as function of the power law exponent α and the prefactor β :

$$E_0 = -\frac{\alpha\beta}{\pi R^2} \quad (3.7)$$

Experimentally, the probed Young's modulus corresponds to the average mechanical properties of the actin cloud between the actin bead surface and the probe-bead surface and does not reflect the variation of the uncompressed actin cloud mechanical properties with position. Physically E_0 corresponds to the Young's modulus as a corrected distance of $d_c = 1\mu m$ (See Fig 3.16) The geometry of the system and the fluorescence signal suggest a decrease of the actin cloud density according to the distance from the actin-bead center. All values reported later represent an estimation of the effective Young's modulus elasticity. The value of this effective Young's modulus is 3 orders of magnitude smaller than the acknowledged elasticity of dendritic gels formed on beads, measured in the order of kPa [Marcy et al. 2004].

This difference in elasticity might explain why the mechanical actions of this actin cloud have not been confirmed before in other measurements, like micro-pipette aspiration, micro needle deformation or Atomic Force Microscopy indentation that have sensitivities in the order of nN, while the forces exerted by this actin cloud are in the order of pN.

Nonetheless, [Gardel et al. 2003] shows that such low moduli can be obtained using sparse entangled actin networks, and confirms the idea that the actin-cloud seen with the optical-tweezer indent experiments, has a fundamentally different structure than the dense dendritic network on the actin bead surface.

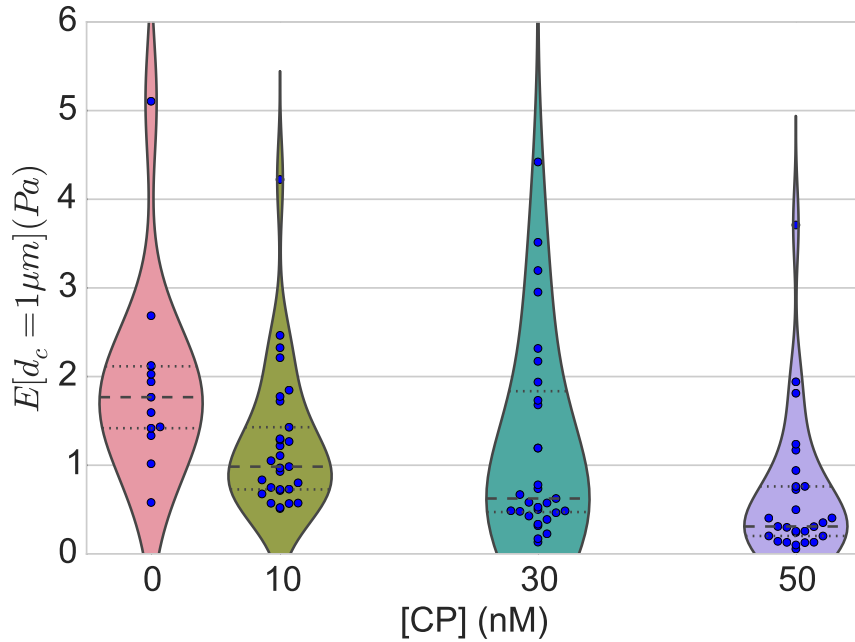


Figure 3.16: Young's Modulus prefactor, as a function of Capping Protein, shows a decrease of the average Young's modulus with an increase of Capping Protein concentration.

3.5.4 Mechanical properties

To investigate the mechanical properties of the network that should arise from a $\alpha = -1$ power law, we modelled the actin cloud deformation by the theory of semi-flexible entangled polymer networks ([Isambert et al. 1996], [MacKintosh et al. 1995], [Morse 1998a]).

The Young's modulus of semi-flexible filaments in a 3D environment can be expressed as a function of the filament contour length density ρ and the entanglement length L_e as [Morse 1998b]:

$$E = \frac{2.(1 + \nu).7.k_B T \rho}{5L_e} \quad (3.8)$$

In which ν is the Poisson's ratio that allows the conversion from shear to elastic modulus. Previous studies have investigated the non-linear stiffening of such actin networks for large deformation [Semmrich et al. 2008] and found that in our condition, the linear description of these networks holds to describe the actin cloud.

As [Morse 1998a] we expressed the entanglement length as a function of persistence length and filament density: $L_e \approx L_p^{1/5} \rho^{-2/5}$. We can reduce the expression of the Young's modulus to a function of the following parameters :

- The Poisson's Ratio ν ,
- The persistence length of actin filaments L_p
- The mesh size of the network $\xi_0^2 = \rho_0$
- The “size” of the cloud, for which we use the distance where the force is first significant d_0

We also need to consider that for a general compressible material, the only variable that changes during compression is the density ρ which can be expressed as a function of the corrected distance $\rho \rightarrow \rho(d_c)$

Thus leading to :

$$E(d_c) = \frac{(1 + \nu).14.k_B T}{5L_p^{1/5}} \times \rho(d_c)^{7/5} \quad (3.9)$$

The scaling exponent of E in equation (3.9) with d_c should match the exponent of the experimentally found power law α . Thus, the density can be expressed in the following form :

$$\rho(d_c) = \rho_0(d_c/d_0)^{5/7 \times \alpha} \quad (3.10)$$

By defining ρ in [Morse 1998a], which is the filament contour length per unit volume, we can determine the mesh-size ξ_0 of the undeformed network:

$$\xi_0 = 1/\sqrt{\rho_0} \quad (3.11)$$

By comparing this to the phenomenological fit, we can express the elastic modulus as a function of the distance, and the mesh size, as a function of the fit parameters and the characteristic scales of the system.

$$\begin{aligned} E(d_c) &= \frac{(1 + \nu).14.k_B T}{5L_p^{1/5}\xi_0^{14/5} d_0^\alpha} \times d_c^\alpha \\ &= E'_0 \times d_c^\alpha \end{aligned} \quad (3.12)$$

In which E'_0 can be identified as E_0 in (3.9) to extract the closed form solution for the mesh size ξ_0 :

$$\xi_0 = \left(-\frac{(2 - \frac{5}{7}\alpha).k_B T \pi R^2}{5\alpha\beta L_p^{\frac{1}{5}} d_0^\alpha} \right)^{\frac{5}{14}} \quad (3.13)$$

The found mesh size is in the order of 0.3 to 0.4 μm , which is consistent with previous findings :Morse1998b. The variation of the mesh size can be seen on figure 3.17 and does not seem to have a correlation with the Capping Protein concentration.

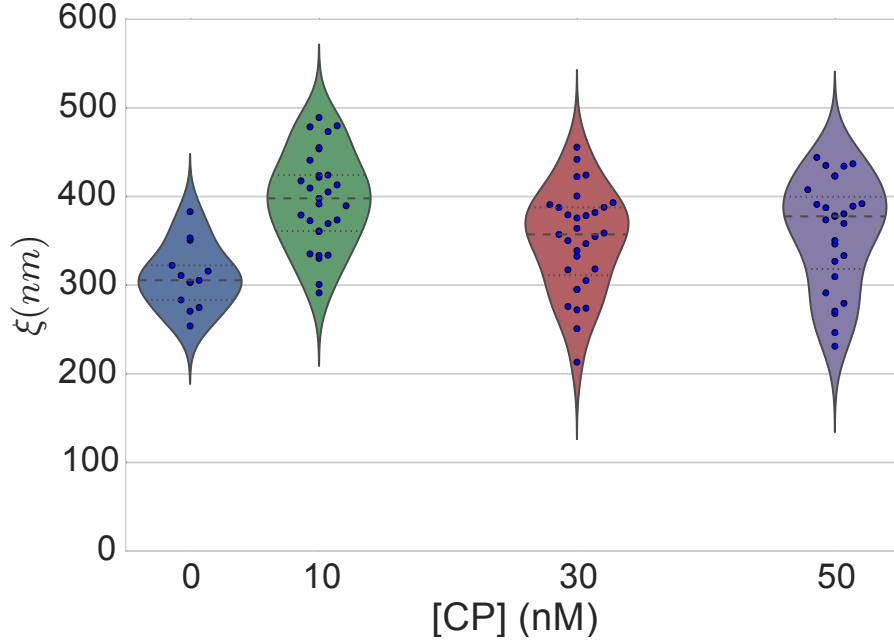


Figure 3.17: Meshsize vs Capping plot.

We explored the correlation between the mesh size and δ by plotting the mesh size against the distance offset δ (Fig 3.18). Figure 3.19 shows the relation between the mesh size and the offset distance δ regardless of each Capping Protein concentration.

From (3.9) and (3.12) by identifying the prefactor, it is also possible to extract the Poisson's ratio (ν) of the compressed material :

$$\nu = \frac{1}{2} \times \left(\frac{5}{7} \cdot \alpha + 1 \right) \quad (3.14)$$

The Poisson's ratio only depends on the power law exponent and thus slightly varies with the amount of Capping Protein concentration. We found a Poisson's ratio value between 0.1 and 0.2, corresponding to compressible foam-like materials that do not highly expand in the direction orthogonal to the compression axis. A previous study of bulk actin network finds a Poisson's ration of 0.5 (incompressible material) for an actin concentration of 21.5 μM . We suspected that the low actin concentration used in our experiments (4 μM) is the reason for the low Poisson's Ratio. The local structure of filaments emanating from the bead may also explain the large compressibility of our actin cloud.

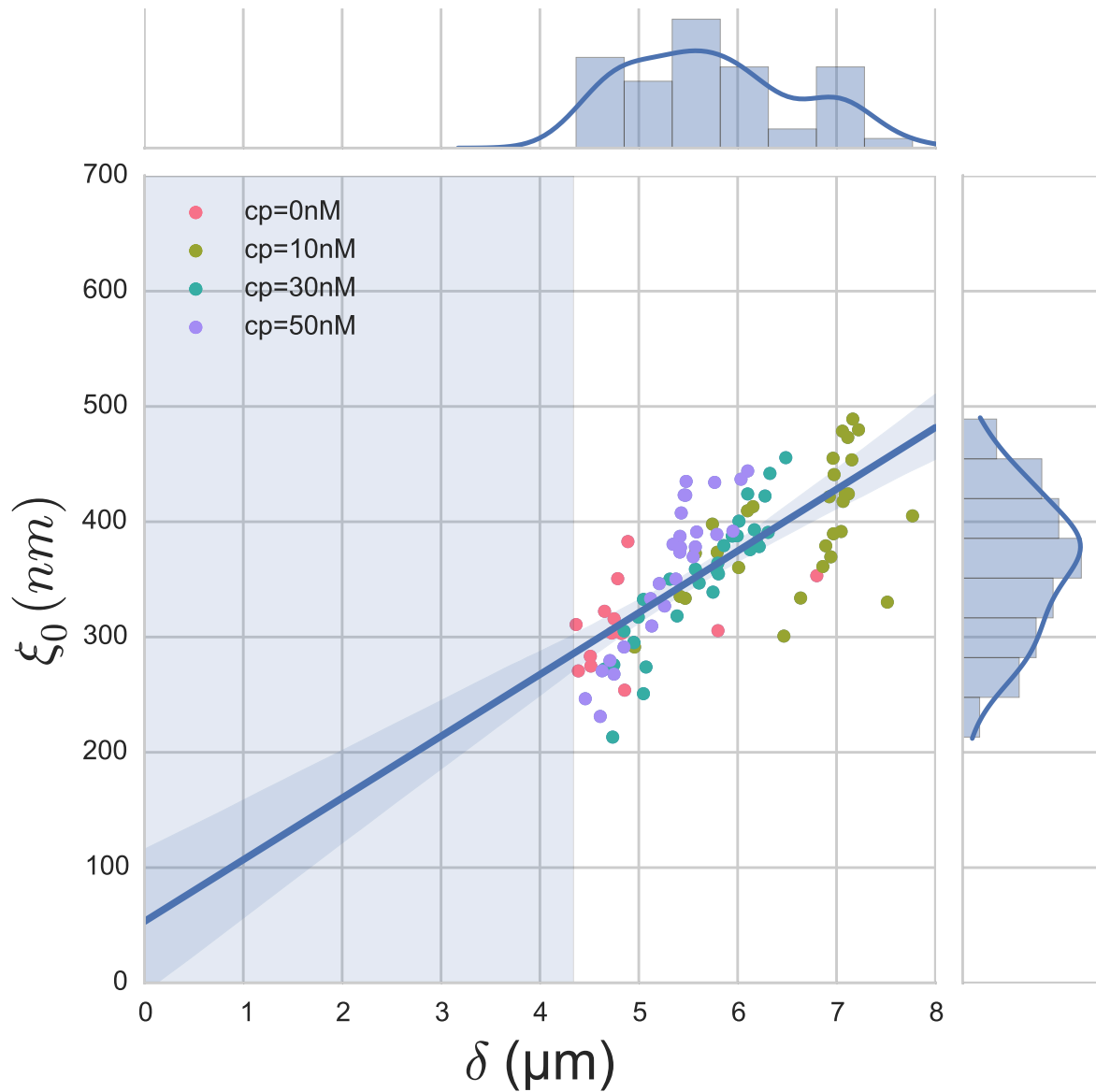


Figure 3.18: Correlation of the meshsize ξ_0 with the distance offset δ , with marginal distribution as per histogram on the side and on the top. Shaded regions represent confidence interval at 95%.

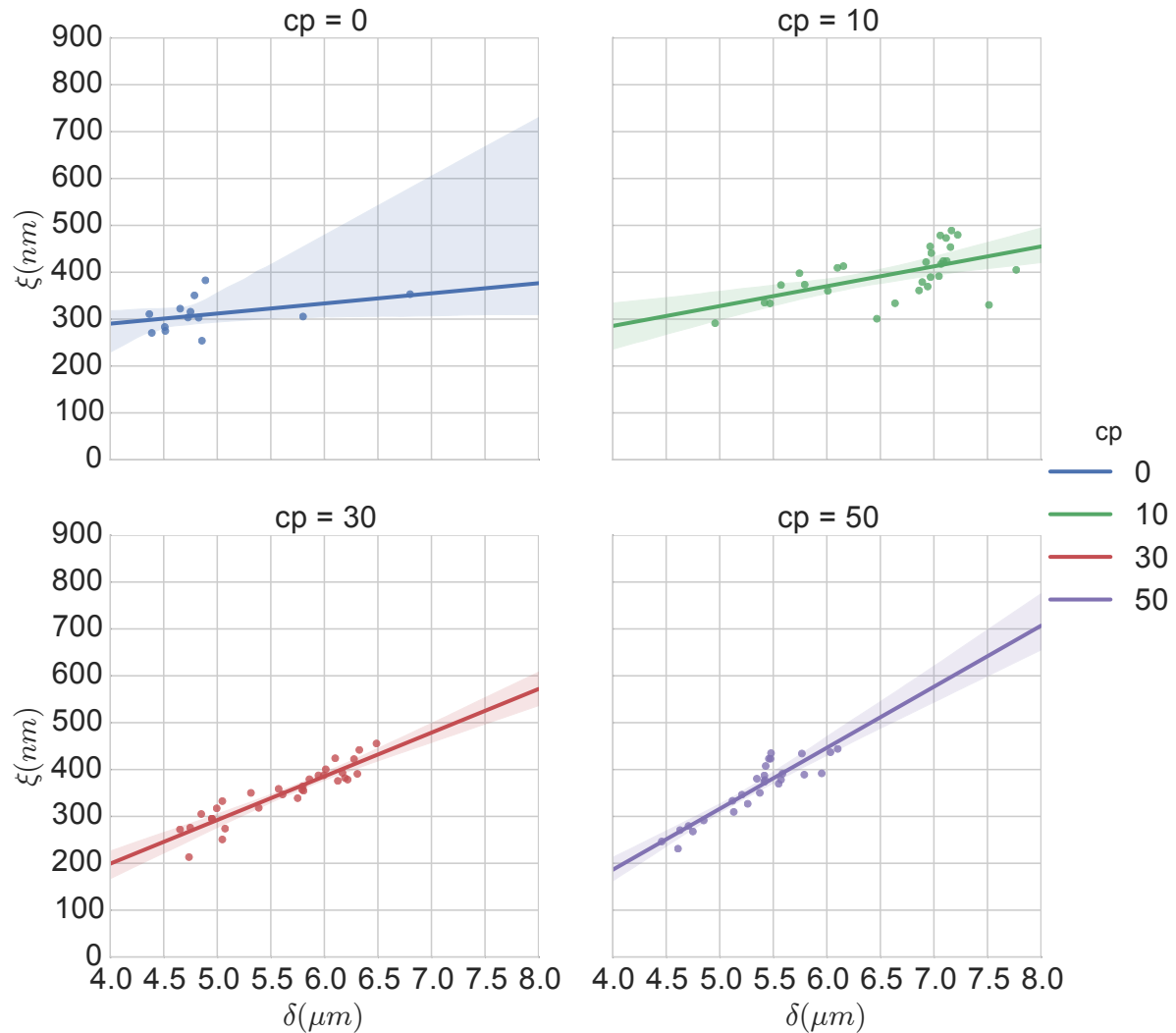


Figure 3.19: Same figure as Fig 3.18 for each concentration of Capping Protein, with linear regression and confidence intervals at 95%.

3.5.5 Interpretation

The results of our data analysis lead to the interpretation that a dense actin gel with an elasticity close to $\sim 1\text{kPa}$ is polymerised on the actin bead surface. This stiff gel cannot be indented by the optical tweezer. Beyond this dense gel, a soft actin cloud with an effective elastic modulus of 1 Pa and below is present and extends on distances several times bigger than the thickness of the reconstituted actin cortex (Fig 3.20). The structure of this actin cloud is expected to be quite different from the dendritic gel and to be mostly constituted of loosely entangled actin filaments.

In this model, the offset distance δ corresponds to the limit of the dense dendritic actin network mimicking the actin cortex that grows on actin beads. The high elastic modulus of this gel makes it impenetrable for the small forces generated by the optical tweezer we use. The values of δ we found are coherent with the measured thickness $e \simeq \delta - 2.R_{bead}$ of the biomimetic actin cortex, as measured by epifluorescence in [Kawska et al. 2012] and found to be in the range of 1 to 2 μm . The decrease of δ with Capping Protein is also coherent with the decrease of gel thickness.

The filaments composing the actin cloud directly emanate from the actin cortex in which the actin polymerisation nucleation started at the bead surface . Eventually, a few filaments can escape from the network and are capped by the Capping Protein provided that the growing extremity is already several micrometers from the bead surface.

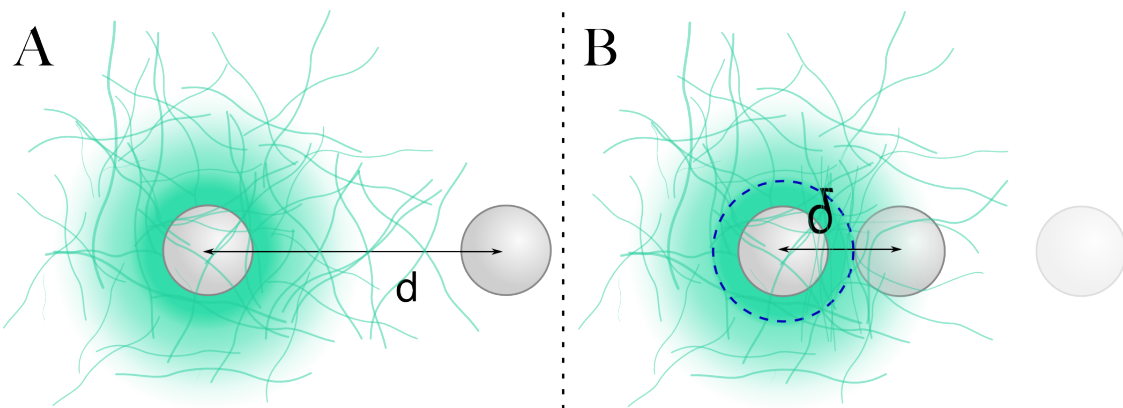


Figure 3.20: A) Schematic of an actin cloud. Left: The actin bead triggers actin polymerisation. Right Probe Bead. On the actin bead surface, a dense and dendritic network forms a biomimetic actin cortex with an elastic modulus close to the kPa (Dark Green). From this actin cortex emanates a softer actin structure : the actin cloud . The actin cloud is a loosely entangled network formed by the filaments escaping from the bead's actin cortex and extending over several micrometers. The actin cloud has an average elastic modulus which is several orders of magnitude softer than the actin cortex. B) From the probe-bead point of view in the optical tweezer, the system (actin-bead+actin cortex) behaves as a hard-sphere of radius $\delta - R$

The actin cortex thickness, e as measured in [Kawska et al. 2012], increases with time during the actin polymerisation. We can predict that the offset distance δ should increase with time, except in the absence of Capping Protein where no actin cortices form. This can be verified on figure 3.21 that shows the evolution of δ as a function of polymerisation time.

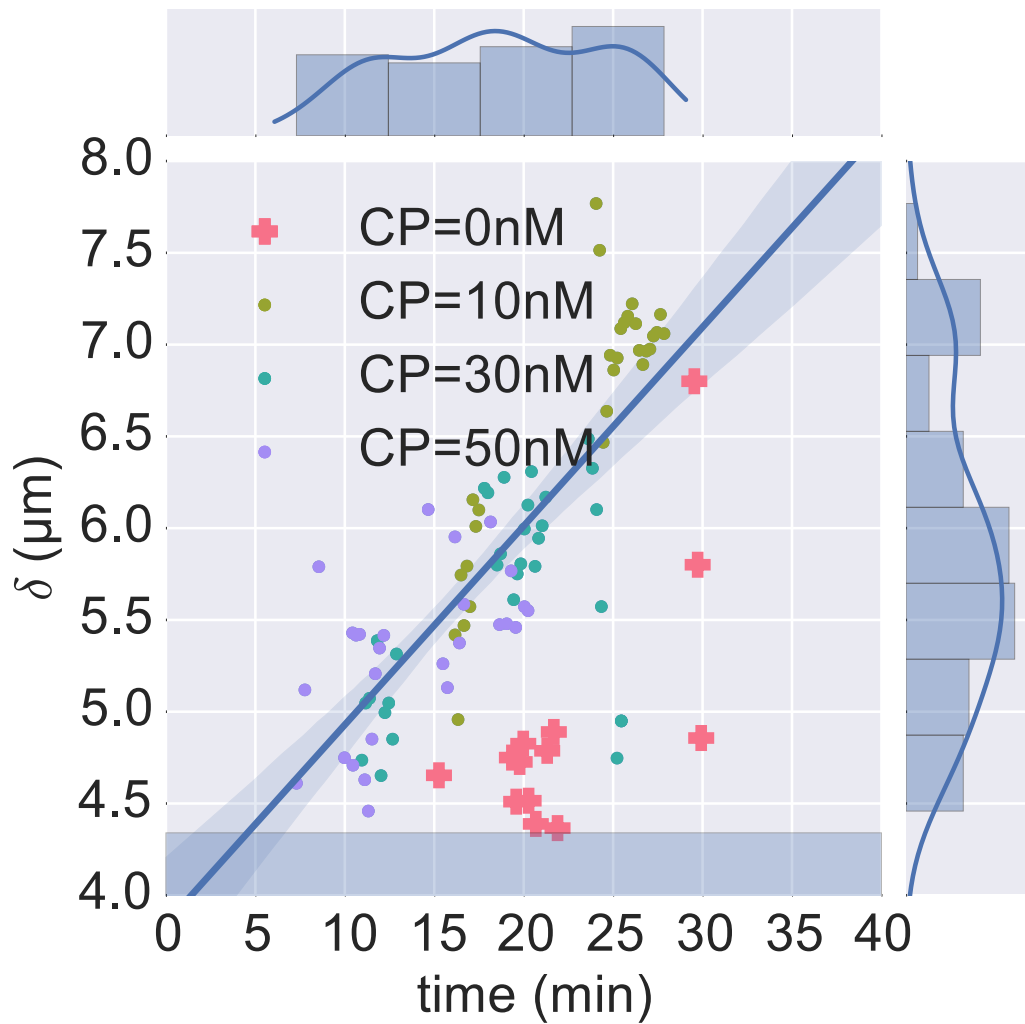


Figure 3.21: Distance offset δ as a function of time (min) since mix of actin, ATP and beads. Linear fit with confidence interval at 95% (light shaded area) and bead surface (dark shaded area). Samples taken in the absence of Capping Protein are not taken into account in the regression (Pink +). The increase of δ with time is coherent with the measured increase of the gel thickness e as measured in [Kawska et al. 2012]

3.6 Relaxation phase

The approach phase of the indentation cycle has been modelled with a purely elastic mode. However, the force-distance plot shows a significant dissipation marked by an hysteresis Fig 3.4. The repetitive indent cycle, giving the same force-distance curves (Fig 3.6), allows to exclude a plastic deformation. We can hence reject the hypothesis of ruptures of the actin meshwork or breakage near the entanglement points.

The entangled filaments networks theory that allowed us to understand the link between the phenomenological model and the mechanical properties of the network, also proposes a relation to explain the network relaxation.

In this model [Morse 1998a], the visco elastic modulus E is a function of time and can be written as $E(t) = E \times \chi(t)$ with

$$\chi(t) = \sum_{n,odd} \frac{8}{n^2\pi^2} \exp\left(-\frac{n^2\pi^2 t}{\tau_{rep}}\right) \quad (3.15)$$

In which $\tau_{rep} = \frac{l_f^2}{D_{rep}}$ is a single fit parameter depending on diffusion constant for filament reptation D_{rep} and the filaments length l_f . In this form, χ is a sum of exponential decays with well defined characteristic timescales and amplitudes that decrease as $1/n^2$. To fit this model to the relaxation phase data, we can limit ourselves to the first 40 terms of the sum, as any of the subsequent terms represent timescales, we cannot reach with our experimental resolution.

It should be noted that the value of $\chi(t = 0)$ is 1 and should be treated particularly in order to ensure continuity of the force applied on the actin-bead in the model.

Using this sum of exponential decays is coherent with the common conclusions of power-laws found in the frequency-dependant shear modulus of both *in vivo* and *in vitro* actin networks, as well as the relaxation behaviour found in cells.

In order to determine τ_{rep} , the Young's modulus established in the approach phase is used and the model is fitted against the relaxation data. A result of such a fit can be observed on figure 3.22. The values of τ_{rep} are highly variable and the fit can be difficult when the relaxation is slow or in the order of the measured noise. The variation of τ_{rep} with the concentration in Capping Protein can be seen on figure 3.23, and one example of fit on the figure 3.22

We can see here that the polymer model introduced in [Morse 1998a] allows to completely fit the succession of approach and relaxation phases. In order to check whether the fit parameters give realistic values, we can estimate the diffusion constant for filament reptation D_{rep} .

$$D_{rep} = \frac{k_b T}{\gamma l_f} \quad (3.16)$$

In which $\gamma \approx 2\pi\eta_s/\ln(\xi_0/d_f)$ is the friction coefficient per unit length. γ depends on the solvent viscosity η_s , the mesh-size ξ_0 and the filament diameter d_f (7nm for actin). We use $\eta_s = 10^{-3} Pa \times s$ for water and a mesh size in the order of 400nm as determined from the approach phase (Fig 3.23). Using τ_{rep} given by the fit, this leads to filaments length ranging from 3 to 8 μm , which is consistent with TIRF experiments and simulation as done in [Kawska et al. 2012].

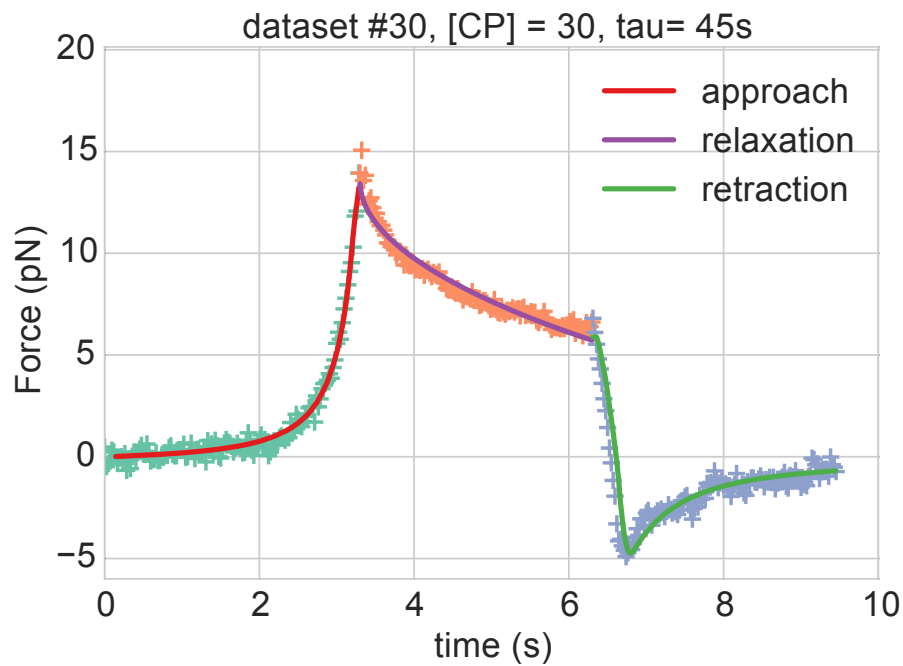


Figure 3.22: Force as a function of time as well as fit for the 3 phases, approach, relaxation and retraction.

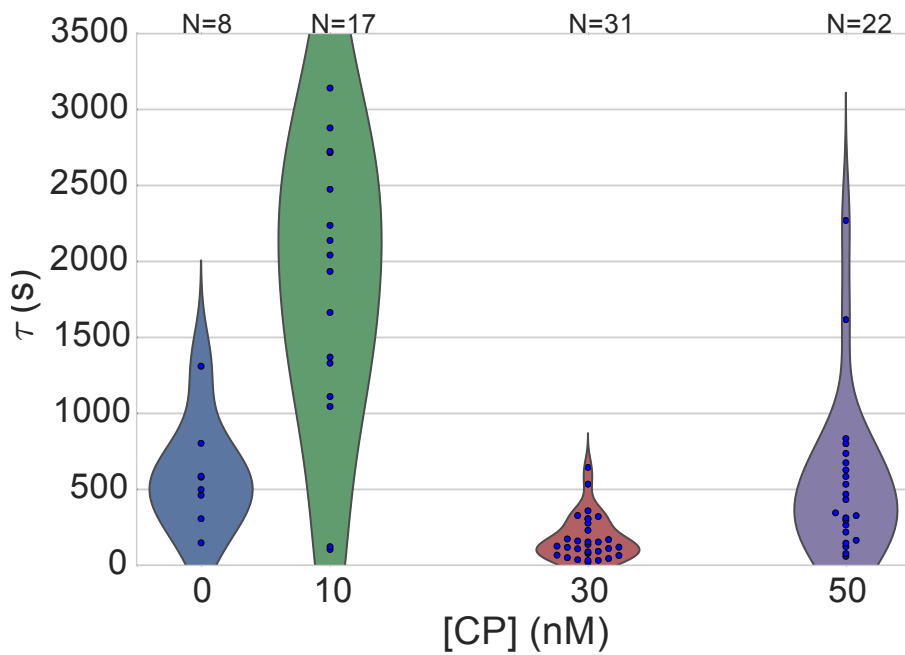


Figure 3.23: Violin plot showing the repartition of τ_{rep} as a function of capping protein. Outlier (τ_{rep} negative or greater than tens of minutes removed)

3.6.1 Retraction Phase

During the retraction phase the force decreases, becomes negative after a retraction of 3 to 4 μm , and shows a slow return to 0 at large distance. Sticking events can be observed when the force becomes abruptly negative before relaxing as fast. [Figure 3.24](#) shows such a sticking event happening during an indentation cycle.

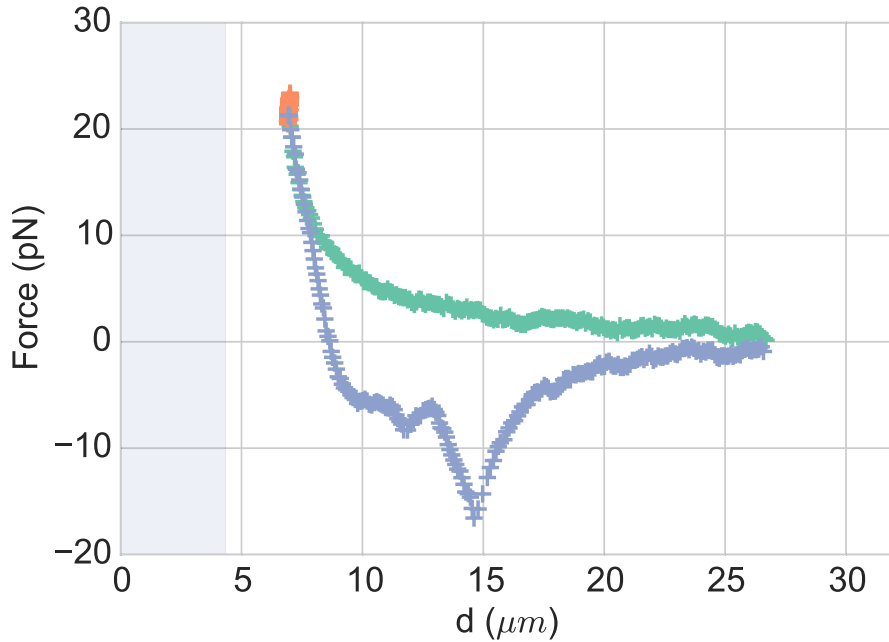


Figure 3.24: A sticking event at $d = 15\mu\text{m}$ where the rapidly decreasing force can be determined to go up to -18 pN, before quickly returning to its normal value. A second smaller sticking event is present at $d = 12\mu\text{m}$. Sticking events roughly appearing in 20% of the experiments.

We assume that the sticking events are characteristic of non-specific interactions between the probe-bead and the actin cloud. If no sticking event is present, we assume the partial closing of the actin cloud beyond the probe-bead during the relaxation phase, and model the retraction curve as a transition between the damped-approach curve and a penetration of the probe-bead through the closing actin cloud.

During the approach phase, the force exerted on the actin-bead is $F(d) = \beta(d - \delta)^\alpha$. During the relaxation phase, the force decreases from $F(t_1)$ to $F(t_2)$ with the relation :

$$\frac{F(t_2)}{F(t_1)} = \chi(t_2 - t_1) \quad (3.17)$$

We can write that the force exerted on the actin-bead during the retraction can be expressed as a sum of the force felt during the approach, damped during the relaxation (F_{da}), plus a force due to the closing of the actin network behind the bead $F_{closing}$.

$$\begin{aligned} F_{ret}(d) &= F_{da}(d) + F_{closing}(d) \\ F_{ret}(d) &= \chi(t_2 - t_1) \cdot \beta(d - \delta)^\alpha + F_{closing}(d) \end{aligned} \quad (3.18)$$

$F_{closing}$ is computed using the fit parameter α , β , δ and τ_{rep} ([Fig 3.25](#)).

On a double logarithmic scale and at long distance $F_{closing}$ also seems to follow a power law (F_{plaw}), when no sticking events are present.

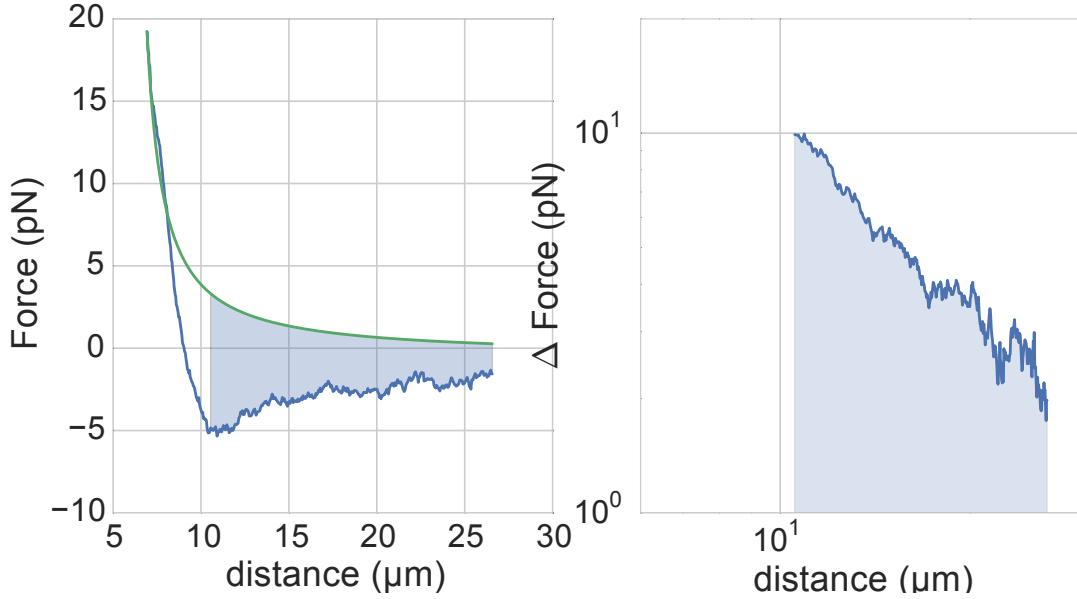


Figure 3.25: Left : Retraction phase, with approach phase fit damped by $\chi(t_2 - t_1)$ in green. Blue area under the curve is plotted on a log-log scale on the right, and follows a power law.

$F_{ret}(d)$ though, seems to follow the force felt during the approach phase, damped by $\chi(t)$ (F_{da}) for $d \simeq D_{bead}$ and $F_{da} + F_{plaw}$ for $d > 10\mu m$. The typical bead size being D_{bead} , we expect the transition from one regime to the other to be done on a length scale of D_{bead} . Thus we use a smoothing function which is a convolution between the projected bead area and a linear ramp function one can observe on [figure 3.26](#)

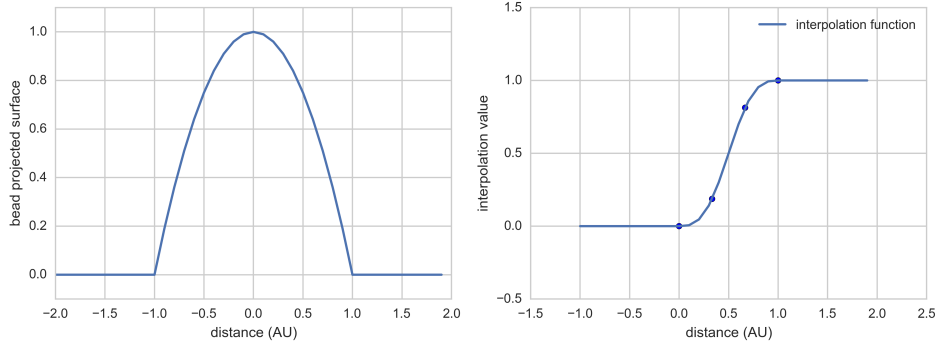


Figure 3.26: Interpolation function used to smooth the transition from F_{da} to $F_{da} + F_{plaw}$

The complete retraction force can be seen on [figure 3.22](#) and is equal to

$$F_{ret}(d) = F_{da}(d) \times (1 - S(d)) + F_{plaw}(d) \times S(d) \quad (3.19)$$

where $S(d)$ is the interpolation function for a $4.34\mu m$ diameter bead. We can notice that the model correctly represents the retraction and especially the position and value of the retraction function minimum without

fitting parameters, when using the probe-bead diameter as a typical scale for the transition when changing direction.

3.7 Discussion

The actin cytoskeleton plays an important role in many cellular functions. The actin cortex, just beneath the cell membrane is not only a crucial structure for both cell motility and cell mechanical properties, it is also an essential component in cell division and spindle positioning. Other actin structures, that spawn from the nucleus to the cell membrane, are responsible for cell organelle positioning, as is the case for plants, where the nucleus is found towards the cell anticlinal wall [Iwabuchi et al. 2010], or during nurse cell maturation, where the nucleus is pushed away from the dumping channel:cite:Huelsmann2013. The mechanical link from the outside of the cells to the nucleus using actin bundles has already been shown [Jaalouk et al. 2009]. We demonstrated here that these actin structures should not be the only ones taken into account to explain organelles positioning.

Our experiments confirmed the existence of a sparse and stiff actin cloud emanating from a biomimetically reconstituted actin cortex. This actin cloud is capable of staining forces of tens of pico Newtons, enough to hold organelles in place. By using polymer physics, we are able to model the behaviour of such an actin cloud and to measure many of its mechanical properties. It provides an actin scaffold capable of deforming non-plastically. At time scales of few seconds it behaves mostly elastically with an elastic module of a few Pascal. The actin cloud Poisson's ratio varies from 0.1 to 0.2, hinting at a sparse structure of loosely entangled filaments, forming a meshwork with a typical mesh size of 300 to 400 nm.

The filaments at the origin of this loosely entangled network could emanate from the dense actin cortex that can be seen and simulated on actin-beads [Kawska et al. 2012] and the evolution of this actin cloud parameters are coherent with the preceding studies on biomimetically reconstituted actin cortices. Recently, the role of actin networks with the same properties as an actin cloud have been described in cells such as *Xenopus* Oocyte [Feric et al. 2013]. The Poisson's ratios of actin networks have been measured in bulk to be higher [Gardel et al. 2003] but are not inconsistent with our measurements at lower actin concentration.

The actin cloud provides a novel structure that should be studied further to understand the positioning of organelles in cells, and to study the role this sparse actin structure plays in the formation of other actin networks inside cells.

In particular, microrheology experiments could be performed on the growing actin cloud in order to further characterise the frequency dependence of the actin cloud mechanical properties. The effect of cross linking and network branching is crucial for the occurrence of symmetry breaking on bead systems, and probably plays a role in the actin cloud structure. A confined geometry and direct polymerisation on membranes, or the effect of myosin motors might alter the actin cloud properties.

All these, could be cellular mechanisms to use the actin cloud in order to efficiently form the structures needed for its function. Further studies of the actin cloud on biomimetic or *in vivo* systems are challenging, but would lead to a better understanding of the cells mechanics and its control.

A Paper based on this study has been accepted for publication in Biophysical Journal and is added for information as appendix of this manuscript.

CHAPTER
FOUR

CORTICAL TENSION MEASURED ON LIPOSOME DOUBLETS

4.1 Introduction

We have seen that in cells, the actin cytoskeleton is a key component to form structures such as the actin cortex, used to transmit forces and bring to cells their mechanical rigidity. In order to drive shape changes, cells regulate the mechanical properties of the sub-micrometer thick actin cortex, beneath the membrane [Clark et al. 2013]. The actin cortex dynamics drives cell shape changes [Salbreux et al. 2012] and the presence of the molecular motor myosin II plays a fundamental role in the tension of the acto-myosin cortex [Tinevez et al. 2009]. The cortical tension can be measured on cells and varies between 50 and 4000 pN/ μ m in accordance with both actin and myosin activity .

These changes of the cortical tension are also affected by cell-cell adhesions [Maitre et al. 2012] whose major role played in cell sorting have already been proved.

Recently, such acto-myosin cortices have been reconstructed on cell-sized liposomes [Carvalho et al. 2013a], which showed that the attachment of the actin cortex to the membrane plays a crucial role in the acto-myosin network behavior and contractility.

In the present study, I collaborated with Kévin Carvalho and Joël Lemière, to further extend the previously developed system [Carvalho et al. 2013a] aiming at monitoring the cortical tension changes in a biomimetic actin cortex formed on liposomes. I mainly contributed to the analysis of the 3D data, acquired by using Spinning Disk Microscopy and , for the analysis developed for this purpose a novel method to get a precise and unbiased measure of the geometrical parameter.

It should be noticed that in a recent works, cell doublets were used to determine the role of cortical tension in cells [Maitre et al. 2012]. In the present case, we formed similar doublets from liposomes, around which we polymerised an actin cortex *in vitro* (Fig 4.1). The shape changes of these liposome doublets allowed the time-dependent monitoring of cortical tension in a non-invasive way. In this project, we hence developed a method for the precise acquisition of doublet deformation, in order to accurately determine the tension increase induced by the injection of myosin motor on the preformed actin cortex.

4.2 Experimental description

4.2.1 Formation of liposomes doublets

Liposomes were obtained by electro-formation (see *Material and methods*) from a mix of EPC and PEG-biotin lipids. The presence of streptavidin in the working buffer allowed liposomes to naturally stick together to form doublets after 15 minutes (*Fig 4.1*).

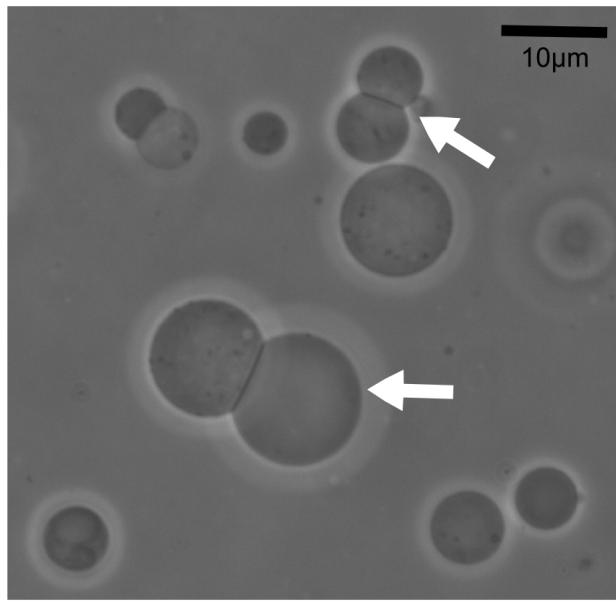


Figure 4.1: Cell-sized liposome doublets. Doublets are indicated by white arrows in the field of view of a phase contrast microscope.

4.2.2 Formation of actin cortex on doublets

The formation of the actin network on doublets was done in a similar way as recently described [Carvalho et al. 2013a]. Briefly, actin filaments including biotinylated monomers were stabilised by phalloidin and linked to PEG-Biotin lipids (see *materials and methods*) via streptavidin, present in the solution (*Fig 4.3*). Besides linking the actin to the membrane, it also cross-linked the filaments. Such a network has already been recently characterised [Carvalho et al. 2013a]. Note that as the actin filaments were only added after the formation of the doublets, the interface between the two liposomes composing the doublets remained free of F-actin (*Fig 4.4, 4.2*). As the added actin was fluorescent, the absence of actin at the liposome interface could be checked by epifluorescence, as it appeared dark compared to the rest of the doublet(*Fig 4.4*).

4.2.3 Visualisation of the interface

In order to visualise the interface between the liposomes, and to avoid the use of fluorescent lipids that might affect the membrane mechanics, [Sandre et al. 1999] the inside buffer of approximately half of the

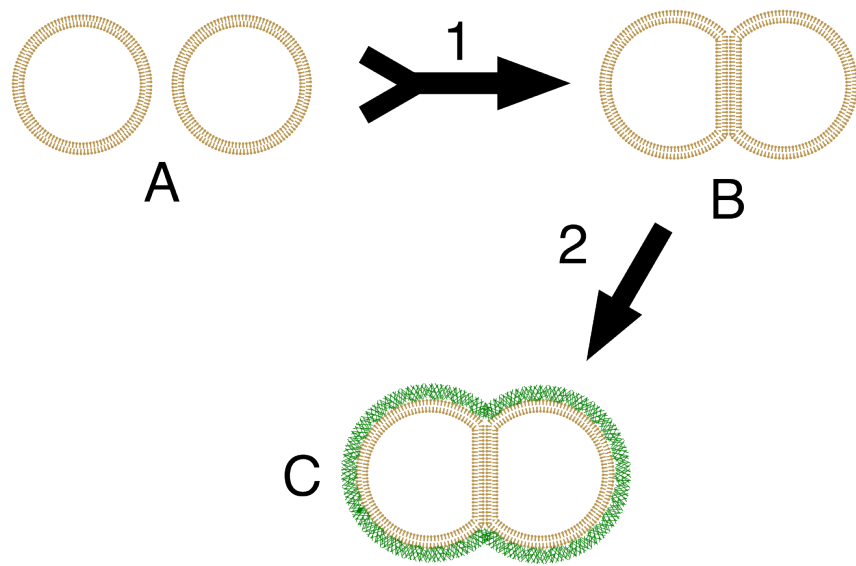


Figure 4.2: Formation of doublets: 1) In the presence of streptavidin, single liposome (A) aggregates into doublets. (B) The addition of biotinylated actin filaments stabilized with phalloidin (2) forms liposome doublets covered with a micrometer-sized actin network (C). The interface between the two liposomes is a double lipid bilayer free of actin filaments.

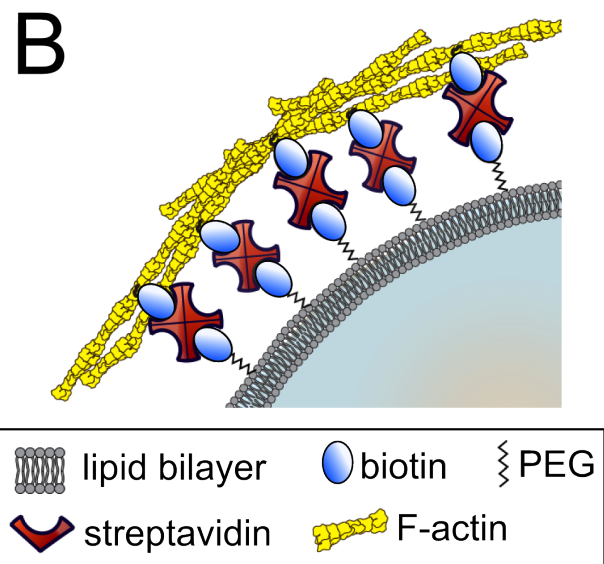


Figure 4.3: Schematic of the stabilized actin cortex at the membrane (proteins not to scale).

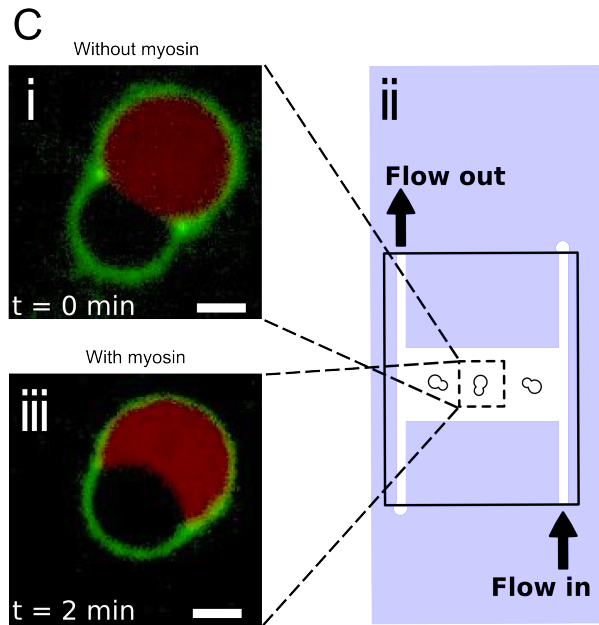


Figure 4.4: i) Flow-chamber designed for buffer exchange. Doublets are visualised in the middle horizontal channel of the H-shaped chamber to avoid movements during the buffer exchange. Spinning disk images of the doublet before i) or after iii) myosin II injection. One liposome contains the fluorophore SRB (red) to visualise the doublet interface. The actin cortex is labeled in green. Scale bar 5 μ m.

liposomes was labeled with 0.9 μ M of sulphorhodamin B (SRB eventually leading to half of the doublets containing a single fluorescent liposome (Fig 4.4 i and iii).

4.2.4 Geometrical parameters

To study the doublet geometry, we modelled each liposome and the interface between them as two spherical caps with their respective center and radius, as sketched in figure 4.5.

The center position in 3D (X,Y,Z) and the radius (R) of the three spherical caps completely determine the doublet geometry, though it is interesting to consider the other parameters of the doublets, which are :

- the total volume of the liposome doublets V
- the contact angle between the two liposomes
- Every “half”-contact angles which are the angles between the interface and each liposome θ_1, θ_2
- The distance between the liposome centers.

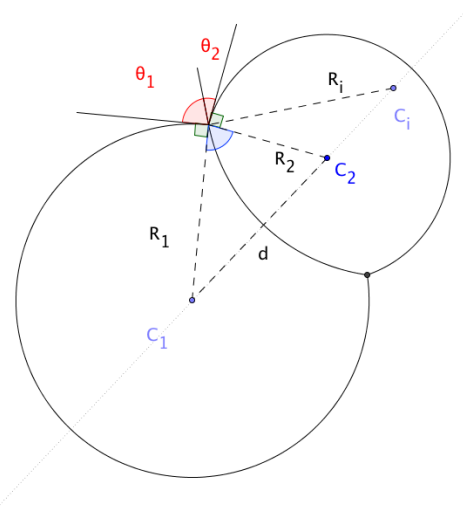


Figure 4.5: The parameters notation for the doublet model: R_1 , R_2 , R_i are respectively the radius of the liposome 1, the liposome 2 and the interface. d is the distance between the liposomes centers. θ_1 and θ_2 are the angles between the tangents of the liposome surface and the tangent to the interface at the contact line. The total contact angle θ is the sum of θ_1 and θ_2 .

4.3 Experimental Observations

4.3.1 Effect of myosin-II injection

We imaged the liposomes doublets in an open chamber either in phase contrast and epifluorescence, or spinning disk microscopy in the red (sulphorhodamin) and the green (actin) channel.

The muscle Myosin II that formed *bipolars filaments* was carefully injected into the chamber, and led within a few minutes to a shape change (Fig 4.6) of the doublets, due to the actin cortex contraction.

The distance between the liposome centers decreased as the total angle $\theta = \theta_1 + \theta_2$ increased. The contact angle and other doublets parameters were obtained by fitting spherical caps onto the 2D epifluorescence images or on the 3D confocal stack as *described later*. In the absence of myosin, the contact angle θ was measured to be $\theta = 64 \pm 16^\circ$ ($n=18$), whereas in the presence of myosin II (200 nM) we found a value of $\theta = 86 \pm 21^\circ$ ($n=5$). Measurements of the contact angle after myosin II injection were done before the cortex ruptures as characterised in [Carvalho et al. 2013a].

4.3.2 Relation between the angles and tension

Each liposome has its respective tension τ_1 , and τ_2 . In the absence of the biomimetic acto-myosin cortex, these tensions only correspond to the tension of the liposome membrane. The interface between the two liposomes is formed by two lipid bilayers, and the inter-facial tension is composed of two contributions: the tension of the lipid bilayer, noted τ_i , and the adhesion energy per surface unit W due to the biotin-streptavidin-biotin link between the two lipid bilayers. The total tension at the interface can thus be written $\tau_t = \tau_i - W$ [Maitre et al. 2012].

As the movement of the contact line during the contraction is slow (order of $\mu\text{m}/\text{min}$) compared to the

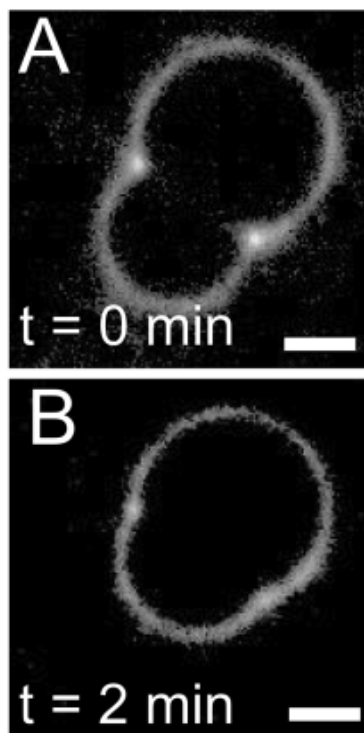


Figure 4.6: Doublets contraction showing a green channel(actin): (A) doublet before myosin II injection. (B) doublet during contraction due to myosin II. Time=0 corresponds to myosin II injection. Scalebar is 5 μm

pressure equilibration across the doublet, we can consider the contact line between the liposomes and the interface to be at equilibrium. Hence, we can apply Young's equation:

$$\sum_{k \in interfaces} \tau_k \cdot \vec{t}_k = \vec{0} \quad (4.1)$$

$$\tau_i \vec{t}_i + \tau_1 \vec{t}_1 + \tau_2 \vec{t}_2 = \vec{0}$$

In which t_k are the vectors tangent to the interface at the contact point, as described in figure 4.7

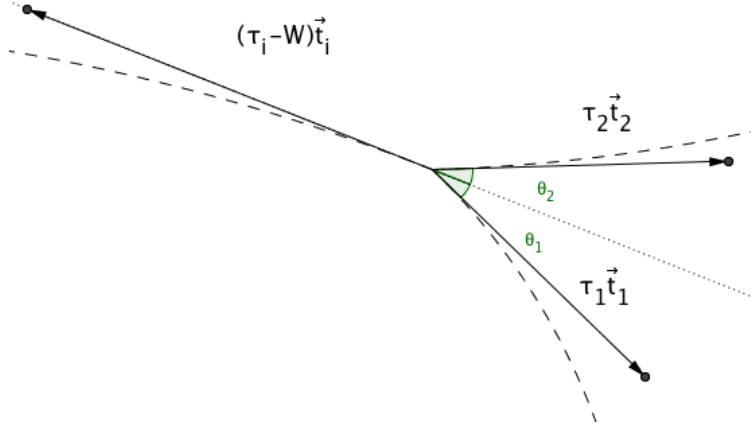


Figure 4.7: Equilibrium of the contact line. Each interface pulls on the line with a force proportional to its tension. As the contact line is at equilibrium, the sum of the forces compensate, thus ensuring a relation between the tensions and the contact angles.

This allows to relate the tension of all the lipid layers and the angle between them at each instance of the contraction. We can in particular project the result of this equation onto the direction of the contact surface tangent (dotted line on figure 4.7):

$$\tau_i - W = \tau_1 \cos(\theta_1) + \tau_2 \cos(\theta_2) \quad (4.2)$$

And on the direction perpendicular to it :

$$\tau_1 \sin(\theta_1) = \tau_2 \sin(\theta_2) \quad (4.3)$$

These equations link the tension to the contact angle before, during and after the contraction and hence remain correct during the experiment. In the following, we will mark the values before the contraction phase by the suffix 0. Thus, for example $\tau_{i,0}$ refers to the interface tension before the addition of myosin, and τ_i refers to the interface tension at any instant of the contraction.

4.3.3 Contact angle dispersion

The value of the contact angle θ varies across the different doublets both before and after the addition of myosin II. This reflects the initial variations of tension in $\tau_{i,0}$, $\tau_{1,0}$, and $\tau_{2,0}$ from doublet to doublet. Such variations could be due to a difference in the liposome tension acquired during the different preparations, but also to a variation of adhesion energy between doublets, or alternatively to an effect of tension build-up

during the actin shell formation. As the dispersion in the contact angle is in the same order as the increase in the angle upon addition of myosin, a statistical analysis of the contact angle before and during contraction is problematic. Thus, to avoid this effect of dispersion, we followed the evolution of θ each individual doublet over time.

4.3.4 Tension of actin-shell

In order to investigate the tension increase due to the acto-myosin network on liposomes, we first characterised the increase, only due to the addition of the actin-shell in the absence of myosin. By destroying the F-actin via photo-bleaching (Fig 4.8) we compared the shape of the same doublets in presence and absence of the actin-shell. It should be noted that it is established that the actin filaments are destroyed by bleaching, as this process frees oxygen radicals that denature the actin monomers. Hence, the bleaching process actually destroys the actin cortex ([vanderGucht et al. 2005]). This investigation showed that the total contact angle changes by $3.4 \pm 2.0^\circ$ ($n=7$) after disruption (Fig 4.9) of the actin network. Thus, we concluded that the tension change due of the actin-shell is negligible compared to the tension change we can observe with myosin.

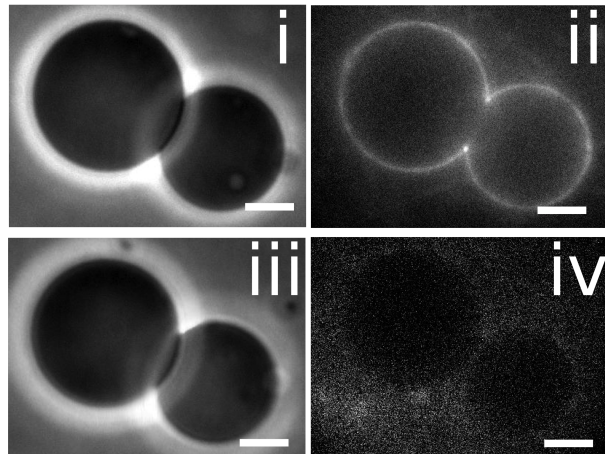


Figure 4.8: Image of an individual doublet coated with fluorescent F-actin before i) ii) and after iii) iv) actin cortex disruption. The actin cortex is visualised by epifluorescence ii) iv) and the doublet by phase contrast i) iii). Scale bar $5\mu\text{m}$.

4.4 3D observation

The three dimensional imaging of the doublets is necessary to get the correct contact angle. This requirement comes from the fact that in simple 2D epifluorescence images, the focal plane would have to correspond to the equatorial plane of the doublets for correct analysis. If this is not the case, the fit will produce a systematic underestimation of the contact angle. This is especially the case when doublets are of different radii, as typically found in our experiments, where the liposomes composing the doublets have a ratio of R_1/R_2 between 1.15 and 1.82.

Time resolved 3D Spinning disk stacks (Fig 4.10 with 3D reconstruction Fig 4.11) are recorded with a time resolution of less than 5 seconds per stack, for an accurate determination of the different doublet parameters

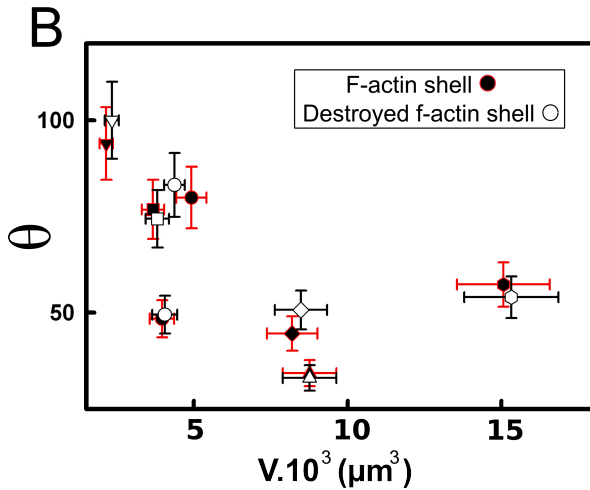


Figure 4.9: Measurement of the contact angle between the two liposomes forming the doublet before (black) and after (white) disruption of the stabilised actin cortex as a function of their volume.

over time. The analysis reveals the contact angle θ (Fig 4.12), the doublet volume V (Fig 4.14) and the distance between liposome centers d (Fig 4.13). All these parameters are obtained by fitting spherical 3D caps on the 3D stack as explained *later*.

During the contraction triggered by myosin, we observed that the contact angle θ increased while the distance between liposome centers d decreased. During this process, the volume remained constant within the error rate? of 10%. These results are consistent with the contact angle measures in freely adhering cell doublet experiments done previously [Maitre et al. 2012].

4.5 Discussion

4.5.1 Cortical tension is homogeneous for single doublet

Combining the equation (4.3) with the finding that $\theta_1 = \theta_2 = \theta/2$, allows to infer the equality of tension on both sides of the doublet during all the experiments. We can hence write $\tau_1 = \tau_2 = \tau$. This result is consistent with the fact that actin is continuously distributed all around the liposome doublet. Hence, myosin II minifilaments pull on a continuous shell. In these conditions, equation (4.2) simplifies to :

$$\tau_i - W = 2.\tau(t).\cos(\theta(t)/2) \quad (4.4)$$

Where $\tau(t)$ and $\theta(t)$ are the tension and the angle at time t after myosin injection. That $\tau_i - W$ may depend on a variability of the initial adhesion between liposomes. Since myosin does not operate at the interface between liposomes as it is actin-free, we can reasonably consider that both the tension and the adhesion energy are constant for a given doublet over time $\tau_i - W = \tau_{i,0} - W_0$. Therefore, we obtain an expression of the tension $\tau(t)$ during the acto myosin contraction that reads :

$$\begin{aligned} \tau(t) &= \frac{\tau_i - W}{2.\cos(\theta/2)} \\ &= \frac{cst}{2.\cos(\theta/2)} \end{aligned} \quad (4.5)$$

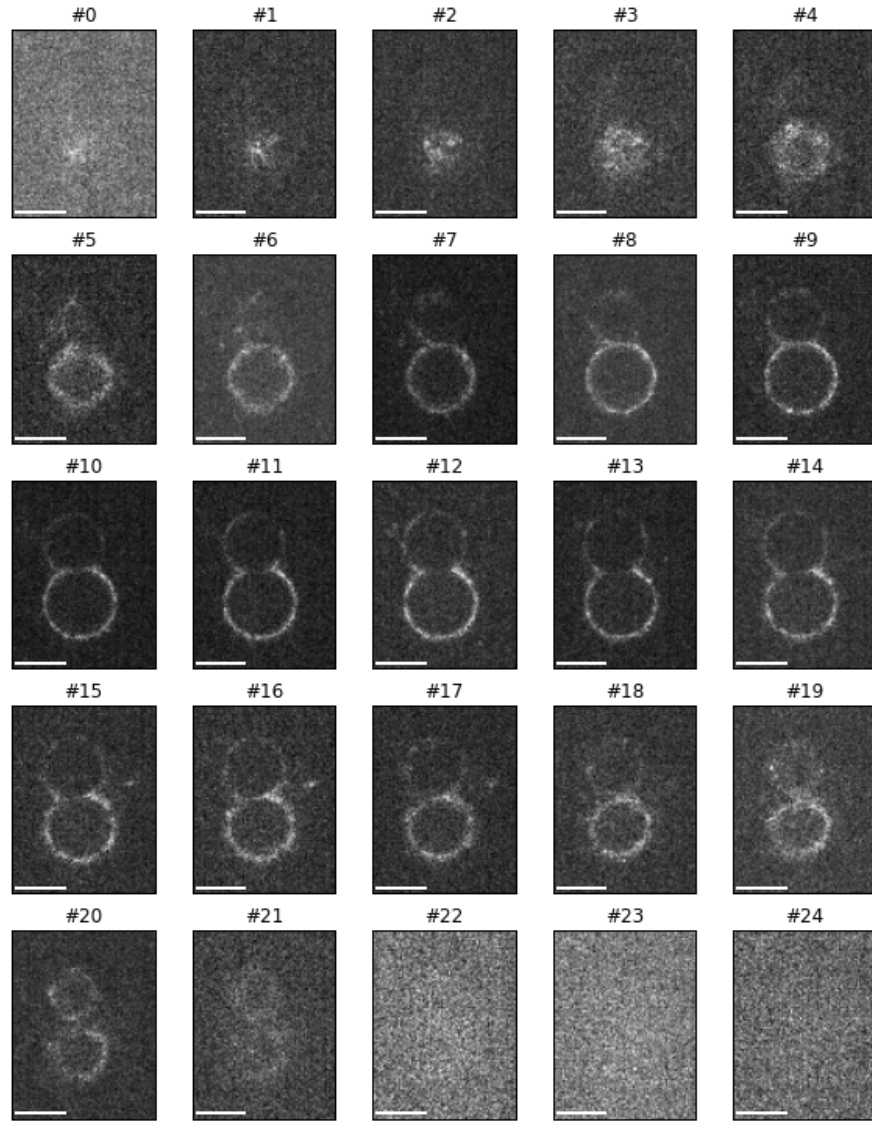


Figure 4.10: Confocal stack of a liposome doublet actin channel, 3D reconstruction in [figure 4.11](#). Note that there is no actin at the interface between the liposomes (Frames #11-#14). The distance between each image is $\Delta z = 0.85 \mu\text{m}$.

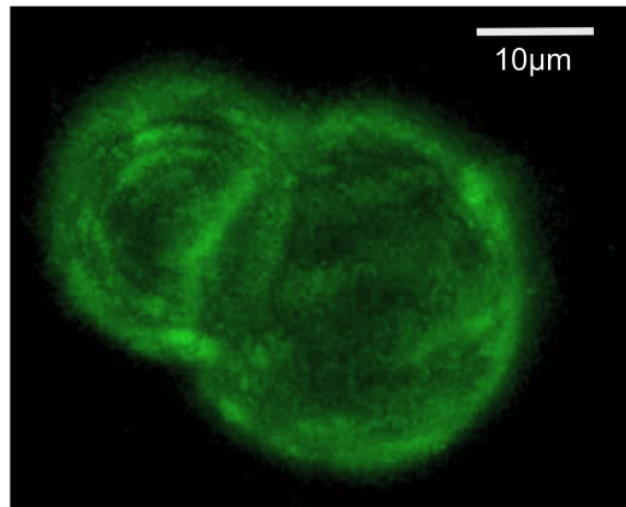


Figure 4.11: 3D reconstruction of a doublet surrounded by actin. The absence of actin on the interface can be more easily observed on [figure 4.10](#).

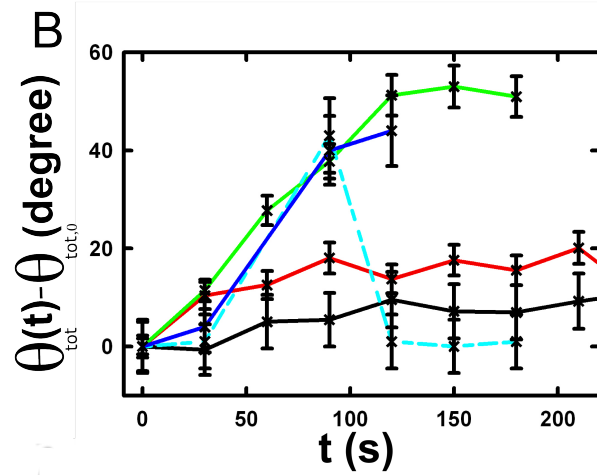


Figure 4.12: Evolution of the contact angle compared to its initial value as a function of time. Each doublet is represented by a different color. The color code corresponds to the doublet shown in figure 4.13, 4.14 and 4.15. A special case is highlighted in the blue dashed line, where the actin cortex on the doublet ruptured, and the cortex is peeled off. The analysis of this case showed that the contact angle after rupture recovers its initial value.

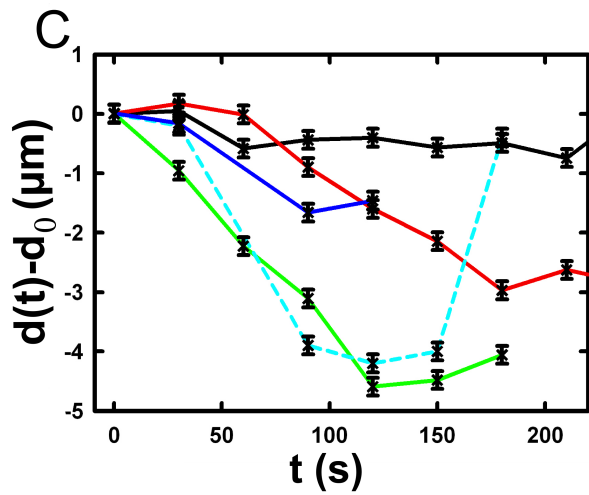


Figure 4.13: Evolution of the distance between liposome centers as a function of time. Same color code for same doublets as in figure 4.12, 4.14 and 4.15. Again, the doublet with the ruptured cortex recovers its initial parameter values.

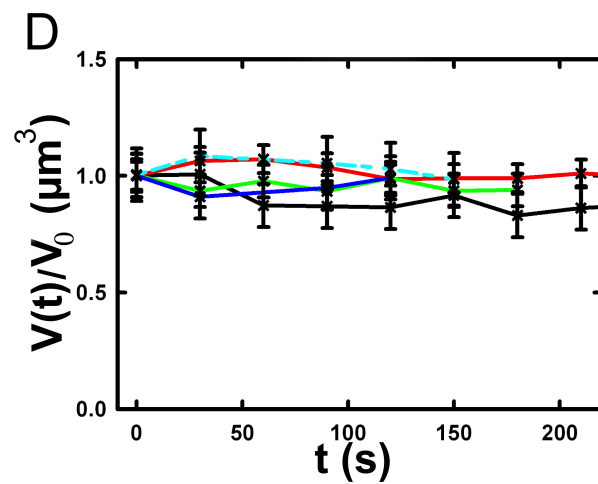


Figure 4.14: Evolution of the volume ratio over time. Same color code for same doublets as in figure 4.12, 4.13 and 4.15.

Consequently, we can evaluate the tension relative to its initial value over time :

$$\frac{\tau(t)}{\tau_0} = \frac{\cos(\theta_0/2)}{\cos(\theta(t)/2)} \quad (4.6)$$

4.5.2 Relative increase in cortical tension

The interaction of myosin II filaments with a biomimetic actin cortex induces tension build-up. The cortical tension, normalised to its initial value, increases and reaches a plateau where $\tau(t) = \tau_{peeling}$ (Fig 4.15), with the same trend as θ . Note that if the acto-myosin shell breaks and peels, the doublet recovers its initial shape (see dashed blue line for d and θ on Fig 4.12, 4.13, 4.14). The average relative tension is found to be $\tau_{peeling}/\tau_0 = 1.56 \pm 0.56$ ($n=5$) in 3D and $\tau_{peeling}/\tau_0 = 1.25 \pm 0.15$ ($n=5$) in epifluorescence, in agreement with the discussed expected underestimation of the contact angle in epifluorescence measurements.

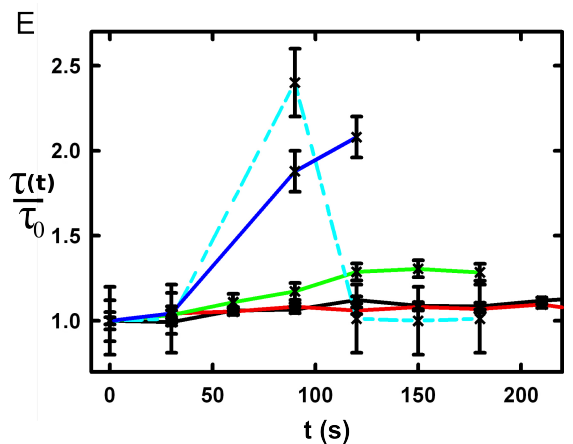


Figure 4.15: Increase of the tension ratio between the tension $\tau(t)$ at time t and the initial one τ_0 . Same color code for same doublets as in figure 4.12, 4.13 and 4.14. The actin cortex rupture in the blue dashed line also presents the highest relative tension increase.

4.5.3 Cortical tension increase in doublets and in cells

In cells, the cortical tension can be as low as 50 pN/ μ m in fibroblast progenitor cells [Krieg et al. 2008] and can go up to 4000 pN/ μ m for dictyostelium [Schwarz et al. 2000]. Surprisingly, when myosin activity is affected, either by drugs or by genetic manipulation, the cortical tension only decreases by a factor of about 2. Cells are also observed to round up during division, where a tension increase by a factor of two is sufficient [Stewart et al. 2011], [Kunda et al. 2008]. Our *in vitro* reconstruction is able to reproduce similar changes of cortical tension, as we observe a cortical tension increase by a factor of up to 2.4.

4.5.4 Different contributions for cortical tension

The cortical tension is the sum of the membrane tension and the tension due to the acto myosin cortex. We questioned how the membrane could contribute to the cortical tension and in our assay, we showed that in some cases, it might account for approximately 50% of the cortical tension. In suspended fibroblast cells,

the membrane tension is estimated to amount to 10% of the cortical tension [Tinevez et al. 2009]. When the actin polymerisation is stimulated, the cortical tension is multiplied by a factor of 5, also showing a strong dependence with actin dynamics [Tinevez et al. 2009]. Therefore, the residual tension in cells might be due to actin dynamics, which is absent in our experiments. How actin contributes to cortical tension is still an open question that needs to be addressed to the cell geometry. Whereas it has been proved that actin polymerisation outside a liposome generated inward pressure, the way this observation can be translated into tension in a different geometry is not yet clear. *In vitro* assays are on their way to mimic actin dynamics in cells [AbuShah et al. 2014]. They will allow to unveil the mechanisms of tension build-up by actin dynamics, the last remaining module that still needs to be understood, as the effect of both myosin and membrane have been clarified in this study.

4.5.5 Conclusion

We provided a biomimetic reconstitution of the tension build-up by acto-myosin contractility, through the use of liposome doublets. Cortical tension changes were visualised *in situ* over time by analysing doublet shape changes. This method allowed us to directly quantify the relative increase in tension due to myosin, regardless of the one due to actin dynamics. So, a thorough understanding of the composite systems contraction, rebuilt brick by brick to finally model a living cell, will hopefully lead the way towards a reconstitution of complex systems like tissues.

4.6 3D fitting

It remains challenging to obtain the doublets geometrical parameter, as in classical phase contrast and epifluorescence microscopy, the acquired images only capture a single focal plane of the doublets. This makes the analysis difficult, as the observation plane should be the equatorial plane of the doublet.

In order to achieve a good precision in the measurements of the contact angle, we decided to use confocal microscopy and to acquire evenly spaced z-stacks. The doublets 3D structure was reconstituted from these stacks, thus allowing to recover the geometrical parameters and the contact angle.

In order to determine the geometrical doublets parameters, we modelled them as two intersecting spheres, determined the expected 3D images and adjusted the model parameters to resemble the obtained experimental data.

I was responsible for developing a fast and precise method to reliably and automatically recover the liposome doublets geometrical parameters, based in the image stacks, acquired by using spinning disk microscopy. In the following part, I will develop the principle of this method and the result on liposomes doublets.

4.6.1 First step: Fitting a single liposome

In this part, we will describe the principle that allowed us to determine the 8 geometrical parameters that characterise a doublet: 2 centers (X,Y,Z) and 2 radii (R_1 and R_2).

As the principle for finding the geometrical parameters does not differ with the number of dimensions, the presented methods can be applied even in higher dimensions (e.g. deformed ellipsoid liposome, or multi channel imaging). Furthermore, as the principles also remain similar in a space with less dimensions, we

will restrict our discussion to a single liposome in a 2D plane (X,Y position of centers and R, radius, hence reducing the parameters to be determined to six instead of eight).

Experimentally, liposomes are observed using fluorescently labeled actin that forms an homogeneous micrometer-sized actin shell. In the observation plane, the liposome is a bright ring of a predetermined thickness (we will refer to this as the *expected signal*). We can observe the experimental noise on top of the image, where the principal sources are identified as the presence of fluorescent actin monomers in the buffer solution and electronic noise from the CCD camera. Eventually, the noise in the outside buffer, due to monomeric actin, can be higher than in the inside buffer, which is actin-free.

The signal from a liposome and the addition of noise can be replicated numerically as per figure 4.16.

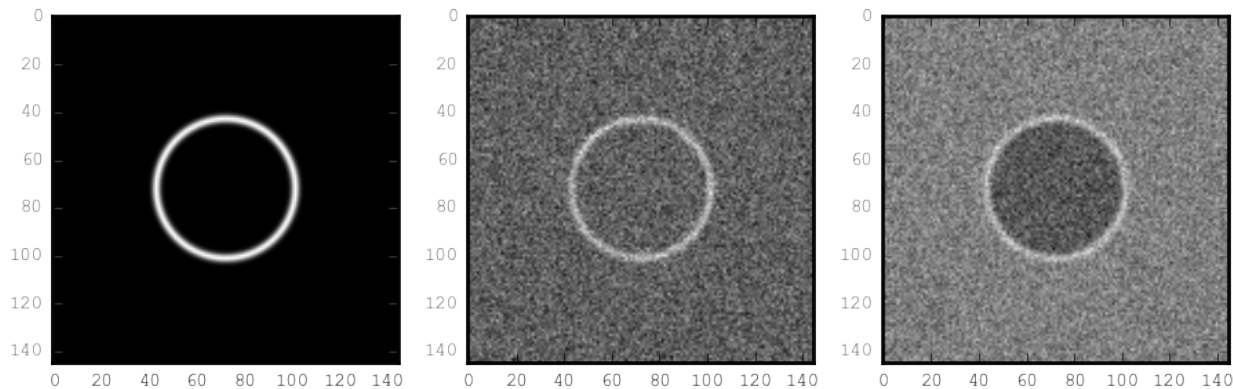


Figure 4.16: Left : A simulation of liposome fluorescent image consisting of a uniform shell or membrane (*expected signal*). Middle: Same Image Adding Gaussian noise. This simulates one plane of a confocal Z-stack. Right: Liposome simulation with a fluorescently labeled actin shell in a fluorescent external buffer and a non fluorescent inside buffer.

The *expected signal* can be modelled numerically, using several parameters of the system (center and radius of liposome, point spread function of microscope, ...).

In order to find the correct parameters for the doublets, we will numerically correlate the acquired data with the numerical model and search for the correlation that best corresponds to the real image. The correlation between the model and the images data can be. expressed as :

$$r_{xy} = \frac{\sum_{i=1}^n (x_i - \bar{x})(y_i - \bar{y})}{(n - 1)s_x s_y} \quad (4.7)$$

In which x_i are the luminosity values of each n pixel in the acquired data, y_i represent the pixels luminosity in the model \bar{x} , \bar{y} correspond to the average values over the images, s_x and s_y are the standard deviation of the luminosity values.

As the monomeric fluorescently labeled actin and the electronic noise are dominant in the acquired images, we can assume a uniform noise on top of the *expected signal*. The correlation between the model and the noise is on average uniform. .. math:

:label: eqa403

```
r_{noise,model}(params) = cst
```

And the correlation between the *expected signal* and the model is expected to be maximal for the model parameters equivalent to the real geometrical doublets parameters.

$$\arg \max_p (r_{data,model(p)}) = \arg \max_p (r_{expectedSignal,model(p)}) \quad (4.8)$$

In which $\arg \max_p$ stands for the argument of the maximum, that is to say, the set of points of the considered argument, for which the given function reaches its maximum value. Thus, searching for parameter values that maximise the correlation between the model and the data, implies that we find the geometrical parameters we are interested in.

We can test the ability to do this numerically by generating data, adding noise to it and trying to recover the parameters of the *expected signal*.

By looking at the correlation value between the generated data and the model as a function of model parameters, we can check that the correlation values are maximal when the model center value corresponds to the *expected signal* center value (Fig 4.17), and when the radius of the model liposome has the same radius in the model and corresponds to the radius in the generated data (Fig 4.18).

We could search the parameter space of the model and maximise the correlation between the model and the experimental data through the use of minimisation techniques. We then could recover the liposomes geometrical parameters by efficiently computing the correlation value within a few hundreds of points, thus giving access to the liposomes' geometrical parameters, in this instance position and radius.

4.6.2 Fitting a doublet

The determination of the contact angle on epifluorescence images or phase contrast images often results in an underestimation, as the imaging plane is not necessarily one of the doublets equatorial planes. Moreover, most determinations of the contact angle on phase contrast and epifluorescence images are handmade [Maitre et al. 2012] and are subject to experimenter's bias, as the experimenter draws the tangent lines at the contact point between the liposomes. Thus, we decided to develop fitting routines for the acquired 3D confocal stacks. In our case, we avoided the usage of fluorescent lipids that could artificially change the membrane tension.

As sketched in figure 4.2, the doublets are covered with a thin micrometer-thick layer of fluorescent actin filaments, which we imaged by confocal spinning disk microscopy. As the actin-layer is attached to the membrane and the contact angle is defined as the angle between the lipid bilayer, imaging the actin-layer corresponded to the angle between the inner surfaces of the two actin networks present on each liposome.

Thus, in order to determine the geometrical parameters of the doublets we also needed to model the actin shell. As the liposomes in contact consist of two spherical caps, the uniform actin layer will also form two spherical caps with a given thickness. The total image is thus the union of two spherical caps blurred by the point spread function of the microscope. This can be seen on figure 4.19. We can notice on this image the presence of the doublet, lying on the chamber surface. We checked in this case that the contact surface between the chamber and the doublet did not change during experiments.

As the doublets contraction is rapid, and the recorded 3D stacks contain a large number of frames, it is hence crucial to be able to compute the model and the correlation in a reasonable time (less than an hour per images). To achieve this besides calculating the model as efficiently as possible, one can replace the exact calculation of two spherical caps and the point spread function of the microscope by the union and subtraction of pre-calculated spheres followed by a 3D numerical Gaussian blur (Fig 4.20).

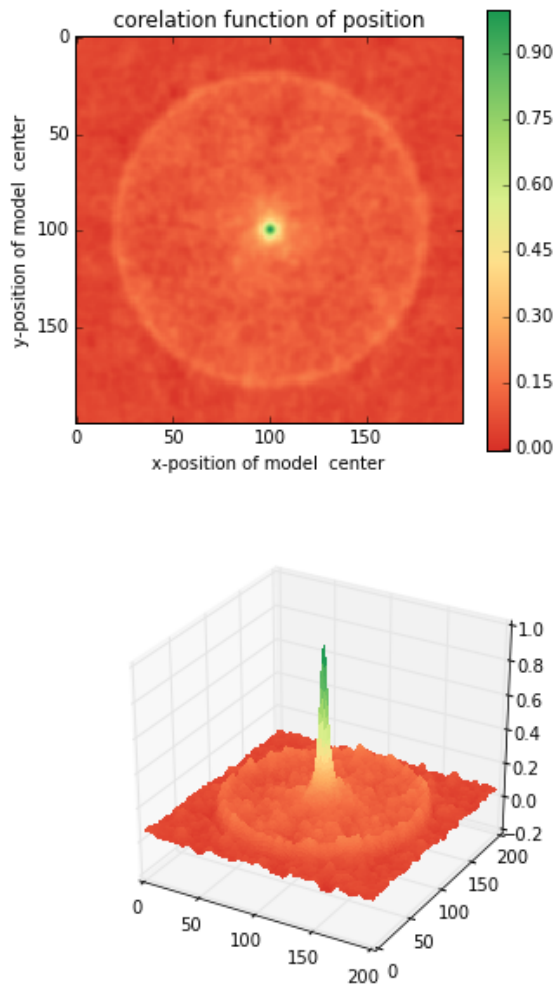


Figure 4.17: Correlation value as a function (arbitrary units) of two among the fit parameters. The liposome radius in the model is taken as equal to the value of the *expected signal*, and the position of the center is varied? in the X and Y directions. The correlation value is maximal for the center position in the model, that equals to the center of the *expected signal*. The local maxima observed on the 3D representation are well below the global maximum value. The peak at the global maxima is sharp, hinting that the search of the maxima requires relatively good initial parameters (lower than $\sim 1/10$ of the liposome radius). The sharpness of the peak point corresponding to the best fit parameters on experimental data, should be robust.

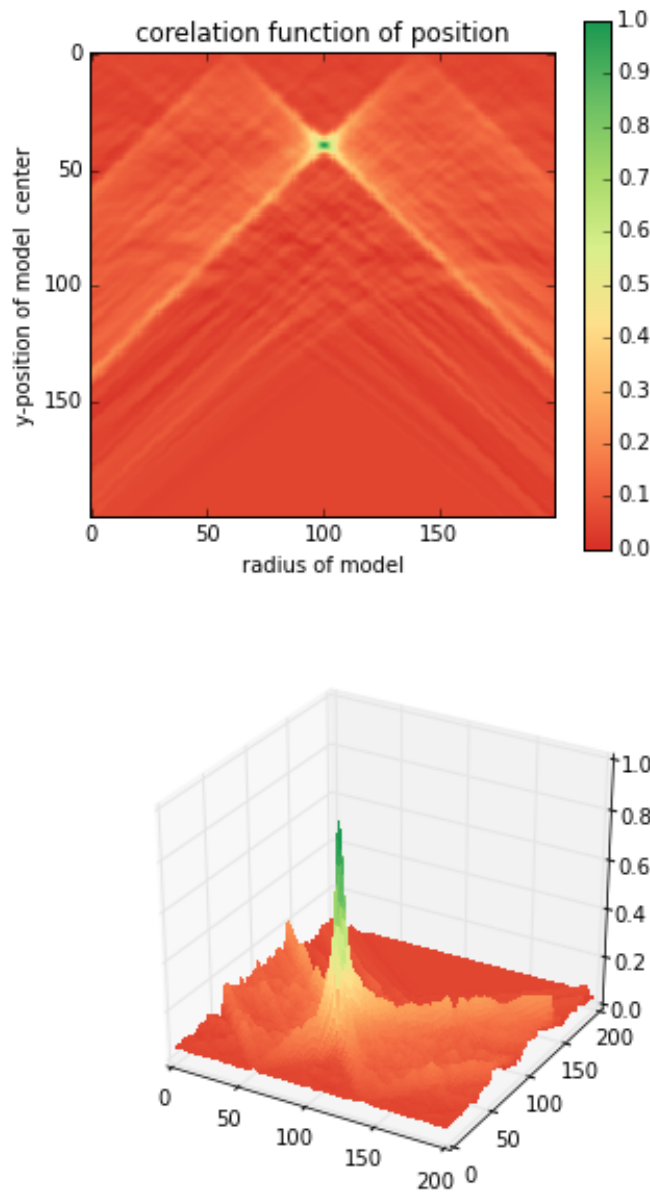


Figure 4.18: Same as [figure 4.17](#) with Y, center position taken as equal to the expected signal, variating X position of the model and radius of the liposome. The graph shows the same properties as before.

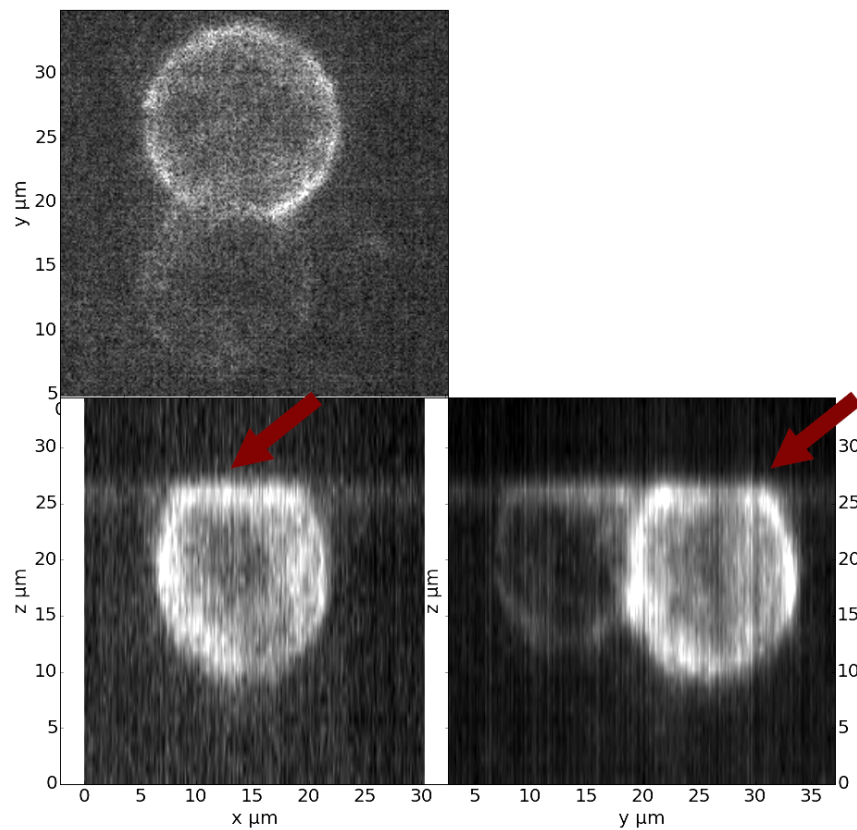


Figure 4.19: Maximum projection along X,Y and Z of recorded stacks, green channel represents actin. One can observe that the liposome doublets are lying on the surface of the observation chamber (arrows).

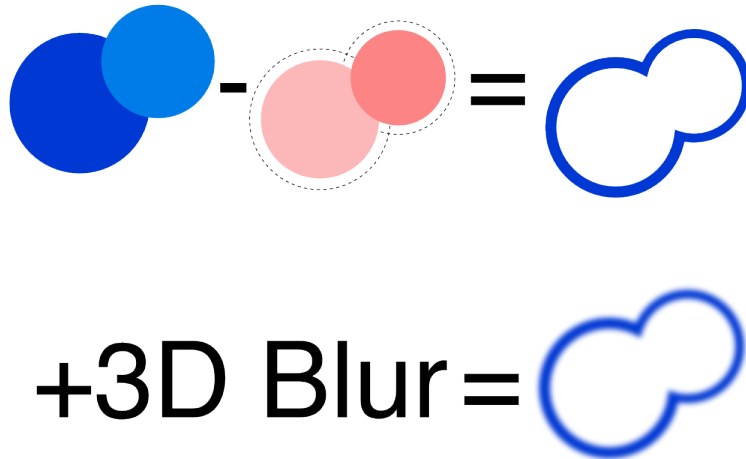


Figure 4.20: Principle of numerically approximating the two spherical caps as intersection of two spheres, followed by a 3D numerical Gaussian blur. Compared to the exact calculation of the fluorescent density, the numerical speed-up allows to make fits on doublets in minutes instead of hours.

However, the use of such numerical techniques is not devoid of artefacts. In the particular case of discrete Z-stacks that are not sufficiently spaced, the different radii in the fluorescent rings within subsequent stacks can lead to a “ring-artefact” (Fig 4.21), when using numerical Gaussian blur. In the case of a too pronounced “ring-artifact”, a “ghost” spheres can appear around each liposome, liable to cause the doublets fitting process to fall into a local maximum of correlation, thus leading to a wrong value of the geometrical parameters.

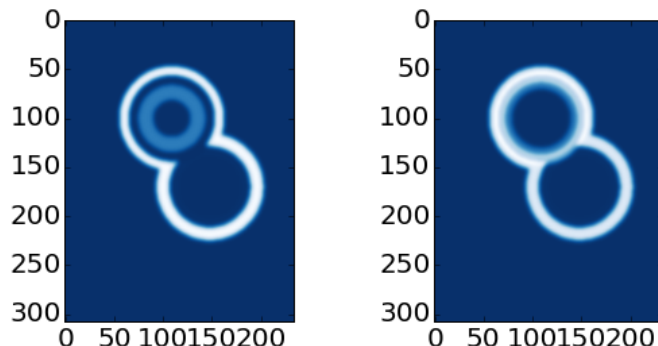


Figure 4.21: Left : One plane of the numerical model with an exaggerated ring artifact due to an under sampling of the model in the Z-direction, stacks from “Far” Z leak onto the current Z-plane and forms a ring. Right : Same model plane with enough sampling plane in the Z-direction, does not show the ring artefact. In this case, we used a sampling with the same number of slices than the recorded data. (X,Y in arbitrary units)

In our case, we had a sufficient number of planes per stack so that the numerical model with the same sample size similar to the data, did not show the ring artefact and had

a smooth transition near the position of the spherical cap. Though, the ring artefact could be eliminated by oversampling/interpolating the model before the numerical Gaussian blur and undersampling afterwards to

reach the correct number of pixels.

The size of the Gaussian blur, which will act as a regularisation function for the value of the correlation between the model and the acquired data, can also be adjusted to be higher (see Fig 4.22), thus smoothing or eliminating local maxima, but reducing the precision in the maxima position.

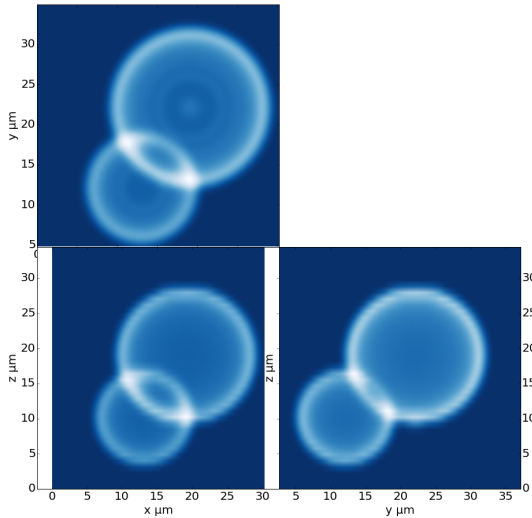


Figure 4.22: Maximum projection along the X,Y and Z of numerical model, the “ring” effect is still slightly visible near the pole of each liposome, but is not sufficient for the fit to be stuck in a local minimum.

The correlation value between the model and the experimentally recorded data can be maximised, by using already available functions, and more particularly the Nelder–Mead simplex algorithm as implemented in `scipy.optimize` python library. This provided us with the 8 parameters of the doublets. Result of the fits are shown in figure 4.23.

of projection.

Using the fast Cython code ([Seljebotn 2009]) also allowed to speed up fitting to a reasonable time: one Z-stack of 3 millions pixels can be fitted in about 40 seconds, thus allowing the fitting of a full 3D movie of a doublets contraction to be completed in less than an hour for 30 to 40 frames.

To ensure fits robustness to doublet center displacement during acquisition, the initial parameter of the fit were chosen manually for each first frame of each sequence. The final fit parameters of each frame are reused as initial fit parameters for the subsequent frame.

In order to test the robustness of the fit, we randomly modified the initial fit parameters by +/- 1μm, and we checked that the final parameters did not vary.

For a couple of parameters, the correlation function values can be plotted to check the regularity of the function and the absence of local maxima. Figure 4.24 and figure 4.25 show the resulting correlation values.

The fit correctness is also checked visually to prevent errors in the procedure. We found that the fit was systematically accurate and coherent with the manual measurements of the contact angle. Whenever the

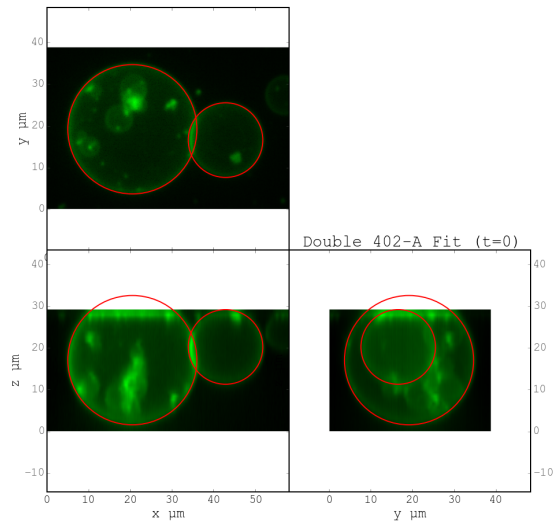


Figure 4.23: Maximum projection of confocal images in the X,Y and Z projections as well as the result of the fits shown as equatorial circles for the three directions

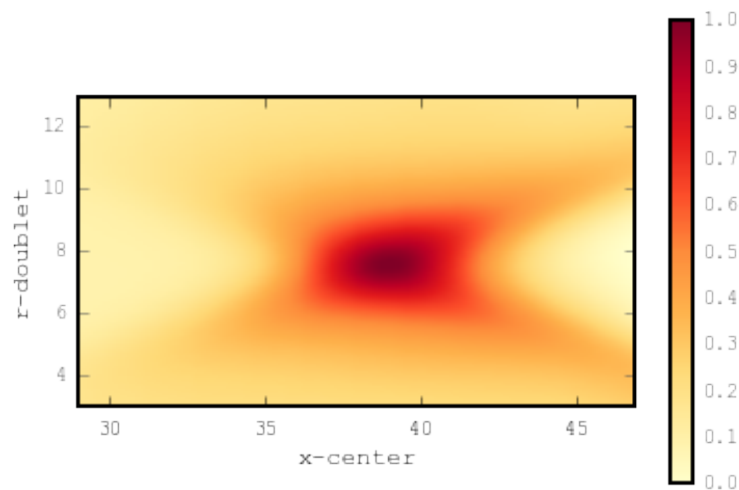


Figure 4.24: Correlation of the model and the data as a function of the center position of one of the model spherical caps along the X axis and the radius of this same spherical cap. Vertical axis in arbitrary unit.

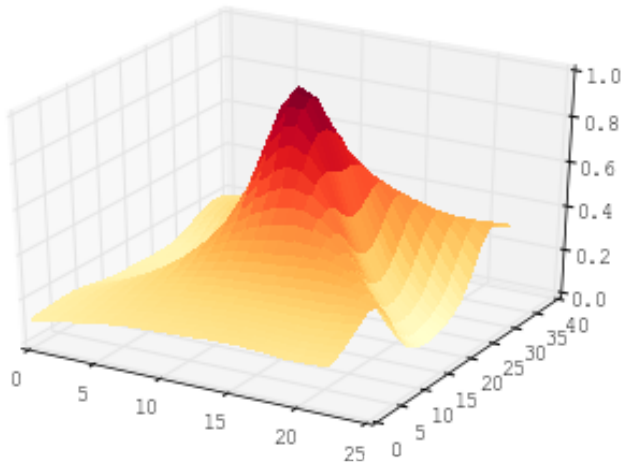


Figure 4.25: 3D representation of the data in figure 4.24, the function shape is the same as the simulation done with the *expected signal* in figure 4.17 and 4.18

red channel was also present and the liposomes contained sulphorhodamin B, we were additionally able to visually check the fits, by using the maximum projection of the red channel. (see Fig 4.26).

4.6.3 Discussion

This part aimed at demonstrating that by modelling the liposome doublet and using fluorescently labeled actin, we were able to develop a technique that automatically and robustly determined the geometrical properties of the liposome doublets.

We noted that the red fluorescent dye present in the inside buffer of the liposome could be used conjointly for the green channel, in order to improve the fit quality, though this would require the extra parameters of the interface radius. As the required computation time to fit the doublets increases rapidly with the parameters number, we came to the conclusion that this solution was impractical. Moreover, the interface curvature is relatively small and the difference between the curved interface and a flat plane close to the optical resolution, hence the risk for the fits to become unstable. The use of fluorescently labeled lipids for the liposome membrane also suffers from the same issues of extra parameters, if one wants to recover the interface position.

4.6.4 Conclusion

We developed a robust and automated method to determine the geometrical parameters of liposome doublets. This allowed to robustly determine the liposome doublets geometrical parameters without any experimenter's measurements bias, thanks to the selection of the illumination plane, the resolution of optics and the luminosity scale.

We determined that liposome doublets with reconstituted acto-myosin cortices were a biomimetic system allowing to measure the changes in cortical tension with time. 3D fitting helped to quantify the tension by obtaining the corresponding contact angles.

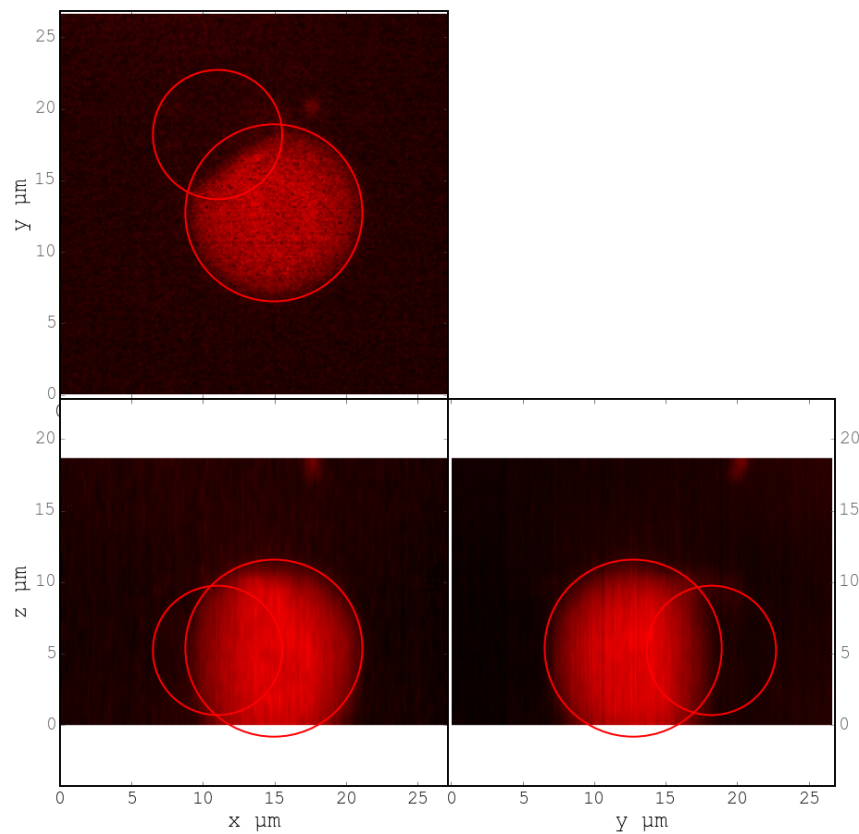


Figure 4.26: Maximum projection of the red channel (*sulphorhodamin*) and fitted parameter for the doublet.

A simultaneous observation of the contraction of multiple liposomes doublets and the ability to automatically determine the geometrical parameters allowed the collection of more samples. A faster and more reliable data acquisition on actin network contractions will lead to a better understanding of the effect of actin network *in vitro* thus also paving the way for the reconstitution of more complex systems.

ACTIVE CYTOPLASM MOVEMENT IN MOUSE OOCYTES

5.1 Introduction

Mouse oocytes are big spherical cells with a diameter around 80 μm . A previous work has established that the spindle positioning during meiotic cell division in oocytes depends on an actin meshwork present in the cell's cytoplasm [Schuh et al. 2008]. This actin meshwork is regulated by formin, localized to endogenous vesicles. Additionally, these vesicles recruit the myosin-Vb motor proteins, that are known to drive the vesicles active movement in the cytoplasm [Holubcova et al. 2013]. In a collaborative project with the group of Marie-Hélène Verlhac and her Postdoc Maria Almonacid at the Collège de France, I designed a way to measure the cytoplasmic activity in mouse oocytes.

figure 5.1 presents a typical mouse oocyte, where the nucleus can be seen positioned at the center of the cell. In this system, current questions relate to the mechanical processes during meiosis such as the chromosome migration, the asymmetric cell division and the organelles positioning by the dynamic remodelling of the actin network. While our team did active and passive microrheology measurements on timescales of 10 seconds, I developed a suitable method for longer timescales in the order of minutes, more relevant for the meiosis process.

5.2 Oocytes

The cytosolic actin meshwork in oocytes is controlled by the activity of formins (Fmn2) that nucleate actin polymerisation, and by the activity of the vesicle-bound molecular motor protein myosin Vb that controls the dynamic movement of the vesicles in the actin meshwork. Hence, it is of interest to study oocytes with formin and myosin Vb deficits. We focused more particularly on three types: 1) Wild type oocytes, 2) oocytes prepared from Formin 2 invalidated female (Fnm2 $^{-/-}$) that lacks the actin meshwork and 3) oocytes injected with the RNA coding for the dominant-negative tail of Myosin Vb (Fig 5.2), thus replacing the active myosin Vb on the vesicles.

5.3 Measure of activity

The diffusive-like motion of actin-positive vesicles that can be observed during oocyte meiosis is reduced in Fmn2 $^{-/-}$ and MyosinVb-tails oocytes when compared to the wild type. While the use of particle tracking algorithms to measure vesicle motion in oocyte is possible, it remains a complex process especially as the vesicles may move outside the microscope focal plane. As a simple approach to measure the vesicle

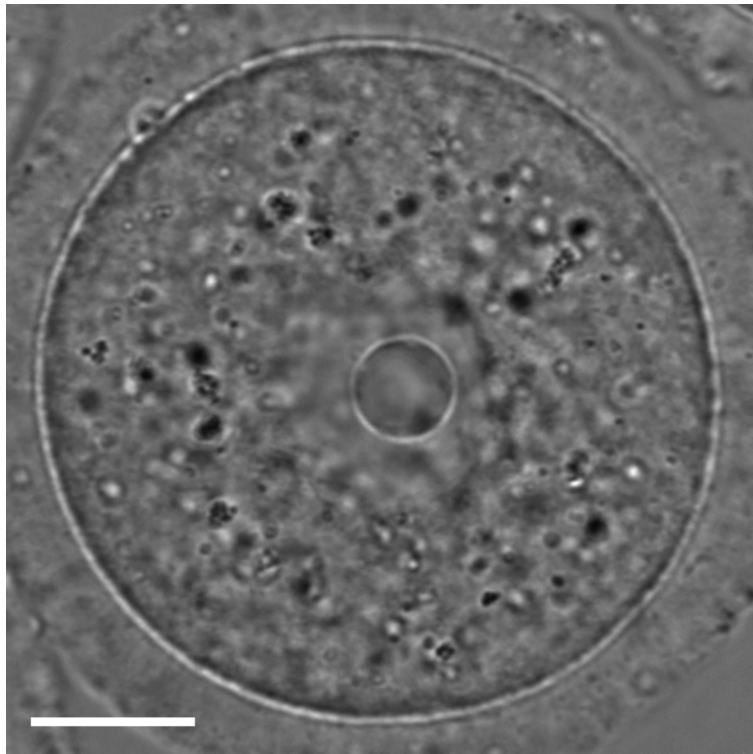


Figure 5.1: Bright field image of a mouse oocyte before meiosis (scale bar is 20 μm). The cell diameter is about 80 μm . The nucleus is positioned at the center of the oocyte during meiosis with the help of the actin network. The positioning is a crucial factor for the normal oocyte division. The oocytes are a good reference system as they provide a clean spherical symmetry and due to their size, give a good spatial difference between the cortex and the cytosol, which helps to measure the spatial variations of mechanical properties and vesicle movement. Image Credit to Maria Almonacid, Collège de France.

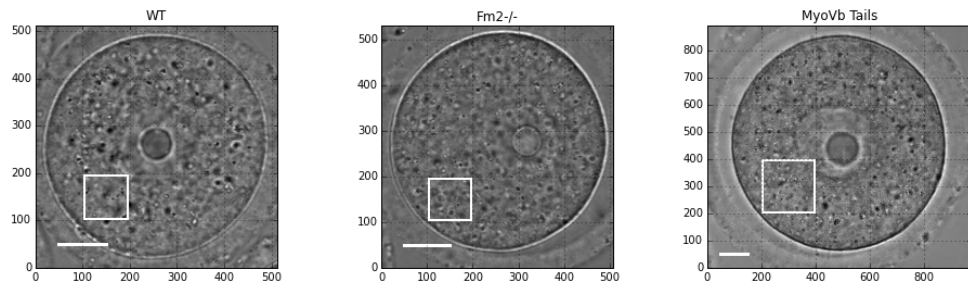


Figure 5.2: Bright field image microscopy of the 3 kinds of oocytes (Credit to Maria Almonacid, Collège de France). WT) Image of Wild Type Oocyte, Scale bar is 20 μm . Fmn2-/-) Oocytes extracted from females with invalidated Formin 2, lacking the actin meshwork. MyoVb Tails) Oocyte injected with the RNA coding for Myosin Vb dominant negative tails. These cells have a less active vesicle population. The white square gives an example of the region used for the analysis presented in this chapter.

activity, we decided to investigate the bright field images temporal variations in mouse oocytes. We could compute the time-dependent difference between predefined regions of interest (ROI) in an image series, to determine how fast the bright field images change. We finally compared the results between wild type, Formin Knockout and MyosinVb dominant negative tails ([Fig 5.3](#)).

difference

rapidly reaches its maximum value (Image J and M similar), whereas for Fmn2-/ and MyoVb, the difference between images at 60 second intervals? (K,L) is much smaller than after 10 minutes (N,O), and defined as follows :

11. is whiter than (N) and (L) is whiter than (O). The change in cytoplasm is thus much faster in WT oocytes ($< min$) while it takes significantly longer in Fmn2-/ and MyosinVb oocytes.

In order to get a quantitative measurement of the speed at which the images difference changes, we can compute the autocorrelation of bright field images through time. The correlation of two images A and B is defined as :

In which A_i and B_i are luminosity values of each n pixel of the images, \bar{A} , \bar{B} correspond to average luminosity values over the images, s_A and s_B are the standard deviations of the luminosity values. The correlation will give us a single value that characterises the images similarity. A correlation of 1 means that the images are identical, a correlation of 0, means that the images have nothing in common, a correlation negative value means that the second image is globally dark where the first one is bright, and bright when the first one is dark. We can thus obtain a measurement of images similarity over time, that should start at 1 for $\Delta t = 0s$ between images. We expect it to decrease until it eventually reaches zero.

We can compare the correlation decrease over time, depending on the oocyte type. In order to extract a single value that represents the activity, we can phenomenologically fit the correlation as a decaying exponential with an offset :

$$r(t) = (1 - off) \cdot e^{(-t/\tau)} + off \quad (5.1)$$

In which t is time, and τ is a characteristic time representing the correlation decay. The offset off represents the correlation value at infinite time to take into account both artifacts in the chosen region of interest and defects in the image, that will not decorrelate over time.

[Figure 5.4](#) gives typical examples of the measured autocorrelation result over time, and of a single exponential decay fit.

The results show that the characteristic time values increase when the actin network is disrupted in Fnm2-/ cells or when the source of its dynamics is removed by inactivating Myosin Vb. We can then use the inverse of τ as an indicator of activity.

Once defined the activity of a precise region of the cell cytoplasm, we can repeat the measurement on different areas of the cytoplasm. This allows to reproduce an activity map in the cell as a position function ([Fig 5.5](#)).

Value of $1/\tau$ plotted as color square overlaying the analysed bright field image. Scale bar is 20 μm . We can see that the activity near the nucleus is lower (blue) than in the middle of the cytoplasm.

The measure of the correlation characteristic decay time can also be done on a time sliding window. This allows to determine the activity of a particular area of the cytoplasm with time.

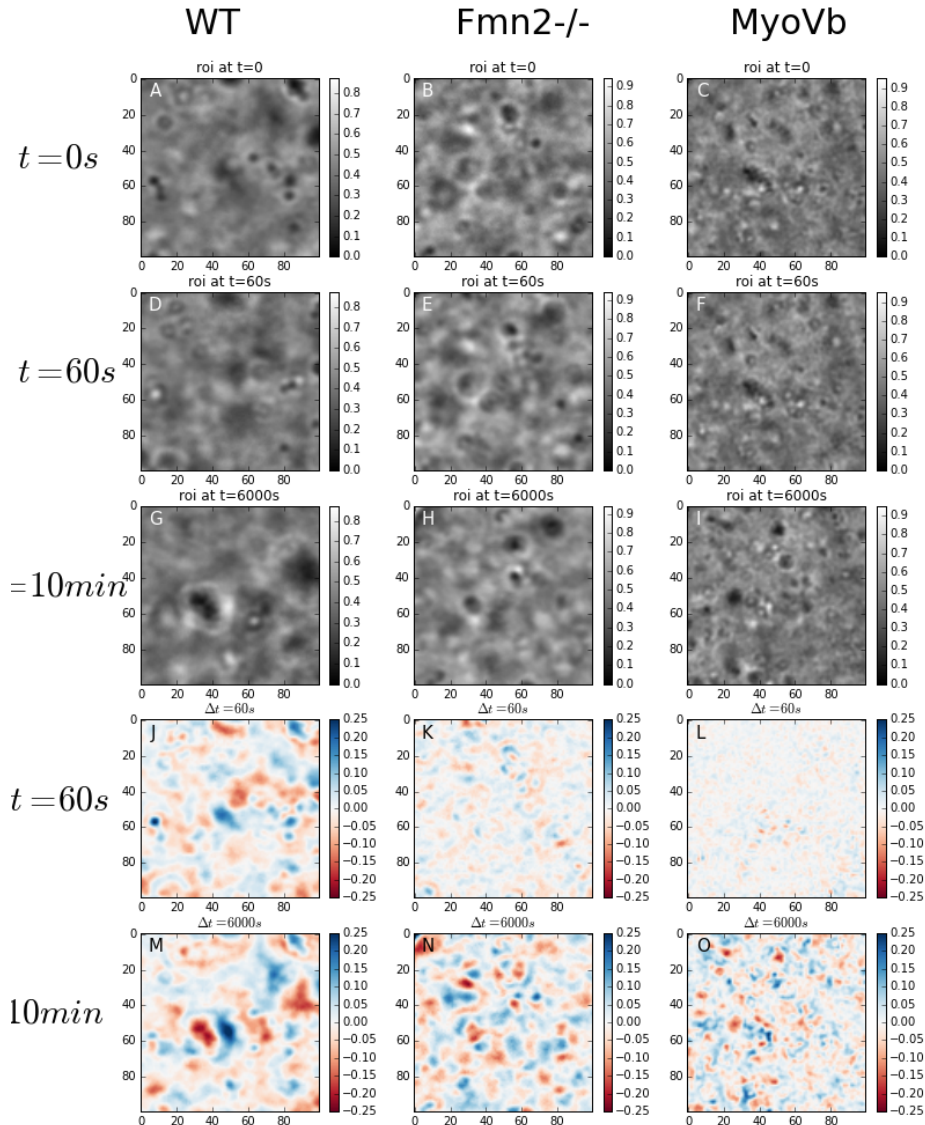


Figure 5.3: Bright field images of the 3 mouse oocyte types : Wild type in the first column, Formin knockout in the second, Myosin Tail dominant negative in the third. Rows 1 to 3 represent the region of interest of figure 5.2 (20 μm side) for each kind of oocyte. Row 1 shows regions of interest at $t=0\text{s}$, row 2 at $t=1\text{min}$ and row 3 at $t=10\text{min}$. The color-coded difference between images at $t=0\text{s}$ and 60s are shown on row 4, and between $t=0\text{s}$ and 10min on row 6. Blue indicates that the later image is brighter than the original one and red indicates that it is darker. For wild type oocytes, the images

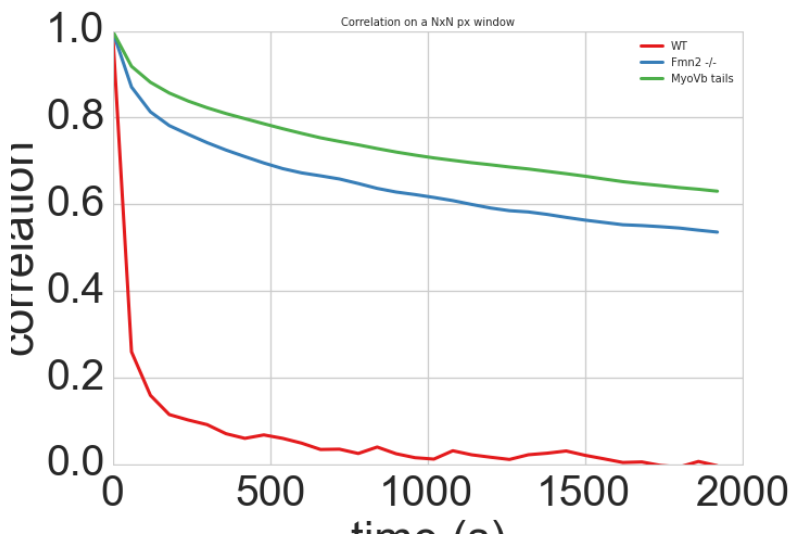


Figure 5.4: Decreasing autocorrelation of images intensity (solid line) over time, with exponential decay fit (dotted lines) as in (5.1). Characteristic decay time of the fit τ in the legend. We can see in the plot that the images correlation decreases much faster in wild type oocyte (red curves, $\tau \sim \text{minute}$) compared to Fmn2 $^{-/-}$ (blue lines $\tau > \text{hour}$) that lacks the actin meshwork, or to dominant negative myosin Vb tails (green $\tau > \text{hour}$). While the fit quality is not impressively good, the overall change in the timescales is well captured.

5.4 Conclusion

In this part, we developed a method that allows to determine the cytoplasmic activity in oocytes by a non-invasive image analysis as well as to measure the spatial and temporal variation of this cytoplasmic activity. A further advantage of this method lies in its flexibility regarding the probed timescales,

extending from second up to hours, keeping in mind that this is similar to the relevant timescales for oocyte maturation. Measurements on minutes timescales are also complementary to such techniques as active optical tweezer-based micro-rheology that can hardly probe timescales beyond tens of seconds, due to thermal drift and cell movement, but can reach on the other hand much shorter timescales, below the ms.

The proposed technique is currently actively applied by Marie-Hélène Verlhac and Maria Almonacid at the Collège de France. It is used to measure the actin networks activity in oocyte and to determine their effects on the mouse oocyte meiosis and on the organelle positioning.

$1/\tau$ map for a wild type oocyte

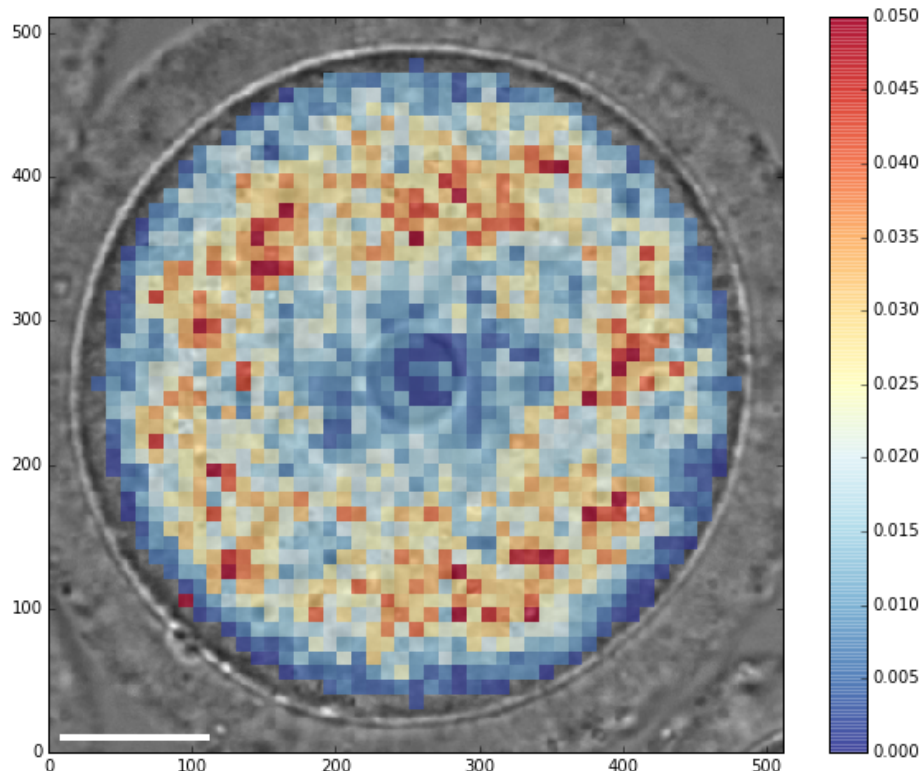


Figure 5.5: Activity of a wild type oocyte for different 10 by 10 pixel regions

CHAPTER

SIX

CONCLUSION

During my PhD I have investigated the mechanics of different actin networks found in living and biomimetic cells.

In the first part, the reconstitution of biomimetic cortices on polystyrene beads allowed to study the actin filaments that emanate from a thin reconstituted cortex. We determine that the mechanical effect of these actin filaments can be already perceived 10 to 15 μm from the bead surface, well beyond the surface of the reconstituted actin cortex ($\sim 1\mu\text{m}$). We coin these extending filaments “actin cloud”, which appears to be mostly elastic at the time scale of tens of second, and have a elasticity of a few Pascals at the most, which is several orders of magnitude smaller than the actin gel visible on the surface of the beads which has been measured to provide elastic moduli of kPa. Nonetheless, this actin cloud appears to be able to sustain forces sufficient to move organelles and seem coherent with several observation made *in-vivo* in cells.

We also studied the change in mechanical properties of this actin cloud under variable biochemical conditions, and in particular as a function of Capping Protein concentration. Using established polymer physics models, we are able to derive information about the structure of the network, like mesh-size and filaments length. We show that the evolution of the model parameters with the concentration of Capping Protein are coherent with previously observed phenomena: The distance offset δ in our model corresponds to the measured gel thickness by the position of the half fluorescence maximum.

Our description thus extends the current knowledge of reconstituted actin cortices. It shows a transition zone beyond the typically studied dense gels forming on the membrane. In this transition we find soft structures with different properties than found in the cortex. These properties have direct impact on the cells mechanics and could be directly involved in the positioning of organelles in cells. This work was recently accepted for publication in Biophysical Journal, with Matthias Bussonnier as the lead author.

The mechanical properties of cells and the actin cortex is not only driven by the dynamics of actin polymerisation. The effect of molecular motors is crucial to understand the well known change in acto-myosin cortex tension that has been shown to contribute to cell-cell adhesion and cell sorting.

In a second project of my PhD I focused on the measurement of cortical tension changes. In order to address the evolution of cortical tension over time, we developed a new biomimetic system composed of liposome doublets. Time resolved 3D imaging allowed the tracking of the key geometrical parameters over time to measure the relative increase of the cortex tension after the addition of myosin motors to a preformed actin cortex. I focused on the development of an automated method to measure the geometrical parameters of liposomes doublets to obtain accurate and robust measurement of contact angle independent from experimenter bias. This non-invasive measurement is a step towards a better understanding of the effect of myosin motors on the cortical tension in cells and its potential consequences on cell motility.

Actin Gels dynamics,

The mechanics and dynamics of the actin network is decisive for cells. In the case of mouse oocytes during meiosis, the actin meshwork is necessary for the correct positioning of different structure of the cells like the mitotic spindle and the nucleus. Without a correct actin network, or without the network dynamics driven by myosin, the oocyte meiosis is severely hindered, leading to non viable cells.

The third part of my PhD was done on these oocytes. In a collaboration with the group of Marie-Helene Verlhac at Collège de France, we used image analysis as a complementary technique to determine the evolution of cytoplasmic activity. In particular we measured the time dependent autocorrelation of bright field image series to determine how fast the cytosol arrangement changes, which is dependent of the overall organelle movement. We investigated the characteristic decay time of the autocorrelation function under different types of oocytes. Our results show that the overall activity strongly depends on the presence of the actin network and the molecular motor myosin Vb. The method developed also allows to determine the temporal and spatial change in activity in the mouse oocyte cytosol. It thus provides a simple method that can extract changes in network dynamics of living cells. This will allow a better understanding of the different phenomenon at the origin of organelle positioning in cells and the role of actin networks.

**CHAPTER
SEVEN**

APPENDIX

7.1 Mechanical detection of a long range actin network emanating from a biomimetic cortex Preprint

Preprint of paper on the actin cloud has been published in biophysical journal under the reference *2014BIO-PHYSJ303916R* and entitled *Mechanical detection of a long range actin network emanating from a biomimetic cortex, [Bussonnier et al. 2014]* the submitted text is attached:

Mechanical detection of a long range actin network emanating from a biomimetic cortex

Matthias Bussonnier^{1,2,3,4,#}, Kevin Carvalho^{1,3,4,#}, Joël Lemière^{1,2,3,4}, Jean-François Joanny^{1,3,4}, Cécile Sykes^{1,3,4}, Timo Betz^{1,3,4,*}

1 Institut Curie, Centre de Recherche, F-75248 Paris, France

2 Univ Paris Diderot, Sorbonne Paris Cité F-75205, Paris, France

3 Sorbonne Universités, UPMC Univ Paris 06, UMR 168, F-75005, Paris, France

4 CNRS, UMR168, F-75248, Paris, France

Abstract

Actin is an ubiquitous globular protein that polymerizes into filaments and forms networks that participate in the force generation of eukaryotic cells. Such forces are used for cell motility, cytokinesis and tissues remodeling. Among those actin networks we focus on the actin cortex, a dense branched network beneath the plasma membrane that is of particular importance for the mechanical properties of the cell. Here we reproduce the cellular cortex by activating actin filament growth on a solid surface. We unveil the existence of a sparse actin network that emanates from the surface and extends over a distance that is at least ten times larger than the cortex itself. We call this sparse actin network the "actin cloud" and characterize its mechanical properties with optical tweezers. We show, both experimentally and theoretically that the actin cloud is mechanically relevant and that it should be taken into account as it can sustain forces as high as several pN. In particular, it is known that in plant cells, actin networks similar to the actin cloud have a role in positioning the nucleus, in large oocytes they play a role in driving chromosome movement and recent evidence shows that such networks even prevent granule condensation in large cells.

Insert Received for publication Date and in final form Date.

MB and KC contributed equally to this work.

* Corresponding author , E-mail: timo.betz@curie.fr

1 Introduction

The actin cytoskeleton plays a major role in cellular mechanics (1), force generation (2) and cell motility (3). Its mechanical properties have been extensively studied in the past decades (4). The detailed characterization and modeling of the actin cytoskeleton has proven to be a complex task, mainly due to the different structures formed by the actin biopolymer in cells. A major experimental approach to understand the architecture and detailed properties of the actin cytoskeleton is to reconstitute the structures commonly found in cells using purified components (5–8). Such controlled *in vitro* studies gave detailed insights into the mechanical properties of cytoskeletal structures like actin bundles (9), actin stress fibers (10) and cortical actin networks (7, 11).

Of particular importance is the mechanical contribution of the actin cortex, which provides a mechanical barrier supporting the plasma membrane against extracellular forces, but also acts as a steric obstacle for intracellular organelles. The actin cortex in cells was estimated to extend over a thickness of a few hundred nanometer underneath the cell membrane (12, 13). However, actin structures connected with the actin cortex appear to be key elements for organelle positioning in plant cells (14, 15) and nuclear positioning in oocytes (14, 16). Moreover, nuclear actin dynamics is involved in the movement of chromosomal foci in large cells like oocytes (17). A recent study shows even that such networks can prevent the condensation of nuclear droplets in large cells (18). How could these actin networks be connected to the cortex and can we envision that they could emanate from the actin cortex are the questions we address here.

How this cortical actin network is nucleated at the membrane is still a debate (19): whereas fluorescence techniques did not allow to detect the presence of the Arp2/3 complex and formins as nucleating agent of the actin network at the membrane (20), the branched structure that is observed under the plasma membrane hints for a contribution of Arp2/3 (12). Therefore, it is important to understand how networks produced by the Arp2/3 complex branching mechanism can impact cell mechanics and behavior. Such a branched and entangled actin network can be reproduced at the surface of beads covered with an activator of the Arp2/3 complex (11). The thickness of such an actin network was detected by epifluorescent microscopy and defined as the distance of the bead surface from the half-maximum intensity position along a radial profile. However, in these experiments, the drop of fluorescence away from the bead is not abrupt as shown in Fig.1A,B (11). This is what we explore here, by characterizing the mechanical and structural organization of this actin network further away from the zone detected by fluorescence. Our experimental system, based on the high force sensitivity of optical tweezers (see Fig.1C), allows to detect a mechanically relevant actin network that is inaccessible to direct visualization. This actin network emanates from the epifluorescence-visible part, which represents only a tenth of the full network size, and opposes resistance to indentation, thus revealing its important mechanical role.

The originality of our work is that we show that the Arp2/3 complex can give rise to a mechanically resistant actin cloud that spans over distances bigger than the dense and branched network close to the Arp2/3 activation. We characterize its mechanical parameters and show that this actin cloud allows sustaining forces able to displace objects on a cellular length-scale. Our findings suggest that even few filaments that may emanate from the actin cortex can lead to sufficient resistance and can generate forces that may explain the role of actin in organelle positioning within the cell. Similar filaments have been recently described to emanate from an nuclear actin cortex in starfish oocytes (21).

2 Materials and Methods

Proteins

Products are obtained from Sigma-Aldrich (St. Louis, MO) unless stated otherwise. Actin and the Arp2/3 complex are purchased from Cytoskeleton (Denver, US), and used without further purification. Fluorescent Alexa-488 actin is obtained from Molecular Probes (Eugene, OR). Capping protein (CP), profilin and pVCA are purified as previously described in (5, 22). Monomeric actin containing 10% molar of labeled Alexa-488 actin in G-Buffer (2mM Tris, 0.2 mM CaCl₂, 0.2 mM DTT at pH 8.0) at a concentration of 40 μM is obtained by keeping the solution one night on ice at 4°C before experiments.

Bead coating

Carboxylated polystyrene beads (Polysciences, Philadelphia, PA) of 4.34 ± 0.239 μm (Standard deviation) diameter were used from for actin and probe-beads.

Probe-beads: polystyrene beads are incubated for 20 min at 20°C under agitation with 10 mg/ml BSA at room temperature for 30 minutes in the working buffer (pH 7.4, 10 mM Hepes, 100 mM KCl, 1 mM MgCl₂, 0.1 mM CaCl₂, 1.8 mM ATP and 1 mg/ml BSA) and stored a few days at 4°C.

Actin-beads: polystyrene beads are first incubated for 20 min at 20°C under agitation with 2 μM pVCA and stored in working buffer (as above) for the day. Then they are placed in the polymerization mix, which is a solution of 4 μM G-actin, 12 μM profilin, 25 nM of Arp2/3 complex and various concentration of CP (0 to 50 nM) in the working buffer. 15 μL of this mix is sealed between coverslips.

Experimental procedure and data analysis

For the bead approach experiments, the pVCA coated beads which will later polymerize actin, are mixed with BSA-passivated probe-beads. Polymerization of actin on the beads is triggered by adding the bead mixture to the polymerization mix. Approximately 15 μL of the mix is sealed between two coverslips and observed in an inverse microscope (Olympus, IX71) using a 60 × water immersion objective (NA=1.2). Optical tweezers are used to trap and manipulate the beads in three dimensions by the gradient forces of a focused infrared fiber laser ($\lambda = 1064\text{ nm}$, YLP-1-1064, IPG, Germany). XY position and trapping forces are controlled by acousto optical deflectors (AODs, AA-Optoelectronics, France). Multiple traps are realized by time-sharing where the laser is switched within ≈ 6 μs between two positions, while resting 20 μs on each position. Position and force applied on each bead are measured using a quadrant photodiode (QPD) positioned in the back focal plane of the condenser (Fig.1). The trap stiffness is calibrated using the power spectral density (PSD) of trapped beads (23), and determined to be 34 pN/μm with the laser power of 119 mW as used during all experiments. The signal from the QPD is recorded with a

sampling rate of 500 kHz using a commercial data acquisition card (NI PCIe-6363, National Instruments, Austin, Texas), and processed using Labview (National Instruments) and Matlab (Mathworks, Natick, MA). Data acquisition and trap positioning are synchronized to recover the individual data for each bead. The signal from the QPD is converted to both the force exerted by the trap on the bead, and the bead position in the trap thanks to previous calibration.

To measure the viscoelastic properties we perform a force-indentation experiment. An actin and a probe-bead are selected, trapped and checked for compromising adhesion to the upper or lower coverslip. The presence of the actin network is confirmed using fluorescence microscopy (200W mercury lamp, Osram, Munich, Germany). All measurements are made on the dynamically polymerizing system, before symmetry breaking of the actin network.

To avoid too strong forces on the beads, which could push them out of the trap, single approach/retraction cycle were done while decreasing the minimal approach distance stepwise by 0.2 to 0.5 μm until the maximum force reached 8 to 10 pN. In these conditions the experimental protocol was stable and multiple consecutive approach experiments were done.

For the approach phase, the 3 fit parameters α , β and δ are estimated using a Levenberg-Marquardt algorithm as provided by Matlab. To facilitate stability in the fit algorithms, distances are expressed in μm and forces in pN.

Phenomenological fit of retraction curve

To fit the retracting part we introduce the function $A(d) = R\beta(d_c)^\alpha$ with $R : 0 \leq R \leq 1$, which corresponds to the elastic part of the actin-cloud, and is hence the discussed forces-distance curve Eq.2 scaled with the relaxation R as described in the main text (Fig.S4, dashed line, and Eq.9). $A(d)$ is fully determined form the approach and the relaxation data. For the plot in the retraction phase, we use the difference between the actual data and the expected elastic forces $A(d)$ to estimate the force that results from the actin cloud that has closed behind the bead. This is attributed for by a second powerlaw function $B(d) = -Z(d_c)^w$ (Fig.S4, red) which is fitted to the difference between the measured force during the retraction and $A(d)$ for the long distance (after force minimum is the retraction phase was reached).

To determine the curve plotted in Fig.4, we smoothly converge from $A(d)$ to $B(d)$ by using a the smoothing function $S(x) = \int_{\mathbb{R}} (1 - (x - t)^2) \times L(t)dt$ that corresponds to a convolution between the projected bead area and a linear ramp function L that is 0 for $t \leq 0$ and 1 for $t \geq 1$. The final model then reads:

$$F(d) = A(d) \times (1 - S(d)) + (A(d) + B(d)) \times S(d) \quad (1)$$

3 Results

Bead system

Polystyrene beads of 4.3 μm diameter are first coated with a nucleation promoting factor, pVCA, which is the VCA domain of N-WASP with the addition of a proline rich region (24). Beads coated with pVCA are then placed in the mix of purified proteins, containing 25 nM of the Arp2/3 complex, 4 μM actin, 12 μM profilin and various amounts of capping protein (CP). In these conditions, a network of actin filaments grows from the bead surface. In the following, these beads, once covered with their actin network, are called "actin-beads" (Fig.2A).

In the absence of CP actin filaments grow with their barbed ends away from the surface (24). The presence of CP limits the filament growth. In a spherical geometry of a bead, a stress builds up since new branches are formed at the surface of the bead, and symmetry breaks in a concentration range of CP from 15 to 35 nM (11, 25).

The choice of a bead diameter of 4.3 μm allows us to do measurements on an actin network that is homogeneous in the angular direction, hence before the appearance of heterogeneities which are a signature of symmetry breaking (Fig.1B). A characteristic symmetry-breaking time for those beads is indeed about 20 minutes (11). As our experiments are performed before symmetry-breaking, both the actin gel and the actin cloud are still growing, and no steady state has been reached. However, as previously investigated (11), the growth velocity is with about 0.1 $\mu\text{m}/\text{min}$ small, so that during the 2 minutes required for the approach experiments the actin-gel grows of about 200nm, negligible compared to the typical distances in the order of 10 μm studied in this work.

Experiment description

Using optical tweezers, the probe-bead is moved toward an actin-bead and the forces on each bead are monitored as shown in Fig.1C. Time shared optical tweezers are used to trap the probe- and actin- beads, see Materials and Methods for more details (26). The displacement of each bead from its trap center is recorded using a quadrant photodiode (QPD) as shown in

Fig.1C. For further analysis we exclusively use forces determined from the stationary trap that holds the actin bead, to avoid systematic errors that might arise from the trap displacement. The absence of interaction between bead and glass cover slip is probed before each experiment by moving it in all directions using the tweezers. A typical experiment starts as follows: the distance between traps is at least set to 20 μm , and beads are positioned at the trap centers. Then, the probe trap approaches the actin-bead at a constant velocity of $v=10 \mu\text{m/s}$ ($0 \leq t \leq t_1$, Fig.2A, left part). During this process, as soon as the actin-bead feels the force exerted by the probe-bead, it becomes off-centered in its trap (Fig.2A, $t \lesssim t_1$). The approach phase is followed by two other phases, a relaxation phase ($t_1 \leq t \leq t_2$; Fig.2A, middle part, white background), and a retraction phase ($t_2 \leq t \leq t_3$, Fig.2A, right part, light yellow background). During the retraction phase, the probe bead returns to its initial position with the same absolute velocity of 10 $\mu\text{m/s}$ as in the approach phase. The duration of the relaxation phase ($t_2 - t_1 = 3\text{s}$) is chosen to be long enough to allow relaxation to happen, and short enough for actin polymerization not to change the properties of the network. The time-dependent force on the actin-bead (Fig.2A) is converted into a force-distance curve as shown in Fig.2B,C where d is the distance between the surfaces of the actin-bead and the probe-bead. The force distance curve Fig.2B reads as follows : i) ($t \leq t_1$) the force between beads starts from an asymptotic zero value at long distance and increases as the distance decreases (green points), ii) ($t_1 \leq t \leq t_2$) the probe-bead stops and relaxation occurs. During the relaxation, the force decreases with a very little distance decrease (red points, up left in Fig.2B). iii) ($t_2 \leq t \leq t_3$) the force decreases, becomes negative, and eventually reaches asymptotically zero again when distance increases (blue points). Those curves are repeatable and show only small changes if multiple approach-retraction cycles are probed (see Fig.2C). Previous experiments suggest that for frequencies higher than 0.1 Hz, viscous relaxation becomes comparable to the elastic properties (27). To check the importance of stress relaxation during the approach phase we verify that the probe trap velocity did not affect the force-distance curves by performing experiments at variable velocities ranging from 5 to 30 $\mu\text{m/sec}$ (Fig.S1 in the Supporting Material). These experiments did not show any striking differences in the recorded measurements, and hence for the analysis of the approach phase we use an elastic model.

4 Experimental observations

Approach phase

The bead system provides a way to reconstruct actin cortices *in vitro*. Moreover, these reconstituted systems can be manipulated to investigate 3D mechanical properties of a biomimetic actin cortex in experimental conditions inaccessible to other microscopy techniques typically used to investigate single actin filament dynamics, like total internal reflection (TIRF). Optical tweezer and force measurements on the bead allow us to precisely probe for the actin network emanating from a bead in a 3D environment. To approximate the size of the actin cloud, we determine the distance d_0 (Tab.1, Fig.2B, dotted lines) where the forces on the probed bead become higher than the experimental noise of the force detection (2pN). The found values for d_0 remain large compared to the fluorescent actin gel thickness. Indeed, the probe bead already feels the presence of actin filaments at a distance from 13 μm to about 4 μm (Fig.1A,B; Tab. 1). This distance depends on CP concentration (Tab.1), but is always much larger than 1 μm , which has been established as an upper estimation of the actin network thickness e , previously measured as the distance of half-maximum fluorescence intensity (11) and Fig.1A.

As the bead distance decreases, the force gradually increases, until the trap stops at the minimal displacement distance. The force-distance data are fitted by a power law with fit parameters β , α and δ (Fig.2A,B).

$$F(d) = \beta \times (d - \delta)^\alpha \quad (2)$$

where we obtain a high fit quality measured by a median $R^2 = 0.97$. Since the power-law exponent, α , is found to be negative (Tab.1), δ corresponds to the offset distance between bead surfaces at which the force would diverge (vertical black line in Fig.2B).

We experimentally find a negative power law exponent close to -1 with a statistical distribution of $\langle \alpha \rangle = -1.10 \pm 0.38$ ($n=103$, mean \pm std) for all CP concentration probed (Fig.2D, inset).

This inverse relation hints for a far reaching network, or "actin cloud", which is mechanically evidenced here. In our experiments it is detectable over distances that are larger than the fluorescence estimated thickness of around 1 μm (Movie S1).

Due to the scale invariance of the power law, we can collapse all 103 experimental curves into a single master curve by normalizing the force with the point of maximal force (F_{max}) reached at t_1 , and the distance between bead surface at the minimal approach (d_{t_1} , Fig.2D). This rescaling procedure allows us to determine the power law exponent of all averaged data curves to be ($\alpha_{rs} = -1.06$) which confirms the -1 exponent.

Nonlinear elastic modulus

To determine the Young's modulus from the force distance curves, we use its definition as given by Hooke's law: $E = \sigma/u$, where $\sigma = F/(\pi R^2)$ is the stress on the projected bead surface, R the bead radius, $u = (d_c - x)/d_c$ the strain where we define $d_c = (d - \delta)$ and x as the the experimentally controlled bead position for the small deformations. Hence $du = -dx/d_c$ where the minus sign reflects the choice of the coordinate system for the deformation, which has to be consistent with the direction of the force to ensure a positive elastic modulus. Here we study the situation in which a predeformation of the gel of d_c is applied, and then we apply a stress σ and strain u when displacing the probe-bead by a small distance. In such a situation, the global Young's modulus as function of d_c reads $E(d_c) = (d\sigma/du)|_{d_c}$. The deformation-dependent Young's modulus can hence be expressed as the derivative of the force with respect to the deformation at the distance d_c to yield:

$$E(d_c) = -\frac{d_c}{\pi R^2} \times \left(\frac{dF}{dx} \right) \Big|_{x=d_c} \quad (3)$$

$$= E_0 \times d_c^\alpha \quad (4)$$

where $E_0 = -\alpha\beta/(\pi R^2)$. In this expression we use the fit function of Eq.2 to calculate the derivative. Interestingly, using the strain at a position d_c gives rise to the same power-law between the nonlinear Young's modulus and the measured force. It should be noted that experimentally we can only access the average mechanical properties between the probe- and the actin-bead. Hence, all reported values present mean values of the material between these two beads. The discussed model describes the reported mean values, and assumes an effectively averaged Young's modulus. Here $E(d_c)$ is then this global Young's modulus that measures the material properties of the actin cloud that is confined between the two beads. These values (Tab.1) are 3 orders of magnitudes smaller than the elasticity of the actin gel generated from an Arp2/3 activated bead (known to be $\approx 1\text{kPa}$ (28)). This large difference in rigidity might explain why the actin cloud was not observed in previous mechanical measurements such as micropipette, micro-needle deformation or AFM indentation that were sensitive to large forces in the nN regime. However, such small moduli are commonly found in loosely entangled actin networks (27). It also shows that the actin cloud is of a fundamentally different network type that results in such a drastic change of mechanical properties as compared to the dense actin gel found at the bead surface. Optical tweezers are the optimal measurement technique to determine such small elastic parameters.

Relaxation phase

In the 3-second resting phase, we observe that the beads move toward the center of their traps, corresponding to a force relaxation (Fig.2A, central part) during which the beads get closer to each other (Fig.2A, $t = t_1$ and $t = t_2$). The force-drop during the relaxation is typically of 20% (see Fig.S3).

Retraction phase

We observe a rapid decrease of the force towards negative forces leading to two different behaviors that may add up. First, a general tendency is that the rapid drop of the force is followed by a slow force increase through an inflection point (Fig.2B lower curve). Second, and only in $\approx 25\%$ of the experiments, we find evidence of rapid detachments that are identified by a sawtooth shape of the force-distance curve (Fig.S2).

Irreversibility

An important finding is that the approach phase does not superimpose with the relaxation and retraction phases, which indicates dissipation of energy during a cycle of approach and retraction. Apart from the relaxation phase, a contribution to this dissipation is the negative force that is reminiscent of the sticky behavior similar to AFM indentation/retraction experiments.

Influence of capping protein concentration

Actin filament length is controlled by the amount of CP in the protein mix (24). To check the influence of the CP concentration on the actin cloud we analyze experiments at 0, 10, 30 and 50 nM CP. As shown in Fig.3 and Tab.1, the value of the power law exponent α does not change significantly with CP concentration. In contrast, we find that the distance offset δ changes under variable conditions and the parameter β decreases five fold when CP concentration increases from 0 to 50nM.

5 Discussion

Approach Phase: Interpretation of the power-law

To further investigate this power-law exponent (of $\simeq -1$), we model the deformation of the actin cloud by the established theory of semiflexible, entangled polymer networks (29–31). In the approach phase, we focus on the elastic properties quantified by the deformation-dependent Young's modulus $E(d_c)$ and neglect any viscous term given that the force in this phase does not depend significantly on the approach speed. The Young's modulus E of semiflexible filaments is well studied and can be expressed as a function of filament contour length density ρ and the entanglement length L_e as $E = 2.(1+\nu).7.k_B T \rho / (5L_e)$ (31). The prefactor is model-dependent and includes the transition from shear to Young's modulus using the Poisson ratio. Previous studies have investigated the non-linear stiffening of actin gels for large deformations comparable to the presented approach protocol (32). For actin concentrations similar to the concentration used in our study, these previous experiments show that a linear description holds, and hence the proposed model should correctly describe the mechanics of the polymer network.

The entanglement length itself can be expressed as a function of density ρ and persistence length L_p as $L_e \approx L_p^{1/5} \rho^{-2/5}$ (31). For the general case of a compressible material, the only variable that might change under the strong deformation is $\rho \rightarrow \rho(d_c)$. Hence, we can express the Young's modulus as a function of density ρ that depends on the compression of the network, therefore noted $\rho(d_c)$:

$$E(d_c) = \frac{(1+\nu).14.k_B T}{5L_p^{1/5}} \times (\rho(d_c))^{7/5} \quad (5)$$

Using the experimentally found power-law, Eq.5 allows to infer a relation for the density $\rho \propto d_c^{5/7 \times \alpha}$. Using the scaling arguments that at the distance d_0 , which corresponds to the undeformed actin cloud, the density is ρ_0 , we can directly express $\rho(d_c) = \rho_0(d_c/d_0)^{5/7 \times \alpha}$. These changes in the density can be also used to estimate the Poisson's ratio of the actin cloud, which connects the distance dependent density and the deformation by $\rho(d_c) = \rho_0(d_c/d_0)^{2\nu-1}$. Hence, we infer for the Poisson's ratio: $\nu = 1/2(1 + 5/7\alpha)$. Due to the definition of ρ which corresponds to the filament contour length per unit volume, we can determine the average mesh-size ξ_0 of the undeformed network by $\rho_0 = 1/\xi_0^3$. Combining these expressions then leads to

$$E(d_c) = \frac{(1+\nu).14.k_B T}{5L_p^{1/5}\xi_0^{14/5} d_0^\alpha} \times d_c^\alpha. \quad (6)$$

$$= E'_0 \times d_c^\alpha \quad (7)$$

To determine the expected mesh-size, we can set E_0 as found in Eq.3 equal to Eq.6:

$$\xi_0 = \left(- \frac{(2 - \frac{5}{7}\alpha).k_B T \pi R^2}{5\alpha\beta L_p^{\frac{1}{5}} d_0^\alpha} \right)^{\frac{5}{14}} \quad (8)$$

The resulting values of ξ_0 are listed in Tab.1, which are in the order of 0.3-0.4 μm . Such average values are consistent with other rheology experiments and have been described previously (31). Unlike previous studies of bulk actin networks that find a bulk Poisson ratio of 0.5 for actin gels formed at actin concentration of 21.5 μM (27), we find that the actin cloud can almost collapse under the applied forces, with approximated Poisson's ratios of 0.1 to 0.2. The difference may be explained by the lower actin concentration (4 μM) or by the geometrical arrangement of the actin network used in our experiments.

Approach Phase: Interpretation of distance offset δ

The third fit parameter in the power-law of Eq.2 is δ , which marks the position at which the power-law diverges. As the actin network around the bead is known to have an elastic modulus of ≈ 1 kPa (28, 33) the forces provided by our optical tweezers (max. 30 pN) are unable to deform this network. This suggests that in our measurements, the actin network close to the bead acts as a rigid object, which in turn suggests to interpret δ as the thickness of the actin network defined by epifluorescence (Fig.1B). As shown in Tab.1, δ decreases with increasing CP concentration. The determined values of $\approx 1 - 2 \mu\text{m}$ are consistent with previous measurements of the actin thickness e by fluorescence microscopy (11). This general dependence is not found in the absence CP, where the system is in a completely different regime because the filament growth away from the

bead is only limited by the amount of G-actin. Indeed, in the absence of capping protein filaments grow mainly away from the bead (11), leading to the absence of symmetry breaking. Therefore, without CP it remains difficult to define an actin shell thickness, as the increasing number of filaments growing away from the bead surface changes the overall structure of the gel, which does not allow to interpret δ .

Relaxation phase

The apparent mechanical effect of the actin cloud shows a dominant elastic component, while the force-distance plot gives a significant dissipation marked by the hysteresis. The repeatable approach-retraction excludes a significant plastic deformation, like breakage of the filaments or rupture of the sparse actin network. To understand the relaxation and the retraction behavior, we further follow the approach inspired by Morse (31), and investigate the proposed relaxation function $\chi(t)$, which determines the time dependence of $E(t) = E \times \chi(t)$:

$$\chi(t) = \sum_{n,odd} \frac{8}{n^2 \pi^2} \exp(-n^2 \pi^2 t / \tau_{rep}) \quad (9)$$

where $\tau_{rep} = \frac{l_f^2}{D_{rep}}$. In this model, the relaxation is a sum of exponential decays with well defined decay times for a reptation dominated relaxation. The unknown parameters are the diffusion constant for filament reptation D_{rep} and the filament length l_f , that are combined in the single fit parameter (τ_{rep}). We limit the fit to the first 40 terms of the sum in eq. 9, since the higher modes relax faster than can be observed with the experimental resolution. Such a sum of exponentials remains consistent with the common finding of a power-law behavior of the shear modulus in *in vitro* actin networks (27) and the relaxation behavior found in cells (34).

To check if the resulting fit parameter gives realistic values, we estimate $D_{rep} = k_b T / (\gamma l_f)$, where $\gamma \approx \frac{2\pi\eta_s}{\ln(\xi/d_f)}$ is the friction coefficient per unit length that depends on the solvent viscosity η_s , the mesh-size ξ , which has been estimated in Eq.8, and the filament diameter d_f . We can also use $\eta_s = 10^{-3}$ Pa·s, $d_f = 7$ nm and the mesh-size in the order of 400nm. Knowing the value of the relaxation parameter τ_{rep} given by the fit, we can estimate the filament length l_f from the two previous expressions in the different CP conditions and determine values in the order of $\approx 3 - 8$ μm (see Tab.1). Interestingly these values are very close to the size of the actin cloud d_0 which we determine independently by the first measurable mechanical signature of the cloud.

Hence, the found values of the fit are directly consistent with the predictions of a decrease of filament length when CP concentration is increased (24). The model of entangled actin filaments can therefore explain both the approach and the relaxation part.

Retraction phase

During the retraction phase we observe two types of events: i) sticking events (Fig.S2), where the force becomes abruptly negative until a threshold value is reached and then quickly relaxes, ii) a continuous decrease of the force that becomes negative after an average retraction of 3.5 μm and returns to zero at large distances. While the sticking can be explained by interaction between the probe-bead and the actin, the second case can be modeled phenomenologically assuming a partial closure of the actin network behind the bead as sketched in Fig.4 (right part of the graph). The details of the fit function are given in the methods section. Briefly, we assume a transition between the elastic force generated by the actin cloud between the two beads and an additional viscoelastic contribution that accounts for the partially closed actin cloud behind the bead during the resting phase.

Biological relevance of the actin cloud emanating from cortical actin

The actin cytoskeleton is involved in many cellular events spanning from setting cell shape to the regulation of gene expression. Further experiments hint for a possible direct mechanical transmission of forces from the outside towards the nucleus via the actin cytoskeleton. Especially since the actin cytoskeleton is already known to be important in the positioning of the nucleus, and hence presents a force transmission role in cells, it can be speculated that such force transmission may directly or indirectly trigger changes in gene expression. The mechanical link from extracellular environment to the nucleus is established by actin bundles that connect integrins and proteins of the nuclear envelope (35). However, to explain the role of actin in organelle and nucleus positioning (14, 15), not only such actin bundles should be taken into account. Our experiments highlight that an actin network emanating from the actin cortex can sustain forces in the range of 10 pN. A force of 10pN

is sufficient for dragging organelles inside cells. Moreover, the capacity of Arp2/3 branched networks to reorganize in para structure, as well as nucleators as formins (6), can allow a constantly polymerizing cortical network to push throughout the inside of a cell and exert sufficient forces to move organelles and chromosomes (17). Indeed, networks observed inside cells are generally anchored to cortical actin network (14, 36–38). Since we show that mechanical parameters of filaments far away from nucleation sites may sustain forces up to 15 pN, we anticipate that unbranched actin filaments connected to cortical actin may provide as a mechanical scaffold for a general mechanism of positioning and long range interplay between organelles in oocytes (39, 40) or even in large scale systems like drosophila development (16). Recently, the role of an actin network with similar properties as the here described actin cloud had been identified in large cells such as *Xenopus* oocytes, which directly shows the mechanical relevance of the actin cloud in intracellular organization (18).

6 Conclusion

The transition from a dense actin network, which is polymerized off an Arp2/3 complex activated surface, to the bulk medium is not abrupt and we identify and characterize a large transition zone, the actin cloud. These actin clouds are very soft compared to the dense actin network that is formed at the location of the Arp2/3 complex activation. Our *in vitro* experiments show that this actin cloud also gives a mechanical support with a far reaching mechanical effect that scales inverse to the distance, a property that can be explained by polymer theory. The predicted viscoelastic properties and extracted material properties are in good agreement with our measurements. The actin cloud can not be ignored in the context of cellular events, like nucleus positioning and oocyte maturation, that have been shown to happen on force scales of several pN (18). Moreover, we enlighten a general mechanical feature of sparse actin networks that can serve as a useful mechanism to displace and organize the different cellular compartments.

Acknowledgments

The authors would like to thank Klaus Kroy, Claus Heussinger and Herv Isambert for helpful discussion. K.C. was supported by ARC, M.B. and J.L. were supported by Axa Research Fund. This work was also founded by the federation "dynamique des systemes complexes" of the University Paris 6 and supported by French Agence Nationale de la Recherche (ANR) Grants ANR-11-JSV5-0002, ANR-09-BLAN-0283 and ANR 12BSV5001401, Fondation pour la Recherche Médicale Grant DEQ20120323737

References

- [1] Fletcher, D. A., and R. D. Mullins, 2010. Cell mechanics and the cytoskeleton. *Nature* 463:485–492. <http://www.nature.com/gate1.inist.fr/nature/journal/v463/n7280/full/nature08908.html>.
- [2] Lecuit, T., P.-F. Lenne, and E. Munro, 2011. Force Generation, Transmission, and Integration during Cell and Tissue Morphogenesis. *Annual Review of Cell and Developmental Biology* 27:157–184. <http://www.annualreviews.org/doi/abs/10.1146/annurev-cellbio-100109-104027>.
- [3] Betz, T., D. Koch, Y.-B. Lu, K. Franze, and J. A. Ks, 2011. Growth cones as soft and weak force generators. *Proceedings of the National Academy of Sciences* 108:13420–13425. <http://www.pnas.org/content/108/33/13420.abstract>.
- [4] Salbreux, G., G. Charras, and E. Paluch, 2012. Actin cortex mechanics and cellular morphogenesis. *Trends in Cell Biology* 22:536–545. <http://www.sciencedirect.com/science/article/pii/S0962892412001110>.
- [5] Bernheim-Grosbawsser, A., S. Wiesner, R. M. Golsteyn, M.-F. Carlier, and C. Sykes, 2002. The dynamics of actin-based motility depend on surface parameters. *Nature* 417:308311. <http://dx.doi.org/10.1038/417308a>.
- [6] Reymann, A.-C., J.-L. Martiel, T. Cambier, L. Blanchoin, R. Boujemaa-Paterski, and M. Thry, 2010. Nucleation geometry governs ordered actin networks structures. *Nature Materials* 9:827–832. <http://www.nature.com/gate1.inist.fr/nmat/journal/v9/n10/full/nmat2855.html>.
- [7] Pontani, L.-L., J. van der Gucht, G. Salbreux, J. Heuvingh, J.-F. Joanny, and C. Sykes, 2009. Reconstitution of an Actin Cortex Inside a Liposome. *Biophysical Journal* 96:192198.
- [8] Carvalho, K., J. Lemire, F. Faqir, J. Manzi, L. Blanchoin, J. Plastino, T. Betz, and C. Sykes, 2013. Actin polymerization or myosin contraction: two ways to build up cortical tension for symmetry breaking. *Philosophical Transactions of the Royal Society B: Biological Sciences* 368:20130005.
- [9] Strehle, D., J. Schnau, C. Heussinger, J. Alvarado, M. Bathe, J. Ks, and B. Gentry, 2011. Transiently crosslinked F-actin bundles. *European Biophysics Journal* 40:93–101. <http://link.springer.com/article/10.1007/s00249-010-0621-z>.
- [10] Thoresen, T., M. Lenz, and M. Gardel, 2013. Thick Filament Length and Isoform Composition Determine Self-Organized Contractile Units in Actomyosin Bundles. *Biophysical Journal* 104:655–665. <http://www.sciencedirect.com/science/article/pii/S0006349512051764>.

- [11] Kawska, A., K. Carvalho, J. Manzi, R. Boujemaa-Paterski, L. Blanchoin, J.-L. Martiel, and C. Sykes, 2012. How actin network dynamics control the onset of actin-based motility. *Proceedings of the National Academy of Sciences* <http://www.pnas.org/content/early/2012/08/16/1117096109>.
- [12] Morone, N., T. Fujiwara, K. Murase, R. S. Kasai, H. Ike, S. Yuasa, J. Usukura, and A. Kusumi, 2006. Three-dimensional reconstruction of the membrane skeleton at the plasma membrane interface by electron tomography. *The Journal of Cell Biology* 174:851–862. <http://jcb.rupress.org/content/174/6/851>.
- [13] Clark, A., K. Dierkes, and E. Paluch, 2013. Monitoring Actin Cortex Thickness in Live Cells. *Biophysical Journal* 105:570–580. <http://www.sciencedirect.com/science/article/pii/S0006349513006450>.
- [14] Iwabuchi, K., R. Minamino, and S. Takagi, 2010. Actin Reorganization Underlies Phototropin-Dependent Positioning of Nuclei in Arabidopsis Leaf Cells. *Plant Physiology* 152:1309–1319. <http://www.plantphysiol.org/content/152/3/1309>.
- [15] Sturmer, K., O. Baumann, and B. Walz, 1995. Actin-dependent light-induced translocation of mitochondria and ER cisternae in the photoreceptor cells of the locust *Schistocerca gregaria*. *Journal of Cell Science* 108:2273–2283. <http://jcs.biologists.org/content/108/6/2273>.
- [16] Huelsmann, S., J. Ylne, and N. H. Brown, 2013. Filopodia-like Actin Cables Position Nuclei in Association with Perinuclear Actin in *Drosophila* Nurse Cells. *Developmental Cell* 26:604–615. [http://www.cell.com/developmental-cell/abstract/S1534-5807\(13\)00483-8](http://www.cell.com/developmental-cell/abstract/S1534-5807(13)00483-8).
- [17] Kumaran, R. I., R. Thakar, and D. L. Spector, 2008. Chromatin Dynamics and Gene Positioning. *Cell* 132:929–934. [http://www.cell.com/abstract/S0092-8674\(08\)00334-6](http://www.cell.com/abstract/S0092-8674(08)00334-6).
- [18] Feric, M., and C. P. Brangwynne, 2013. A nuclear F-actin scaffold stabilizes ribonucleoprotein droplets against gravity in large cells. *Nature Cell Biology* 15:1253–1259. <http://www.nature.com.gate1.inist.fr/ncb/journal/v15/n10/full/ncb2830.html>.
- [19] Smith, B. A., S. B. Padrick, L. K. Doolittle, K. Daugherty-Clarke, I. R. Corral, M.-Q. Xu, B. L. Goode, M. K. Rosen, and J. Gelles, 2013. Three-color single molecule imaging shows WASP detachment from Arp2/3 complex triggers actin filament branch formation. *eLife* 2. <http://elife.elifesciences.org/content/2/e01008>.
- [20] Charras, G. T., C.-K. Hu, M. Coughlin, and T. J. Mitchison, 2006. Reassembly of contractile actin cortex in cell blebs. *The Journal of Cell Biology* 175:477490.
- [21] Mori, M., K. Somogyi, H. Kondo, N. Monnier, H. J. Falk, P. Machado, M. Bathe, F. Ndlec, and P. Lnrt, 2014. An arp2/3 nucleated f-actin shell fragments nuclear membranes at nuclear envelope breakdown in starfish oocytes. *Current biology: CB* 24:1421–1428.
- [22] Paluch, E., J. van der Gucht, and C. Sykes, 2006. Cracking up: symmetry breaking in cellular systems. *The Journal of Cell Biology* 175:687692.
- [23] Gittes, F., and C. F. Schmidt, 1998. Interference model for back-focal-plane displacement detection in optical tweezers. *Optics Letters* 23:7–9. <http://ol.osa.org/abstract.cfm?URI=ol-23-1-7>.
- [24] Achard, V., J.-L. Martiel, A. Michelot, C. Gurin, A.-C. Reymann, L. Blanchoin, and R. Boujemaa-Paterski, 2010. A Primer-Based Mechanism Underlies Branched Actin Filament Network Formation and Motility. *Current Biology* 20:423428. [http://www.cell.com/current-biology/abstract/S0960-9822\(10\)00052-7](http://www.cell.com/current-biology/abstract/S0960-9822(10)00052-7).
- [25] Sykes, C., and J. Plastino, 2010. Cell biology: actin filaments up against a wall. *Nature* 464:365–366.
- [26] Lemire, J., K. Guevorkian, C. Campillo, C. Sykes, and T. Betz, 2013. -Hemolysin membrane pore density measured on liposomes. *Soft Matter* 9:3181–3187.
- [27] Gardel, M. L., M. T. Valentine, J. C. Crocker, A. R. Bausch, and D. A. Weitz, 2003. Microrheology of Entangled F-Actin Solutions. *Physical Review Letters* 91:158302. <http://link.aps.org/doi/10.1103/PhysRevLett.91.158302>.
- [28] Marcy, Y., J. Prost, M.-F. Carlier, and C. Sykes, 2004. Forces generated during actin-based propulsion: A direct measurement by micromanipulation. *Proceedings of the National Academy of Sciences of the United States of America* 101:5992–5997. <http://www.pnas.org/content/101/16/5992.abstract>.
- [29] Isambert, H., and A. C. Maggs, 1996. Dynamics and Rheology of Actin Solutions. *Macromolecules* 29:10361040. <http://dx.doi.org/10.1021/ma946418x>.
- [30] MacKintosh, F. C., J. Kas, and P. A. Janmey, 1995. Elasticity of semiflexible biopolymer networks. *Physical Review Letters* 75:4425–4428.
- [31] Morse, D. C., 1998. Viscoelasticity of Concentrated Isotropic Solutions of Semiflexible Polymers. 2. Linear Response. *Macromolecules* 31:7044–7067. <http://dx.doi.org/10.1021/ma980304u>.
- [32] Semmrich, C., R. J. Larsen, and A. R. Bausch, 2008. Nonlinear mechanics of entangled F-actin solutions. *Soft Matter* 4:1675.
- [33] Pujol, T., O. d. Roure, M. Fermigier, and J. Heusinger, 2012. Impact of branching on the elasticity of actin networks. *Proceedings of the National Academy of Sciences* 109:10364–10369. <http://www.pnas.org/content/109/26/10364>.
- [34] Fabry, B., G. N. Maksym, J. P. Butler, M. Glogauer, D. Navajas, and J. J. Fredberg, 2001. Scaling the microrheology of living cells. *Phys Rev Lett* 87:148102.
- [35] Jaalouk, D. E., and J. Lammerding, 2009. Mechanotransduction gone awry. *Nature Reviews Molecular Cell Biology* 10:63–73. <http://www.nature.com.gate1.inist.fr/nrm/journal/v10/n1/full/nrm2597.html>.
- [36] Schuh, M., and J. Ellenberg, 2008. A New Model for Asymmetric Spindle Positioning in Mouse Oocytes. *Current Biology* 18:1986–1992. <http://www.sciencedirect.com/science/article/pii/S0960982208015029>.
- [37] Chaigne, A., C. Campillo, N. S. Gov, R. Voituriez, J. Azoury, C. Umaa-Diaz, M. Almonacid, I. Queguiner, P. Nassoy, C. Sykes, M.-H.

- Verlhac, and M.-E. Terret, 2013. A soft cortex is essential for asymmetric spindle positioning in mouse oocytes. *Nature Cell Biology* 15:958–966. <http://www.nature.com/ncb/journal/v15/n8/full/ncb2799.html>.
- [38] Lnr, P., C. P. Bacher, N. Daigle, A. R. Hand, R. Eils, M. Terasaki, and J. Ellenberg, 2005. A contractile nuclear actin network drives chromosome congression in oocytes. *Nature* 436:812–818. <http://www.nature.com/nature/journal/v436/n7052/full/nature03810.html>.
- [39] Li, H., F. Guo, B. Rubinstein, and R. Li, 2008. Actin-driven chromosomal motility leads to symmetry breaking in mammalian meiotic oocytes. *Nature cell biology* 10:1301–1308.
- [40] Azoury, J., K. W. Lee, V. Georget, P. Hikal, and M.-H. Verlhac, 2011. Symmetry breaking in mouse oocytes requires transient F-actin meshwork destabilization. *Development* 138:2903–2908. <http://dev.biologists.org/content/138/14/2903>.

Table 1: Listing of the fit parameters found for different CP concentrations. N represents the number of data-points for each CP concentration. Exponent of the model α , prefactor in the model β , distance offset δ and $E_{1\mu m}$ the elastic modulus at a distance of 1 μm . ξ_0 is the average mesh size as calculated for an homogeneous network. ν is the Poisson's ratio. d_0 the distance at which the average force is over 2pN. The viscoelastic model used also allows to predict the average filament length l_f from the relaxation behaviors. The median R^2 values are given to quantify the fit quality for the different conditions.

CP [nM]	0	10	30	50
N	13	29	31	30
α	-1.2±0.1	-0.9±0.2	-1.1±0.2	-1.2±0.5
$\beta[pN\mu m]$	24.3±10.7	18.7±8.1	16.9±16.0	6.1±5.9
$\delta[\mu m]$	0.5±0.6	2.2±0.7	1.2±0.6	1.0±0.5
ν	0.1±0.05	0.2±0.06	0.1±0.07	0.1±0.2
$E_{1\mu m}[Pa]$	1.93 ± 1.05	1.24 ± 0.78	1.39 ± 1.61	0.59 ± 0.76
$\xi_0[nm]$	310	397	350	376
$d_0[\mu m]$	8.6 ± 2.9	13.3 ± 2.4	6.5 ± 3.1	3.7 ± 6.3
$l_f[\mu m]$	10.8±2.2	9.1±5.5	2.5±0.5	3.1±3.8
median(R^2)	0.982	0.989	0.936	0.850

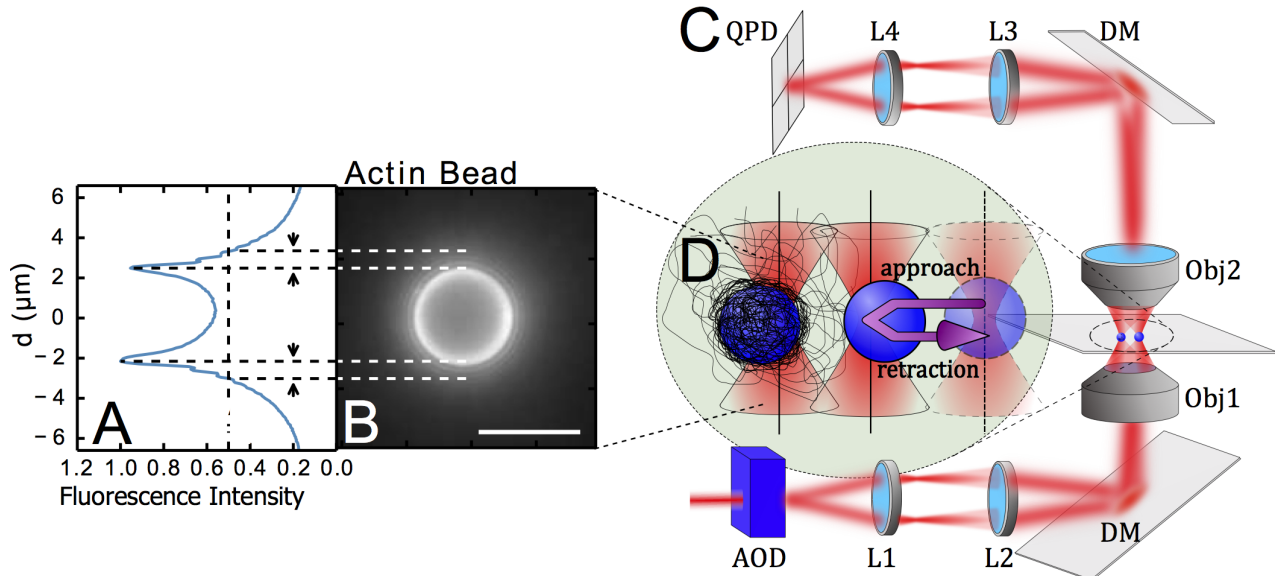


Figure 1: Sketch describing the experimental situation: **A)** Normalized intensity profile of the fluorescent actin cortex shown in B, taken along the bead diameter. Arrowheads represent gel thickness measured as the half maximal intensity of the epifluorescence signal. **B)** Fluorescence Image of a $4.3 \mu\text{m}$ actin-bead, 25 nM Arp2/3, 10 nM CP after 30 min. Bar is $5 \mu\text{m}$. **C)** To probe the mechanics of the actin cloud we use multiplexed optical tweezers generating 2 traps. A 1 W IR fiber laser (IPG Photonics, $\lambda=1064 \text{ nm}$) is steered by 2 acousto optical deflectors (AOD) and multiplexed by time-sharing. The resulting beams are imaged in the back focal plane of a water immersion objective (Obj1, 60X, NA=1.2), by a 2 fold magnification telescope (with focal of the L_x lenses being $f_{L1} = 10 \text{ cm}$, $f_{L2} = 20 \text{ cm}$). The light is coupled in the optical path of an Olympus IX71 microscope by a dichroic mirror (DM). After interaction with the beads, the light is collected by a water immersion objective (Obj2, 40X, NA=0.9) and the back focal plane of Obj2 is imaged onto a quadrant-photo-diode (QPD) via 2 lenses ($f_{L3} = 6 \text{ cm}$, $f_{L4} = 3 \text{ cm}$). **D)** The lasers trap the actin-bead (left) and the probe bead. During the experiments, the probe bead is approaching the actin-bead and moved from an initial position (light, right) to a final position at a velocity v , resting 3 s at the closest proximity (middle) and retracting back to the original position (movement indicated by the purple arrow). The displacement of the two beads from their respective trap center (marked by a straight line) is recorded by the QPD during the whole time. Optical forces are calculated using the calibrated trap stiffness.

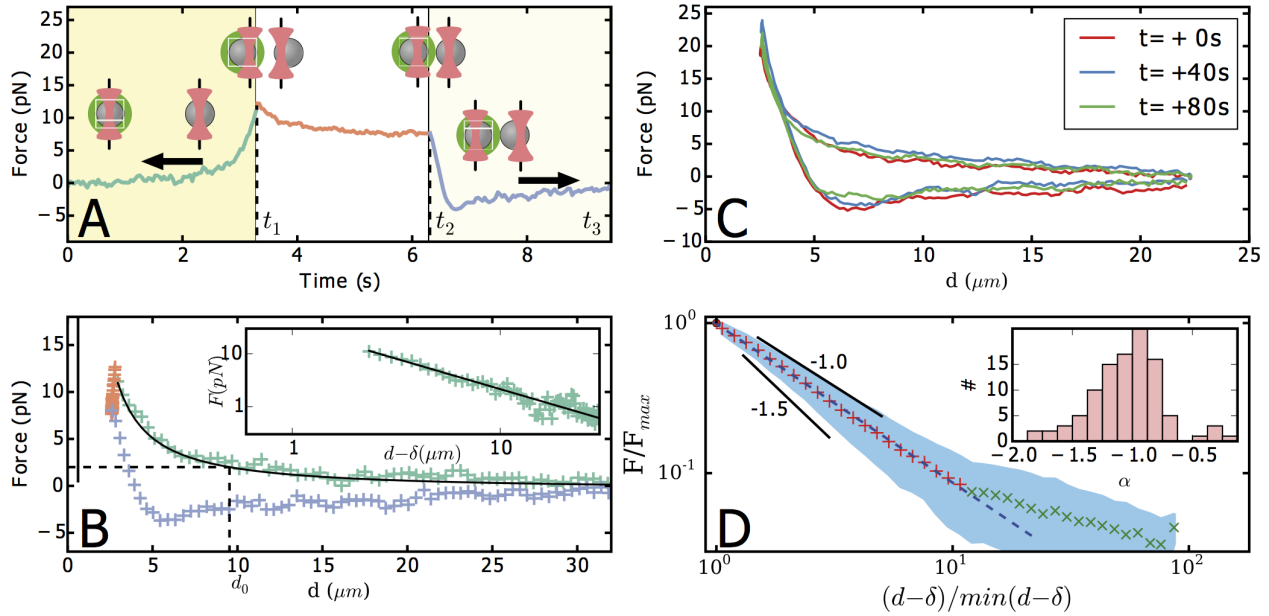


Figure 2: A) Force of an actin-bead as a function of time in the presence of 30 nM CP. t_1 and t_2 respectively correspond to the beginning of the relaxation and retraction phases. Here, the sample is measured 12 min after adding actin to bead mix. Color of the points marks the different phases of approach (green), relaxation (red) and retraction (blue). **B)** Force on an actin-bead as a function of the distance d between bead surfaces of the data presented in A. The zero force is fixed by the average of force at large distance. d_0 is the distance at which the mean force is higher than the standard deviation measured for the resting bead (before the approach). We use this distance d_0 as size of the actin cloud for the presented analysis. However, it should be noted that this measure may depend on the measurement method and the size of the probe beads. The color code used corresponds to panel A. The sample was measured 17 min after adding actin to the bead mix. The straight black line represents δ , the distance at which the force extrapolated by the fit would be infinite. Inset: Power-law fit of the approach (solid line) and log-log representation. Examples of graph A and B for different amount of capping protein are available in Fig. S5, S6, S7. **C)** Repeated approach-retraction experiments (3 out of 8 shown) give reproducible data. The example shown was acquired under 10nM CP concentration. **D)** Log-log representation of the rescaled experimental data. Red and green crosses (+, \times), correspond to mean values and the filled blue area corresponds to average plus/minus standard deviation for each averaged bin. Blue dashed line (---) correspond to a linear fit of the data, $(d - \delta)/(d - \delta)_{min} < 10$, slope is -1.06 . Slopes of $-1, -1.5$ are represented as visual guides. Inset: Distribution of power law exponent values obtained for each approach experiment for all CP concentration value ($n=103$). We excluded 24 experiments out of 127, that gave fit results with negative and non-physical value for δ .

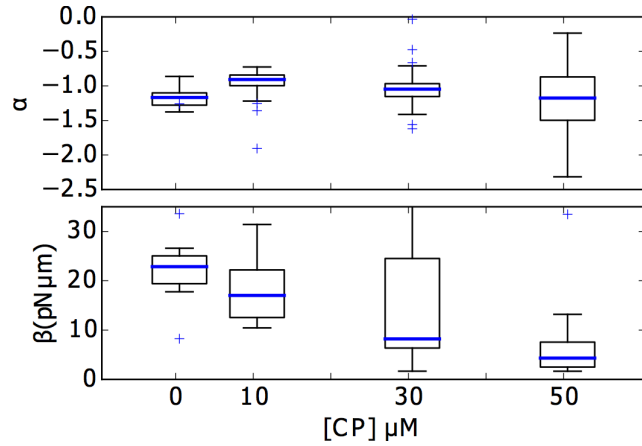


Figure 3: **Distribution of power exponent α and prefactor β for different concentrations in CP (see Tab.1).**

Box plot: blue line defines mean, box limit represent first(q1) and third(q3) quartiles, whiskers extend to the most extreme data point within $1.5 \times (q3 - q1)$ data range. None of the value of α are statistically different than the value for $[\text{CP}] = 50 \mu\text{M}$

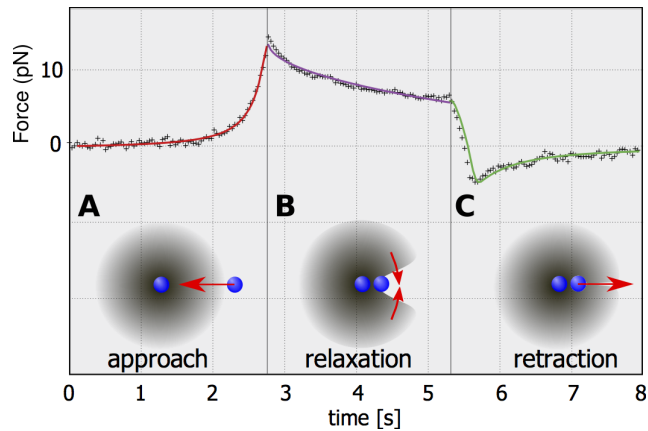


Figure 4: **Model and example of a full fit for the measured force-evolution.** A) (red) While approaching, the bead deforms the full actin cloud between the two beads leading to the measured forces that are fitted by the model of polymer elasticity including the discussed nonlinear Young's modulus. B) (violet) subsequent viscoelastic relaxation of the network between the two beads following the theory of polymer relaxation of sparse actin networks as discussed in Eq.9. To understand the negative forces in the retracting phase we imply that the network behind the bead is starting to relax into the void that has been created by the bead during the approach phase (red arrows). C) (green) This leads then to an additional elastic constraint while the bead returns to the initial position, hence explaining the negative force during the return phase.

Supplementary Information

June 11, 2014

Repeated approach on same bead as function of velocity, cp = 30

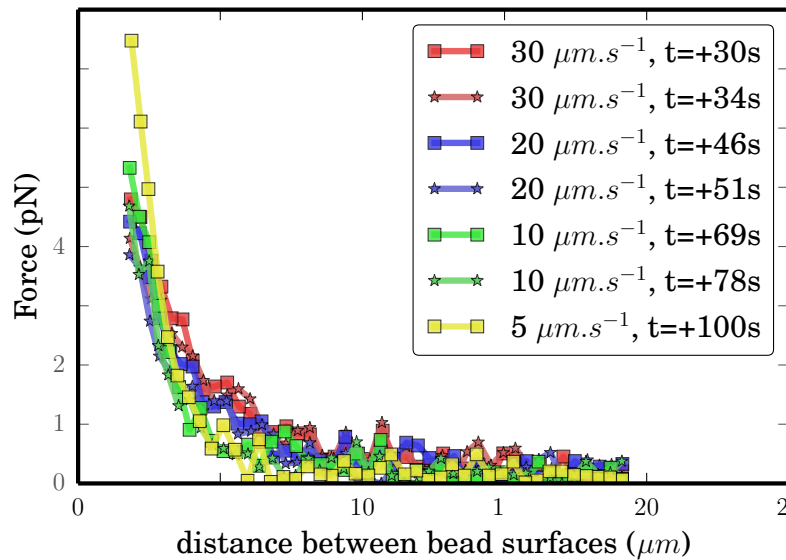


Figure 1: S1: Repeated approach curves at difference speeds (30, 20, 10 and $5\mu\text{m/s}$) on the same bead, by decreasing velocity. Indentation time t represents the instant at which the probe-bead started approaching the actin-bead, where $t=0$ corresponds to the time at which both beads were trapped. Starting distance and minimal approach distance where kept the same across all speed. The difference of maximum force between the first indentation (30 $\mu\text{m/s}$) and the last indentation (5 $\mu\text{m/s}$) can be explained by the fact that the actin is still growing on the bead surface.

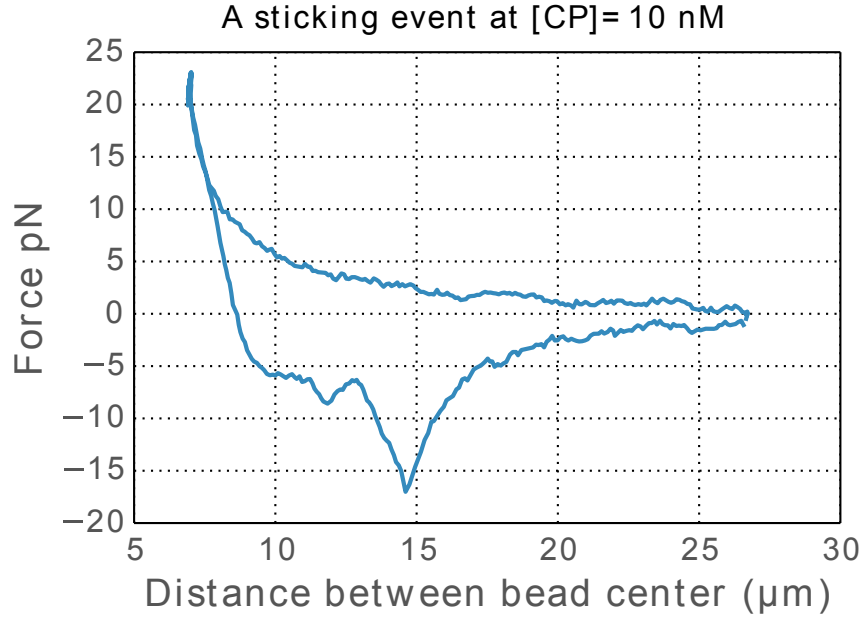


Figure 2: S2: Sawtooth like sticking events as observed for $\approx 25\%$ of experiments.

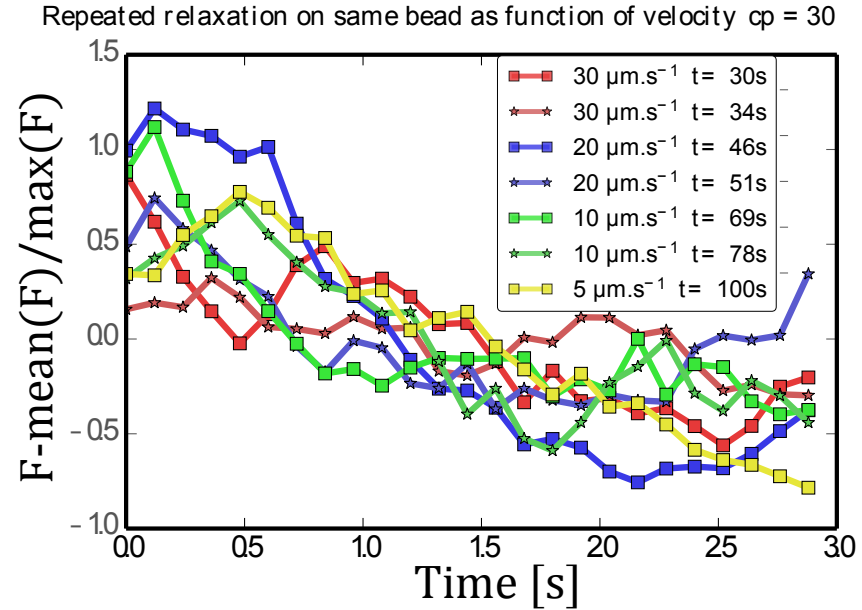


Figure 3: S3: Renormalized relaxation at different speeds for the same experiment as presented in Fig. S1.

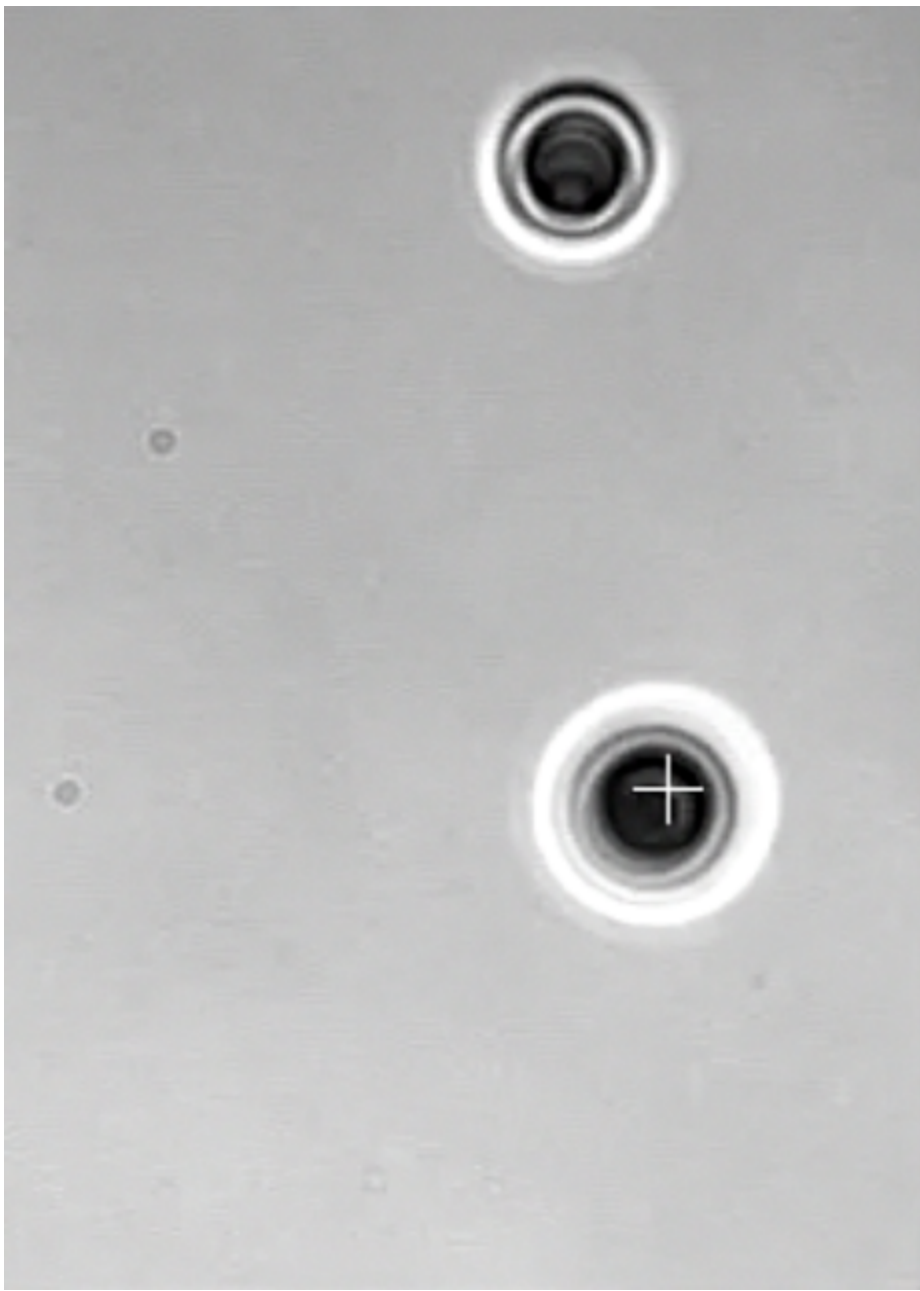


Figure 4: Video S4 : Actin bead trapped by an optical tweezer (white cross). When the stage is displaced. neighbouring particles experience a repulsive force. Timescale is realtime.

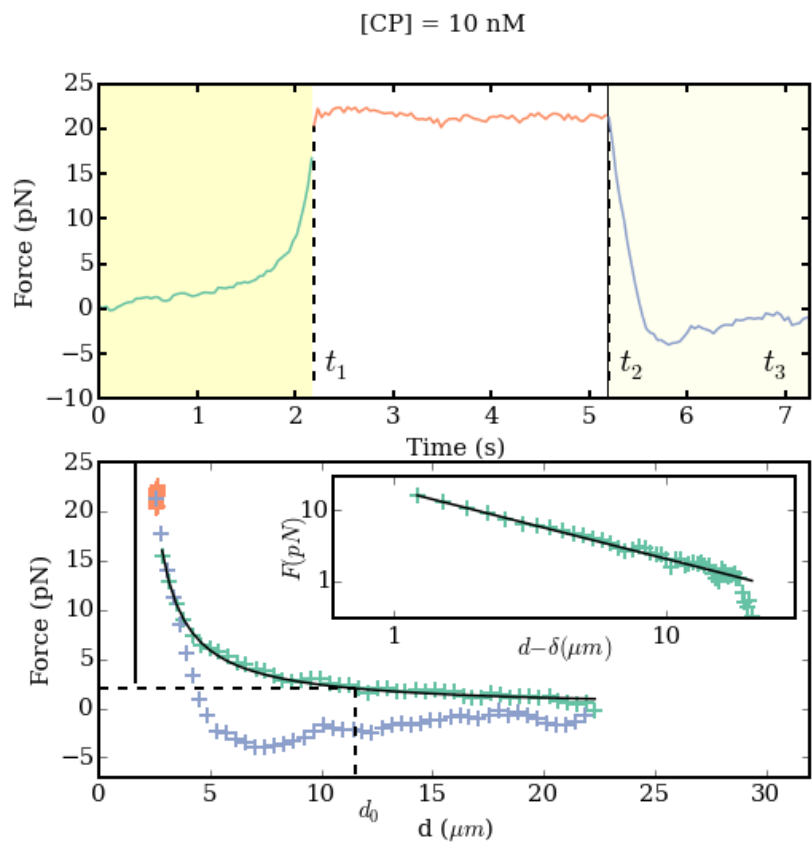


Figure 5: S5:One sample of the approach-retraction curves shown both as a function of time and distance for concentration of capping protein of 10nM.

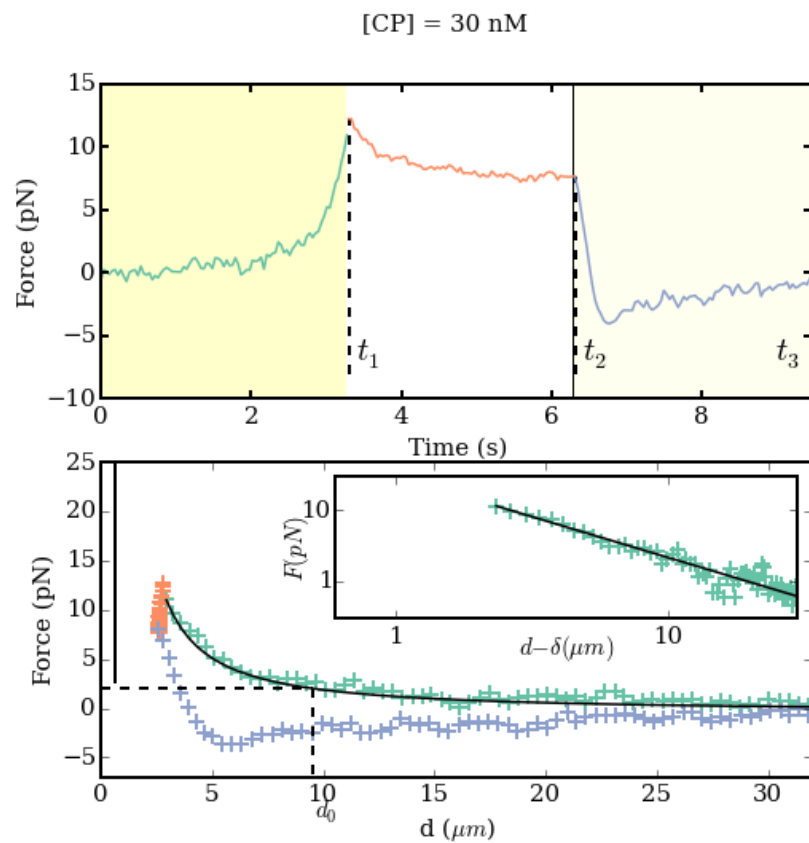


Figure 6: S6:One sample of the approach-retraction curves shown both as a function of time and distance for concentration of capping protein of 30nM.

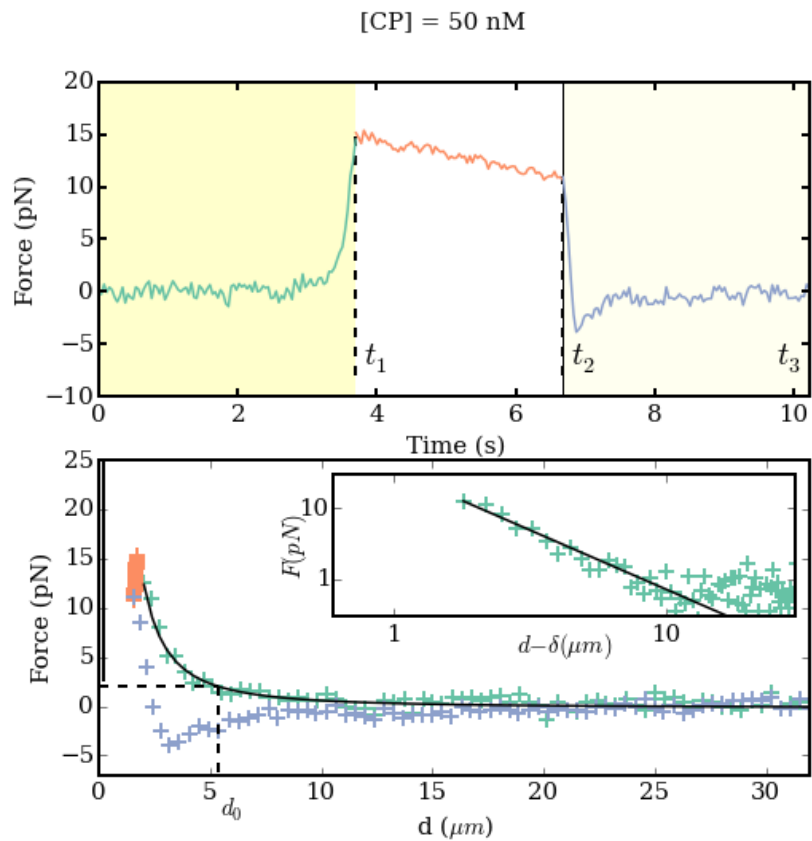


Figure 7: S7:One sample of the approach-retraction curves shown both as a function of time and distance for concentration of capping protein of 50.

7.2 Cell-sized liposome doublets reveal active cortical tension build up Draft

The part on liposomes doublets used to measure the increase of cortical tension on biomimetic cortices is subject of a draft submitted at Elife sciences:



24 Hills Road, P 01223 855346
Cambridge W elifesciences.org
CB2 1JP T @elife_sciences

FOR PEER REVIEW - CONFIDENTIAL

Cell-sized liposome doublets reveal active cortical tension build up

Tracking no: 26-08-2014-RA-eLife-04511

Joël Lemière (Institut Curie), Matthias Bussonnier (Institut Curie), Timo Betz (Institut Curie), Cécile Sykes (Institut Curie), and Kevin Carvalho (Institut Curie)

Abstract:

Cells are able to generate contractile forces and modulate their shape to fulfill their specific functions. The cell cortex, a thin actin shell bound to the plasma membrane, mediates these essential behaviours. It is the substrate for myosin activity which contributes to cortical tension build up, together with actin dynamics. Here, we dissect the sole effect of myosin II on cortical tension increase with a non-invasive method. Cell-sized biomimetic liposomes are arranged in doublets and covered with a stabilized actin cortex anchored to the membrane. The addition of myosin II minifilaments to this doublet triggers a shape change unambiguously related to cortical-tension increase. Our assay paves the way for a quantification of cortical-tension changes triggered by various actin-associated proteins in a cell-sized system.

Impact statement: The action of actin and myosin in the cell cortex is mimicked and quantified using the rounding up of liposome doublets

Competing interests: No competing interests declared

Author contributions:

Joël Lemière: ; Conception and design; Acquisition of data; Analysis and interpretation of data; Drafting or revising the article; Contributed unpublished essential data or reagents Matthias Bussonnier: ; Analysis and interpretation of data; Drafting or revising the article; Contributed unpublished essential data or reagents Timo Betz: ; Contributed unpublished essential data or reagents Cécile Sykes: ; Analysis and interpretation of data; Drafting or revising the article Kevin Carvalho: ; Conception and design; Acquisition of data; Analysis and interpretation of data; Drafting or revising the article; Contributed unpublished essential data or reagents

Funding:

ANR: Joël Lemière, Cécile Sykes, Kevin Carvalho, 09BLAN0283; ANR: Joël Lemière, Cécile Sykes, Kevin Carvalho, 12BSV5001401; ANR: Matthias Bussonnier, Cécile Sykes, 11JSV50002; FRM: Joël Lemière, Cécile Sykes, Kevin Carvalho, DEQ20120323737; Joël Lemière, Matthias Bussonnier, PhD Student fellowship; Fondation ARC pour la recherche sur le cancer: Joël Lemière, Kevin Carvalho, PhD Student/Postdoc fellowship The funders had no role in study design, data collection and interpretation, or the decision to submit the work for publication.

Datasets:

N/A

Ethics:

Human Subjects: No Animal Subjects: No

Author Affiliation:

Joël Lemière(UMR 168 Physico-chimie Curie, Institut Curie, France; UMR 168, CNRS, France) Matthias Bussonnier(UMR 168 Physico-chimie Curie, Institut Curie, France; UMR 168, CNRS, France) Timo Betz(UMR 168 Physico-chimie Curie, Institut Curie, France; UMR 168, CNRS, France) Cécile Sykes(UMR 168 Physico-chimie Curie, Institut Curie, France; UMR 168, CNRS, France) Kevin Carvalho(UMR 168 Physico-chimie Curie, Institut Curie, France; UMR 168, CNRS, France)

Dual-use research: No

Permissions: Have you reproduced or modified any part of an article that has been previously published or submitted to another journal?
No

Cell-sized liposome doublets reveal active cortical tension build up

2 Joël Lemière^{a,b,c,d}, Matthias Bussonnier^{a,b,c,d}, Timo Betz^{a,b,c}, Cécile Sykes^{a,b,c} & Kevin
Carvalho^{a,b,c}

4 ^a Institut Curie, Centre de Recherche, Paris, F-75248 France

^b CNRS, UMR 168, Paris, F-75248 France

6 ^c Sorbonne Universités, UPMC Univ Paris 06, UMR 168, Paris, F-75005 France

^d Univ Paris Diderot, Sorbonne Paris Cité, Paris, F-75205 France

8

Abstract

10 Cells are able to generate contractile forces and modulate their shape to fulfill
their specific functions. The cell cortex, a thin actin shell bound to the plasma
12 membrane, mediates these essential behaviours. It is the substrate for myosin
activity which contributes to cortical tension build up, together with actin dynamics.
14 Here, we dissect the sole effect of myosin II on cortical tension increase with a non-
invasive method. Cell-sized biomimetic liposomes are arranged in doublets and
16 covered with a stabilized actin cortex anchored to the membrane. The addition of
myosin II minifilaments to this doublet triggers a shape change unambiguously
18 related to cortical-tension increase. Our assay paves the way for a quantification of
cortical-tension changes triggered by various actin-associated proteins in a cell-sized
20 system.

22 **Introduction**

Cells are highly dynamic and need to change their shape in almost all cellular
24 events spanning from division and motility to tissue remodeling. One of the major
components involved in these processes is the contractile actin cytoskeleton
26 arranged in a sub-micrometer thick network linked to the plasma membrane,
containing myosin motors, and called the acto-myosin cortex [1]. It drives cell-shape
28 changes as well as cell polarization [2] and governs tissue remodeling [3]–[6]. This
cortex also insures tension in cells, called cortical tension [7]–[9], modulated by
30 membrane-cytoskeleton attachment, actin network organisation and myosin motor
activity. Micromanipulation of cells allows to measure the cortical tension, which was
32 found to be between 50 and 4000 pN/ μ m depending on cell type, myosin activity and
actin dynamics [7], [10]–[12]. Moreover, as shown for cell doublets, cell-cell
34 adhesion is able to modulate cortical tension [13], a mechanism that is involved in
cell sorting for tissue formation [14]. Recently, acto-myosin cortices have been
36 reconstructed on supported lipid bilayers [15] and on cell-sized liposomes [16] where
those reconstructions allowed to understand how crosslinking, attachment to the
38 membrane, and actin-filament length influence contraction by myosin activity and
actin polymerization [17].

40 In this study, we determine cortical-tension changes by the use of cell-sized
doublet liposomes around which an acto-myosin cortex is reproduced *in vitro*.
42 Variations in cortical tension are quantified by analysing doublet-shape change. This
approach is reminiscent of cell-cell doublets used to uncover the role of cell adhesion
44 in cortical-tension change [14]. Our assay allows isolating the role of myosin motors
on cortical-tension build up, independently of actin dynamics and membrane tension.

Results

48 Formation of liposome doublets

Liposomes are obtained by electroformation [18] from a mixture of egg-phosphatidylcholine (EPC) and biotin-PEG lipids (**See Methods**). We take the advantage of biotin PEG lipids to stick liposomes together by adding streptavidin to the liposome solution (**See Methods**). In these conditions, several doublets are formed within 15 minutes (**Fig. 1A**).

54 Attachment of actin on doublet liposomes

Phalloidin-stabilized fluorescent actin filaments, obtained in the presence of biotinylated actin monomers, stick to the membrane of the preformed doublets through a biotin-streptavidin-biotin link (**Fig. 1B**) and form a crosslinked homogeneous coat, as already characterized on liposomes [16]. Note that the interface between the two liposomes is free of actin filaments (**Fig. 1C - i**). To avoid the use of fluorescent lipids that may affect membrane mechanics [19], this interface is visualized by fluorescently labelling the inside buffer of only one of the liposomes with 0.9 μ M of sulforhodamin B (SRB) (**See Methods and Fig. 1C - i**).

Effect of myosin injection

64 Myosin II motors, which assemble into bipolar filaments, are injected in the observation chamber by exchanging the external solution using an H-shaped flow
66 chamber where doublets are imaged (**Fig. 1C - ii**). Myosin II motors trigger a shape change of the doublets within minutes (**Fig. 1C - iii**) and the following geometrical
68 characteristics of the liposome doublets are modified: the distance between liposome

centers (d), the radii of the liposomes 1 and 2, R_1 and R_2 , respectively ($R_1 > R_2$), the
 70 radius of curvature of the interface R_i , the volume of the doublet V , the angles
 between the interface and the liposome 1 or 2, θ_1 and θ_2 , respectively. We define the
 72 total contact angle $\theta_{tot} = \theta_1 + \theta_2$ (**Fig. 1D**). These parameters are geometrically
 linked (**Fig. 1D**), and obtained by adjusting two spherical caps in contact, either in
 74 2D- (phase contrast and epifluorescence) images or 3D-(spinning disk) stacks (**See**
 Methods). We use the total contact angle θ_{tot} as a reporter for shape change. We
 76 find that myosin addition produces an increase of θ_{tot} . Indeed, on epifluorescence
 images and in the absence of myosin, we measure a total contact angle θ_{tot} of $(64 \pm$
 78 $16)^\circ$ ($n=18$, standard deviation) whereas in the presence of 200 nM myosin and
 before the actin cortex ruptures, we find a θ_{tot} value of $(86 \pm 21)^\circ$ ($n=5$, standard
 80 deviation). This difference is statistically significant ($p=0.0186$)

Angles are related to tensions

82 Liposomes 1 and 2 have uniform tensions τ_1 and τ_2 respectively. Tension
 refers to the sole membrane tension in the absence of actin and myosin, and to
 84 cortical tension in their presence. The tension at the interface between liposome 1
 and 2 has two components: a membrane tension τ_i and the adhesion energy per unit
 86 surface W which is due to biotin-streptavidin-biotin adhesion, and reads $(\tau_i - W)$. The
 Young's equation, which relates tensions and angles, can be applied to the contact
 88 line between the two doublet liposomes (**Fig1. D**). When projected on the tangent to
 the interface between liposomes, the Young's equation reads:

$$90 \quad \tau_i - W = \tau_1 \cos \theta_1 + \tau_2 \cos \theta_2 \quad (1)$$

When projected orthogonally to the contact surface tangent, one finds:

92

$$\tau_1 \sin \theta_1 = \tau_2 \sin \theta_2 \quad (2)$$

Contact-angle dispersion

94 Dispersion in θ_{tot} , in a population of doublets before myosin injection is $\pm 16^\circ$.
It reflects a difference in tension, which could be due either to the dispersion of
96 tension during liposome preparation, or to a difference in adhesion at the interface
between doublet liposomes, or to contribution of the actin shell in tension build up.
98 Contact angle increase upon myosin addition and this dispersion, have roughly the
same value, which prompted us to characterize many individual doublets as a
100 function of time.

The sole presence of an actin shell does not modify the contact angle

102 We now investigate how the actin shell affects the contact angle, and thus the
tension, in the absence of myosin. We compare the shape of the same doublet in the
104 presence or in the absence of an actin shell by photo-damaging the actin filamentous
network (**Fig. 2A**) [20]. The total contact angle changes only by $(3.4 \pm 2)^\circ$ ($n = 7$),
106 (**Fig. 2B**) which is negligible compared to the change due to myosin activity (see
above).

108 3D observations

The plane of epifluorescence images is generally not parallel to the doublet
110 equatorial plane (R_1/R_2 varies between 1.15 and 1.82), hence leading to an
underestimate of the angle θ_{tot} . Therefore, 3D spinning disk image stacks are
112 recorded (**Fig. 3A**) for an accurate determination of θ_{tot} , V and d (see above for
definition), which are obtained by fitting spherical caps on 3D stacks (**Fig.3_figure**
114 **supplement 1** and **Methods**). All initial values before myosin addition are labelled

θ_{tot}^1 , V^1 , d^1 and $\theta_{tot}(t)$, $V(t)$, $d(t)$ after addition of 50 to 100 nM myosin II at t=0. We
116 observe that $\theta_{tot}(t)$ increases, whereas $d(t)$ decreases when myosin filaments are
added (**Fig. 3B-D**). During these geometric changes, the volume remains constant
118 within 10%, consistent with experiments performed on cell doublets [14], [21] (**Fig.**
3D).

120 Visual inspection of our images reveals that the interface between liposome 1
and 2 only differs from a flat interface by a few pixels (**Fig.3_figure supplement 2**).
122 The curvature $1/R_i$ (**Fig. 1D**) is generally much smaller than $1/R_1$ and $1/R_2$, which are
comparable. This observation leads to the assumption that $\theta_1 = \theta_2 = \theta$ within our
124 resolution.

Discussion

126 **Cortical tension is homogeneous for a single doublet**

The use of **equation (2)** with $\theta_1(t) = \theta_2(t) = \theta_{tot}(t)/2 = \theta(t)$ leads to the equality of
128 tensions on both sides of the doublet, thus, $\tau_1(t) = \tau_2(t) = \tau(t)$. This result is
consistent with the fact that actin is distributed continuously all around the liposome
130 doublet. Thus, myosin II mini-filaments contract a continuous shell. Under these
conditions, **equation (1)** simplifies to:

132
$$\tau_i - W = 2\tau(t) \cdot \cos \theta(t), \quad (3)$$

with the reasonable assumption that $\tau_i - W$ is considered constant over time for a
134 given doublet although it may depend on the variability of initial adhesion in our
experiments. Therefore, we obtain the tension $\tau(t)$, which varies during acto-myosin
136 contraction, by:

$$\tau(t) = \frac{\text{cst}}{2 \cdot \cos \theta(t)} . \quad (4)$$

138 The tension relative to its initial value reads:

$$\frac{\tau(t)}{\tau^I} = \frac{\cos \theta^I}{\cos \theta(t)} \quad (5)$$

140 **Relative increase of cortical tension**

Interaction of myosin II filaments with a biomimetic actin cortex induces
 142 tension build up. The cortical tension, normalized to its initial value $\frac{\tau(t)}{\tau^I}$, increases and reaches a maximal value $\frac{\tau^{max}}{\tau^I}$ (**Fig. 3E**). Conditions of myosin concentration (50 to
 144 200nM) allow to visualise doublet deformations before cortex breakage (peeling [16]).
 Cortex breakage however leads to the recovery of the doublet initial shape, before
 146 myosin injection (**see dashed blue line for d and θ Fig. 3**). The relative maximal
 change in tension is found to be $\frac{\tau^{max}}{\tau^I} = 1.56 \pm 0.56$ (n=5) in spinning-disk imaging
 148 and $\frac{\tau^{max}}{\tau^I} = 1.25 \pm 0.15$ (n=5) in epifluorescence. This difference is in agreement with
 the fact that contact angle is underestimates in epifluorescence (see above).

150 **Cortical-tension increase in doublets and in cells**

In cells, cortical tension can be as low as 50 pN/ μ m in fibroblast progenitor
 152 cells [10] and can go up to 4000 pN/ μ m for dictyostelium [11]. Surprisingly, when
 myosin activity is impaired – either by drugs or by genetic manipulation – cortical
 154 tension only decreases about twofold [7], [10], [11], [22]. Our *in vitro* reconstruction is
 able to capture this feature in the change of cortical tension. Indeed, we observe an
 156 increase in cortical tension by a factor 1.1 to 2.4 upon addition of myosin II
 minofilaments.

158 **Different contributions for cortical tension**

Cortical tension is the sum of the membrane tension and the tension due to
160 the actomyosin cortex. On average, in our assay, we find an increase of cortical
tension of 1.56 relative to the situation with actin only. Cortical tension is unchanged
162 by the presence of the sole actin shell (see above), therefore, membrane tension
contributes for 64% to cortical tension in the presence of myosin. In suspended
164 fibroblast cells however, membrane tension is estimated to be only 10% of the
cortical tension [7]. This difference may be explained by the absence of actin
166 dynamics in our assay, in line with the increase of cortical tension when
polymerization is stimulated in cells [7], [13]. How actin polymerization contributes to
168 cortical tension is still an open question that needs to be addressed taking into
account the geometry of the cell with actin polymerization at the inner membrane
170 leaflet. Whereas actin polymerization outside a liposome has been clearly shown to
generate inward pressure, is not yet clear how this can be translated into tension in a
172 different geometry. *In vitro* assays are on their way to mimic actin dynamics in cells
[23], [24] and will allow unveiling the mechanism of tension build up by actin
174 dynamics. This is the remaining module that needs to be understood, while the effect
of myosin is distinguished from the one of membrane in this study.

176 **Conclusion**

We provide a biomimetic reconstitution of tension build up through acto-
178 myosin contractility using liposome doublets. Cortical tension is monitored *in situ* over
time by analysing changes in doublet shape. This method allows us to directly
180 quantify the relative increase in tension due to myosin, separately from the one due
to actin dynamics. Understanding contraction of composite systems built brick by

182 brick on the model of a cell tile the road for the reconstitution of complex systems like
tissues.

184 Acknowledgments: This work was supported by the French Agence Nationale pour la
Recherche (ANR), grant ANR 09BLAN0283, ANR 12BSV5001401 and ANR-11-
186 JSV5-0002, and by the Fondation pour la Recherche Médicale (FRM), grant
DEQ20120323737. We thank Dr Agnieszka Kawska at IlluScientia for schemes. JL
188 and MB thank the AXA Research Fund for doctoral fellowships. JL and KC were also
supported by la Fondation ARC pour la recherche sur le cancer. We thank Thomas
190 Risler and Clément Campillo for critical reading of the manuscript

192 **Bibliography**

- [1] A. G. Clark, K. Dierkes, E. K. Paluch, « Monitoring Actin Cortex Thickness in
194 Live Cells », *Biophys. J.*, vol. 105, n° 3, p. 570-580, 2013.
- [2] G. Salbreux, G. Charras, E. Paluch, « Actin cortex mechanics and cellular
196 morphogenesis », *Trends Cell Biol.*, 2012.
- [3] E. Munro, J. Nance, J. R. Priess, « Cortical flows powered by asymmetrical
198 contraction transport PAR proteins to establish and maintain anterior-posterior
polarity in the early *C. elegans* embryo », *Dev. Cell*, vol. 7, n° 3, p. 413-424,
200 2004.
- [4] T. Lecuit, P.-F. Lenne, « Cell surface mechanics and the control of cell shape,
202 tissue patterns and morphogenesis », *Nat. Rev. Mol. Cell Biol.*, vol. 8, n° 8, p.
633-644, 2007.
- [5] M. Rauzi, P.-F. Lenne, T. Lecuit, « Planar polarized actomyosin contractile flows
204 control epithelial junction remodelling », *Nature*, vol. 468, n° 7327, p. 1110-1114,
206 2010.
- [6] M. Rauzi P.-F. Lenne, « Cortical forces in cell shape changes and tissue
208 morphogenesis », *Curr. Top. Dev. Biol.*, vol. 95, p. 93-144, 2011.

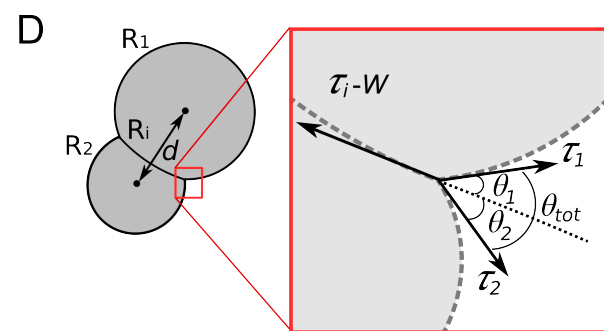
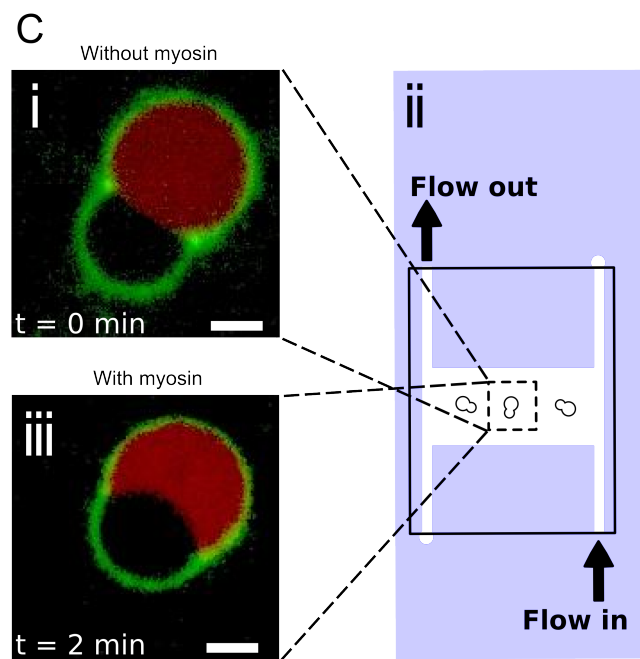
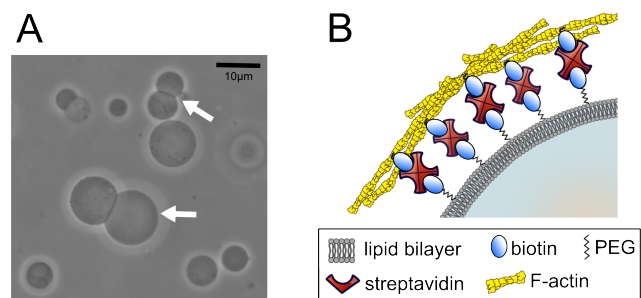
- 210 [7] J.-Y. Tinevez, U. Schulze, G. Salbreux, J. Roensch, J.-F. Joanny, E. Paluch,
« Role of cortical tension in bleb growth », *Proc. Natl. Acad. Sci. U. S. A.*, vol.
106, n° 44, p. 18581-18586, 2009.
- 212 [8] R. Nambiar, R. E. McConnell, M. J. Tyska, « Control of cell membrane tension
by myosin-I », *Proc Natl Acad Sci U S A*, vol. 106, n° 29, p. 11972-11977, 2009.
- 214 [9] D. Raucher, T. Stauffer, W. Chen, K. Shen, S. Guo, J. D. York, M. P. Sheetz, T.
Meyer, « Phosphatidylinositol 4,5-bisphosphate functions as a second
216 messenger that regulates cytoskeleton-plasma membrane adhesion », *Cell*, vol.
100, n° 2, p. 221-228, 2000.
- 218 [10] M. Krieg, Y. Arboleda-Estudillo, P.-H. Puech, J. Käfer, F. Graner, D. J. Müller,
C.-P. Heisenberg, « Tensile forces govern germ-layer organization in
220 zebrafish », *Nat. Cell Biol.*, vol. 10, n° 4, p. 429-436, 2008.
- 222 [11] E. C. Schwarz, E. M. Neuhaus, C. Kistler, A. W. Henkel, T. Soldati,
« Dictyostelium myosin IK is involved in the maintenance of cortical tension and
affects motility and phagocytosis », *J. Cell Sci.*, vol. 113 (Pt 4), p. 621-633,
224 2000.
- 226 [12] T. Luo, K. Mohan, P. A. Iglesias, D. N. Robinson, « Molecular mechanisms of
cellular mechanosensing », *Nat. Mater.*, vol. 12, n° 11, p. 1064-1071, 2013.
- 228 [13] W. Engl, B. Arasi, L. L. Yap, J-P. Thiery, V. Viasnoff, « Actin dynamics modulate
mechanosensitive immobilization of E-cadherin at adherens junctions », *Nat.
Cell Biol.*, vol. 16, n° 6, p. 587-594, 2014.
- 230 [14] J.-L. Maître, H. Berthoumieux, S. F. G. Krens, G. Salbreux, F. Jülicher, E.
Paluch, C.-P. Heisenberg, « Adhesion Functions in Cell Sorting by Mechanically
232 Coupling the Cortices of Adhering Cells », *Science*, vol. 338, n° 6104, p. 253-
256, 2012.
- 234 [15] M. P. Murrell, M. L. Gardel, « F-actin buckling coordinates contractility and
severing in a biomimetic actomyosin cortex », *Proc. Natl. Acad. Sci.*, 2012.
- 236 [16] K. Carvalho, F. C. Tsai, E. Lees, R. Voituriez, G. H. Koenderink, C. Sykes,
« Cell-sized liposomes reveal how actomyosin cortical tension drives shape
238 change », *Proc. Natl. Acad. Sci.*, 2013.
- 240 [17] K. Carvalho, J. Lemière, F. Faqir, J. Manzi, L. Blanchoin, J. Plastino, T. Betz, C.
Sykes, « Actin polymerization or myosin contraction: two ways to build up
cortical tension for symmetry breaking », *Philos. Trans. R. Soc. B Biol. Sci.*, vol.
242 368, n° 1629, 2013.

- [18] M. Angelova, D. Dimitrov, « Liposome electroformation », *Faraday Discuss.*, vol. 81, p. 303+, 1986.
- [19] O. Sandre, L. Moreaux, F. Brochard-Wyart, « Dynamics of transient pores in stretched vesicles », *Proc. Natl. Acad. Sci. U. S. A.*, vol. 96, n° 19, p. 10591-10596, 1999.
- [20] J. van der Gucht, E. Paluch, J. Plastino, C. Sykes, « Stress release drives symmetry breaking for actin-based movement », *Proc. Natl. Acad. Sci. U. S. A.*, vol. 102, n° 22, p. 7847-7852, 2005.
- [21] J. Sedzinski, M. Biro, A. Oswald, J.-Y. Tinevez, G. Salbreux, E. Paluch, « Polar actomyosin contractility destabilizes the position of the cytokinetic furrow », *Nature*, vol. 476, n° 7361, p. 462-466, 2011.
- [22] P. Kunda, A. E. Pelling, T. Liu, B. Baum, « Moesin controls cortical rigidity, cell rounding, and spindle morphogenesis during mitosis », *Curr. Biol. CB*, vol. 18, n° 2, p. 91-101, 2008.
- [23] E. Abu Shah, K. Keren, « Symmetry breaking in reconstituted actin cortices », *eLife*, vol. 3, p. e01433, 2014.
- [24] T. Luo, V. Srivastava, Y. Ren, D. N. Robinson, « Mimicking the mechanical properties of the cell cortex by the self-assembly of an actin cortex in vesicles », *Appl. Phys. Lett.*, vol. 104, n° 15, p. 153701, 2014.
- [25] G. H. Koenderink, Z. Dogic, F. Nakamura, P. M. Bendix, F. C. MacKintosh, J. H. Hartwig, T. P. Stossel, D. A. Weitz, « An active biopolymer network controlled by molecular motors », *Proc. Natl. Acad. Sci. U. S. A.*, vol. 106, n° 36, p. 15192-15197, 2009.
- [26] Y. Y. Toyoshima, S. J. Kron, E. M. McNally, K. R. Niebling, C. Toyoshima, J. A. Spudich, « Myosin subfragment-1 is sufficient to move actin filaments in vitro », *Nature*, vol. 328, n° 6130, p. 536-539, 1987.
- [27] M. S. E. Silva, M. Depken, B. Stuhrmann, M. Korsten, F. C. Mackintosh, G. H. Koenderink, « Active multistage coarsening of actin networks driven by myosin motors », *Proc. Natl. Acad. Sci. U. S. A.*, 2011.

Figure legends

274

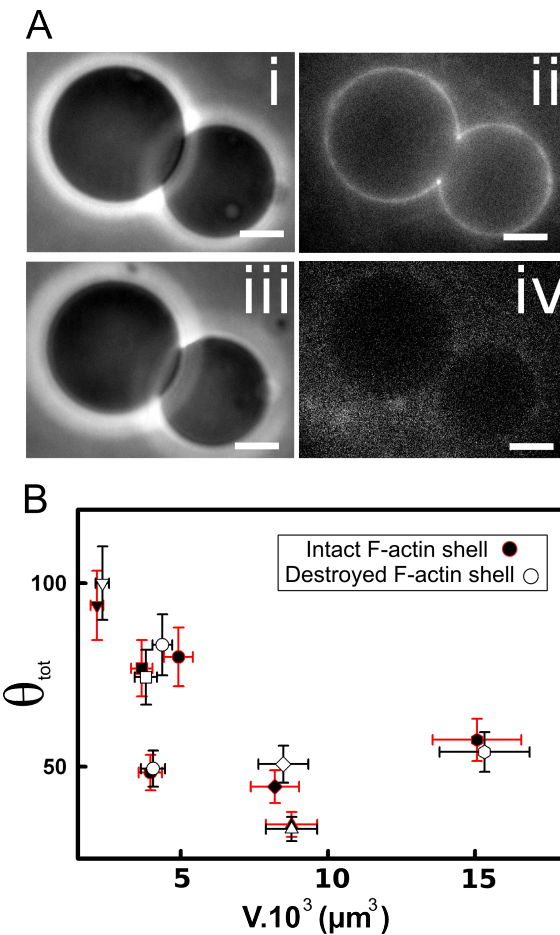
Figure 1: **Cell-sized liposome doublets.** A) Doublets, indicated by white arrows, in
276 the field of view of a phase contrast microscope. B) Schematic of the stabilized actin
cortex at the membrane (proteins not to scale). C) ii) Macrofluidics chamber designed
278 to exchange the outside buffer. Doublets are visualized in the middle horizontal
channel of the H shape chamber to avoid movement during the buffer exchange.
280 Spinning disk images of the doublet before i) or after iii) myosin II injection. One
liposome contains SRB (red) to visualize the interface of the doublet, the actin cortex
282 is labelled in green. Scale bar 5 μ m. D) Scheme of the doublet with the three
characteristic radii. Inset: enlargement of the contact interface between the two
284 liposomes with the Young's tension vectors and the contact angles.



286

288

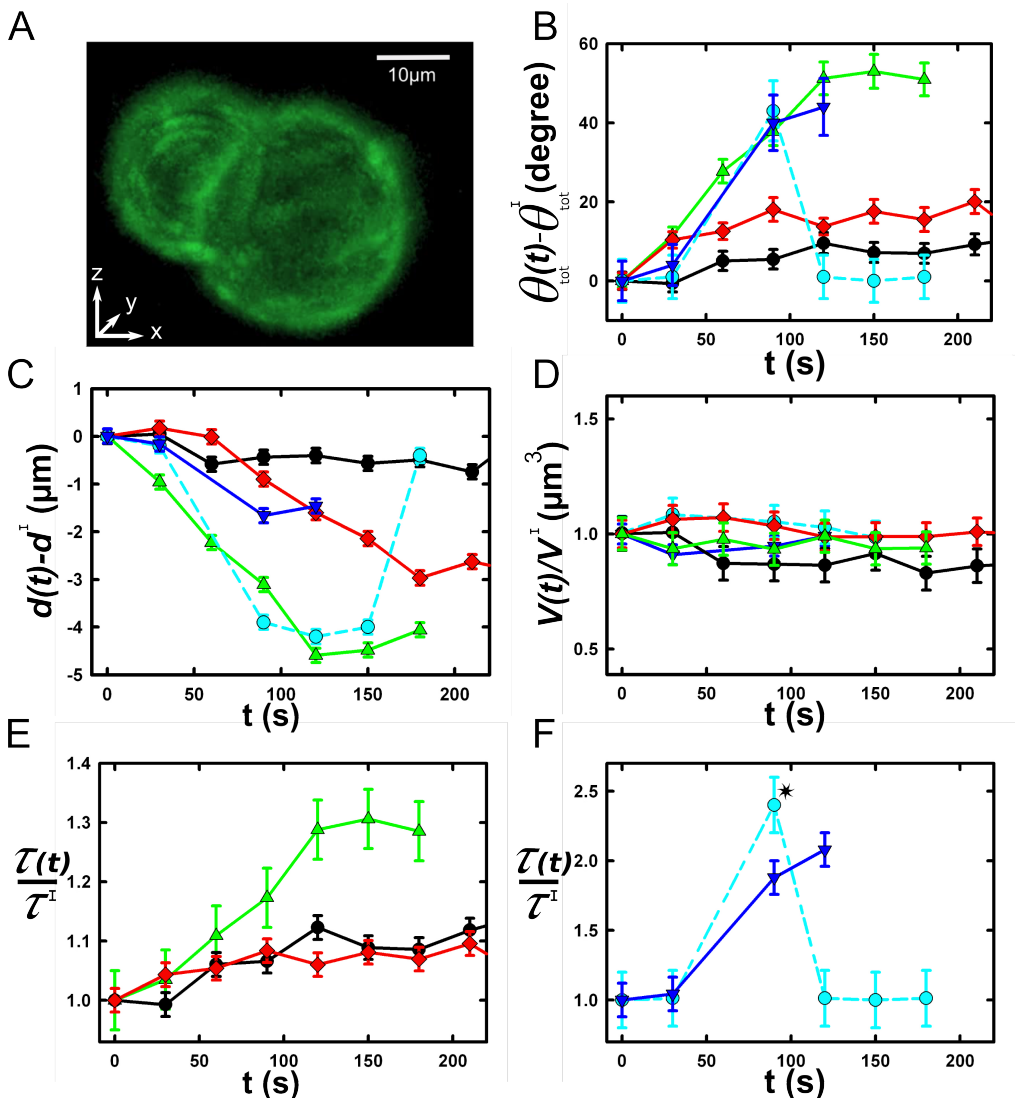
Figure 2: **Effect of an actin cortex on the doublet's shape.** A) Image of the same
 290 doublet coated with fluorescent actin before i) ii) and after iii) iv) actin cortex
 disruption. The actin cortex is visualized by epifluorescence ii) iv) and the doublet by
 292 phase contrast i) iii). Scale bar 5 μ m. B) Measurement of the contact angle between
 the two liposomes as a function of their volume, before (black) and after (white)
 294 disruption of the stabilized actin cortex. Error bars represent standard error.



296

298

Figure 3: **Geometrical parameters over time.** A) 3D reconstruction of a doublet surrounded by actin. Note that there is no actin on the membranes separating the two liposomes. Evolution of the contact angle (B), the distance between centers (C), compared with the initial ones as a function of time. Evolution of the volume ratio (D) and the tension ratio (E, F) compared with the initial ones as a function of time. Increase. B-F: each doublet is represented by a different colour and the blue dashed line corresponds to a doublet where cortex ruptures (*).



306

308 **Methods.**

Lipids, reagents and proteins. Chemicals are purchased from Sigma Aldrich (St. Louis, MO, USA) unless specified otherwise. L-alpha-phosphatidylcholine (EPC) and 1,2-distearoyl-sn-glycero-3-phosphoethanolamine-N-[biotinyl polyethylene glycol 2000] (biotinylated lipids), 1,2-dioleoyl-sn-glycero-3-phosphocholine are purchased from Avanti polar lipids (Alabaster, USA). Actin and biotinylated actin are purchased from Cytoskeleton (Denver, USA) and used with no further purification. Fluorescent Alexa-488 actin is obtained from Molecular Probes. Monomeric actin containing 10% or 20% of labeled Alexa-488 actin and 0.25% of biotinylated actin is diluted in G-Buffer (2mM Tris, 0.2mM CaCl₂, 0.2mM DTT at pH 8.0). Myosin II is purified from rabbit skeletal muscle and fluorescent myosin II is prepared as previously described [25] and its functionality is confirmed by motility assays showing an average gliding speed of $4.5 \pm 1.5 \mu\text{m/s}$ ($N = 27$) [26]. The working buffer contains 25 mM imidazole, 50 mM KCl, 70 mM sucrose, 1mM Tris, 2 mM MgCl₂, 1 mM ATP, 0.1 mM DTT, 0.02 mg/ml β -casein, adjusted to pH 7.4. All proteins are mixed in the working buffer and myosin II forms minifilaments of approximately 0.7 micrometer length with about 100 motors [27].

Formation of liposome doublets, actin cortices on doublets. Liposomes are electroformed [18]. Briefly, 20 μL of a mixture of EPC lipids and biotin PEG lipids present at 0.1 molar ratio with a concentration of 2.5 mg/ml in chloroform/methanol 5:3 (v:v) are spread on ITO-coated plates and dried under nitrogen flow, then placed under vacuum for 2 hours. A chamber is formed using the ITO plates (their conductive sides facing each other) filled with sucrose buffer (200mM sucrose, 2mM Tris adjusted at pH 7.4, containing or not sulforhodamin B 0.9 μM), and sealed with hematocrit paste (Vitrex medical, Denmark). Liposomes are formed by applying an

alternate current voltage (1V - 10 Hz) for 1hour and 15 minutes. Then liposomes are
334 incubated with 160 nM streptavidin for 15 min and diluted 30 times. Note that for the
observation of the interface between the doublet liposomes, we prepare separately
336 liposomes in the presence or in the absence of sulforhodamin B, and mix them at
equal volume before incubation with streptavidin. At this stage we have doublets
338 coated with streptavidin. Waiting more than 15 min would increase the quantity of
liposome aggregates and decrease the quantity of doublets and single liposomes. A
340 bulk solution of 40 μ M actin monomers (Cytoskeleton, Denver USA) containing 10%
fluorescently labeled actin and 1/400 biotinylated actin monomers is polymerized at 1
342 μ M by diluting 40 times in the working buffer (25 mM imidazole, 50 mM KCl, 70 mM
sucrose, 1mM Tris, 2 mM MgCl₂, 1 mM ATP, 0.1 mM DTT, 0.02 mg/ml β -casein,
344 adjusted at a pH 7.4) for 1 hour in the presence of 1 μ M of phalloidin (to prevent
depolymerization). Actin filaments are then diluted 10-fold to 0.1 μ M, mixed with
346 streptavidin-coated doublets of liposomes, and incubated for 15 min. The mix is
diluted 5 times for observation to reduce background fluorescence from actin
348 filaments.

Observation chamber design, formation and myosin II injection. Observation
350 chambers are made by heating Parafilm stripes (as spacer) with an H-shape
between two coverslips. The solution containing doublets is injected in the chamber
352 and let few minutes in order to allow gentle sedimentation of the doublets (**Fig. 1C**).
Then myosin II filaments are injected in the chamber and the H-shape and doublets
354 are imaged over time in the middle of the chamber (**Fig. 1C**). Conditions
(streptavidin, actin filament length) are the same as in [16] but observations are
356 made before breakage of the acto-myosin shell.

Observation of doublets. Epifluorescence and phase contrast microscopy are
358 performed using an IX70 Olympus inverted microscope with a 100x or a 60x oil-
immersion objective. Spinning-disk confocal microscopy is performed on a Nikon
360 Eclipse T1 microscope with an Andor Evolution Spinning Disc system and a 60x
water immersion objective and a z distance between z-slices of 1/25 of the doublet
362 size.

Image processing and data analysis. 2D-images: the contact angle is measured by
364 adjusting two circles on binarised liposome images taken by phase contrast or
epifluorescence microscopy. 3D-images: the geometrical parameters of the doublets
366 are determined by optimizing the correlation between simulated and acquired 3D
recording. Simulated 3D stacks, using [Python], [Numpy] and [Cython] are obtained
368 by creating two spherical caps in contact and reproducing the fluorescent signal of
actin at the external surface. Optimizing the correlation between simulated and
370 acquired data is done using [Python] and [SciPy] (Nelder–Mead simplex method from
the "optimize" submodule). Initial fit parameters of the first frame of each timelapse
372 are determined visually. For the subsequent frame, we use the optimized parameters
as initial parameters. Robustness of fit is checked by several repeats while changing
374 the initial fit parameters by a random amount drawn from a normal distribution (mean
0µm and standard deviation 0.5µm). The obtained eight parameters (2 centers with
376 X,Y,Z coordinate and 2 liposomes radii) geometrically define the contact angle and
the distance between centers. All the data processing was done in an [IPython]
378 environment.

This version of the manuscript is based on the source files repository version b'082496dbc580393d76ed1c235dc4f7cbd0958752n', available on [github](#), and [bitbucket](#). It is also available [online](#) as HTML and epub.

BIBLIOGRAPHY

- [Alberts et al. 2008] B Alberts, A Johnson, J Lewis, M Raff, K Roberts, and P And Walter. *Molecular Biology of the Cell*. volume 54. Garland, 2008. URL: <http://discovery.ucl.ac.uk/1099731>.
- [Angelova et al. 1986] Miglena I. Angelova and Dimitar S. Dimitrov. Liposome electroformation. *Faraday Discussions of the Chemical Society*, 81:303, 1986. URL: <http://xlink.rsc.org/?DOI=dc9868100303>, doi:10.1039/dc9868100303.
- [Azoury et al. 2011] Jessica Azoury, Karen Wingman Lee, Virginie Georget, Pascale Hikal, and Marie-Hélène Verlhac. Symmetry breaking in mouse oocytes requires transient F-actin mesh-work destabilization.. *Development (Cambridge, England)*, 138(14):2903–8, July 2011. URL: <http://dev.biologists.org/content/138/14/2903.long>, doi:10.1242/dev.060269.
- [BernheimGroswasser et al. 2002] Anne Bernheim-Groswasser, Sebastian Wiesner, Roy M. Golsteyn, Marie-France Carlier, and Cecile Sykes. The dynamics of actin-based motility depend on surface parameters. *Nature*, 417(6886):308–311, May 2002. URL: <http://dx.doi.org/10.1038/417308a> <http://www.nature.com/nature/journal/v417/n6886/full/417308a.html>, doi:10.1038/417308a.
- [Berridge 2012] Michael J. Berridge. Cell Signalling Biology: Module 4 - Sensors and Effectors. 2012. doi:10.1042/csb0001004.
- [Bornschlogl 2013] Thomas Bornschlögl. How filopodia pull: what we know about the mechanics and dynamics of filopodia.. *Cytoskeleton (Hoboken, N.J.)*, 70(10):590–603, October 2013. URL: <http://www.ncbi.nlm.nih.gov/pubmed/23959922>, doi:10.1002/cm.21130.
- [Buss et al. 2008] Folma Buss and John Kendrick-Jones. How are the cellular functions of myosin VI regulated within the cell?. *Biochemical and biophysical research communications*, 369(1):165–175, April 2008. URL: <http://www.sciencedirect.com/science/article/pii/S0006291X07025508>, doi:10.1016/j.bbrc.2007.11.150.
- [Bussonnier et al. 2014] Matthias Bussonnier, Kevin Carvalho, Joël Lemière, Jean-François Joanny, Cécile Sykes, and Timo Betz. Mechanical Detection of a Long-Range Actin Network Emanating from a Biomimetic Cortex. *Biophysical Journal*, 107(4):854–862, August 2014. URL: <http://www.cell.com/article/S0006349514007243/fulltext>, doi:10.1016/j.bpj.2014.07.008.
- [Carvalho et al. 2013a] Kevin Carvalho, Joël Lemière, Fahima Faqir, John Manzi, Laurent Blanchoin, Julie Plastino, Timo Betz, and Cécile Sykes. Actin polymerization or myosin contraction: two ways to build up cortical tension for symmetry breaking.. *Philosophical transactions of the Royal Society of London. Series B, Biological sciences*, 368(1629):20130005, January 2013. URL: <http://www.ncbi.nlm.nih.gov/pubmed/24062578>, doi:10.1098/rstb.2013.0005.

- [Carvalho et al. 2013b] Kevin Carvalho, Feng-Ching Tsai, Edouard Lees, Raphaël Voituriez, Gijsje H Koenderink, and Cecile Sykes. Cell-sized liposomes reveal how actomyosin cortical tension drives shape change.. *Proceedings of the National Academy of Sciences of the United States of America*, 110(41):16456–61, October 2013. URL: <http://www.pnas.org/content/110/41/16456> <http://www.ncbi.nlm.nih.gov/pmc/articles/3799374/>&tool=pmcentrez&rendertype=abstract, doi:10.1073/pnas.1221524110.
- [Chaigne et al. 2013] Agathe Chaigne, Clément Campillo, Nir S Gov, Raphaël Voituriez, Jessica Azoury, Claudia Umaña-Díaz, Maria Almonacid, Isabelle Queguiner, Pierre Nassoy, Cécile Sykes, Marie-Hélène Verlhac, and Marie-Emilie Terret. A soft cortex is essential for asymmetric spindle positioning in mouse oocytes.. *Nature cell biology*, 15(8):958–66, August 2013. URL: <http://dx.doi.org/10.1038/ncb2799> <http://www.ncbi.nlm.nih.gov/pubmed/23851486>, doi:10.1038/ncb2799.
- [Charras et al. 2008] Guillaume Charras and Ewa Paluch. Blebs lead the way: how to migrate without lamellipodia.. *Nature reviews. Molecular cell biology*, 9(9):730–6, September 2008. URL: <http://dx.doi.org/10.1038/nrm2453> <http://www.ncbi.nlm.nih.gov/pubmed/18628785>, doi:10.1038/nrm2453.
- [Clark et al. 2013] Andrew G. Clark, Kai Dierkes, and Ewa K. Paluch. Monitoring actin cortex thickness in live cells.. *Biophysical journal*, 105(3):570–80, August 2013. URL: <http://www.ncbi.nlm.nih.gov/pubmed/23931305>, doi:10.1016/j.bpj.2013.05.057.
- [Dabiri et al. 1990] G A Dabiri, J M Sanger, D A Portnoy, and F S Southwick. Listeria monocytogenes moves rapidly through the host-cell cytoplasm by inducing directional actin assembly.. *Proceedings of the National Academy of Sciences of the United States of America*, 87(16):6068–72, August 1990. URL: <http://www.ncbi.nlm.nih.gov/pmc/articles/3799374/>&tool=pmcentrez&rendertype=abstract, doi:10.1073/pnas.87.16.6068.
- [Engler et al. 2006] Adam J. Engler, Shamik Sen, H. Lee Sweeney, and Dennis E. Discher. Matrix elasticity directs stem cell lineage specification.. *Cell*, 126(4):677–89, August 2006. URL: <http://www.ncbi.nlm.nih.gov/pubmed/16923388>, doi:10.1016/j.cell.2006.06.044.
- [Faix et al. 2006] Jan Faix and Klemens Rottner. The making of filopodia.. *Current opinion in cell biology*, 18(1):18–25, February 2006. URL: <http://www.sciencedirect.com/science/article/pii/S095506740500178X>, doi:10.1016/j.ceb.2005.11.002.
- [Feric et al. 2013] Marina Feric and Clifford P Brangwynne. A nuclear F-actin scaffold stabilizes ribonucleoprotein droplets against gravity in large cells. *Nature Cell Biology*, 15:1253–1259, 2013. URL: <http://dx.doi.org/10.1038/ncb2830>, doi:10.1038/ncb2830.
- [Fletcher et al. 2010] Daniel A Fletcher and R Dyche Mullins. Cell mechanics and the cytoskeleton.. *Nature*, 463(7280):485–92, January 2010. URL: <http://dx.doi.org/10.1038/nature08908>, doi:10.1038/nature08908.
- [Gardel et al. 2003] M. L Gardel, M. T Valentine, J. C Crocker, A. R Bausch, and D. A Weitz. Microrheology of entangled F-actin solutions.. *Physical review letters*, 91(15):158302, October 2003. URL: <http://www.ncbi.nlm.nih.gov/pubmed/14611506> <http://link.aps.org/doi/10.1103/PhysRevLett.91.158302>, doi:10.1103/PhysRevLett.91.158302.
- [Goley et al. 2006] Erin D Goley and Matthew D Welch. The ARP2/3 complex: an actin nucleator comes of age.. *Nature reviews. Molecular cell biology*, 7(10):713–26, October 2006. URL: <http://dx.doi.org/10.1038/nrm2026>, doi:10.1038/nrm2026.

- [Hartman et al. 2012] M. A. Hartman and J. A. Spudich. The myosin superfamily at a glance. *Journal of Cell Science*, 125(7):1627–1632, May 2012. URL: <http://jcs.biologists.org/content/125/7/1627.full> <http://jcs.biologists.org/cgi/doi/10.1242/jcs.094300>, doi:10.1242/jcs.094300.
- [Helfrich 1973] W Helfrich. Elastic properties of lipid bilayers: theory and possible experiments.. *Zeitschrift für Naturforschung. Teil C: Biochemie, Biophysik, Biologie, Virologie*, 28(11):693–703, 1973. URL: <http://www.ncbi.nlm.nih.gov/pubmed/4273690>.
- [Holubcova et al. 2013] Zuzana Holubcová, Gillian Howard, and Melina Schuh. Vesicles modulate an actin network for asymmetric spindle positioning.. *Nature cell biology*, 15(8):937–47, August 2013. URL: <http://www.pubmedcentral.nih.gov/articlerender.fcgi?artid=3797517&tool=pmcentrez&rendertype=abstract>, doi:10.1038/ncb2802.
- [Huelsmann et al. 2013] Sven Huelsmann, Jari Yläne, and Nicholas H Brown. Filopodia-like actin cables position nuclei in association with perinuclear actin in Drosophila nurse cells.. *Developmental cell*, 26(6):604–15, September 2013. URL: <http://www.pubmedcentral.nih.gov/articlerender.fcgi?artid=3791400&tool=pmcentrez&rendertype=abstract>, doi:10.1016/j.devcel.2013.08.014.
- [Isambert et al. 1996] H. Isambert and A. C. Maggs. Dynamics and Rheology of Actin Solutions. *Macromolecules*, 29(3):1036–1040, January 1996. URL: <http://dx.doi.org/10.1021/ma946418x> <http://pubs.acs.org/doi/abs/10.1021/ma946418x> <http://pubs.acs.org/doi/full/10.1021/ma946418x> <http://pubs.acs.org/doi/pdf/10.1021/ma946418x>, doi:10.1021/ma946418x.
- [Isambert et al. 1995] H. Isambert, P. Venier, A. Maggs, A. Fattoum, R. Kassab, D. Pantaloni, and M. Carrier. Flexibility of actin filaments derived from thermal fluctuations. Effect of bound nucleotide, phalloidin, and muscle regulatory proteins. *Journal of Biological Chemistry*, 270(19):11437–11444, May 1995. URL: <http://www.jbc.org/content/270/19/11437.short>, doi:10.1074/jbc.270.19.11437.
- [Iwabuchi et al. 2010] Kosei Iwabuchi and Shingo Takagi. Actin-based mechanisms for light-dependent intracellular positioning of nuclei and chloroplasts in Arabidopsis.. *Plant signaling & behavior*, 5(8):1010–3, August 2010. URL: <http://www.plantphysiol.org/content/152/3/1309>, doi:10.1104/pp.109.149526.
- [Jaalouk et al. 2009] Diana E Jaalouk and Jan Lammerding. Mechanotransduction gone awry.. *Nature reviews. Molecular cell biology*, 10(1):63–73, January 2009. URL: <http://www.pubmedcentral.nih.gov/articlerender.fcgi?artid=2668954&tool=pmcentrez&rendertype=abstract>, doi:10.1038/nrm2597.
- [Jahnel et al. 2011] Marcus Jahnel, Martin Behrndt, Anita Jannasch, Erik Schäffer, and Stephan W. Grill. Measuring the complete force field of an optical trap. *Optics Letters*, 36(7):1260–1262, April 2011. URL: <http://ol.osa.org/abstract.cfm?URI=ol-36-7-1260> <http://www.opticsinfobase.org/ol/abstract.cfm?URI=ol-36-7-1260>, doi:10.1364/OL.36.001260.
- [Kawska et al. 2012] Agnieszka Kawska, Kévin Carvalho, John Manzi, Rajaa Boujemaa-Paterski, Laurent Blanchoin, Jean-Louis Martiel, and Cécile Sykes. How actin network dynamics control the onset of actin-based motility.. *Proceedings of the National Academy of Sciences of the United States of America*, 109(36):14440–5, September 2012. URL: <http://www.pnas.org/content/109/36/14440.short>, doi:10.1073/pnas.1117096109.
- [Krieg et al. 2008] M Krieg, Y Arboleda-Estudillo, P-H Puech, J Käfer, F Graner, D J Müller, and C-P Heisenberg. Tensile forces govern germ-layer organization in zebrafish.. *Nature cell biology*, 10(4):429–36, April 2008. URL: <http://dx.doi.org/10.1038/ncb1705>, doi:10.1038/ncb1705.

- [Kruse et al. 2005] Karsten Kruse, J F Joanny, Frank Jülicher, J Prost, and K Sekimoto. Generic theory of active polar gels: a paradigm for cytoskeletal dynamics.. *The European physical journal. E, Soft matter*, 16(1):5–16, January 2005. URL: <http://link.springer.com/article/10.1140/epje/e2005-00002-5> <http://www.ncbi.nlm.nih.gov/pubmed/15688136>, doi:10.1140/epje/e2005-00002-5.
- [Kunda et al. 2008] Patricia Kunda, Andrew E Pelling, Tao Liu, and Buzz Baum. Moesin controls cortical rigidity, cell rounding, and spindle morphogenesis during mitosis.. *Current biology : CB*, 18(2):91–101, January 2008. URL: <http://www.ncbi.nlm.nih.gov/pubmed/18207738>, doi:10.1016/j.cub.2007.12.051.
- [Liverpool 2006] Tanniemola B Liverpool. Active gels: where polymer physics meets cytoskeletal dynamics.. *Philosophical transactions. Series A, Mathematical, physical, and engineering sciences*, 364(1849):3335–55, December 2006. URL: <http://www.ncbi.nlm.nih.gov/pubmed/17090463>, doi:10.1098/rsta.2006.1897.
- [Loisel et al. 1999] T P Loisel, R Boujemaa, D Pantaloni, and M F Carlier. Reconstitution of actin-based motility of Listeria and Shigella using pure proteins.. *Nature*, 401(6753):613–6, October 1999. URL: <http://www.ncbi.nlm.nih.gov/pubmed/10524632>, doi:10.1038/44183.
- [Lenart et al. 2005] Péter Lénárt, Christian P Bacher, Nathalie Daigle, Arthur R Hand, Roland Eils, Mark Terasaki, and Jan Ellenberg. A contractile nuclear actin network drives chromosome congression in oocytes.. *Nature*, 436:812–818, 2005. doi:10.1038/nature03810.
- [Machesky et al. 1999] L. M. Machesky, R. D. Mullins, H. N. Higgs, D. A. Kaiser, L. Blanchoin, R. C. May, M. E. Hall, and T. D. Pollard. Scar, a WASp-related protein, activates nucleation of actin filaments by the Arp2/3 complex. *Proceedings of the National Academy of Sciences*, 96(7):3739–3744, March 1999. URL: <http://www.pnas.org/content/96/7/3739.full>, doi:10.1073/pnas.96.7.3739.
- [MacKintosh et al. 1995] F. MacKintosh, J. Käs, and P. Janmey. Elasticity of Semiflexible Biopolymer Networks. *Physical Review Letters*, 75(24):4425–4428, December 1995. URL: <http://link.aps.org/doi/10.1103/PhysRevLett.75.4425>, doi:10.1103/PhysRevLett.75.4425.
- [Mahaffy et al. 2004] R E Mahaffy, S Park, E Gerde, J Käs, and C K Shih. Quantitative analysis of the viscoelastic properties of thin regions of fibroblasts using atomic force microscopy.. *Biophysical journal*, 86(3):1777–93, March 2004. URL: [http://www.ncbi.nlm.nih.gov/article/1304012&tool=pmcentrez&rendertype=abstract](http://www.ncbi.nlm.nih.gov/article/1304012), doi:10.1016/S0006-3495(04)74245-9.
- [Maitre et al. 2012] Jean-Léon Maitre, Hélène Berthoumieux, Simon Frederik Gabriel Krens, Guillaume Salbreux, Frank Jülicher, Ewa Paluch, and Carl-Philipp Heisenberg. Adhesion functions in cell sorting by mechanically coupling the cortices of adhering cells.. *Science (New York, N.Y.)*, 338(6104):253–6, October 2012. URL: <http://www.sciencemag.org.rproxy.sc.univ-paris-diderot.fr/content/338/6104/253.long> <http://www.ncbi.nlm.nih.gov/pubmed/22923438> <http://www.sciencemag.org/content/338/6104/253> <http://www.sciencemag.org/content/338/6104/253.abstract>, doi:10.1126/science.1225399.
- [Marcy et al. 2004] Yann Marcy, Jacques Prost, Marie-France Carlier, and Cécile Sykes. Forces generated during actin-based propulsion: a direct measurement by micromanipulation.. *Proceedings of the National Academy of Sciences of the United States of America*, 101(16):5992–7, April 2004. URL: <http://www.pnas.org/content/101/16/5992.abstract> <http://www.pnas.org/content/101/16/5992.full>, doi:10.1073/pnas.0307704101.
- [Mizuno et al. 2007] Daisuke Mizuno, Catherine Tardin, C. F. Schmidt, and F C Mackintosh. Nonequilibrium mechanics of active cytoskeletal networks.. *Science (New York, N.Y.)*,

- 315(5810):370–3, January 2007. URL: <http://www.sciencemag.org/content/315/5810/370.abstract> <http://www.sciencemag.org/content/315/5810/370.short> <http://www.ncbi.nlm.nih.gov/pubmed/17234946>, doi:10.1126/science.1134404.
- [Morone et al. 2006] Nobuhiro Morone, Takahiro Fujiwara, Kotono Murase, Rinshi S Kaisai, Hiroshi Ike, Shigeki Yuasa, Jiro Usukura, and Akihiro Kusumi. Three-dimensional reconstruction of the membrane skeleton at the plasma membrane interface by electron tomography.. *The Journal of cell biology*, 174(6):851–62, September 2006. URL: <http://www.pubmedcentral.nih.gov/articlerender.fcgi?artid=2064339&tool=pmcentrez&rendertype=abstract> <http://jcb.rupress.org/content/174/6/851.long>, doi:10.1083/jcb.200606007.
- [Morse 1998a] David C Morse. Viscoelasticity of concentrated isotropic solutions of semi-flexible polymers. 2. Linear response. *Macromolecules*, 9297(98):7044–7067, 1998. URL: <http://pubs.acs.org/doi/abs/10.1021/ma980304u>.
- [Morse 1998b] David C. Morse. Viscoelasticity of Concentrated Isotropic Solutions of Semi-flexible Polymers. 1. Model and Stress Tensor. *Macromolecules*, 31(20):7030–7043, October 1998. URL: <http://pubs.acs.org/doi/abs/10.1021/ma9803032> <http://dx.doi.org/10.1021/ma9803032>, doi:10.1021/ma9803032.
- [Nieminan et al. 2007] Timo A Nieminan, Gregor Knöner, Norman R Heckenberg, and Halina Rubinsztein-Dunlop. Physics of optical tweezers.. *Methods in cell biology*, 82:207–36, January 2007. URL: <http://www.sciencedirect.com/science/article/pii/S0091679X06820066>, doi:10.1016/S0091-679X(06)82006-6.
- [Noguera 2012] Philippe Noguera. *Etude du rôle de la protéine VASP dans la dynamique et la mécanique des réseaux d'actine avec un système biomimétique de la motilité cellulaire*. PhD thesis, Paris 7, September 2012. URL: <http://tel.archives-ouvertes.fr/tel-00834288>.
- [Parekh et al. 2005] Sapun H Parekh, Ovijit Chaudhuri, Julie A Theriot, and Daniel A Fletcher. Loading history determines the velocity of actin-network growth.. *Nature cell biology*, 7(12):1219–23, December 2005. URL: <http://www.nature.com/gate1.inist.fr/ncb/journal/v7/n12/full/ncb1336.html> <http://www.ncbi.nlm.nih.gov/pubmed/16299496>, doi:10.1038/ncb1336.
- [Plastino et al. 2005] Julie Plastino and Cécile Sykes. The actin slingshot. *Current Opinion in Cell Biology*, 17(1):62–66, 2005. URL: <http://www.sciencedirect.com/science/article/pii/S0955067404001693>.
- [Pollard 1986] T D Pollard. Rate constants for the reactions of ATP- and ADP-actin with the ends of actin filaments.. *The Journal of cell biology*, 103(6 Pt 2):2747–54, December 1986. URL: <http://www.pubmedcentral.nih.gov/articlerender.fcgi?artid=2114620&tool=pmcentrez&rendertype=abstract>, doi:10.1083/jcb.103.6.2747.
- [Pollard et al. 2000] T D Pollard, L Blanchoin, and R D Mullins. Molecular mechanisms controlling actin filament dynamics in nonmuscle cells.. *Annual review of biophysics and biomolecular structure*, 29:545–76, January 2000. URL: <http://www.ncbi.nlm.nih.gov/pubmed/10940259>, doi:10.1146/annurev.biophys.29.1.545.
- [Pollard et al. 2003] Thomas D. Pollard and Gary G. Borisy. Cellular motility driven by assembly and disassembly of actin filaments.. *Cell*, 112(4):453–65, February 2003. URL: <http://linkinghub.elsevier.com/retrieve/pii/S009286740300120X> <http://www.ncbi.nlm.nih.gov/pubmed/12600310>, doi:10.1016/S0092-8674(03)00120-X.

- [Pontani et al. 2009] Léa-Laetitia Pontani, Jasper van der Gucht, Guillaume Salbreux, Julien Heuvingh, Jean-François Joanny, and Cécile Sykes. Reconstitution of an actin cortex inside a liposome.. *Biophysical journal*, 96(1):192–8, January 2009. URL: [http://www.cell.com/biophysj/abstract/S0006-3495\(08\)00038-6](http://www.cell.com/biophysj/abstract/S0006-3495(08)00038-6) http://www.sciencedirect.com/science?_ob=MIImg&_i, doi:10.1016/j.bpj.2008.09.029.
- [Pring et al. 2003] Martin Pring, Marie Evangelista, Charles Boone, Changsong Yang, and Sally H Zigmond. Mechanism of formin-induced nucleation of actin filaments.. *Biochemistry*, 42(2):486–96, January 2003. URL: <http://dx.doi.org/10.1021/bi026520j>, doi:10.1021/bi026520j.
- [Pruyne et al. 2002] David Pruyne, Marie Evangelista, Changsong Yang, Erfei Bi, Sally Zigmond, Anthony Bretscher, and Charles Boone. Role of formins in actin assembly: nucleation and barbed-end association.. *Science (New York, N.Y.)*, 297(5581):612–5, July 2002. URL: <http://www.sciencemag.org/content/297/5581/612.abstract>, doi:10.1126/science.1072309.
- [Pujol et al. 2012] Thomas Pujol, Olivia du Roure, Marc Fermigier, and Julien Heuvingh. Impact of branching on the elasticity of actin networks.. *Proceedings of the National Academy of Sciences of the United States of America*, 109(26):10364–9, June 2012. URL: <http://www.pnas.org/content/early/2012/06/05/1121238109>, doi:10.1073/pnas.1121238109.
- [Salbreux et al. 2012] Guillaume Salbreux, Guillaume Charras, and Ewa Paluch. Actin cortex mechanics and cellular morphogenesis.. *Trends in cell biology*, 22(10):536–45, October 2012. URL: <http://www.sciencedirect.com/science/article/pii/S0962892412001110> <http://www.ncbi.nlm.nih.gov/pubmed/22871642>, doi:10.1016/j.tcb.2012.07.001.
- [Sandre et al. 1999] O Sandre, L Moreaux, and F Brochard-Wyart. Dynamics of transient pores in stretched vesicles.. *Proceedings of the National Academy of Sciences of the United States of America*, 96(19):10591–6, September 1999. URL: <http://www.ncbi.nlm.nih.gov/article.fcgi?artid=17927&tool=pmcentrez&rendertype=abstract>.
- [Schafer 2004] Dorothy A Schafer. Cell biology: barbed ends rule.. *Nature*, 430(7001):734–5, August 2004. URL: <http://www.nature.com.rproxy.sc.univ-paris-diderot.fr/nature/journal/v430/n7001/full/430734a.html>, doi:10.1038/430734a.
- [Schuh et al. 2008] Melina Schuh and Jan Ellenberg. A new model for asymmetric spindle positioning in mouse oocytes.. *Current biology : CB*, 18(24):1986–92, December 2008. URL: <http://www.ncbi.nlm.nih.gov/pubmed/19062278>, doi:10.1016/j.cub.2008.11.022.
- [Schwarz et al. 2000] E C Schwarz, E M Neuhaus, C Kistler, A W Henkel, and T Soldati. Dictyostelium myosin IK is involved in the maintenance of cortical tension and affects motility and phagocytosis.. *Journal of cell science*, 113 (Pt 4):621–33, February 2000. URL: <http://www.ncbi.nlm.nih.gov/pubmed/10652255>.
- [Seljebotn 2009] Dag Sverre Seljebotn. Proceedings of the Python in Science Conference (SciPy): Fast numerical computations with Cython. 2009. URL: http://conference.scipy.org/proceedings/SciPy2009/paper_2/.
- [Semmrich et al. 2008] Christine Semmrich, Ryan J. Larsen, and Andreas R. Bausch. Nonlinear mechanics of entangled F-actin solutions. *Soft Matter*, 4(8):1675, 2008. URL: <http://xlink.rsc.org/?DOI=b800989a>, doi:10.1039/b800989a.

- [Soeno et al. 1998] Y Soeno, H Abe, S Kimura, K Maruyama, and T Obinata. Generation of functional beta-actinin (CapZ) in an *E. coli* expression system.. *Journal of muscle research and cell motility*, 19(6):639–46, August 1998. URL: <http://www.ncbi.nlm.nih.gov/pubmed/9742448>.
- [Stewart et al. 2011] Martin P Stewart, Jonne Helenius, Yusuke Toyoda, Subramanian P Ramanathan, Daniel J Muller, and Anthony A Hyman. Hydrostatic pressure and the actomyosin cortex drive mitotic cell rounding.. *Nature*, 469(7329):226–30, January 2011. URL: <http://dx.doi.org/10.1038/nature09642> <http://www.ncbi.nlm.nih.gov/pubmed/21196934>, doi:10.1038/nature09642.
- [Sturmer et al. 1995] K Stürmer, O Baumann, and B Walz. Actin-dependent light-induced translocation of mitochondria and ER cisternae in the photoreceptor cells of the locust *Schistocerca gregaria*.. *Journal of cell science*, 108 (Pt 6):2273–2283, 1995.
- [Thoumine et al. 1997] O Thoumine and A Ott. Time scale dependent viscoelastic and contractile regimes in fibroblasts probed by microplate manipulation.. *Journal of cell science*, 110 (Pt 1):2109–16, September 1997. URL: <http://www.ncbi.nlm.nih.gov/pubmed/9378761>.
- [Tinevez et al. 2009] Jean-Yves Tinevez, Ulrike Schulze, Guillaume Salbreux, Julia Roensch, Jean-Francois Joanny, and Ewa Paluch. Role of cortical tension in bleb growth. *Proceedings of the National Academy of Sciences of the United States of America*, 106(44):18581–18586, November 2009. URL: <http://www.ncbi.nlm.nih.gov/pmc/articles/PMC2765453/> <http://www.ncbi.nlm.nih.gov/pmc/articles/PMC2765453/pdf/zpq04409018581.pdf>, doi:10.1073/pnas.0903353106.
- [Valiron et al. 2001] O. Valiron, N. Caudron, and D. Job. Microtubule dynamics. *Cellular and Molecular Life Sciences*, 58(14):2069–2084, December 2001. URL: <http://link.springer.com/10.1007/PL00000837>, doi:10.1007/PL00000837.
- [vanderGucht et al. 2005] Jasper van der Gucht, Ewa Paluch, Julie Plastino, and Cécile Sykes. Stress release drives symmetry breaking for actin-based movement. *Proceedings of the National Academy of Sciences of the United States of America*, 102(22):7847 –7852, May 2005. URL: <http://www.pnas.org/content/102/22/7847.abstract> <http://www.pnas.org/content/102/22/7847.full.pdf> <http://www.pnas.org/content/102/22/7847.short>, doi:10.1073/pnas.0502121102.
- [Vasilev et al. 2012] Filip Vasilev, Jong T. Chun, Giovanni Gragnaniello, Ezio Garante, and Luigia Santella. Effects of ionomycin on egg activation and early development in starfish.. *PloS one*, 7(6):e39231, January 2012. URL: <http://www.pubmedcentral.nih.gov/articlerender.fcgi?artid=3377674&tool=pmcentrez&rendertype=abstract>, doi:10.1371/journal.pone.0039231.
- [Vermeulen et al. 2006] Karen C Vermeulen, Joost van Mameren, Ger J. M Stienen, Erwin J. G Peterman, Gijs J. L Wuite, and Christoph F Schmidt. Calibrating bead displacements in optical tweezers using acousto-optic deflectors. *Review of Scientific Instruments*, 77(1):013704, January 2006. URL: http://rsi.aip.org/resource/1/rsinak/v77/i1/p013704_s1?isAuthorized=no <http://scitation.aip.org/content/aip/journal/rsi/77/1/10.1063/1.2165568>, doi:10.1063/1.2165568.
- [Yao et al. 2011] Norman Y Yao, Daniel J Becker, Chase P Broedersz, Martin Depken, Frederick C MacIntosh, Martin R Pollak, and David A Weitz. Nonlinear viscoelasticity of actin transiently cross-linked with mutant α -actinin-4.. *Journal of molecular biology*, 411(5):1062–71, September 2011. URL: <http://www.sciencedirect.com/science/article/pii/S0022283611007376>, doi:10.1016/j.jmb.2011.06.049.
- [Yarmola et al. 2009] Elena G Yarmola and Michael R Bubb. How depolymerization can promote polymerization: the case of actin and profilin.. *BioEssays : news and reviews*

- in molecular, cellular and developmental biology*, 31(11):1150–60, November 2009. URL: <http://www.ncbi.nlm.nih.gov/pubmed/19795407>, doi:10.1002/bies.200900049.
- [AbuShah et al. 2014] E. Abu Shah and K. Keren. Symmetry breaking in reconstituted actin cortices. *eLife*, 3:e01433–e01433, April 2014. URL: <http://elifesciences.org/content/3/e01433.abstract>, doi:10.7554/eLife.01433.
- [DosRemedios et al. 2003] C G Dos Remedios, D Chhabra, M Kekic, I V Dedova, M Tsubakihara, D A Berry, and N J Nosworthy. Actin binding proteins: regulation of cytoskeletal microfilaments.. *Physiological reviews*, 83(2):433–73, April 2003. URL: <http://www.ncbi.nlm.nih.gov/pubmed/12663865>, doi:10.1152/physrev.00026.2002.
- [SoareseSilva et al. 2011] Marina Soares e Silva, Martin Depken, Björn Stuhrmann, Marijn Korsten, Fred C MacKintosh, and Gijsje H Koenderink. Active multistage coarsening of actin networks driven by myosin motors.. *Proceedings of the National Academy of Sciences of the United States of America*, 108(23):9408–13, June 2011. URL: <http://www.pnas.org/content/108/23/9408>, doi:10.1073/pnas.1016616108.